DOCTORAL THESIS

Development of CdS/Sb_2Se_3 Thin Film Solar Cells: Implications of CdS Processing on Absorber Layer Properties and Device Performance

Sajeesh Vadakkedath Gopi

TALLINNA TEHNIKAÜLIKOOL
TALLINN UNIVERSITY OF TECHNOLOGY
TALLINN 2025

TALLINN UNIVERSITY OF TECHNOLOGY
DOCTORAL THESIS
83/2025

Development of CdS/Sb_2Se_3 Thin Film Solar Cells: Implications of CdS Processing on Absorber Layer Properties and Device Performance

SAJEESH VADAKKEDATH GOPI

TAL TECH PRESS

TALLINN UNIVERSITY OF TECHNOLOGY
School of Engineering
Department of Materials and Environmental Technology

This dissertation was accepted for the defence of the degree 21/10/2025

Supervisor: Asst. Prof. Dr. Nicolae Spalatu
School of Engineering
Tallinn University of Technology
Tallinn, Estonia

Co-supervisor: Dr. Atanas Katerski
School of Engineering
Tallinn University of Technology
Tallinn, Estonia

Opponents: Prof. Alessandro Romeo
Laboratory for Photovoltaics and Solid-State Physics
Department of Computer Science
University of Verona, Italy

Prof. Aile Tamm
Institute of Physics
Physical Optics Laboratory
University of Tartu, Estonia

Defence of the thesis: 27/11/2025, Tallinn

Declaration:
Hereby I declare that this doctoral thesis, my original investigation and achievement, submitted for the doctoral degree at Tallinn University of Technology has not been submitted for doctoral or equivalent academic degree.

Sajeesh Vadakkedath Gopi

_____
signature

European Union
European Regional Development Fund

Investing in your future

Copyright: Sajeesh Vadakkedath Gopi, 2025
ISSN 2585-6898 (publication)
ISBN 978-9916-80-405-6 (publication)
ISSN 2585-6901 (PDF)
ISBN 978-9916-80-406-3 (PDF)
DOI https://doi.org/10.23658/taltech.83/2025

Vadakkedath Gopi, S. (2025). *Development of CdS/Sb_2Se_3 Thin Film Solar Cells: Implications of CdS Processing on Absorber Layer Properties and Device Performance* [TalTech Press]. https://doi.org/10.23658/taltech.83/2025

TALLINNA TEHNIKAÜLIKOOL
DOKTORITÖÖ
83/2025

CdS/Sb_2Se_3 õhukesekilelise päikesepatarei arendus: CdS kihi tehnoloogia mõju absorberkihi omadustele ja seadise efektiivsusele

SAJEESH VADAKKEDATH GOPI

TAL TECH
KIRJASTUS

Contents

Contents 5
List of publications 7
Author's contribution to the publications 8
Introduction 9
Abbreviations 12
1 Literature review 14
1.1 Generations of solar cells 15
1.2 Established and emerging PV technologies with their status 16
1.2.1 Established PV technologies 16
1.2.2 Emerging solar cells 17
1.3 Sb_2Se_3 absorber 19
1.3.1 Structural properties Sb_2Se_3 films 19
1.3.2 Optoelectronic properties of Sb_2Se_3 films 21
1.3.3 Sb_2Se_3 thin film deposition techniques 21
1.3.4 CSS and VTD deposition 23
1.4 Electron Transport Layer (ETL) in thin film solar cells 25
1.5 CdS ETL properties 26
1.6 CdS thin film preparation 29
1.6.1 Physical deposition methods 29
1.6.2 Chemical deposition methods 30
1.7 CdS/Sb_2Se_3 solar cells architecture and performance 31
1.8 Post-deposition thermal annealing treatment of CdS ETL in Sb_2Se_3 solar cells 36
1.9 Post-deposition chloride treatment of CdS ETL in Sb_2Se_3 solar cells 37
1.10 Defects in CdS/Sb_2Se_3 solar cells 39
Summary of the literature review and aims of the study 42
2 Experimental 45
2.1 Fabrication of CdS and Sb_2Se_3 thin films and CdS/Sb_2Se_3 solar cells 45
2.2 Characterisation of thin films 47
2.3 Characterisation of CdS/Sb_2Se_3 solar cells 49
3 Results and discussion 50
3.1 Impact of post-deposition annealing treatment of CdS films on its properties and CdS/Sb_2Se_3 solar cells. 50
3.1.1 The effect of post-deposition annealing on CdS film properties 50
3.1.2 The effect of CdS post-deposition annealing on Sb_2Se_3 film properties 56
3.1.3 The effect of CdS post-deposition annealing on CdS/Sb_2Se_3 solar cell properties. 59

3.2 Impact of In-situ chlorine incorporation in CdS films on its properties and CdS/Sb_2Se_3 solar cells. 61
3.2.1 The effect of in situ chlorine incorporation on CdS film properties 62
3.2.2 The effect of in situ chlorine incorporation in CdS films on Sb_2Se_3 film properties 67
3.2.3 Elemental composition of Cl incorporated CdS and CdS/Sb_2Se_3 interface 68
3.2.4 The effect of in situ chlorine incorporation in CdS films on CdS/Sb_2Se_3 solar cell properties 70
3.3 Impact of Sb_2Se_3 growth rate via VTD on defect formation and PV performance of CdS/Sb_2Se_3 solar cells 72
3.3.1 The influence of D_{So-Sub} and growth rate during VTD on Sb_2Se_3 film properties . 72
3.3.2 The effect of D_{So-Sub} and growth rate during VTD on CdS/Sb_2Se_3 solar cells .. 75
3.3.3 Influence of thermodynamic conditions and VTD system geometry in Sb_2Se_3 film growth and device performance 78
3.3.4 The defect analysis of non-Cl-CdS and Cl-CdS based Sb_2Se_3 solar cells 80
Conclusions 86
References 88
Acknowledgements 104
Abstract 105
Kokkuvõte 108
Appendix 1 111
Appendix 2 125
Appendix 3 141
Curriculum vitae 157
Elulookirjeldus 160

List of publications

The list of the author's publications, based on which the thesis has been prepared:

I **S. V. Gopi**, N. Spalatu, M. Basnayaka, R. Krautmann, A. Katerski, R. Josepson, R. Grzibovskis, A. Vembris, M. Krunks, I. Oja Acik, "Post deposition annealing effect on properties of CdS films and its impact on CdS/Sb_2Se_3 solar cells performance," Frontiers in Energy Research, vol. 11, 2023, Art. no. 1162576, DOI: 10.3389/fenrg.2023.1162576.

II **S. V. Gopi,** N. Spalatu, A. Katerski, J. Kuliček, B. Razek, E. Ukraintsev, M. Š. Bařinková, G. Zoppi, R. Grzibovskis, A. Vembris, and L. Ignatane, "An alternative chlorine-assisted optimization of CdS/Sb_2Se_3 solar cells: Towards understanding of chlorine incorporation mechanism," Journal of Alloys and Compounds, vol. 1005, p. 176175, Nov. 2024, DOI: 10.1016/j.jallcom.2024.176729.

III **S. V. Gopi**, R. Krautmann, A. Katerski, R. Josepson, D. Untila, J. Hiie, M. Krunks, I. Oja Acik, N. Spalatu, "Optimization of VTD Sb_2Se_3 absorber growth rate in CdS/Sb_2Se_3 thin film solar cells: A defect perspective on chloride vs non-chloride based devices", Solar Energy Materials and Solar Cells, vol. 293, 2025, DOI: https://doi.org/10.1016/j.solmat.2025.113856.

Author's contribution to the publications

Contributions to the papers in this thesis are:

I Deposition of Sb_2Se_3 by close-spaced sublimation (CSS) and CdS thin films by chemical bath deposition (CBD), post-deposition annealing treatment of CdS thin films; material characterization by X-ray diffraction (XRD), Van der Pauw, and device characterization by JV curves and external quantum efficiency (EQE) measurement; data analysis and visualization; major role in writing.

II Deposition of CdS films by CBD and Sb_2Se_3 thin films by vapor transport deposition (VTD); material characterization by XRD, device characterization by JV curves, EQE, Scanning Kelvin Probe (SKP) measurement and analysis, SIMS analysis, data analysis and visualization; major role in writing.

III Deposition of CdS films by CBD and Sb_2Se_3 thin films by VTD; material characterization by XRD, device characterization by JV curves, EQE, and temperature-dependent admittance spectroscopy (TAS) measurement and analysis; major role in writing.

Introduction

The urgent need to address climate change and environmental degradation has intensified the global pursuit of sustainable energy solutions. Traditional energy sources, particularly fossil fuels, are increasingly recognized as unsustainable due to their significant carbon emissions and environmental impact. In this context, the transition toward low-carbon and renewable energy sources has become a global imperative. Among these, solar energy stands out as a leading candidate capable of meeting a substantial portion of the world's growing energy demand. Over the past decades, photovoltaic (PV) technology has seen remarkable advancements, both in terms of efficiency and accessibility, contributing to its widespread adoption. The European Union, for instance, has committed to reducing carbon emissions by 55% by 2030 and achieving full carbon neutrality by 2050. This policy momentum has translated into a dramatic increase in solar energy deployment, with installed capacity growing from 3 GW in 2016 to 65.5 GW in 2024, and projections reaching 816 GW by 2030 [1]. However, to sustain and further accelerate this growth, PV technologies must evolve to offer enhanced efficiency, long-term operational stability, and reduced dependence on energy-intensive or scarce materials. While silicon-based solar cells continue to dominate the commercial market, their high manufacturing energy requirements and relatively elevated costs have driven research into alternative technologies. Emerging thin-film solar cell technologies, such as copper indium gallium selenide (CIGS), copper zinc tin sulfide (CZTS), and antimony chalcogenide-based absorbers, offer promising pathways to lower energy and material costs without compromising device performance and stability [2]. These technologies, alongside newer innovations like perovskite and tandem solar cells, are opening doors to applications beyond conventional utility-scale installations, such as integration into Internet of Things (IoT) devices and building-integrated photovoltaics (BIPV), ultimately enabling broader and more flexible utilization of solar energy [3].

This doctoral thesis is primarily focused on the development and optimisation of antimony selenide (Sb_2Se_3) solar cells, a promising thin-film PV technology within the broader class of antimony chalcogenide-based absorbers. Sb_2Se_3 exhibits several advantageous properties that make it highly suitable for next-generation photovoltaics, including earth abundance, low toxicity, a high absorption coefficient (~10^5 cm^{-1}), a favourable direct bandgap of approximately 1.2 eV, and relatively low processing temperatures (~500 °C). As a simple binary compound, Sb_2Se_3 is less prone to secondary phase formation compared to more complex multi-element systems, thereby improving phase purity and material reproducibility. Moreover, its unique one-dimensional crystal structure, consisting of $(Sb_4Se_6)_n$ ribbons held together by van der Waals forces, promotes anisotropic carrier transport along the ribbon axis and contributes to the material's inherent tolerance to grain boundary defects. The theoretically predicted maximum power conversion efficiency (PCE) for Sb_2Se_3-based solar cells approaches 30%; however, the highest experimentally reported PCE to date is approximately 10.5% [4]. This discrepancy highlights the presence of limiting factors that continue to impede performance and indicates substantial room for further optimisation. Although Sb_2Se_3 thin films have been fabricated using both chemical and physical deposition techniques, physical methods, particularly close-spaced sublimation (CSS) and vapour transport deposition (VTD), have shown considerable promise. These methods offer better control over film morphology, especially in achieving vertically oriented, columnar grain structures that are beneficial for carrier transport. Furthermore, the scalability of CSS and

VTD makes them suitable for large-area deposition, positioning them as viable techniques for future commercialisation of Sb_2Se_3-based solar cells [5].

To achieve optimal power conversion efficiency (PCE) from Sb_2Se_3 solar cells, the selection of a suitable partner or ETL (Electron transport layer) is of critical importance. In this doctoral work, cadmium sulfide (CdS) was chosen as the ETL layer for Sb_2Se_3 solar cell fabrication. The choice was primarily motivated by the favourable band alignment between CdS and Sb_2Se_3, the wide band gap of CdS (~2.3 eV), and the practical advantages associated with its deposition via the well-established chemical bath deposition (CBD) technique [6]. The CBD method offers a low-cost, scalable, and reliable route for producing thin, uniform, and adherent CdS films, making it highly compatible with photovoltaic applications. Significant progress has already been reported in the literature regarding the development of CdS/Sb_2Se_3 solar cells. Reported PCEs have reached 9.2% for core-shell structured devices, 10.12% for devices fabricated in substrate configuration, and 10.57% for those employing a superstrate configuration (Publication II).

Although CdS/Sb_2Se_3 solar cells have been the subject of extensive research, systematic studies focused on optimising the CdS ETL through post-deposition treatment (PDT), such as annealing under different ambient conditions and temperatures, are still lacking. In other thin-film technologies like CIGS and CdTe, PDT has been shown to improve ETL quality and interface properties, but similar investigations in Sb_2Se_3 systems remain underexplored. This represents a significant knowledge gap, as fine-tuning the structural, optical, and electronic properties of CdS is essential for enhancing its compatibility with Sb_2Se_3 and improving overall device efficiency. Even with such optimisation, challenges like interface recombination and defect states may persist. Prior studies have attempted to address these issues by applying $CdCl_2$ or $AlCl_3$ treatments on CdS and Sb_2Se_3, resulting in modest improvements in open-circuit voltage (V_{OC}) [7]. However, the direct incorporation of chlorine into the CdS ETL via precursor modification has not been systematically studied before.

To address these gaps, this thesis explores a novel approach by doping CdS with chlorine through the addition of NH_4Cl in the CBD process, allowing Cl incorporation. This strategy is aimed at modifying both the bulk properties of the CdS film and its interface with Sb_2Se_3. In parallel, the deposition parameters of the Sb_2Se_3 absorber layer were optimized, specifically the source-to-substrate distance ($D_{So\text{-}Sub}$) and the introduction of inert Ar gas to better control film morphology and growth kinetics. Together, these studies investigate the fundamental mechanisms and defect states that influence performance, offering new insights into how interface and bulk engineering can be combined to improve the performance of Sb_2Se_3-based solar cells. Advanced characterization such as secondary ion mass spectroscopy (SIMS) has been used to confirm and study the chloride incorporation in the CdS films and the Cd interdiffusion from CdS to Sb_2Se_3. The temperature-dependent admittance spectroscopy (TAS) measurement at different bias voltages confirmed the V_{Sb} and Se_{Sb} defects and the defects closer to the heterojunction.

Based on the research findings, this doctoral thesis is organised into three main chapters. Chapter 1 presents a comprehensive literature review on solar cell technologies, including an overview of different absorbers and ETLs. Special emphasis is given to antimony chalcogenide-based solar cells (Sb_2Se_3, Sb_2S_3, and Sb_2SSe_3), covering their fundamental properties and historical development in terms of efficiency improvements. The chapter also explains the role and characteristics of the CdS ETL, along with detailed descriptions of various deposition techniques for both CdS and Sb_2Se_3 thin films.

Chapter 2 outlines the experimental methodology employed throughout the thesis. It details the deposition methods and processing conditions used for the fabrication of CdS and Sb_2Se_3 layers, supplemented with real and schematic representations of the experimental setups. Additionally, this chapter provides an overview of the characterization techniques used to investigate the structural, optical, and electronic properties of the individual layers, along with the characterization of the complete CdS/Sb_2Se_3 solar cells. Chapter 3 is divided into three sections, each corresponding to the peer-reviewed articles forming the core of this thesis. The first section focuses on the effect of PDT of CdS films on their properties and the subsequent impact on CdS/Sb_2Se_3 device performance. The optimized PDT conditions identified in this study were then used in the second section, which explores a novel approach for chlorine incorporation into the CdS layer via NH_4Cl addition in the CBD process. The final section investigates the impact of growth rate optimization on Sb_2Se_3 absorber properties by tuning the VTD process parameters, particularly the source-to-substrate distance and inert gas introduction. The thesis concludes with a summary of key findings and their implications for the future development of high-performance Sb_2Se_3 solar cells.

Abbreviations

PV	Photovoltaics
CIGS	Copper Indium Gallium Selenide
CZTS	Copper Zinc Tin Sulfide
IoT	Internet of things
BIPV	Building-integrated PV
Sb_2Se_3	Antimony Selenide
Sb_2S_3	Antimony Sulfide
$Sb_2(S,Se)_3$	Antimony Sulfoselenide
Sb_2X_3	Antimony chalcogenide – Sb_2Se_3, Sb_2S_3, $Sb_2(S,Se)_3$
CdTe	Cadmium Telluride
ETL	Electron Transport Layer
HTL	Hole Transport Layer
GaAs	Gallium Arsenide
Si	Silicon
a-Si	Amorphous Silicon
Mo	Molybdenum
E_g	Bandgap energy
α	Photo absorption coefficient
TiO_2	Titanium dioxide
ZTO	Zinc Tin Oxide
CSS	Close-Spaced Sublimation
RTE	Rapid Thermal Evaporation
VTD	Vapor Transport Deposition
PLD	Pulsed Laser Deposition
TE	Thermal Evaporation
CVD	Chemical Vapor Deposition
CBD	Chemical Bath Deposition
CdO	Cadmium Oxide
$Cd(OH)_2$	Cadmium hydroxide
FTO	Fluorine-doped Tin Oxide
ITO	Indium-doped Tin Oxide
RF	Radio Frequency
PDT	Post-Deposition Treatment
SIMS	Secondary Ion Mass Spectroscopy
V_{OC}	Open-circuit voltage
J_{SC}	Short-circuit current density
FF	Fill factor
PCE	Power Conversion Efficiency
EQE	External Quantum Efficiency

SKP	Scanning Kelvin Probe
SEM	Scanning Electron Microscope
E_A	Activation energy
$D_{So\text{-}Sub}$	Source to substrate distance
C	Capacitance
Cl-CdS	Chloride-processed CdS films
k_B	Boltzmann constant
TAS	Temperature-dependent Admittance Spectroscopy
C-CdS	Cubic-CdS
H-CdS	Hexagonal-CdS
T	Temperature
TC	Texture coefficient
V_{Sb}	Vacancy of antimony (Sb) defect
Se_{Sb}	Selenium on Antimony antisite defect
V_{Se}	Vacancy of selenium (Se) defect

1 Literature review

The rapid increase in the global population has significantly heightened the demand for energy resources. The depletion of fossil fuels, which have long served as the primary energy source, has necessitated the exploration of sustainable and future-proof alternatives. Among various renewable energy sources, solar energy stands out due to its abundance, sustainability, and ease of application. The amount of solar radiation reaching the Earth's surface annually is estimated to be approximately 3,400,000 EJ, which vastly exceeds the total estimated reserves of all non-renewable energy sources, including fossil fuels and nuclear energy. Even if only 0.1% of this solar energy were harnessed at an efficiency of just 10%, it would generate nearly four times the world's total electricity production capacity of approximately 3,000 GW [8]. This immense potential makes solar energy one of the most viable and promising solutions for addressing the world's growing energy demands.

Solar energy conversion into electricity primarily relies on photovoltaic (PV) technology, which enables the direct conversion of sunlight into electrical energy. Over the past decade, significant advancements have been made in photovoltaic research, leading to the rapid growth of the solar cell commercial market. Among various solar cell technologies, crystalline silicon (c-Si) solar cells have remained the dominant and most widely adopted technology. The global push towards zero-carbon energy production has further accelerated interest in photovoltaics, particularly with the increasing adoption of electric vehicles (EVs). As nations strive to transition towards sustainable and carbon-free energy solutions, it is imperative that the electricity required to power EV's comes from renewable energy sources, such as solar power, to achieve true decarbonization in the energy sector [8].

A solar cell, also known as a photovoltaic (PV) cell, operates based on a *p*-*n* junction, which establishes an internal built-in potential at the interface. When exposed to sunlight, incident photons excite electrons and holes, generating charge carriers that are subsequently extracted to the external circuit, producing electricity. The design of *p*-*n* junction solar cells involves careful selection of semiconductor materials for the *p*-type (absorber) and *n*-type (ETL) layers to maximize the extraction of photogenerated carriers [1], [8].

The *p*-type material, referred to as the absorber layer, typically possesses a direct bandgap within the range of 1.2–2.0 eV and a high absorption coefficient of 10^4–10^5 cm^{-1}, enabling efficient light absorption. The *n*-type material, also known as the buffer layer, historically (from CdTe) it was called "buffer" and now it is widely accepted to use the term electron transport layer (ETL) terminology, generally exhibits a wide bandgap (2–4 eV) and high optical transparency, facilitating effective charge separation while allowing light to reach the absorber. In addition to these layers, transparent conductive oxides (TCOs) play a crucial role as front contacts, ensuring efficient carrier extraction while maintaining high optical transmittance to enable maximum light absorption at the *p*-*n* junction. Furthermore, thin-film solar cells increasingly incorporate hole transport layers (HTLs) to enhance the selective extraction of holes, while simultaneously blocking electron backflow, thereby improving overall charge transport efficiency and device performance.

Solar cells have been integrated into society for several decades, playing a crucial role in the transition toward renewable energy solutions. However, one of the primary challenges in the widespread adoption of silicon (Si) solar cells has been the energy-intensive process required for the preparation of semiconductor-grade Si wafers,

which significantly increases production costs. The high energy investment associated with Si-based photovoltaics has driven research efforts toward the development of alternative materials that are low-cost, energy-efficient, and composed of earth-abundant elements to serve as viable complementary technologies for silicon solar cells.

This demand has led to the advancement of thin-film solar cell technologies, including cadmium telluride (CdTe), copper indium gallium selenide (CIGS), copper zinc tin sulfide (CZTS), antimony chalcogenide (Sb-based) solar cells, perovskite, and organic solar cells. These next-generation photovoltaic technologies offer promising advantages, such as lower material consumption, reduced manufacturing costs, and compatibility with flexible and lightweight substrates, making them ideal candidates for scalable and sustainable energy production. The continued innovation in thin-film solar cells represents a significant step toward achieving carbon-neutral renewable energy sources, aligning with global efforts to mitigate climate change and reduce dependence on fossil fuels.

1.1 Generations of solar cells

Solar cell technologies are generally classified into three distinct generations based on their material systems, device architecture, manufacturing processes, and technological maturity.

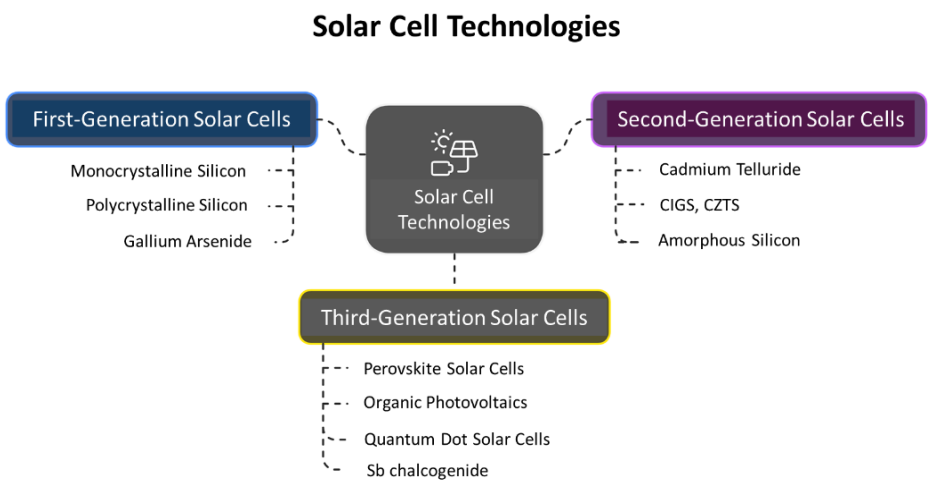

Figure 1. Solar cell technologies in generations.

The evolution of photovoltaic technologies can be broadly classified into three generations (Figure 1). First-generation solar cells, including monocrystalline and polycrystalline silicon (c-Si) and gallium arsenide (GaAs), dominate the market due to their high efficiency and long-term stability, though they require high material consumption and energy-intensive fabrication. Second-generation devices, known as thin-film solar cells, such as cadmium telluride (CdTe), copper indium gallium selenide (CIGS), copper zinc tin sulfide (CZTS), and amorphous silicon (a-Si), offer advantages of reduced material usage, lower processing temperatures, and substrate flexibility but generally show lower efficiencies and stability. Third-generation solar cells, still largely at the research stage, aim to exceed the Shockley-Queisser limit (~30%) using novel architectures like tandem and multijunction structures, though challenges remain in stability and scalability. This

group includes perovskite, organic photovoltaic (OPV), quantum dot, and dye-sensitized solar cells (DSSC), as well as emerging materials like antimony chalcogenides (Sb_2Se_3, Sb_2S_3, $Sb_2(S,Se)_3$), which show promising stability and power conversion efficiency (PCE).

1.2 Established and emerging PV technologies with their status

In this section, a detailed description of the currently available PV technologies, along with their status, is provided.

1.2.1 Established PV technologies

Established PV technologies encompass those solar cell architectures that have undergone extensive research, demonstrated long-term operational stability, and achieved widespread industrial-scale production. These technologies are designated as "established" due to their technological maturity, well-understood fabrication processes, and consistent performance in diverse environmental conditions. Their commercial viability and global market penetration make them reliable benchmarks in the field of solar energy conversion. In this section, a detailed description of these types of solar cells is provided.

Silicon (Si)-based solar cells remain the most commercially dominant PV technology worldwide [9], [10]. Their technological maturity, high efficiency, and stability have secured their leading position in the market. With a theoretical Shockley–Queisser efficiency limit of ~29.4% for single-junction cells (Eg ≈ 1.1 eV) [11], laboratory-scale crystalline Si (c-Si) devices have reached 26.6% efficiency through advanced material engineering, device architectures, and defect passivation techniques [12]. Among different Si technologies, monocrystalline Si solar cells provide superior electrical properties and stability, though at higher cost, while polycrystalline, amorphous, and thin-film Si cells offer lower-cost alternatives with reduced efficiencies and lifetimes [13]. Current research focuses on tandem structures, particularly perovskite/Si tandems, which aim to overcome the single-junction efficiency limit. Theoretical efficiencies up to 44% are predicted [14], while four-terminal perovskite/Si tandems have already demonstrated 29.8% [15]. Despite significant cost reductions over the past decades, the energy-intensive production of high-purity Si wafers and high material consumption remain critical limitations for large-scale deployment [16].

Group III–V semiconductors, particularly gallium arsenide (GaAs), represent another class of high-efficiency PV materials. With a direct band gap of 1.42 eV, high absorption coefficient, and superior thermal and radiation stability, GaAs single-junction solar cells have achieved record efficiencies exceeding 29%, while commercial devices typically deliver 20–25% with anti-reflective coatings [17], [18]. Their robustness under extreme conditions makes them particularly valuable for space applications, where Si devices degrade more rapidly. GaAs is also a key material in multijunction and concentrated photovoltaic (CPV) systems, where it often functions as a middle or top cell, enabling efficiencies above 30% [18], [19]. However, the high production cost restricts its use to specialised and space-based applications rather than large-scale terrestrial deployment.

Cadmium telluride (CdTe) is one of the most successful thin-film PV technologies, offering near-optimal optoelectronic properties with a direct band gap of 1.45 eV and a high absorption coefficient (>10^5 cm^{-1}) [20], [21]. CdTe solar cells have reached a laboratory efficiency of 22.1%, close to the theoretical 25% single-junction limit [22]. The material can be doped both *n*- and *p*-type, although high-quality *p*-type CdTe is more commonly utilised [23]. Large-scale deployment, however, faces challenges from the scarcity of tellurium [24] and a negative temperature coefficient (~–0.4%/°C), which causes

performance degradation under high-temperature operation [25]. Environmental concerns related to cadmium toxicity also necessitate stringent safety and recycling measures, despite Cd being chemically stabilised within the CdTe compound [26].

Copper indium gallium selenide (CIGS) is another widely researched thin-film absorber material with high absorption (>10^5 cm^{-1}) in layers as thin as ~2 µm [27]. CIGS offers a tunable band gap from 1.01–1.68 eV depending on gallium content, enabling spectral optimisation and tandem integration [28]. CIGS cells demonstrate strong low-light response and favourable temperature coefficients, making them attractive for diverse environments [30]. Record efficiencies of 23.6% were reported in 2023 [29], with potential to surpass 24% through further optimisation. Nonetheless, challenges persist in scaling CIGS technology, particularly the cell-to-module efficiency gap, long-term stability, and production complexity. Moreover, reliance on scarce and expensive elements such as indium and gallium raises concerns regarding material availability and sustainability [30].

1.2.2 Emerging solar cells

Emerging PV technologies refer to novel solar cell materials and architectures that are currently under active research and development, but have not yet achieved large-scale commercial deployment. These technologies are termed “emerging“ due to their potential to offer significant advantages over established systems such as lower fabrication costs, improved efficiency, or enhanced material sustainability while still requiring further optimization in terms of stability, scalability, and long-term performance. In this section, well-known emerging PV technologies are explained.

Kesterite (CZTS/Se, Cu_2ZnSnS_4/Se_4) solar cells have attracted significant attention as sustainable thin-film absorbers composed of earth-abundant, non-toxic, and low-cost elements [31], [32], [33]. With a direct band gap of 1–1.5 eV and a high absorption coefficient (>10^4 cm^{-1}), CZTSSe is well suited for light harvesting and laboratory-scale devices [34] have reached efficiencies of 14.9% [35], while theoretical studies predict a potential above 30% [36]. Despite these advantages, their performance is limited by intrinsic defects such as Cu_{Zn} and Sn_{Zn} antisites, severe non-radiative recombination losses, V_{OC} deficits, and undesirable secondary phases [37], [38]. Continued research on defect passivation and interface engineering is essential to close the efficiency gap toward commercialization [39].

Dye-sensitized solar cells (DSSCs), introduced in the 1990s, represent an alternative class of third-generation PV devices [40]. They consist of a mesoporous TiO_2 photoanode sensitized with dyes, a redox electrolyte, and a counter electrode such as platinum [41]. Their advantages include low-cost fabrication, environmental compatibility, and design flexibility [42]. DSSCs have demonstrated up to 14.3% efficiency in laboratory studies and 12.3% in NREL-certified devices [43]. However, limitations such as liquid electrolyte instability, charge recombination at the TiO_2/electrolyte interface, and dependence on costly counter electrodes hinder further progress [44], [45], [46]. Research efforts now focus on solid-state electrolytes, cost-effective electrodes, and advanced sensitizers to improve efficiency and stability.

Organic solar cells (OSCs) are another third-generation technology, offering benefits such as mechanical flexibility, lightweight design, low-cost fabrication, and transparency for potential building-integrated photovoltaics (BIPV). Their active layers typically use conjugated polymers such as P3HT and PEDOT, with fullerene derivatives (e.g., PCBM) as electron acceptors [47], [48], [49]. Charge transport layers like MoO_3 and LiF enhance

carrier extraction [50], while chemical modifications enable tunable band gaps for broad-spectrum absorption [51]. Recent developments have led to single-junction efficiencies of up to 18.7% [52]. However, poor long-term stability due to moisture, UV, and thermal sensitivity continues to limit commercial viability [53], [54], [55].

Quantum dot solar cells (QDSCs) employ semiconductor nanocrystals as light absorbers, whose size-dependent band gap tuning enables harvesting across the UV–IR spectrum [56]. Their potential for multiple exciton generation (MEG) offers a theoretical efficiency limit as high as 66% [57]. Recent advancements have delivered record PCEs of 19.1% in QDSCs and 16.6% in colloidal systems [58], [59]. While promising, challenges remain in improving stability, interface quality, and scalable fabrication.

Perovskite solar cells (PSCs) have rapidly emerged as leading third-generation PVs, built on the ABX_3 perovskite structure where A is a monovalent cation (e.g., MA^+, FA^+, Cs^+), B a divalent metal (Pb^{2+}, Sn^{2+}), and X a halide (Cl^-, Br^-, I^-) [60], [61], [62]. Their exceptional optoelectronic properties and solution-processability have enabled efficiencies above 26.7% for single-junction devices and 34.6% for perovskite/Si tandems, while perovskite/organic tandems have achieved 26.4% [58], [63]. PSCs combine high efficiency with low-cost and flexible processing routes [64]. However, stability issues, lead toxicity, and scalability challenges remain major barriers to industrial deployment [65], [66].

Sb chalcogenide-based solar cells

Among the emerging PV technologies, the Sb-chalcogenide solar cells have grabbed more attention from the researchers due to their very interesting material properties. The primary absorber materials used in this category include binary compounds such as Sb_2S_3 and Sb_2Se_3, along with the ternary alloy $Sb_2(S,Se)_3$, which offers tunable bandgaps ranging from 1.1 to 1.8 eV [67]. Belonging to the V–VI group, structurally, Sb chalcogenides possess a unique ribbon-like quasi-one-dimensional (1D) crystal structure (Figure 2), resulting in anisotropic optoelectronic properties, high absorption coefficients, and excellent physicochemical stability [68], [69]. Remarkably, these compounds crystallise in a stable orthorhombic phase, ensuring high phase purity and minimising the likelihood of secondary phase formation during both physical and chemical thin-film deposition processes. Composed of earth-abundant, low-cost, and non-toxic elements, Sb chalcogenide solar cells offer excellent sustainability and environmental benefits [4], [70]. These features have driven intensive research over the past decade, leading to remarkable improvements in both device performance and publication output (Figure 3), positioning them as promising alternatives to CdTe and CIGS/CZTS solar cells [71].

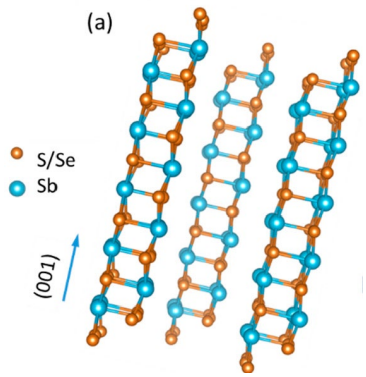

Figure 2. Sb chalcogenide 1D ribbon structure [72].

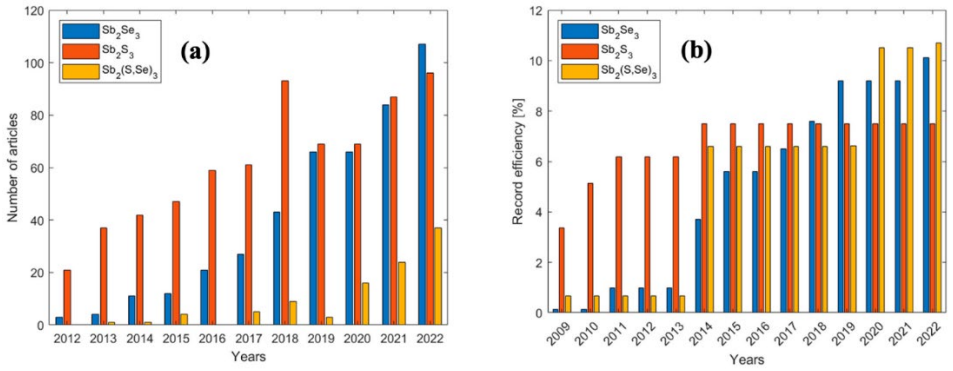

Figure 3. Number of (a) publications and (b) efficiency improvement of Sb chalcogenide solar cells [71].

Sb_2Se_3 and Sb_2S_3 are binary compounds which can be easily deposited through chemical (spin, dip, spray, hydrothermal, atomic layer deposition (ALD)) as well as physical (CSS, VTD, sputtering, rapid thermal evaporation (RTE)) deposition methods [73], [74], [75], [76], [77], [78], [79], [80], [81]. Among these, the development of Sb_2Se_3 absorber layers has shown more promising results when deposited through rapid high-temperature processes, particularly due to their ability to promote a well-aligned columnar grain structure, which is essential for enhancing carrier transport and reducing recombination losses in photovoltaic devices [82]. In contrast, Sb_2S_3 absorber layers have demonstrated superior device performance when deposited using chemical deposition methods. One of the remarkable features of Sb_2S_3-based solar cells is their ability to achieve relatively high PCE with extremely thin absorber layers. This characteristic makes Sb_2S_3 particularly attractive for applications in BIPV, Internet of Things (IoT) devices, and indoor PV systems, where flexibility, transparency, and lightweight features are crucial [3], [83]. The highest reported efficiency for Sb_2Se_3 solar cells is 10.5% using the CBD method [73], while CSS-deposited Sb_2Se_3 devices have achieved efficiencies of up to 9.2% [84] and VTD-deposited ones achieved a maximum of 7.6% [85]. In comparison, Sb_2S_3 solar cells have reached a maximum reported efficiency of 8% in 2022 [86], primarily using chemical deposition techniques. A comprehensive discussion on the material properties of Sb_2Se_3 absorber layers and their influence on device performance will be provided in Section 1.3 of this thesis.

1.3 Sb_2Se_3 absorber

Among the antimony chalcogenide solar cell materials, Sb_2Se_3 holds special significance due to its excellent long-term stability and favourable structural and optoelectronic properties. Its near-optimal bandgap, high absorption coefficient, and unique quasi-one-dimensional crystal structure make it particularly suitable for thin-film photovoltaic applications. In this section, the structural and optoelectronic characteristics of Sb_2Se_3 films are discussed in detail, along with a review of the relevant research that has contributed to understanding and optimizing these properties for solar cell performance.

1.3.1 Structural properties Sb_2Se_3 films

Sb_2Se_3 is a binary compound that crystallizes in a single-phase orthorhombic structure and belongs to the space group *Pbnm* (with lattice constants a = 11.62 Å, b = 11.70 Å, and c = 3.962 Å) or alternatively *Pnma* (with a = 11.793 Å, b = 3.9858 Å, and c = 11.6478 Å.

The crystal structure, as illustrated in Figure 4a, consists of two distinct antimony sites (Sb1 and Sb2) and three selenium sites (Se1, Se2, and Se3), forming quasi-one-dimensional ribbons [87], [88]. These ribbons are strongly bonded within the chain but are held together by weak van der Waals forces in the [010] direction, which gives rise to the material's inherently anisotropic properties.

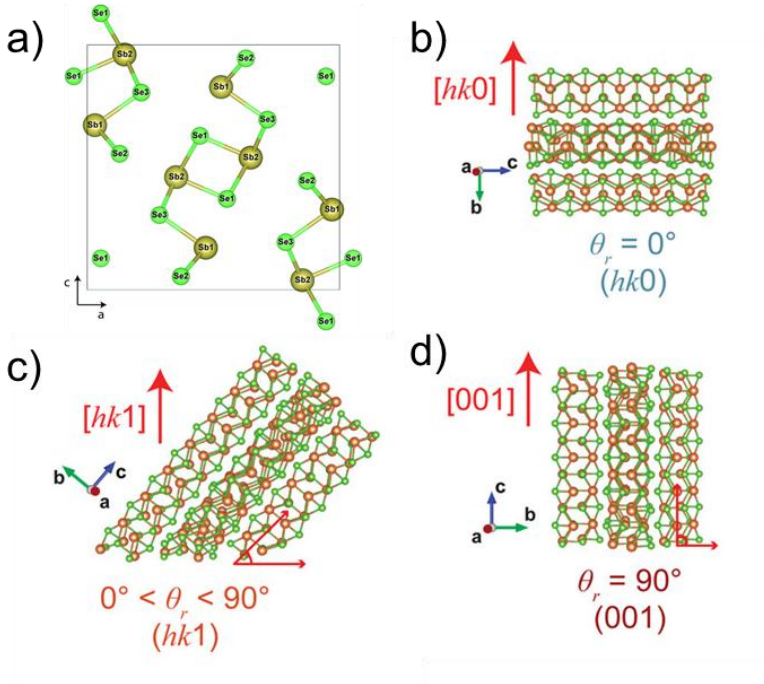

Figure 4. a) Schematic diagram of the Sb_2Se_3 unit cell and crystallographic orientations b) [hk0] c) [hk1] and d) [001][87], [89].

The preferred orientation of these ribbons, particularly the vertical growth of grains along the [001] direction, is considered beneficial for photovoltaic applications, as it promotes efficient carrier transport along the ribbon axis and minimises recombination losses. In practice, such vertical alignment is often characterised by (001) or tilted (hk1) orientations in thin films. Figure 4b, c and d summarise the commonly observed orientations (001, hk0, and hk1) in Sb_2Se_3 thin films. Achieving this desirable orientation depends on several factors, including deposition method, substrate selection, processing temperature, post-deposition annealing, selenization and seed layer incorporation [90], [91], [92]. In superstrate configurations, Sb_2Se_3 is typically deposited on ETL's such as CdS, ZnO, or TiO_2, while in substrate configurations, it is deposited on back contacts like molybdenum (Mo). Notably, PVD methods often favour (hk1) orientation. Krautmann et al. [5] demonstrated that seed layer introduction can enhance vertical grain orientation on TiO_2 substrates. Similarly, Kumar et al. [93] and Zhang et al. [94] reported that post-deposition selenization and thermal treatments significantly improved grain size, compactness, and [hk1] orientation, resulting in enhanced PCE's.

1.3.2 Optoelectronic properties of Sb_2Se_3 films

Sb_2Se_3 is predominantly considered a *p*-type semiconductor, attributed mainly to the presence of intrinsic defects such as selenium antisites (Se_{Sb}). It exhibits a high absorption coefficient exceeding 10^5 cm^{-1}, enabling strong light absorption within a thin absorber layer, which is an essential property for efficient thin-film photovoltaic applications. The optimal bandgap for single junction solar cells is generally accepted to be around 1.2 eV; however, Sb_2Se_3 presents a direct bandgap of approximately 1.03 eV and an indirect bandgap of about 1.17 eV, as reported by Chen et al. [95]. The energy difference between the direct and indirect transitions is notably small, with reported values of 0.04 eV and 0.025 eV by Birkett et al. [96], indicating that Sb_2Se_3 can effectively function as a direct bandgap material for practical purposes.

While most studies confirm the *p*-type behaviour, there have also been observations of *n*-type conductivity in Sb_2Se_3 films, particularly when there are unintentional chlorine impurities present in the material, as reported by Hobson et al. [97] Chlorine impurities are known to act as shallow donor dopants, thereby altering the majority carrier type of the material. Notably, such *n*-type behaviour has been reported in TiO_2/Sb_2Se_3 solar cells by Spalatu et al. [5], suggesting the formation of *n*-*n* heterojunctions, which can still yield appreciable PCE.

Furthermore, the electrical conductivity of Sb_2Se_3 exhibits a strong anisotropy, consistent with its quasi-one-dimensional crystal structure. Charge carrier mobility and conductivity are significantly higher along the ribbon direction (typically the [001] crystallographic orientation), with reported conductivity values being nearly twice as high compared to those measured perpendicular to the ribbon axis. This directional dependence highlights the importance of achieving vertical orientation in Sb_2Se_3 thin films to optimize carrier transport and minimise recombination losses in photovoltaic devices.

1.3.3 Sb_2Se_3 thin film deposition techniques

Chemical deposition techniques

The chemical deposition of Sb_2Se_3 thin films involves the formulation of a stoichiometrically balanced precursor solution, its deposition onto a substrate, followed by thermal treatment to remove residual solvents and facilitate the crystallization of the Sb_2Se_3. Several chemical methods have been employed for this purpose, including spin coating, spray pyrolysis, hydrothermal synthesis and chemical bath deposition (CBD). Each technique offers specific advantages and challenges in terms of cost, control over film morphology, and compatibility with large-scale processing.

Spin coating is one of the most widely used methods due to its simplicity and good control over film thickness and uniformity. In this technique, centrifugal force is used to distribute the precursor solution uniformly across the substrate surface, typically under ambient conditions or within a controlled glovebox atmosphere. Notably, Ma et al. [98] reported a PCE of 5.4% for a superstrate configuration device (FTO/CdS/Sb_2Se_3/Spiro-OMeTAD/Au) using spin-coated Sb_2Se_3 films.

Spray coating, another cost-effective and scalable deposition method, involves atomising the precursor solution using either an ultrasonic or pneumatic spray nozzle and directing it onto a heated substrate. This technique facilitates rapid film formation and is particularly advantageous for large-area deposition. Rajpure et al. demonstrated the fabrication of *p*-type Sb_2Se_3 films with a reported bandgap of 1.88 eV at a film thickness of 500 nm using this method [99].

Hydrothermal synthesis presents a markedly different approach, relying on the chemical reaction of precursors under high-pressure, high-temperature conditions within a sealed autoclave. This method enables precise control over crystallinity and phase purity. Dan Liu et al. [100] successfully employed hydrothermal synthesis to fabricate Sb_2Se_3-based solar cells with a PCE of 7.6% in a similar FTO/CdS/Sb_2Se_3/Spiro-OMeTAD/Au architecture.

CBD, although traditionally used for the deposition of CdS ETL's, has also been explored for Sb_2Se_3 absorber layer fabrication. Zhao et al. reported a remarkable PCE of 10.57% for a device employing CBD-deposited Sb_2Se_3, highlighting the technique's potential for high-performance solar cell fabrication [73].

While chemical deposition techniques are advantageous due to their low cost, simplicity, reproducibility, and scalability, they also present significant challenges. Chief among these is the need for precise stoichiometric control of the precursor solution to avoid secondary phase formation and maintain film uniformity. Additionally, the choice of solvents and additives can significantly influence the morphology and optoelectronic properties of the resulting films. A critical limitation of chemical methods for Sb_2Se_3 deposition is the difficulty in achieving the preferred [hk1] or [001] crystallographic orientations, which are essential for efficient charge transport along the quasi-one-dimensional ribbon structure of Sb_2Se_3 [101].

Physical deposition techniques

These techniques for Sb_2Se_3 absorber layers are typically carried out under high vacuum conditions (10^{-3} to 10^{-6} mbar), which significantly minimises contamination and enables the controlled evaporation of source material at elevated temperatures (~500 °C). These methods allow precise manipulation of film thickness, composition, and crystallinity, making them highly suitable for photovoltaic applications. Commonly used physical vapour deposition (PVD) techniques for Sb_2Se_3 include rapid thermal evaporation (RTE), CSS, vapor transport deposition (VTD), sputtering, electron beam evaporation (EB), and pulsed laser deposition (PLD).

In EB evaporation, a focused high-energy electron beam is directed at the Sb_2Se_3 source material to induce localised heating and vaporisation. The evaporated material condenses onto a preheated substrate, typically maintained at ~300 °C. Films deposited using this method tend to be Sb-rich and often require post-deposition selenium treatment (selenization) to achieve the desired stoichiometry. Tiwari et al. reported substrate-configuration solar cells fabricated using EB-deposited Sb_2Se_3 films with [hk0] orientation and a resulting PCE of 4% [102].

The RTE technique enables rapid deposition by evaporating the Sb_2Se_3 material at a fast rate (~1 µm/min) in a vacuum environment. The source material, placed in a crucible made of alumina, graphite, or quartz, is heated either directly via Joule heating or indirectly using infrared lamps [103]. The vaporised material condenses on the substrate maintained at a lower temperature (~300 °C). Tang et al. successfully deposited Sb_2Se_3 films, but they were oriented in the [hk0] direction. Meanwhile, a maximum PCE of 7.6% was reported using this method by other groups [104].

Sputtering, a widely used deposition technique, involves the bombardment of a solid Sb target by high-energy argon ions, causing atoms to be ejected and deposited onto the substrate. This process is typically conducted in a vacuum and followed by selenization or selenium co-evaporation to form stoichiometric Sb_2Se_3. Tang et al. [105] fabricated substrate configuration solar cells (glass/Mo/Sb_2Se_3/CdS/ITO/Ag) with a PCE of 5.52% using this method. Luo et al. [106] further enhanced the performance to 6.11% through

sputtering of Sb metal followed by controlled selenization. Post-deposition thermal annealing is reported to be a crucial step in optimizing the performance of sputtered Sb_2Se_3 films. For example, Tang et al. [107] demonstrated a significant PCE enhancement from 5.37% to 8.64% after annealing. However, in the superstrate configuration, sputtered Sb_2Se_3 films tend to yield lower PCE's compared to those deposited thermal method. This has been attributed to damage at the ETL interface, arising from the impingement of high-energy Sb or Se atoms during the sputtering deposition [71].

PLD offers another route for depositing Sb_2Se_3 films by utilising high-energy laser pulses to sublimate the target material in a vacuum chamber. The evaporated/sublimated species condense onto the heated substrate to form a thin film. This technique provides excellent control over stoichiometry, often replicating the source material composition with high accuracy. The deposition environment can be modified with partial pressures of inert or reactive gases to fine-tune the film properties. PLD is also suitable for depositing a variety of layers, including CdS ETL's. Yang et al. fabricated superstrate configuration Sb_2Se_3 solar cells ($FTO/SnO_2/CdS/Sb_2Se_3/Au$) using PLD and reported a PCE of 4.4% [108].

1.3.4 CSS and VTD deposition

Among the physical deposition methods, CSS and VTD methods are well known for their ability to prepare vertically oriented Sb_2Se_3 films and have reported remarkable efficiencies. Given their significance, a detailed examination and comparative analysis of CSS and VTD techniques is presented in the following section.

Comparison of CSS and VTD of Sb_2Se_3 films

The CSS method involves the direct sublimation of Sb_2Se_3 material, typically in the form of granules or powder, followed by its condensation onto a heated substrate. The deposition is carried out in a vacuum chamber maintained at a pressure of approximately 10^{-6} mbar. A critical feature of this method is the small distance between the source material and the substrate, typically 2–3 cm (Figure 5). This short spacing allows high temperature, rapid deposition of the material. In this thesis, a custom-designed CSS reactor was employed for the deposition of Sb_2Se_3 thin films. A detailed schematic of the reactor and deposition parameters used in this PhD work is provided in Chapter 2 of the thesis.

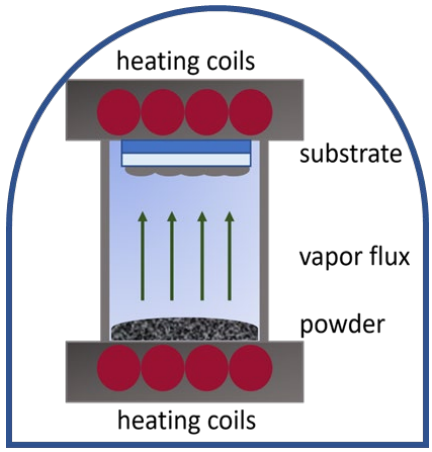

Figure 5. Schematic diagram of the CSS system [109].

Typically, the deposition rate exceeds 1 µm/min, with source temperatures around 500 °C and substrate temperatures ranging from 300–450 °C. These parameters may vary depending on the geometry of the CSS reactor. In most reported studies, CSS deposition is performed in a static vacuum environment, which characterizes this method as a vertical deposition technique [71]. Under these conditions, the deposition rate increases with higher source temperature and decreases with higher chamber pressure. To control the deposition rate while maintaining elevated source temperatures, researchers, including Hobson et al. [97], have introduced inert gases such as N_2 or Ar into the chamber.

For Sb_2Se_3 films, the CSS technique effectively promotes columnar grain growth, which is most observed along the [hk1] orientation. Among these, the [211] orientation, representing a tilted grain growth direction, is predominantly reported. High-efficiency devices employing CSS-grown Sb_2Se_3 absorber films have been demonstrated in both substrate and superstrate configurations. For instance, Li et al. [84] reported a PCE of 9.2% using a substrate configuration of $Mo/MoSe_2/Sb_2Se_3/TiO_2/CdS/i\text{-}ZnO/AZO/Ag$. In a superstrate configuration, Don et al. [110] achieved an efficiency of 8.12% using RF-sputtered TiO_2 as the ETL. Additionally, Guo et al. [111] reported a PCE of 7.3% using CdS as the ETL and NiO as the hole transport layer in a device structure of $glass/FTO/CdS/Sb_2Se_3/NiO_x/Au$.

The VTD technique (Figure 6), also referred to as a horizontal deposition method, is typically carried out within a quartz process tube wherein the Sb_2Se_3 source material is thermally evaporated and subsequently transported to the substrate with the assistance of a carrier gas. RTE and CSS, which utilise a close and fixed source-to-substrate distance typically in the range of 2-10 cm, the VTD setup allows for greater flexibility in adjusting this distance. The use of inert carrier gases such as nitrogen (N_2) or argon (Ar) facilitates controlled vapor transport and contributes to the stabilisation of the vapor phase environment during deposition. The schematic of the VTD setup and deposition parameters used for the deposition of Sb_2Se_3 films for this thesis research is provided in Chapter 2.

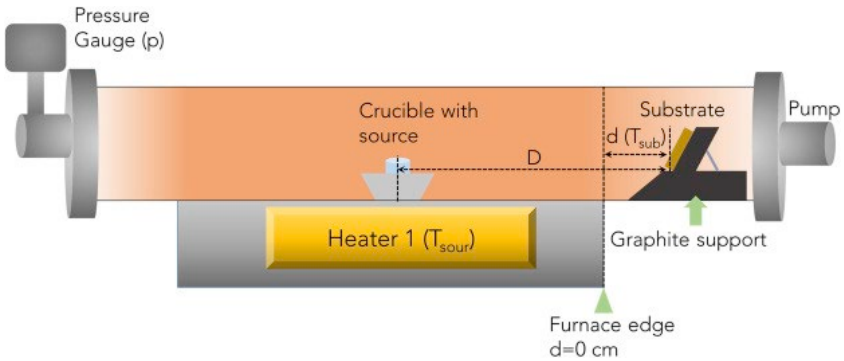

Figure 6. Schematic diagram of VTD setup used for thin film deposition [112].

This enhanced tunability of deposition parameters, particularly the source-to-substrate distance and carrier gas flow rate, enables improved control over the nucleation and growth mechanisms of Sb_2Se_3 thin films. Consequently, VTD has been shown to promote the formation of vertically oriented columnar grains along the [hk1] direction. Improved crystallinity and preferred grain orientation in VTD-grown films have been associated with a reduction in bulk and interface-related defects, thereby contributing to enhanced

device performance. Notably, Wen et al. [85] reported a PCE of 7.6% using CdS as the ETL in a superstrate configuration (glass/FTO/CdS/Sb_2Se_3/Au).

When comparing VTD with CSS, it is evident that both methods are capable of producing vertically oriented Sb_2Se_3 films with columnar morphology. However, the fixed short distance in CSS may lead to re-evaporation of the deposited material from the substrate surface, potentially resulting in the formation of non-uniform or defective films. In contrast, the VTD technique offers greater flexibility in tuning the deposition environment, enabling more precise control over film crystallinity, thickness, and uniformity.

1.4 Electron Transport Layer (ETL) in thin film solar cells

The ETL, is a critical component in thin-film solar cells, enabling efficient extraction and transport of photo-generated electrons to the front contact while preventing direct absorber–electrode interaction that could increase recombination losses. An ideal ETL requires high electron mobility, proper conduction band alignment with the absorber, good optical transparency, and thermal/chemical stability during fabrication.

In thin-film technologies such as CdTe, CIGS, CZTS, Sb_2Se_3, Sb_2S_3, and $Sb_2(S,Se)_3$, ETL selection is guided by band alignment and optoelectronic properties, which dictate charge extraction and recombination behaviour. Common ETL materials include CdS, TiO_2, ZnO, SnO_2, ZnS, ZTO, and ZnMnO [113], [114], [115], [116], [117], [118], [119], with CdS being the most widely employed. CdS exhibits excellent lattice matching with CIGS (<1% mismatch), though larger mismatches exist for CdTe (~10%) and CZTS (~7%) [120], [121]. Alternative ETLs such as ZnS reduce this mismatch to ~1% with CZTS [122]. Additionally, TiO_2 deposited by USP has been successfully applied to Sb_2S_3 solar cells, yielding PCE values up to ~7% [3], [78].

ETLs in Sb_2Se_3 thin-film solar cells

In Sb_2Se_3 solar cells, the lattice mismatch between CdS and Sb_2Se_3 is reported to exceed 10%, which can theoretically lead to strain generation, defect formation, and enhanced non-radiative recombination losses at the interface [123]. To overcome this challenge, several strategies have been explored to minimise lattice mismatch and improve the interface quality. One of the commonly employed approaches involves modifying the deposition environment of the Sb_2Se_3 absorber layer. Deposition under oxygen-rich conditions has been reported to passivate dangling bonds at the CdS/Sb_2Se_3 interface, thereby reducing interface defect density and improving device performance [124].

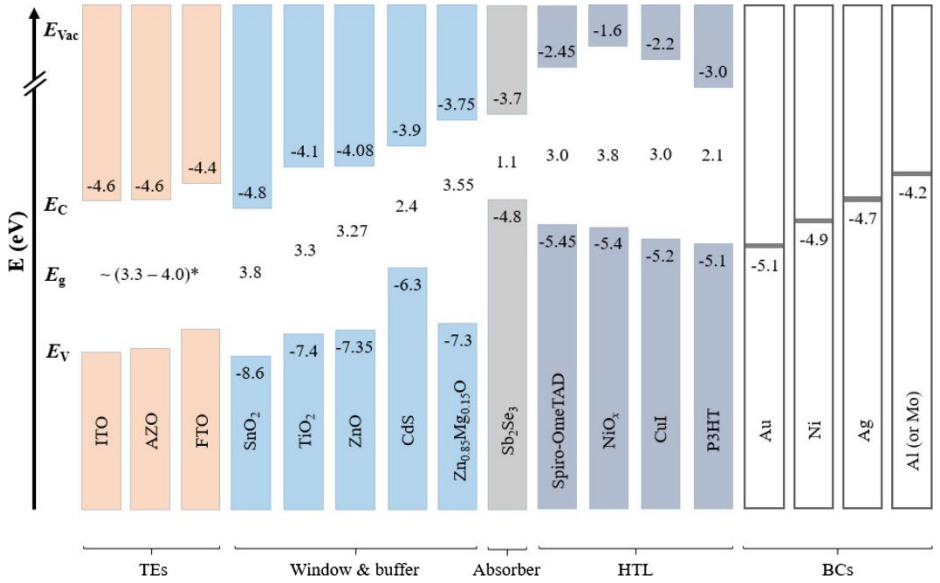

Figure 7. Schematic of the band alignment of Sb_2Se_3 solar cells with various ETL (SnO_2,TiO_2, ZnO, CdS, ZnMnO) along with front and back contacts [122].

Furthermore, the use of alternative ETL materials such as ZnO has also shown promising results in reducing defect densities at the interface [125]. Don et al. [110] and Chen et al. [118] has studied the application of RF sputtered and spin deposited TiO_2 layer on the Sb_2Se_3 solar cells and achieved a PCE of a maximum of 8% and 5.48% respectively. Despite the significant lattice mismatch, CdS still remains the most widely employed ETL in Sb_2Se_3-based solar cells, primarily due to its suitable band alignment, well-established deposition protocols, and successful integration in existing thin-film solar cell fabrication processes. Figure 7 shows the suitable band alignment of the CdS and its comparison to the other possible alternative ETL with the Sb_2Se_3 absorber layer. These advantages make CdS a promising candidate for future applications, particularly in large-area, scalable, thin-film photovoltaic technologies.

1.5 CdS ETL properties

CdS is a II–VI compound semiconductor extensively studied for its role in optoelectronic and photovoltaic devices. First synthesised by Joseph Louis Gay-Lussac in 1818 and initially used as a yellow pigment, CdS later gained importance as a semiconductor material owing to its direct band gap of ~2.4 eV, high transparency, and favourable band alignment with many absorber layers [126]. Its ability to facilitate efficient charge separation and electron transport, while suppressing recombination losses, has established CdS as the most common ETL in thin-film solar cells.

Considering the structural properties, CdS crystallises primarily in two phases: the thermodynamically stable hexagonal wurtzite ($P6_3mc$) and the metastable cubic zinc blende (F-43m), both of which exhibit tetrahedral coordination but differ in stacking and symmetry, leading to subtle variations in electronic and optical properties [127], [128], [129], [130], [131] (Figure 8). The hexagonal phase dominates bulk and thin-film CdS grown under standard deposition conditions, whereas the cubic phase is stabilised under nanoscale or kinetically controlled environments [128], [129]. Thermal annealing strongly

influences grain growth and crystallinity but can also promote secondary phase formation. At elevated temperatures in oxidising atmospheres, CdS undergoes partial oxidation, producing CdO or $Cd(OH)_2$-derived CdO, both of which alter lattice parameters and degrade electronic properties [129], [131], [132], [133], [134], [135]. Additives such as sodium hexametaphosphate (SHMP) or polyvinyl pyrrolidone (PVP) can modify nucleation pathways, affecting crystallite size, surface energy, and phase stability, while precursor chemistry and stoichiometry critically determine final phase purity [131], [136].

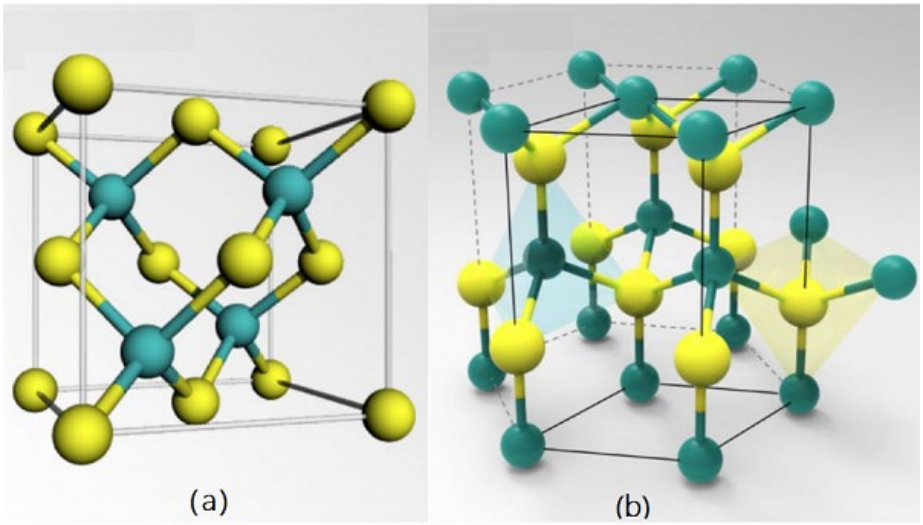

Figure 8. a) Cubic zinc blende and b) hexagonal wurtzite crystal structures of CdS [127].

CdS exhibits a direct band gap in the range of 2.35-2.50 eV, ensuring high transparency across the visible spectrum while supporting efficient photo-generated carrier transport [137], [138], [139]. Several factors, such as thermal annealing, Substrate temperature, elemental doping, deposition method, thickness and chlorine incorporation, could affect the opto-electronic properties of the fabricated CdS films. A detailed dependence of these factors on the bandgap, carrier concentration, resistivity and mobility reported in the literature has been summarised in Table 1. Overall, the structural phase, microstructure, and opto-electronic properties of CdS films directly govern their performance as ETLs, highlighting the need for careful deposition and annealing control to ensure compatibility with absorber layers such as Sb_2Se_3.

Table 1. The effect of different parameters on the optoelectronic properties of CdS films.

No.	Factor	Effect on band gap	Bandgap (eV)	Carrier concentration (/cm^3)	Resistivity (Ω.cm)	Mobility (cm^2.V^{-1} .S^{-1})	Ref
1.	Thermal Annealing	Decreases band gap due to improved crystallinity	2.43-2.57	10^{15}-10^{17}	10-10^2	1-50	[138], [139], [140], [141]
2	Substrate temperature	Slight increase in band gap	2.42-2.48	10^{16}-10^{18}	10^{-1}-10	5-80	[142], [143], [144]
3.	Doping (Zn-La)	Zn↑, La↓ bandgap	2.09-2.5	10^{17}-10^{19}	10^{-2}-10	10-100	[137], [145]
4.	Deposition method	Morphology dependent	2.35-2.5	10^{15}-10^{17}	10-10^4	0.1-10	[137], [141], [142], [143], [145], [146]
5.	Thickness/ crystalline size	Blue shift with reduced size	2.42-2.5	10^{15}-10^{16}	10^2-10^4	0.1-5	[143], [145], [146]
6.	Chlorine incorporation	Increase at particular conc.	2.45-2.47	10^{13}-10^{14}	10^4	NA	Publication II

1.6 CdS thin film preparation

A wide range of deposition techniques has been utilized to fabricate CdS thin films, which can be broadly classified into physical and chemical deposition methods. Physical deposition techniques, typically performed in vacuum environments, include CSS, Thermal Evaporation (TE), Radio Frequency (RF) Sputtering, and PLD, among others. These methods offer precise control over film thickness and composition but often require specialized equipment and vacuum conditions. In contrast, chemical deposition techniques, such as Chemical Bath Deposition (CBD), Spray Pyrolysis, Chemical Vapor Deposition (CVD), and Electrodeposition, are more cost-effective. Each of these methods influences the structural, optical, and electrical properties of CdS films in distinct ways. In this section, we provide a comprehensive review of these deposition techniques.

1.6.1 Physical deposition methods

CdS films deposited by physical methods such as CSS, RF sputtering, and PLD have shown superior properties, making them attractive for high-performance solar cells.

CSS-CdS ETLs deposited at high vacuum and short source-to-substrate distances (0.3–2 cm) exhibit enhanced crystallinity, large grain sizes, and high optical transmittance (245–1700 nm), which reduce defect density and improve carrier transport [147], [148], [149]. Post-deposition annealing in oxygen atmospheres further improves V_{OC}, while reducing atmospheres show detrimental effects [150]. Optimised CSS-CdS films achieve resistivity as low as 2.2×10^{-3} Ω.cm and carrier concentrations of 8.3×10^{12} cm^{-3} [151]. Though CBD-CdS can yield a stronger short-wavelength response [152], CSS films provide superior stability and transport, with Spalatu et al. reporting higher PCEs in Sb_2Se_3 devices compared to CBD-CdS due to reduced grain sintering [4].

Structural, optical, and electronic properties of CdS films fabricated by RF sputtering strongly depend on deposition parameters. Increasing RF power (50–150 W) promotes a transition to the hexagonal wurtzite phase with larger grains and reduced dislocation density [153]. Optimised substrate temperatures (200–250 °C) and annealing at 400 °C enhance crystallinity, yield ~2.43 eV bandgaps, and increase transmittance up to 72.25% [154], [155]. Sputtered films also achieve low resistivity ($<10^3$ Ω.cm) and high carrier concentrations ($>10^{16}$ cm^{-3}), critical for minimising series resistance [155], [156], though sputtering pressure requires optimisation due to trade-offs between crystallinity and transparency [157].

PLD enables precise control of film thickness and uniformity, producing smooth, uniform CdS layers with polycrystalline preferential orientation as confirmed by XRD and Raman studies [158], [159]. These films show high visible transmittance and a direct bandgap near 2.4 eV [159]. SEM (Scanning Electron Microscope) and AFM (Atomic Force Microscopy) analyses reveal uniform morphologies beneficial for interface quality and stability. Furthermore, PLD avoids liquid precursors, reducing chemical waste and offering an environmentally friendly alternative [160], [161]. In CIGS solar cells, however, PLD-CdS yielded lower efficiencies (~13%) compared to CBD-CdS (~16%), attributed to the presence of CdO and $Cd(OH)_2$ phases in CBD films that improve lattice matching with absorbers [147].

1.6.2 Chemical deposition methods

Chemical Vapor Deposition (CVD) methods, particularly aerosol-assisted CVD (AACVD) and metal-organic CVD (MOCVD), have proven effective for producing high-quality CdS films. AACVD using precursors such as $Cd[(SP^{i}Pr_2)_2N]_2$ enables uniform growth and crystallinity, as confirmed by XRD and Raman analysis [162]. In MOCVD, deposition kinetics are strongly dependent on substrate temperature and precursor pressures, allowing precise control of microstructure and phase. Reports also highlight cadmium bis(O-alkylxanthates) as a potential single-source precursor [163]. The resulting films generally exhibit high crystallinity, smooth morphology, and band gaps near 2.4 eV, ensuring effective optical transmittance and heterojunction formation with absorbers.

Spray Pyrolysis has also been employed to deposit CdS thin films, with substrate temperature being a critical parameter. Higher deposition temperatures (~500 °C) yield improved crystallinity, smoother surfaces, and enhanced optical transmittance [164], while intermediate temperatures (~300 °C) reduce series resistance and improve V_{OC} and FF [165]. Optimising precursor molarity and Cd/S ratios further enhances crystallite size, conductivity, and transmittance [166], with optical bandgap tuning reported between 2.2–2.5 eV depending on conditions [167].

Electrodeposition offers a low-cost, controllable route for CdS ETL fabrication. Optimised electrolyte compositions (e.g., 0.10 mol/L $CdCl_2$, 0.01 mol/L $Na_2S_2O_3$, pH 1.5–2.0, 55–65 °C) and applied voltages (~1450 mV) produce hexagonal wurtzite CdS films with compact morphology, crystallite growth, and band gaps of 2.2–2.47 eV [168], [169], [170], [171]. The addition of tartaric acid improves film uniformity by preventing precipitation, while substrate pretreatments enhance adhesion. Although AC electrodeposition methods have shown improved CdS quality, issues remain with controlling thickness and electrical properties [172].

Chemical Bath Deposition (CBD)

CBD is a widely utilised method for fabricating thin films, especially in the context of photovoltaic device fabrication, owing to its simplicity, cost-effectiveness, and adaptability. Among the various deposition techniques, CBD stands out for its ability to yield conformal, uniform thin films over large substrate areas at low processing temperatures, making it particularly advantageous for scale-up in solar cell manufacturing [148], [173]. The first report on CBD-deposited CdS films was published by Mokrushin et al. in 1961 [174].

The CBD process is based on the controlled chemical reaction between cadmium and sulfur precursors in an aqueous solution. Typically, a sulfur source such as thiourea decomposes under alkaline conditions to release HS^- ions, which then react with cadmium ions (commonly from cadmium acetate ($Cd(O_2CCH_3)_2(H_2O)_2$), cadmium sulfate ($CdSO_4$) or cadmium chloride ($CdCl_2$)) to form CdS on the substrate surface [173], [175], [176]. The reaction kinetics and film characteristics are strongly influenced by the use of complexing agents (e.g., NH_4OH, NH_4Cl, $Na_3C_6H_5O_7$), which moderate the free ion concentrations and deposition rate. The bath conditions, such as pH, temperature, and reactant concentrations, are critical in determining the morphology, thickness, crystallinity, and optoelectronic properties of the resulting films [177].

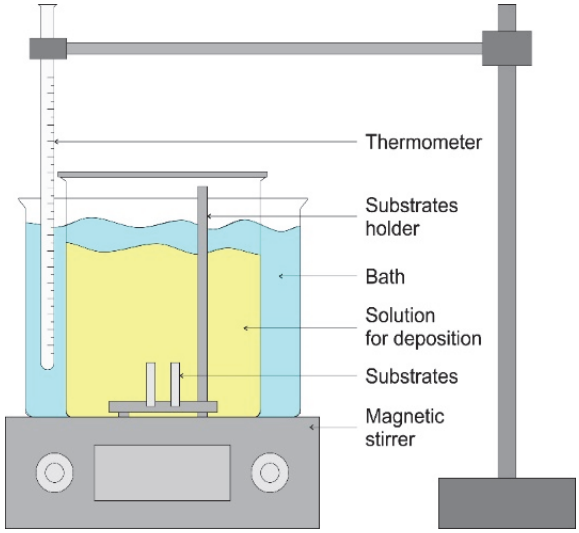

Figure 9. Schematic diagram of the CBD procedure of CdS films [174].

CBD-deposited CdS films exhibit suitable optical transparency in the visible region as well as the band gaps (~2.4 eV), making them well-suited for use as ETL's in heterojunction solar cells [141]. Furthermore, these films are generally characterised by uniform surface morphology and minimal pinholes, both essential attributes for interface stability and reduced recombination. The use of CBD-grown hexagonal-phase CdS (H-CdS) films in Sb_2Se_3 solar cells has led to an efficiency improvement of up to 80% by reducing interfacial recombination and enhancing spectral response [178]. Post-deposition treatment of the CBD CdS films, such as post-deposition annealing in air or ambient conditions (N_2, Ar, Vacuum and H_2) has helped to fine-tune the electrical as well as the structural properties to have better alignment and matching to CdTe as well as Sb_2Se_3 solar cells [174], [179]. Alternative materials such as CdSe, ZnS and TiO_2 deposited by other various methods are also being explored for ETL, but CBD-grown CdS remains a benchmark due to its reliability and favourable band alignment with CdTe, CZTS, CIGS and Sb_2Se_3 absorber layers.

Compared to other deposition techniques such as physical vapor deposition (PVD), pulsed laser deposition (PLD), or electrodeposition, CBD offers several distinct advantages. It is inherently low-cost, operates under atmospheric pressure, and does not require complex vacuum systems, thereby enabling straightforward scalability for industrial processes [180]. Furthermore, its adaptability to various substrates, including flexible materials, and its ability to produce high-quality, pinhole-free films with controlled thickness make CBD an ideal technique for fabricating CdS ETL in high-performance thin-film solar cells.

1.7 CdS/Sb_2Se_3 solar cells architecture and performance

This section provides an overview of the most commonly used CdS/Sb_2Se_3 device architectures and their constituent layers, followed by a summary of the key performance achievements documented in the literature.

CdS/Sb_2Se_3 solar cells are typically fabricated in two distinct configurations: superstrate and substrate (as illustrated in Figure 10). In the superstrate configuration,

the device stack is built upon a transparent conductive oxide (TCO), such as fluorine-doped tin oxide (FTO) or indium tin oxide (ITO), which serves as the front contact supported by a glass substrate. CdS film deposited by CBD or other suitable methods functions like the ETL and is followed by the Sb_2Se_3 absorber layer. On top of the absorber, a hole transport layer (HTL), commonly Spiro-OMeTAD or poly(3-hexylthiophene) (P3HT) is applied, and the device is completed with a gold (Au) back contact. In this configuration, incident solar radiation enters the device through the glass substrate and passes sequentially through the TCO and ETL layers to reach the Sb_2Se_3 absorber layer.

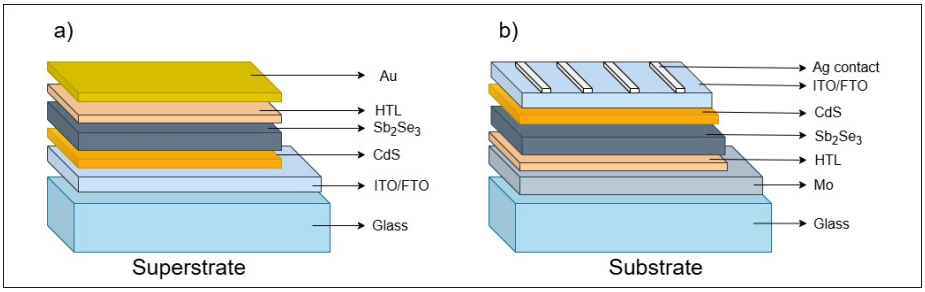

Figure 10. a) superstrate and b) substrate configuration of CdS/Sb_2Se_3 solar cells.

In contrast, the substrate configuration begins with a metal back contact, typically molybdenum (Mo) sputtered or thermally evaporated onto a glass substrate. Subsequently, the HTL and Sb_2Se_3 absorber layers are deposited, followed by the CdS ETL and finally the front TCO layer (FTO or ITO). Metallic grid contacts, such as Ag or Au, are deposited on top of the TCO to facilitate charge collection. In this configuration, the incident light passes directly through the top TCO and CdS layers to reach the absorber, while the glass substrate primarily serves as a mechanical support without contributing to optical transmission.

Both device configurations are designed to facilitate efficient charge transport and minimise recombination losses at the interfaces. However, each presents specific challenges that can impact device performance. In the superstrate configuration, the high temperature deposition of the Sb_2Se_3 absorber layer onto the underlying CdS ETL can lead to the formation of CdSe alloy at the interface. Several studies have reported that this intermixing may be detrimental to device performance. Conversely, substrate configuration devices often experience optical shading losses due to the presence of metallic front contacts (e.g., Ag), which can reduce the effective area available for light absorption. Additionally, the interface between the Mo back electrode and the Sb_2Se_3 absorber layer has issues related to lattice mismatch and poor adhesion. This challenge is typically mitigated by employing a selenization step, which induces the formation of a thin interfacial $MoSe_2$ layer.

CdS/Sb_2Se_3 solar cells have been the focus of extensive research over the past decade, demonstrating significant advancements in both superstrate and substrate configurations. A variety of deposition techniques have been employed to fabricate the Sb_2Se_3 absorber layer, each influencing the film quality, interface characteristics, and PCE. A comprehensive summary of the reported CdS/Sb_2Se_3 solar cells, highlighting the PV parameters obtained using different Sb_2Se_3 deposition methods, is presented in Table 2.

Table 2. An overview of CdS/Sb_2Se_3 solar cell performance using different deposition methods for the Sb_2Se_3 absorber layer.

No.	Sb_2Se_3 fabrication method	Configuration	Device architecture	Device parameter				Ref
				V_{OC} (mV)	J_{SC} (mA/cm^2)	FF (%)	PCE (%)	
1	Spin coating	Superstrate	FTO/CdS/Sb_2Se_3/SpiroOMeTAD/Au	312	21.6	48.2	3.3	[98]
		Superstrate	FTO/CdS/S:Sb_2Se_3/SpiroOMeTAD/Au	258	19.5	41.2	2.06	[101]
		Superstrate	FTO/CdS/Te:Sb_2Se_3/SpiroOMeTAD/Au	360	29.0	51.5	5.4	[101]
		Superstrate	FTO/TiO_2/CdS/Sb_2Se_3/SpiroOMeTAD/Au	340	27.2	41.9	3.9	[181]
2	e-beam	Substrate	Mo/Sb_2Se_3/CdS/i-ZnO/ITO	371	22.41	51.4	4.2	[102]
3	TE	Superstrate	ITO/CdS/O:Sb_2Se_3/Au	360	25.3	52.5	4.8	[124]
		Superstrate	ITO/CdS/Sb_2Se_3/Au	290	20.9	46.0	2.8	[124]
		Substrate	Mo/Sb_2Se_3/CdS/ZnO/ITO/Ag	427	17.11	58.15	4.25	[182]
4	RTE	Superstrate	FTO/CdS/Sb_2Se_3/Au	401	25.10	55.7	5.6	[72]
		Superstrate	FTO/CdS/Sb_2Se_3/MoO_3/Au	410	27.45	56.82	6.33	[183]
		Substrate	Mo/Sb_2Se_3/CdS/ZnO/Al:ZnO/Al	414	16.0	52.0	3.47	[184]
		Superstrate	ITO/CdS/Sb_2Se_3/ PbS/Au	427	25.50	59.30	6.50	[185]
		Superstrate	FTO/CdS/Si_3N_4/Sb_2Se_3/Au	348	31.47	50.32	5.52	[186]
		Superstrate	ITO/CdS/Sb_2Se_3/Au	410	29.0	59.3	7.04	[187]
5	VTD	Superstrate	ITO/CdS/Sb_2Se_3/Au	420	29.9	60.4	7.6	[85]
		Substrate	Mo/Sb_2Se_3/CdS/ITO/Ag	513	24.56	58.74	7.4	[188]

		Substrate	PI/ITO/CdS/Sb_2Se_3/Au	419	24.5	5	5.95	[101]
		Superstrate	ITO/CdS/Sb_2Se_3/Au	425	29.0	59.8	7.37	[101]
		Superstrate	ITO/CdS/Sb_2Se_3/CuSCN/Au	423	30.8	57	7.4	[189]
		Superstrate	ITO/SnO_2/CdS/Sb_2Se_3/Au	431.9	27.6	63.2	7.5	[190]
6	CSS	Substrate	Mo/$MoSe_2$/Sb_2Se_3/CdS/i-ZnO/Al:ZnO/Ag	400	32.58	70.3	9.2	[84]
		Superstrate	FTO/CdS/Sb_2Se_3/C:Ag	377	25.68	43.0	4.16	[191]
		Substrate	FTO/CdSe/Sb_2Se_3/C:Ag	354	27.57	46.13	4.51	[191]
		Superstrate	FTO/CdS/Sb_2Se_3/VO_x/Au	409	31.62	48.96	6.33	[192]
		Superstrate	FTO/CdS/Sb_2Se_3/Au	358	31.89	48.52	5.53	[192]
		Superstrate	FTO/CdS/Sb_2Se_3/NiO_x/Au	410	30.94	57.26	7.29	[111]
		Superstrate	FTO/CdS/Sb_2Se_3/Au	400	29.62	55.63	6.64	[111]
		Superstrate	FTO/CdS/Sb_2Se_3/C/Ag	414	29.11	50.8	6.12	[193]
		Superstrate	FTO/CdS:O/Sb_2Se_3/C/Ag	432	29.87	54.0	7.01	[193]
7	Sputtering	Substrate	Mo/Sb_2Se_3/CdS/ITO/Ag	455	22.75	59.5	6.15	[106]
		Substrate	Mo/Sb_2Se_3/CdS/ZnO/Al:ZnO/Ag	437	15.93	48	3.35	[194]
		Substrate	Mo/Sb_2Se_3/CdS/ITO/Ag	494	25.91	47.73	6.06	[91]
		Superstrate	ITO/CdS/Sb_2Se_3/Au	270	9.47	33.26	0.84	[101]

		Substrate	$Mo/Sb_2Se_3/CdS/ITO/Ag$	448	24.95	53.2	5.52	[105]
		Substrate	$Mo/Sb_2Se_3/CdS/ITO/Ag$	504	24.91	54.47	6.84	[195]
		Substrate	$Mo/Sb_2Se_3/CdS//i\text{-}ZnO/Al:ZnO/Ag$	505	27.74	60.7	8.5	[196]
		Substrate	$Mo/Sn:Sb_2Se_3/I:Sb_2Se_3/ITO/Ag$	280	22.45	34.51	2.17	[197]
8	Sputtering + PLD(selenisation)	Substrate	$Mo/Sb_2Se_3/CdS/ITO/Ag$	520	27.8	59.8	8.64	[107]
		Superstrate	$FTO/CdS/Sb_2Se_3/Au$	318	26.81	42	3.58	[108]
		Superstrate	$FTO/SnO_2/CdS/Sb_2Se_3/Au$	329	28.87	46.4	4.41	[108]

1.8 Post-deposition thermal annealing treatment of CdS ETL in Sb_2Se_3 solar cells

CdS films deposited via the CBD method exhibit a range of properties that can differ significantly from those required for efficient ETL functionality in thin-film solar cells. To tailor these properties, post-deposition thermal annealing is considered an essential processing step. In the case of CBD-CdS films, annealing plays a critical role in modifying their structural and optoelectronic characteristics. Several studies have reported that thermal treatment induces recrystallisation within the CdS films [198]. For instance, Guo H. et al. [178] demonstrated that annealing can induce a phase transformation from cubic to hexagonal CdS, a structural change that improves lattice matching with Sb_2Se_3 (Figure 11) and CdTe absorber layers, thereby enhancing heterojunction quality in thin-film solar cells [199].

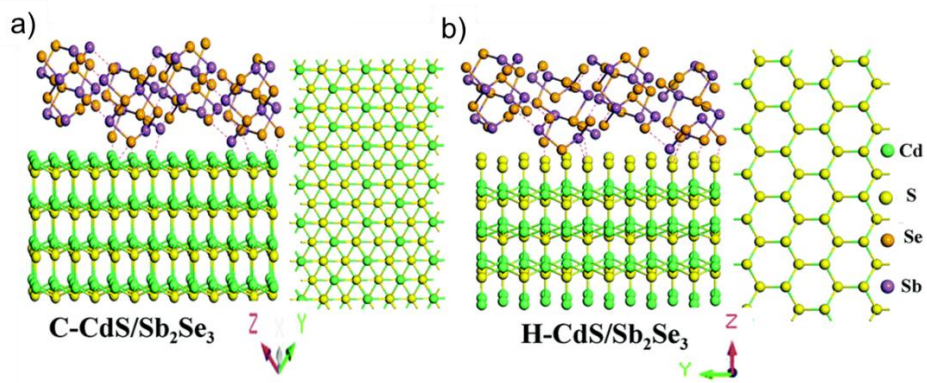

Figure 11. growth diagram of Sb_2Se_3 on, a) cubic (C-CdS) and b) hexagonal (H-CdS) CdS films.

The effects of annealing are highly dependent on processing parameters such as the ambient atmosphere (e.g., H_2, N_2, H_2S, vacuum, or ambient air), temperature, and duration. Annealing in ambient air at relatively low temperatures (~200 °C) has been shown to induce the cubic to hexagonal phase transformation [133], [200]. However, higher annealing temperatures may promote surface oxidation of CdS, which can alter the band gap and significantly increase the film's resistivity [201]. Conversely, annealing in reducing environments such as H_2 has been reported to remove oxygen from the film, thereby decreasing resistivity while maintaining the cubic phase structure [202], [203]. Annealing in inert or neutral atmospheres such as N_2 or vacuum also promotes improved crystallinity, reduced resistivity, and induces the desired cubic to hexagonal phase transition features that are particularly advantageous for applications in Sb_2Se_3 solar cells [199]. Furthermore, both annealing temperature and duration are critical in determining the changes of film properties. Extended annealing at elevated temperatures can lead to adverse effects such as crack formation and pinhole generation, which negatively impact device performance [204]. It has also been reported that thermal annealing contributes to a reduction in the optical band gap of CdS films, further influencing their suitability as ETL's [133]. Overall, the annealing process requires precise control to optimize film quality and ensure compatibility with the subsequent absorber layers.

The optimization of CdS through thermal annealing has been extensively explored within CdTe solar cell technology, where its influence on film crystallinity and interface

properties is well established. Building on this foundation, these annealing strategies have been subsequently applied to Sb_2Se_3-based solar cells. For instance, Guo et al. investigated the effect of air annealing on thermally deposited CdS films and its impact on CdS/Sb_2Se_3 device performance [178]. However, a comprehensive study focusing on the thermal annealing of CBD-CdS films, particularly with respect to their structural, optical, and electronic properties and the subsequent influence on CdS/Sb_2Se_3 solar cell performance, remains lacking. To address this knowledge gap, a systematic investigation into the annealing of CBD-CdS layers is essential for gaining deeper insights into interface engineering and enhancing device efficiency, thereby contributing to the advancement of Sb_2Se_3 photovoltaic research.

1.9 Post-deposition chloride treatment of CdS ETL in Sb_2Se_3 solar cells

The CdS ETL has been widely utilized in thin-film solar cell technologies and remains one of the most extensively studied layers in photovoltaic device architectures. Numerous investigations have been conducted to enhance the optoelectronic properties and interfacial compatibility of CdS with various absorber layers, including Sb_2Se_3, Sb_2S_3, and CdTe. Strategies to improve its performance include in situ doping with elements such as La, Zn, and Cl, which can effectively modulate the electrical and optical characteristics of the CdS films. Another widely adopted approach involves post-deposition treatments (PDT) of the CdS layer prior to absorber deposition, particularly in superstrate-configured devices. Among these, the $CdCl_2$ treatment has demonstrated notable improvements in device performance. This process typically involves the deposition of a thin (~20 nm) $CdCl_2$ layer onto the CdS film, followed by the deposition of the Sb_2Se_3 absorber layer.

The impact of ETL modification on device performance is evident from historical efficiency trends. Figure 12a illustrates the chronological improvement in PCE of Sb_2Se_3 solar cells employing different ETLs. The highest reported PCEs for devices with untreated CdS, $CdCl_2$-treated CdS, and TiO_2 ETLs are 10.1%, 8.4%, and 7.6%, respectively. These findings confirm that both untreated and chloride-treated CdS layers can support high-efficiency Sb_2Se_3-based devices. Furthermore, a bibliometric analysis of peer-reviewed publications from 2009 to 2024 (Figure 12b) reveals that approximately 59 studies have reported solar cell fabrication and efficiency using untreated CdS ETLs, while 26 studies have employed $CdCl_2$-treated CdS. This analysis excludes publications focused solely on material synthesis or characterization without solar cell performance data. The overall trend highlights the sustained research efforts aimed at optimizing ETLs to enhance the photovoltaic performance of Sb_2Se_3 solar cells.

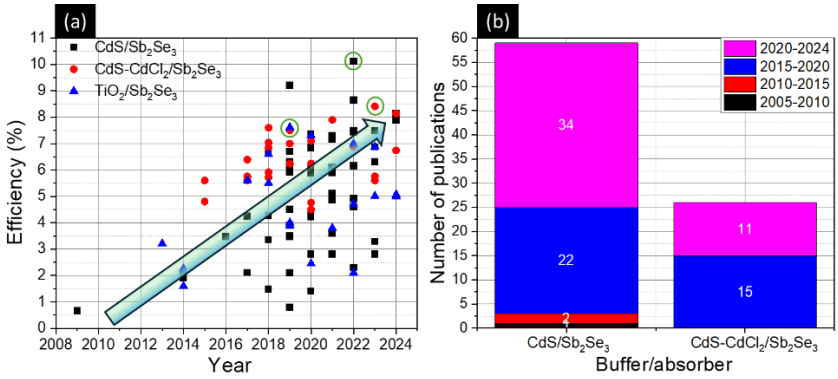

Figure 12. a) Evolution of Sb_2Se_3 solar cell efficiency with CdS, $CdCl_2$-CdS and TiO_2 ETLs and b) the corresponding number of publications.

It is worth noting that promising PCE values have also been reported for CdS/Sb_2Se_3 solar cells utilizing CBD-CdS films without the incorporation of any additional post-deposition treatments (PDTs). However, numerous studies emphasize the necessity of such treatments, particularly the application of a $CdCl_2$-based PDT conducted in ambient air at temperatures ≥ 400 °C for durations ranging between 5–10 minutes [205]. This step has frequently been cited as critical for achieving acceptable PCE in superstrate configuration CdS/Sb_2Se_3 solar cells, with many groups adopting it as a standardized procedure originally transferred from CdTe thin-film technology [205], [206]. Despite the widespread implementation of this treatment, the underlying mechanisms are often ambiguously described and not thoroughly validated.

Beyond the role of PDT, a large body of literature has drawn attention to the phenomenon of intermixing at the CdS/Sb_2Se_3 interface, which is increasingly recognised as a fundamental limitation in this device architecture [4]. This intermixing primarily results from the diffusion of Cd into the Sb_2Se_3 absorber or Se into the CdS layer, subsequently forming a CdSe interfacial layer [113]. The influence of this CdSe layer remains a topic of ongoing debate, with conflicting reports suggesting either a positive contribution to carrier transport or a detrimental role in acting as a barrier to charge extraction at the heterojunction [85], [207].

In this context, the $CdCl_2$-based PDT conducted in air has also been postulated to play a regulatory role in controlling the extent of interfacial intermixing [208]. Additionally, the presence of oxygen alone during annealing has demonstrated beneficial effects on CBD-CdS layers, even at moderate annealing temperatures around 200 °C, by stabilizing the ETL and inhibiting excessive interdiffusion at the CdS/Sb_2Se_3 interface (Publication I). Furthermore, the impact of various metal halide-based PDT's, including $CdCl_2$ and $AlCl_3$, has been explored as a strategy to optimise both the interfacial chemistry and the passivation of interface-related defect states in CdS/Sb_2Se_3 thin-film solar cells [82], [94], [205].

Despite extensive studies, there remains no clear consensus within the photovoltaic research community regarding the definitive role, whether beneficial or detrimental, of metal halide-based PDT's such as $CdCl_2$ for CdS/Sb_2Se_3 solar cells. Furthermore, it remains uncertain whether such treatments should be interpreted strictly as a PDT or instead as a method for controlled chlorine incorporation during the CBD process, followed by thermal annealing under varying environmental conditions. In terms of chlorine incorporation into the CdS lattice, it is well established that chlorine acts as a shallow-type

dopant. Its incorporation, dependent on concentration, can significantly increase the free electron density in CdS films, irrespective of the deposition method employed [6].

In support of this, the role of chlorine as an effective *n*-type dopant has also been confirmed for Sb_2Se_3. Specifically, intrinsic Sb_2Se_3 crystals synthesised from elemental precursors demonstrated *n*-type conductivity upon intentional doping with $MgCl_2$, highlighting chlorine's ability to modulate electrical properties [97]. Additionally, interdiffusion processes occurring at the CdS/Sb_2Se_3 interface have revealed that Cd diffusion from CdS into Sb_2Se_3 can lead to a conductivity type conversion from *p*-type to *n*-type through the introduction of donor-like defect states [209]. Consequently, metal halide-based PDT's not only influence the interfacial chemistry but may also play a pivotal role in determining whether the resulting heterojunction is an *n-n* isotype or an *n-p* type. This interfacial configuration directly impacts charge recombination mechanisms, thereby affecting key PV parameters and the ultimate PCE of the device.

Importantly, this literature survey reveals no unified conclusion regarding the efficacy of metal halide-based PDT's particularly $CdCl_2$ treatment in air at ≥400 °C or chlorine doping strategies for improving the CdS/Sb_2Se_3 interface and device PCE. Although this statement may invite considerable debate, it is substantiated by the following observations: (i) As indicated in Figure 12b, a significant number of publications do not provide conclusive outcomes either positive or negative on the use of $CdCl_2$ PDT (or alternative halide-based treatments) concerning their effect on CdS film quality and the final PCE of CdS/Sb_2Se_3 devices, regardless of whether the architecture is superstrate or substrate configuration; (ii) Several studies, conversely, report a positive correlation between $CdCl_2$-treated CdS and enhanced solar cell performance [4], [82], [94], [205].

Thus, based on the accumulated evidence and the foundational knowledge drawn from CdTe-based systems, the direct transferability of $CdCl_2$ PDT (especially in air at 400 °C) to the CdS/Sb_2Se_3 system remains highly questionable. In our preliminary investigations to replicate the $CdCl_2$ PDT within our laboratory, $CdCl_2$ was spin-coated onto CBD-CdS films, followed by annealing at 400 °C in ambient air for 30 minutes. Sb_2Se_3 absorber layers were deposited onto these CdS layers by CSS or VTD method, but the Sb_2Se_3 films exhibited severe delamination from the CdS layer along with the formation of numerous pinholes, rendering the devices non-functional or low efficient. Based on these findings and the literature review, a new strategy involving the in-situ incorporation of chlorine during the CBD process of CdS emerges as a novel approach. This method, and its subsequent impact on the structural, chemical, and optoelectronic properties of CdS films as well as on the performance of CdS/Sb_2Se_3 solar cells, should be systematically investigated to gain advance understanding in this area.

1.10 Defects in CdS/Sb_2Se_3 solar cells

Sb_2Se_3 solar cells exhibit a range of intrinsic and extrinsic defects that critically influence their optoelectronic performance and PCE. These defects typically originate from multiple sources, including unfavourable grain orientation (horizontal alignment), interfacial recombination, interdiffusion between the absorber and ETLs, and the incorporation of unintended impurities from the precursor materials. Such imperfections often serve as non-radiative recombination centers, leading to reduced carrier lifetimes and a significant loss in V_{OC} and overall device performance.

Based on a statistical study of 63 reported articles from 2009 to 2024 about CdS/Sb_2Se_3 solar cells (Figure 13), among the various defect types, the most frequently reported are selenium vacancies (V_{Se}), antimony antisites (Sb_{Se}), selenium antisites (Se_{Sb}),

cadmium antisites (Cd_{Sb}), antimony vacancies (V_{Sb}), and interstitial selenium (Se_i). It is also revealed that V_{Se} is the most prevalent defect, appearing in approximately 37.5% of the studies reviewed. Se_{Sb} and Sb_{Se} defects were each identified in around 20.83% of the studies, while Se_i was the least observed, reported in only 4.71% of cases (Figure 13a).

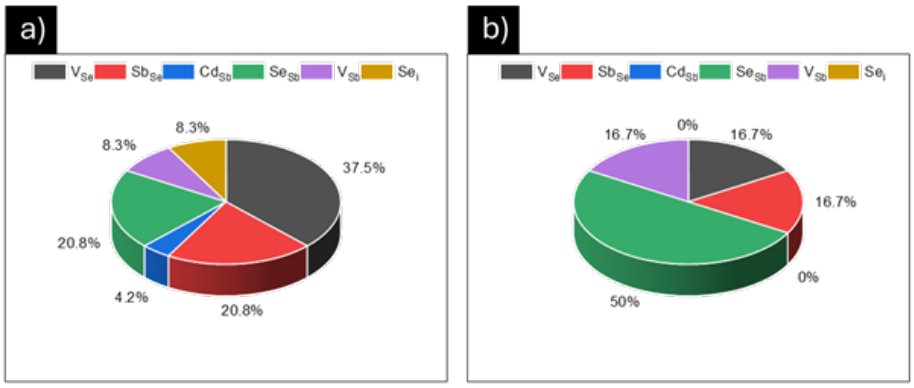

Figure 13. Statistical study of the defects reported in articles for a) CdS/Sb_2Se_3 and b) $CdS/CdCl_2/Sb_2Se_3$ solar cells in 2009–2024.

Among these, V_{Se} defects are of particular concern, as they act as donor-like centers that can induce unintentional *n*-type conductivity in Sb_2Se_3, contributing to increased carrier recombination and degradation of V_{OC}. Numerous studies, including those by Fan et al. [210], Tang et al. [91], Tiwari et al. [102], [211], Li et al. [211], Chen et al. [212], Liang et al. [195], Lin et al. [180], and Duan et al. [213], have reported the presence of V_{Se} defects in their devices. For instance, Fan et al. reported a V_{Se} defect with an activation energy (E_A) of 237 meV, along with an Sb_{Se} defect at 468 meV. Chen et al. identified an E_A of 358 meV attributed to both V_{Se} and Sb_{Se}. Similarly, Liang et al. observed a V_{Se} defect with E_A of 386 meV and an Sb_{Se} defect at 426 meV. Lin et al. documented a V_{Se} defect with E_A of 321 meV and a defect density of ~10^{16} cm^{-3}.

To address the prevalence of V_{Se} defects, post-deposition selenium treatments have been widely investigated. These treatments aim to compensate the selenium loss in Sb_2Se_3 films, thus mitigating V_{Se}-induced recombination. However, such strategies can also lead to the emergence of secondary defects, including V_{Sb}, Se_{Sb}, and Se_i. Among these, the Se_{Sb} defect is particularly detrimental, as it acts as a shallow acceptor and can trap photogenerated carriers, further contributing to recombination losses. Tiwari et al. reported a Se_{Sb} defect density of 10^{16} cm^{-3}, while Luo et al. reported a Se_{Sb} defect with an E_A of 566 meV.

A comparative review of literature focused on $CdCl_2$-treated CdS/Sb_2Se_3 solar cells (Figure 13b) shows that Se_{Sb} becomes the dominant defect type following PDT of the CdS ETL, representing approximately 50% of all reported defects. Several researchers, Cai et al. [214], Liu et al. [100], Luo et al. [82], Wen et al. [215], Chen et al. [216], Liu et al. [124], and Hu et al. [215] have confirmed the emergence of Se_{Sb} defects in interface-engineered CdS/Sb_2Se_3 devices. For example, Chen et al. identified a Se_{Sb} defect with an E_A of 0.11 eV and a density of ~10^{16} cm^{-3}.

The introduction of chloride treatment for the CdS ETL as discussed in sections 3.2 and 3.3 of the thesis, holds significant potential for mitigating interfacial defects and enhancing the performance of CdS/Sb_2Se_3 solar cells. Nevertheless, a detailed understanding of defect formation and suppression in these NH_4Cl-treated systems remains lacking.

In particular, no in-depth studies have yet addressed the correlation between Cl-induced changes in defect chemistry and their impact on the photovoltaic parameters of CdS/Sb_2Se_3 solar cells. These findings collectively highlight a critical knowledge gap in understanding the role of point defects, particularly in the context of interface modifications and chemical treatments.

Summary of the literature review and aims of the study

The literature review is summarised as follows,

1. Sb chalcogenides (Sb_2S_3, Sb_2Se_3, and $Sb_2(S,Se)_3$) are promising thin-film absorber materials due to their tunable bandgaps (1.1–1.8 eV), high absorption, stable orthorhombic structure, and use of earth-abundant, non-toxic elements. Among them, Sb_2Se_3 stands out with its near-optimal bandgap, quasi-one-dimensional crystal structure enabling efficient carrier transport, and long-term stability, positioning it as a sustainable alternative to CdTe and CIGS technologies.
2. Sb_2Se_3 crystallizes in an orthorhombic lattice of quasi-1D $(Sb_4Se_6)_n$ ribbons, strongly bonded within chains but weakly linked by van der Waals forces along [010], giving rise to pronounced anisotropy. Carrier mobility and conductivity are higher along the ribbon axis, making a [001] grain orientation highly desirable for efficient transport and reduced recombination. The material is typically *p*-type due to selenium antisites, though unintentional chlorine can act as a shallow donor, inducing *n*-type behavior. With a high absorption coefficient ($>10^5$ cm^{-1}) and anisotropic transport, Sb_2Se_3 performance strongly depends on deposition method, substrate choice, and post-deposition processing to optimize orientation and defect control.
3. The chemical routes of deposition for Sb_2Se_3 are low-cost and scalable but struggle to control crystallographic orientation, which is crucial for charge transport. CSS and VTD stand out among physical methods as they promote vertically oriented [hk1] columnar grains, enhancing carrier mobility and reducing recombination. CSS offers rapid growth through a short source–substrate distance, while VTD provides flexible control of deposition via carrier gas transport, enabling improved crystallinity and uniformity.
4. CdS is a II–VI direct bandgap semiconductor (~2.4 eV) widely used as the ETL in Sb_2Se_3 solar cells due to its high transparency, favorable band alignment, and suitable electron affinity, which enable efficient charge separation and extraction with minimal optical losses.
5. CdS primarily crystallizes in the stable hexagonal wurtzite phase but can also form cubic or CdO phases under certain conditions, affecting its electronic behavior. It exhibits intrinsic *n*-type conductivity (10^{15}–10^{18} cm^{-3} carrier concentration, 0.1–100 $cm^2.V^{-1}.S^{-1}$ mobility), with properties tunable via deposition, annealing, or doping, ensuring transparency and band alignment suitable for Sb_2Se_3 ETLs.
6. CdS/Sb_2Se_3 solar cells have advanced significantly in both superstrate and substrate configurations, with efficiencies strongly dependent on deposition and interface engineering. While early spin-coated or evaporated devices showed 2–5% PCE, CBD has delivered record 10.57% efficiency, and physical methods such as RTE and sputtering achieved 6-8.6%. CSS and VTD, known for promoting vertical grain orientation, reached 9.2% and 7.6%, respectively, confirming Sb_2Se_3 as a promising absorber with efficiencies now approaching 10%.
7. Post-deposition annealing of CBD-CdS films critically influences crystallinity, phase, and optoelectronic properties, with low-temperature air annealing (~200 °C) improving lattice matching and junction quality, while higher temperatures risk oxidation and degradation. Although well studied in CdTe, systematic investigations for Sb_2Se_3 solar cells remain limited, highlighting the need for precise process control to optimize ETL performance.

8. Chlorine treatment of CdS, typically via $CdCl_2$, has been adapted from CdTe to Sb_2Se_3 solar cells to improve ETL quality and interface properties. While it can enhance crystallinity, passivate defects, and modify junction behaviour through shallow *n*-type doping, its impact remains debated, with reports of both efficiency gains and detrimental effects such as CdSe formation.
9. Sb_2Se_3 solar cells are strongly affected by intrinsic and extrinsic defects such as V_{Se}, Sb_{Se}, Se_{Sb}, and Se_i, which act as non-radiative recombination centers, reducing carrier lifetimes and V_{OC}. A survey of 63 studies (2009-2024) shows V_{Se} as the most common defect (~37.5%), often causing unintentional *n*-type conductivity, while Se_{Sb} becomes dominant after $CdCl_2$ treatment (~50%). The selenium treatments and interface engineering have been explored to suppress these defects.

Based on the literature review of CdS/Sb_2Se_3 solar cells, several critical research gaps were identified:

1. Post-Deposition Treatment (PDT) of CdS in Sb_2Se_3 solar cells

Although PDT is well established in CdTe and CIGS technologies for improving ETL quality, systematic studies exploring its role in CdS/Sb_2Se_3 heterojunctions remain limited. Specifically, the effects of annealing environment (air and vacuum) and temperature on CdS film properties and subsequent Sb_2Se_3 growth have not been comprehensively addressed.

2. Chlorine incorporation into CdS films

While thin interfacial $CdCl_2$ or $AlCl_3$ treatment between CdS and Sb_2Se_3 has been reported to improve open-circuit voltage, no systematic studies exist on in situ chlorine incorporation into CdS during CBD deposition. The mechanisms by which chlorine impacts CdS film properties, influences Cd interdiffusion, and affects heterojunction band alignment and Sb_2Se_3 device performance remain poorly understood.

3. Optimisation of Sb_2Se_3 deposition by VTD

VTD is recognised as a scalable technique capable of producing vertically oriented Sb_2Se_3 grains, yet the influence of process parameters such as source-to-substrate distance (which determines the growth rate) and carrier gas introduction on morphology, grain orientation, defect formation, and photovoltaic performance has not been fully explored.

4. Defect states at the CdS/Sb_2Se_3 interface

A lack of detailed defect characterization hampers the understanding of recombination mechanisms at the CdS/Sb_2Se_3 interface. In particular, the distinction between bulk and interface-related defects in Sb_2Se_3 (e.g., V_{Sb}, Sb_{Se}), as well as their dependence on CdS processing and chlorine incorporation, has not been systematically studied.

5. Correlation between ETL processing and absorber growth

The direct impact of CdS processing conditions (PDT, Cl incorporation) on Sb_2Se_3 absorber morphology, preferred orientation, and defect density remains underexplored. Establishing this correlation is essential for optimising heterojunction quality and achieving higher PCE.

Based on these findings, the aim of this thesis is to develop CdS/Sb_2Se_3 solar cells by the vapor transport deposition, from a fundamental study of the fabrication process, implication of CdS processing and related interface, to the fabrication of complete device, their optimisation and defect characterization. To achieve this aim, the following objectives were formulated.

1. Systematically, investigate and identify the optimal PDT conditions of CBD-CdS ETL under vacuum and air atmospheres at 200–400 °C, and correlate the resulting structural, optical, and electronic changes with Sb_2Se_3 absorber growth deposited by CSS and device performance.
2. Develop an alternative strategy to conventional $CdCl_2$ post-deposition treatment of CdS films by incorporating controlled amounts of NH_4Cl via precursor modification and study its impact on structural, electrical, and interfacial properties of CdS films and on CdS/Sb_2Se_3 device performance.
3. Optimise the VTD process for Sb_2Se_3 absorbers by systematically investigating the influence of source-to-substrate distance and carrier gas flow on Sb_2Se_3 film quality and device performance.
4. Compare CdS/Sb_2Se_3 solar cells with and without chloride-processed CdS, to establish a growth protocol that minimises interfacial intermixing, enhances absorber crystallinity, reduces defects and improves photovoltaic efficiency.
5. Provide possible mechanisms on the interlink between the processing of CdS ETL, Sb_2Se_3 absorber properties, and device performance.

2 Experimental

In this chapter, a detailed description of the deposition methods, processing parameters, and characterization techniques employed for the fabrication and analysis of CdS and Sb_2Se_3 thin films, as well as for evaluating the PCE of CdS/Sb_2Se_3 devices, is presented.

2.1 Fabrication of CdS and Sb_2Se_3 thin films and CdS/Sb_2Se_3 solar cells

Substrate preparation (glass/FTO)

Fluorine-doped tin oxide substrates (FTO) were used for the preparation of the thin films as well as the superstrate configuration solar cells, where FTO films will act as a front contact in the devices. These substrates were purchased from Sigma Aldrich with a film thickness of 200 nm, and sheet resistance <20 Ω/Sq on a soda lime glass substrate of 2 mm thickness. These purchased glass/FTO substrates were cut into 20×20 mm (for Publication I) and 18×18 mm (for publications II and III). These substrates were immersed in a degreasing solution containing 10g of potassium dichromate ($K_2Cr_2O_7$), 100 ml of concentrated sulfuric acid and 10 ml of deionised water for 2–3 hours [135]. After that, the glass/FTO substrates were washed and boiled in distilled water. The substrates were then dried using a hot gun and then kept in a desiccator.

CdS film (ETL) deposition by chemical bath deposition (CBD)

The deposition of the CdS thin films on glass/FTO substrates was carried out using the traditional chemical bath deposition method. The deposition was carried out in a closed jar containing $CdSO_4$ (1 mM), $(NH_4)_2SO_4$ (0.7 M), NH_4Cl (0.1 μM (publication II), 0, 1, 2, 4 and 8 mM (publications II and III), NH_4OH (30 mM), and thiourea (10 mM) dissolved in de-ionized (DI) water at 85 °C (publication I) 79 °C (publication II) and stirred at 500 rpm (Figure 14). The chlorine content in the precursor was changed by the addition of different concentrations of NH_4Cl during the deposition. The deposition duration was optimised to be 10 minutes to get a 100 nm thick CdS layer. After deposition, the films were ultrasonicated in distilled water with a few drops of triethanolamine, followed by washing again in distilled water and dried with a hot (100–150 °C) air gun. The prepared CdS samples were kept in a vacuum chamber and were only taken outside for characterization.

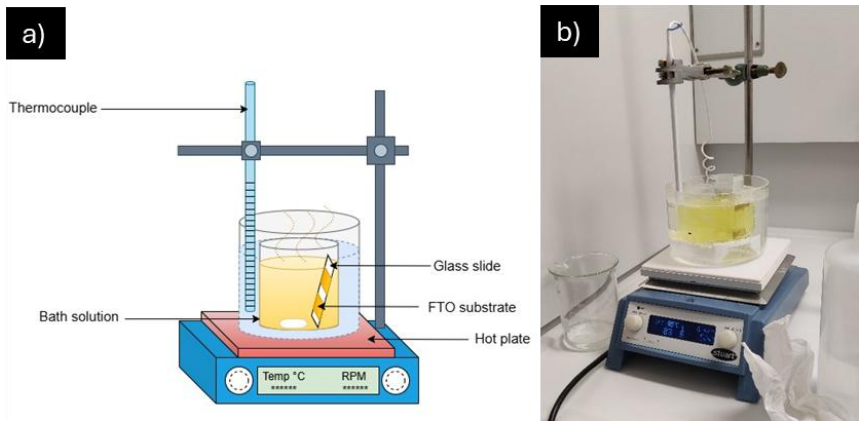

Figure 14. CBD set up a) schematic illustration and b) photograph of the actual experimental setup.

Annealing treatment of CdS films

In publication I, the CdS films were annealed in a vacuum at 120 °C for 15 min to remove impurities such as water, hydroxides, and organic compounds which may have stayed on the films. The resulting films are called "as-deposited" CdS films and then they are divided into two batches. One batch is annealed in air and the other one is in a vacuum at different temperatures (200, 250, 300, 350, and 400 °C). The air annealing was carried out in a single-zone quartz tube furnace. The samples were loaded into the preheated quartz tube at the desired temperature and then kept there for 30 min. The samples were removed from the tube immediately after the annealing time for rapid cooling. The vacuum annealing was also carried out in the single-zone quartz tube furnace. The samples are loaded into the quartz tube at room temperature and then evacuated using a rotary pump up to ~10^{-5} mbar pressure. The quartz tube was placed in a single-zone furnace, and the temperature was ramped to the set value. Once the temperature reaches the set value, it is maintained for 30 min. After the annealing time, the samples are allowed to cool down gradually to room temperature while keeping the vacuum. Once it reaches room temperature, the vacuum is released, and the samples are taken out. The samples with glass/CdS are used for the CdS film characterisation.

Sb_2Se_3 film deposition by close-spaced sublimation (CSS)

In publication I, the absorber layer Sb_2Se_3 was deposited using a close-spaced sublimation technique. A schematic diagram of the CSS reactor is shown in Figure 15. Sb_2Se_3 granules of 5N purity (Sigma Aldrich) were used as source material and the substrate was kept at a 4 cm distance from the source material. The source material is kept at 490 °C and the substrate at 460 °C during the deposition to maintain a deposition rate of 1 µm/min. A thickness of ~1.5 µm was optimised.

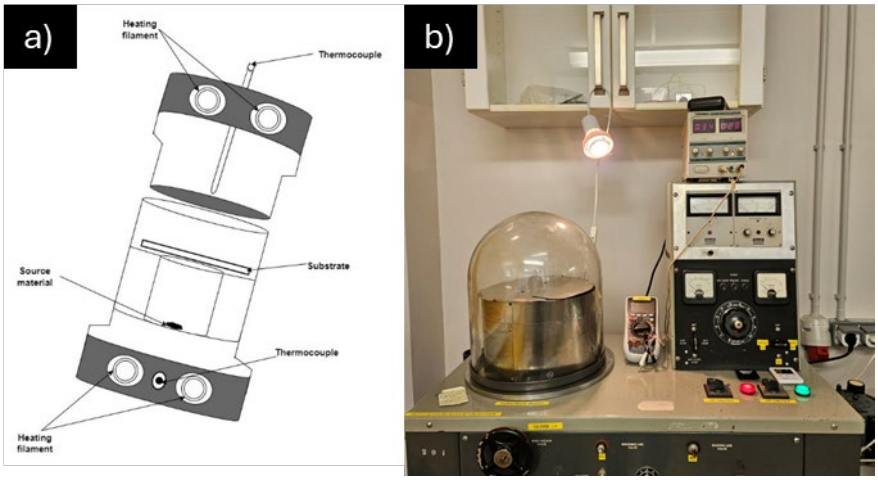

Figure 15. CSS set up a) schematic illustration and b) photograph of the actual experimental setup.

Sb_2Se_3 film deposition by vapor transport deposition (VTD)

In publications II and III, Sb_2Se_3 films were deposited on the glass/FTO/CdS substrates with different chlorine concentrations by VTD using a three-zone tubular furnace (Carbolite) (Figure 16). Sb_2Se_3 granules of 5N purity (Sigma Aldrich) were used as source materials. Initially, the quartz tube was evacuated using a combination of rotary and turbomolecular pumps (Pfeiffer vacuum) down to 10^{-5} mbar. The substrate-to-source distance was varied

(2, 3, 6, 10 cm). In publication III, argon gas was introduced into the tube through a needle valve to bring more control to the rate of deposition. This reduced the working pressure to 1×10^{-3} mbar. The temperature of the source and substrate was ramped at 20 °C/min until it reached 500 °C and 400 °C, respectively. This temperature was kept for 5 min to obtain the desired thickness of 1 µm. In publication III, the source-to-substrate distance was varied so that to maintain the same thickness, the deposition time was adjusted. After deposition, the furnace lid was opened, exposing the quartz tube to the ambient air. The vacuum pump was promptly shifted from turbo to rotary, reducing the vacuum level to 10^{-2} mbar to stop the deposition of Sb_2Se_3 films. The quartz tube was allowed to cool down to 30 °C, and then it was ventilated to take the sample outside.

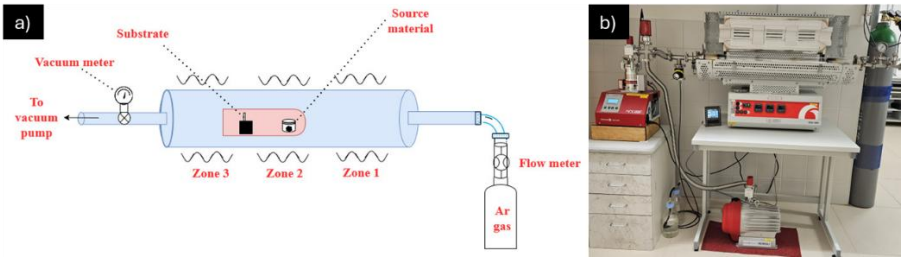

Figure 16. VTD set up a) schematic illustration and b) photograph of the actual experimental setup.

Gold thin film (back contact) deposition by thermal evaporation (TE)

The superstrate configuration solar cells with glass/FTO/CdS/Sb_2Se_3/Au structure (Figure 17) were completed by deposition of Au using the thermal evaporation method. High pure gold wire bought from Alfa Aesar was used as the source material. The chamber was evacuated to ~10^{-5} mbar vacuum with the help of rotary and diffusion pump combination. A custom-made stainless steel mask with a circular coating area of 7.063 mm^2 was used to get the perfect contact area. To avoid any damage during the device measurements, indium pads are used on top of the Au films.

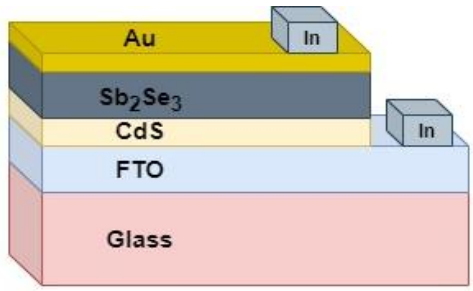

Figure 17. Superstrate configuration of solar cells used in this thesis study.

2.2 Characterisation of thin films

X-ray diffraction (XRD)

The crystal structure and the phase composition of the CdS and Sb_2Se_3 thin films were analysed by X-ray diffractogram. The Rigaku Ultima IV system using monochromator Cu Kα radiation (λ = 1.54 Å, 40 kV, 40 mA) equipped with D/teX Ultra silicon line detector in the 2θ (Bragg-Brentano) regime using a 2θ step of 0.04°, a counting time 2–10 s/step with

sample rotation. The XRD patterns were compared with the standard powder diffraction data (Joint Committee on Powder Diffraction Standards (JCPDS)) and analysed using Rigaku PDXL2 software.

Scanning electron microscopy (SEM)

The morphology and thickness of the CdS and Sb_2Se_3 films were analysed using SEM analysis. For publications I and III, the images of films were made by Zeiss EVO-MA15 scanning electron microscope (SEM) equipped with a Zeiss HR FESEM Ultra 55 system at Taltech. For publication II, the image of the films was obtained using a scanning electron microscope (SEM) Zeiss EVO 10 at Czech Technical University, Prague. These SEM images were acquired at 10kV, magnification of 20 kX and working distance (WD) of 7.55mm in the regime of secondary electrons (SE) using an off-beam detector.

Hall measurement

The electrical properties, such as carrier concentration, mobility, and resistivity of CdS films, were measured at room temperature using a Hall and van der Pauw controller H-50. The thickness of the films (~100 nm) was estimated from the cross-section SEM images and was added to the software. Indium pads were used as contacts, and the films were measured a minimum of five times to reduce the error.

Ultraviolet-visible spectroscopy

In publication II, the total transmittance and reflectance spectra of the CdS films were recorded using an ultraviolet-visible (UV-VIS) spectrophotometer over the 300–1100 nm range on Jasco V-670 ultraviolet-visible-near infrared spectrometer. The optical band gaps (E_g) of the films were calculated from the absorption spectra using Tauc plots.

Kelvin probe measurement

In publication II, the contact potential difference (CPD) in the dark and under the illumination of CdS and Sb_2Se_3 films was measured by a Scanning Kelvin Probe (SKP) system from KP Technology. The CPD data were recalculated to the work function values using the equation:

$$WF_{sample} = (CPD_{sample} - CPD_{ref}) \times 10^{-3} + WF_{ref} \quad (1)$$

As the WF reference (WF_{ref}), the Au reference sample from KP Technology was used. SKP measurements were done in a glove box using a grounded steel probe tip of 2mm diameter. The CPD was measured in the dark-light-dark-light-dark cycle by switching solar simulator illumination (AM1.5G filter, class AAA solar simulator HAL-C100, Asahi Spectra, Japan). CPD was measured as a function of time for 13.75minutes (1250 data points). Multiple locations were tested on each sample. The surface photovoltage (SPV) was determined as the difference between WF_{light} and WF_{dark}. The second part of the SKP experiment was the mapping of WF across the scanned area of 4.89×4.89 mm^2 using a matrix of 12×12 points (hence 0.4075 mm per point). WF mapping was also performed in the dark and under the solar simulator illumination. This measurement was carried out at Czech Technical University, Prague, under the supervision of Dr. Bohuslav Rezek.

Secondary ion mass spectroscopy(SIMS)

In publication II, the elemental depth profiling was acquired via secondary ion mass spectroscopy (SIMS). Positive and negative ion profiles were recorded using a hidden analytical IG20 gas ion gun and EQS1000 quadrupole detector. Samples were bombarded with Ar^+ ions (5keV and 200nA on the sample surface) and the beam was rastered

over an area of 500×500 mm^2. A data gating of 10% was applied for the analysis. This measurement was done at Northumbria University, under the supervision of Dr. Guillaume Zoppi.

Temperature-dependent admittance spectroscopy(TAS)

Temperature-dependent admittance spectroscopy measurements were made at 20 K to 320 K with a temperature step of ΔT = 10 K using a Wayne Kerr 6500B impedance analyser. Impedance Z and phase angle θ were measured as a function of frequency ƒ and temperature T. Frequency ƒ was varied from 20 Hz to 10 MHz, and a minimum AC voltage of 30 mV was applied to remove the background noise. To gain a deeper understanding of the defects, dark measurements were carried out at 0, 0.2, and 0.4V forward DC bias conditions. This measurement was carried out at the division of physics, Taltech, under the supervision of Dr. Raavo Josepson.

2.3 Characterisation of CdS/Sb_2Se_3 solar cells

The performance of superstrate configuration solar cells with a Glass/FTO/CdS/Sb_2Se_3/Au structure was evaluated using current-voltage (J-V) measurements. These measurements were conducted using an AUTOLAB PGSTAT 30 potentiostat in conjunction with an Oriel Class A solar simulator (model 91159A) under standard test conditions (AM 1.5G, 100 mW/cm^2). Additionally, external quantum efficiency (EQE) measurements were performed over the wavelength range of 300–1000 nm. The EQE setup comprised a Newport 300 W Xenon lamp (model 69911) as the light source, a Newport Cornerstone 260 monochromator for wavelength selection, and a silicon-calibrated detector (Merlin) for signal detection.

3 Results and discussion

This chapter highlights the main findings in publications I, II and III. Section 3.1 focuses on the optimisation of the post-deposition annealing treatment of CdS films and its effect on CdS films and CdS/Sb_2Se_3 solar cells (publication I). Section 3.2 focuses on the impact of in situ chlorine incorporation on the CdS films and CdS/Sb_2Se_3 solar cells (publication II). Section 3.3 focuses on the optimisation of the VTD method through source-to-substrate distance adjustment and Ar gas incorporation to control the growth rate of the Sb_2Se_3 films and their dependence on CdS/Sb_2Se_3 solar cells and their defects (publication III).

3.1 Impact of post-deposition annealing treatment of CdS films on its properties and CdS/Sb_2Se_3 solar cells.

In this section, the effects of post-deposition annealing treatment (PDT) on the properties of CdS thin films and the performance of CdS/Sb_2Se_3 solar cells are comprehensively discussed. The results presented herein have been published in publication I.

3.1.1 The effect of post-deposition annealing on CdS film properties

Structural and morphological properties

The XRD analysis of CdS films deposited on a glass substrate and annealed at 200–400 °C (Figure 18) was used to study the impact of annealing on the structural properties of the CdS film. The XRD patterns are compared with standard data (ICDD: 01-089-0440 and 01-074-9665) [200]. This revealed distinct diffraction peaks corresponding to the (100), (101), (110), (103), and (004) planes of the CdS crystal structure (Figure 18a and b). Notably, the XRD pattern of the sample annealed at 400 °C exhibited an additional diffraction peak indexed to the (200) plane of the CdO phase (ICDD: 00-005-0640), indicating the oxidation in the CdS layer under elevated air annealing temperature conditions. In contrast, the XRD patterns of CdS films subjected to vacuum annealing displayed only the characteristic peaks of the CdS phase, with no evidence of secondary phases, regardless of the annealing temperature applied.

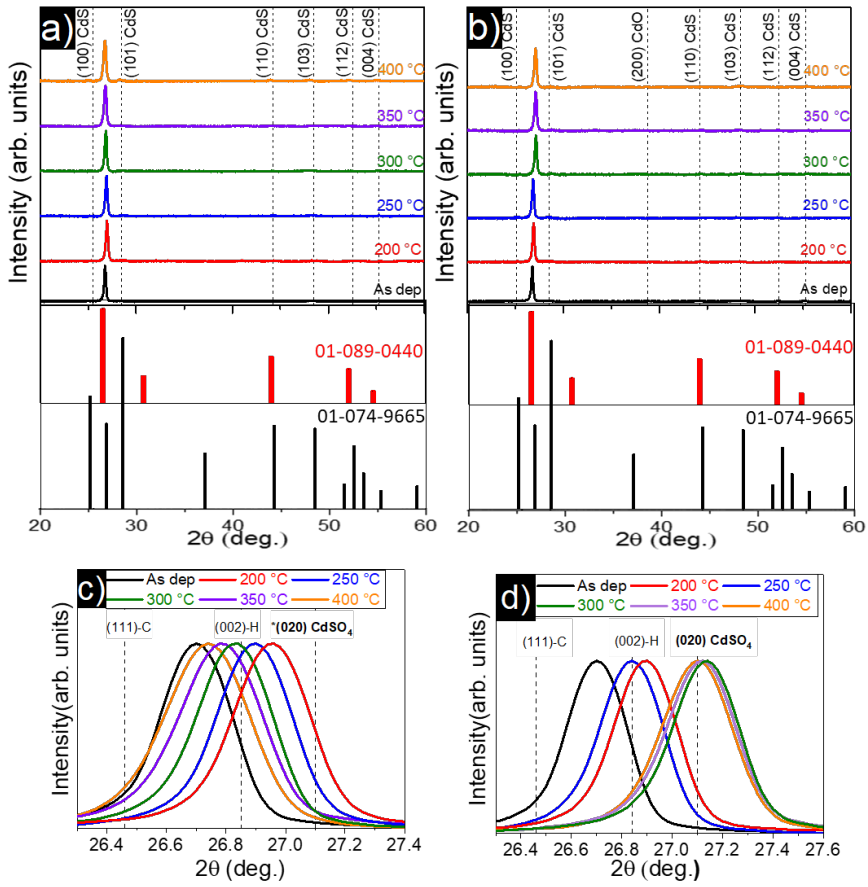

Figure 18. XRD pattern of a) vacuum annealed and b) air annealed CdS films, at 200°C–400°C temperatures for 30 min; displacement of dominant XRD peak depending on the c) vacuum and d) air annealing conditions.

To further investigate the structural modifications induced by different annealing atmospheres, a detailed analysis was conducted in the 2θ range of 26°–27°, as presented in Figure 18c and d. This region encompasses the prominent (111) diffraction peak, which has been previously attributed to both cubic and hexagonal modifications of CdS [132], [179]. But in these films, the structure of the CdS remained hexagonal. A comparison of the (111) peak evolution with increasing annealing temperature reveals distinct behaviours between vacuum and air annealed samples. In the case of vacuum annealed samples, the (111) peak showed a notable shift towards higher 2θ values (~27°) at 200 °C compared to the as-deposited CdS film. As the annealing temperature increased from 200 °C to 400 °C, the (111) peak gradually shifted towards lower 2θ values, eventually returning to a position close to that of the as-deposited sample at 400 °C. Conversely, the air annealed samples exhibited a continuous shift of the (111) peak towards higher 2θ values with increasing annealing temperatures. Specifically, at 300 °C, 350 °C, and 400 °C, the peak approached a position corresponding to the 020 plane of the $CdSO_4$ phase (ICDD: 00-014-0352), suggesting the potential formation of additional secondary phases at elevated air annealing temperatures. However, apart from the CdO-related peak observed in the 400 °C

air annealed sample, no other diffraction peaks corresponding to $CdSO_4$ were detected in the XRD patterns.

The observed shifts in the primary XRD peak and the emergence of oxide phases can be interpreted by considering several interrelated structural and chemical phenomena. Firstly, the appearance of the CdO phase at higher annealing temperatures, as evidenced in Figure 18b. This is mainly due to the thermal decomposition of cadmium sulfate ($CdSO_4$), which usually forms within the CdS lattice and later reacts with atmospheric oxygen during air annealing [133], [217].

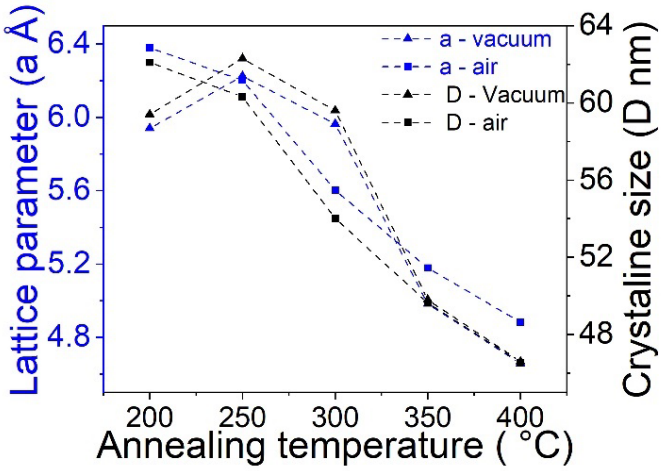

Figure 19. Variation of lattice parameter (a) and crystalline size (D) depending on the vacuum and air annealing temperatures.

In the case of vacuum-annealed samples, the shift of the primary XRD peak can be linked to the decomposition of cadmium hydroxide ($Cd(OH)_2$), which is known to crystallise within the CdS lattice during the CBD process. The incorporation of $Cd(OH)_2$ during deposition has been recognised as a key factor influencing the variation in lattice parameters, particularly the differences observed between hexagonal and cubic CdS crystal structures. With increasing annealing temperature, the $Cd(OH)_2$ phase undergoes thermal dissociation into CdO and water vapour. This transformation results in significant structural rearrangements within the CdS lattice, thereby inducing changes in the lattice parameters (Figure 19).

Additionally, the reduction in lattice constants observed under both air and vacuum annealing conditions may be attributed to the increased mobility and out-diffusion of hydroxyl (OH^-) groups within the CdS lattice. A supporting indicator of this process is the observed decrease in crystallite size as the annealing temperature increased from 200 °C to 400 °C, under both atmospheric conditions (Figure 19). Although such a trend in crystallite size reduction with increasing annealing temperature may initially appear counterintuitive, previous studies [134] have suggested that the out-diffusion of OH^- impurities exert a contracting effect on the CdS lattice, thereby reducing crystallite dimensions.

Furthermore, for air-annealed samples, the main XRD peak located at approximately 27.15° closely aligns with the 2θ position of the (020) diffraction peak of the $CdSO_4$ phase, raising the possibility of incipient formation of sulfate-based secondary phases. Although the corresponding peaks for $CdSO_4$ were not explicitly observed in the XRD patterns,

the proximity of this diffraction signal suggests partial phase transformation or structural distortion induced by sulfur oxidation at elevated temperatures.

The presence of such phase mixtures comprising CdS, CdO, and potentially $CdSO_4$ can have a significant influence on the optoelectronic properties of the CdS layer. These structural and compositional variations are likely to affect the band alignment, interface quality, and carrier transport characteristics in CdS/Sb_2Se_3 heterojunctions, thereby impacting the overall performance of the solar cell device.

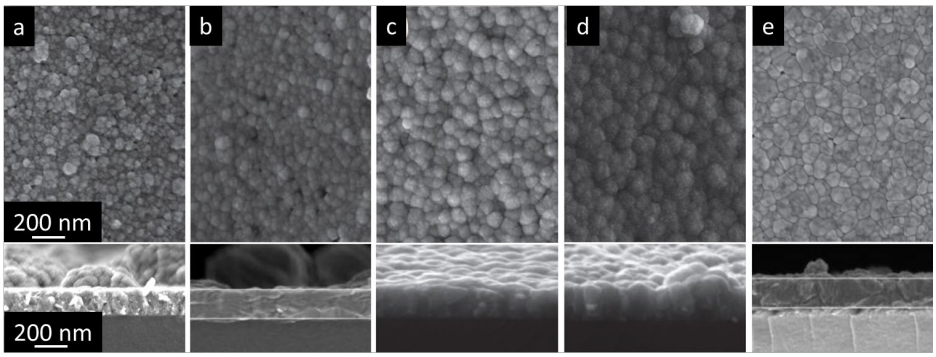

Figure 20. Surface and cross-section SEM images of CdS films deposited on glass substrates: a) as deposited, b) annealed in vacuum at 200 °C, c) annealed in air at 200 °C, d) annealed in vacuum at 400 °C, e) annealed in air at 400°C with an annealing duration of 30 minutes.

The surface morphology and cross-sectional structure of the as-deposited and annealed CdS films on glass and FTO substrates were examined using SEM, as shown in Figures 20 and 21. The as-deposited CdS layer (Figure 20a) exhibited small grains with visible agglomeration into localized clusters, indicating a non-uniform growth pattern. Upon vacuum annealing at 200 °C, no significant changes were observed in the grain size or overall surface morphology, as shown in Figure 20b, suggesting limited thermal activation at this temperature under vacuum conditions. In contrast, air annealing at the same temperature resulted in a more uniform grain size distribution (Figure 20c), implying enhanced surface modification through grain growth facilitated by the presence of oxygen. Interestingly, vacuum annealing at a higher temperature of 400 °C (Figure 20d) yielded a surface morphology comparable to that observed for the 200 °C air annealed sample, indicating that higher thermal energy in vacuum is required to achieve similar morphological evolution. Most notably, air annealing at 400 °C (Figure 20e) produced films with densely packed grains and improved grain connectivity. This morphological transformation suggests that air annealing at elevated temperatures promotes recrystallisation and sintering processes, thereby enhancing the compactness and structural integrity of the CdS films.

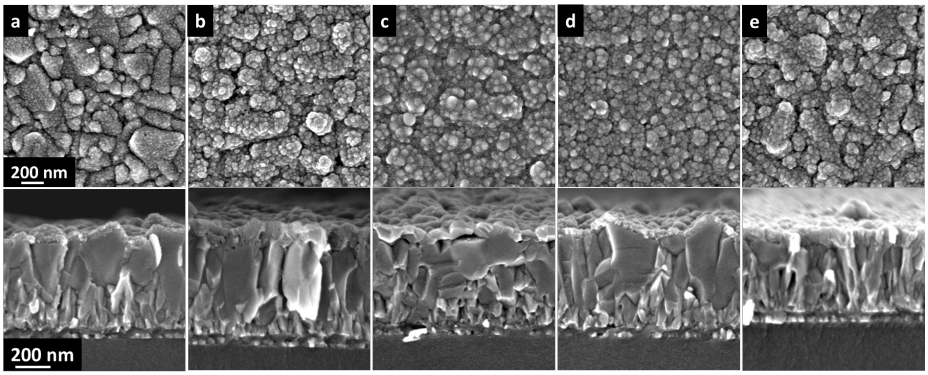

Figure 21. Surface and cross-section SEM images of CdS films deposited on FTO/glass substrates: a) as deposited, b) annealed in vacuum at 200 °C, c) annealed in air at 200 °C, d) annealed in vacuum at 400 °C, e) annealed in air at 400 °C with an annealing duration of 30 minutes.

Since the CdS is deposited on FTO for solar cell fabrication, the morphology of the CdS deposited on FTO substrates was also analysed (Figure 21). As-deposited and 200 °C vacuum annealed CdS films grown on FTO exhibit similar morphology to CdS deposited on glass. In this case, the porous layers comprising small grains and some grain conglomerates cover uniformly the relatively large FTO grains. Air annealing at 200 and 400 °C and vacuum annealing at 400 °C lead to significant densification of the CdS film (Figure 4a-e).

Electrical and optical properties

To study the effect of PDT on the electrical properties (carrier concentration, mobility, and resistivity) of CdS films, Hall measurements of the films deposited on glass substrates annealed at 200–400 °C for 30 minutes were carried out. As Table 3 shows, the as-deposited CdS films exhibit *n*-type conductivity with an electron concentration of 4.4×10^{15} cm^{-3}, electron mobility of 5 cm^2/Vs, and a resistivity of 2.8×10^2 Ω.cm. All films retained their *n*-type conductivity regardless of the annealing conditions. The variation in electrical parameters with respect to annealing conditions can be categorised into three distinct temperature regimes:

i. In the 200 °C–250 °C range, the resistivity decreases significantly from 4.2 to 2.6 Ω.cm for air annealing and from 3.2 to 0.2 Ω.cm for vacuum annealing. Concurrently, the carrier concentration increases by approximately one order of magnitude, from 10^{17} to 10^{18} cm^{-3} in the case of air annealing, and from 10^{18} to 10^{19} cm^{-3} under vacuum conditions.
ii. At 300 °C annealing temperature, a reverse trend is observed, where resistivity increases to 45 Ω.cm and 8.5 Ω.cm, while the carrier concentration decreases by an order of magnitude to 10^{17} cm^{-3} for air-annealed films and 10^{18} cm^{-3} for vacuum-annealed films.
iii. In the high-temperature regime of 350 °C–400 °C, a pronounced increase in resistivity is observed: from 7.7×10^3 to 4.2×10^4 Ω.cm for air annealed samples and from 4.6×10^1 to 1×10^4 Ω.cm for vacuum annealed films. Correspondingly, the carrier concentration exhibits a dramatic decrease, by approximately three and seven orders of magnitude for air and vacuum annealing, respectively.

Table 3. Electrical properties of CdS films annealed at different annealing temperatures in air and vacuum.

T(°C)	Air			Vacuum		
	Carrier Conc. (cm^{-3})	Mobility (cm^2/Vs)	Resistivity (Ω cm)	Carrier Conc. ($/cm^3$)	Mobility (cm^2/Vs)	Resistivity (Ω cm)
No annealing	4.4×10^{15}	5	2.8×10^{2}	4.4×10^{15}	5	2.8×10^{2}
200	6.3×10^{17}	3.1	4.2	1.7×10^{18}	1.2	3.2
250	3×10^{18}	3.3	2.6	1.4×10^{19}	2.2	2×10^{-1}
300	2.1×10^{17}	0.7	4.5×10^{1}	8.5×10^{17}	0.9	8.5
350	1.6×10^{13}	6.1	7.7×10^{3}	1.2×10^{18}	1.0	4.6×10^{1}
400	1.2×10^{10}	12	4.2×10^{4}	5×10^{11}	13	1×10^{4}

A similar dependence of carrier concentration on annealing temperature under air atmosphere has been previously reported by Maticiuc et al. [132], who attributed the trend to the mobility and eventual dissociation of hydroxide (OH^-) groups within the CdS lattice. These OH^- groups are incorporated during CBD process and have been proposed to act as shallow donors [218]. At lower annealing temperatures (e.g., 200 °C), the OH^- groups are thermally unstable and tend to decompose, releasing water and generating sulfur vacancies (V_S). Since V_S is known donor defects, their increased formation at these temperatures accounts for the abrupt rise in electron concentration.

At elevated annealing temperatures (350 °C and 400 °C), conditions become favourable for the substantial out-diffusion or removal of OH^- species from the CdS lattice, leading to a notable reduction in free carrier concentration. Although this mechanism has been primarily described for hydrogen and air-annealed CdS layers, the results obtained in this study suggest that it is also applicable to vacuum-annealed films. Furthermore, in the case of air annealing at 400 °C, the presence of CdO secondary phases (XRD analysis in Figure 18b) may contribute to the significant decline in carrier concentration, reaching values as low as ~10^{10} cm^{-3}.

The observed low mobility values at intermediate annealing temperatures (200 °C–300 °C) can be ascribed to enhanced scattering of charge carriers by ionised impurities present in the lattice. At higher annealing temperatures (350 °C and 400 °C), the progressive removal of these impurities results in increased carrier mobilities, consistent with previous observations reported by Spalatu et al. [135].

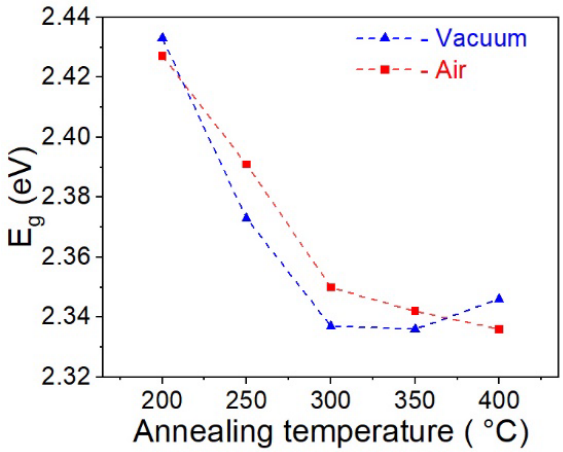

Figure 22. Variation in the bandgap of CdS films with vacuum and air annealing temperature.

The optical band gap of CdS thin films deposited on glass substrates was evaluated using Tauc plot analysis derived from UV-VIS absorption measurements. The as-deposited CdS films exhibited a direct optical band gap of approximately 2.42 eV. Upon post-deposition annealing in the temperature range of 200 °C to 400 °C under both air and vacuum conditions, a consistent decrease in the band gap was observed, as illustrated in Figure 22. In the case of vacuum annealing, the reduction in band gap can be attributed to the thermal decomposition of cadmium hydroxide ($Cd(OH)_2$) into cadmium oxide (CdO) and water, a phenomenon previously reported by Maticiuc et al. [133]. For air-annealed samples, the narrowing of the band gap is correlated with the formation of CdO secondary phases, as confirmed by X-ray diffraction analysis. The presence of CdO, a material with a lower band gap than CdS, contributes to the observed redshift in the absorption edge, as supported by earlier studies [201].

3.1.2 The effect of CdS post-deposition annealing on Sb_2Se_3 film properties

As a step towards the fabrication of a solar cell device, Sb_2Se_3 absorber films were deposited on a glass/FTO/CdS stack by CSS method and the structure and morphology of Sb_2Se_3 films were analysed. Figure 23 shows the XRD patterns and texture coefficients (TC) of Sb_2Se_3 films grown on as-deposited, 200 °C and 400 °C air annealed, and 200, 400 °C vacuum annealed CdS samples. Texture coefficients were performed according to Krautmann et al. [5]. The values were calculated using equation (2):

$$TC = \frac{I\,(hkl)}{I_0(hkl)} \times \left[\frac{1}{N}\sum_{i=0}^{n}\frac{I(h_i k_i l_i)}{I_0(h_i k_i l_i)}\right]^{-1} \quad (2)$$

XRD analysis of the Sb_2Se_3 thin films revealed prominent diffraction peaks at 2θ values of 28.2°, 31.1°, 32.2°, 45.1°, and 45.6°. These peaks were identified, by comparison with standard reference data (JCPDS No. 15-0861), as corresponding to the (211), (221), (301), (151), and (002) crystallographic planes of orthorhombic Sb_2Se_3. In films where Sb_2Se_3 was deposited on air-annealed CdS substrates, a preferential growth along the (002) plane was observed. This orientation was especially pronounced for Sb_2Se_3 grown on CdS films annealed in air at 400 °C, where the intensity of the (002) reflection significantly surpassed that of the other detected peaks. Conversely, Sb_2Se_3 films deposited on vacuum-annealed CdS layers exhibited a consistent (221) orientation across all annealing

temperatures. These observations suggest that Sb_2Se_3 films show a tendency for more vertically oriented growth on air annealed CdS substrates when compared to vacuum annealed counterparts. However, despite these tendencies, the XRD data do not present unequivocal evidence for a strong preferential orientation in any of the Sb_2Se_3 samples. For instance, although the (221) reflection appears slightly more intense in Sb_2Se_3 layers grown on CdS annealed under vacuum at 400 °C, the overall distribution of diffraction intensities suggests that the films are predominantly randomly oriented.

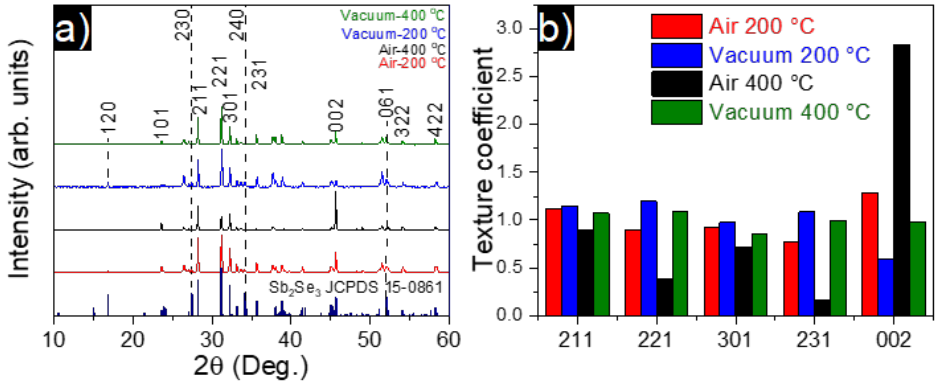

Figure 23. a) XRD spectrum and b) texture coefficient of Sb_2Se_3 on CdS annealed in vacuum and air at 200 °C and 400 °C.

One plausible explanation for the enhanced 002 texture in Sb_2Se_3 films deposited on 400 °C air annealed CdS films may be related to the modified surface morphology of the CdS under these conditions. SEM analysis (Figure 21) demonstrated that these CdS films exhibit a more compact, sintered grain structure with larger grains, which could lead to increased surface energy and consequently influence the nucleation dynamics of Sb_2Se_3, favouring growth along the 002 direction. Additionally, the oxidation of CdS, evidenced by the formation of CdO as detected in the XRD patterns (Figure 18b), may also play a role in altering the growth orientation of the Sb_2Se_3 layer.

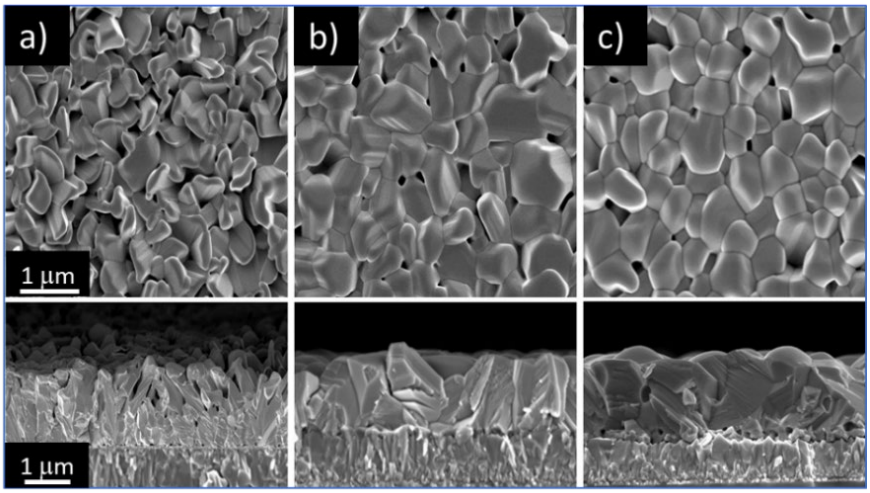

Figure 24. SEM images of superstrate configuration glass/FTO/CdS/Sb_2Se_3 stack with CSS Sb_2Se_3 absorber layer deposited at 460 °C: a) top-and cross-sectional view of absorber film deposited onto as-deposited CdS, b) top-and cross-sectional view of absorber deposited onto vacuum annealed CdS at 200 °C and c) top-and cross-sectional view of absorber deposited onto air annealed CdS at 200 °C.

To know more about the morphology of the Sb_2Se_3 grains deposited on CdS films, surface and cross-sectional SEM images of CdS/Sb_2Se_3 stacks (Figure 24), where the CdS layers were subjected to different annealing treatments: as-deposited, vacuum-annealed at 200 °C, and air-annealed at 200 °C, were analysed. The absorber layer deposited on the as-deposited CdS (Figure 24a) is characterised by irregularly shaped grains with sharp edges and exhibits significantly higher inner porosity compared to the Sb_2Se_3 films deposited on annealed CdS layers. In contrast, when Sb_2Se_3 is deposited on CdS annealed in vacuum at 200 °C (Figure 24b), the resulting absorber displays larger, more compact, and densely packed grains. A similar morphological improvement is observed in the absorber deposited on air-annealed CdS at 200 °C, which exhibits a more homogeneous grain size and shape distribution across the film. Notably, when the CdS layers were annealed at 400 °C, either in vacuum or in air, the morphology of the overlying Sb_2Se_3 absorbers remained consistent with that observed for the films grown on CdS annealed at 200 °C, as seen in Figure 24c. These observations collectively indicate a strong correlation between the morphological evolution of the absorber layer and the structural and microstructural properties of the underlying CdS.

The high degree of porosity observed in the Sb_2Se_3 layer deposited on as-deposited CdS (Figure 24a) can be attributed to the presence of organic residues within the CdS film. These residues originate from the CBD process and remain embedded in the film in the absence of a post-deposition annealing treatment. During the subsequent CSS deposition of Sb_2Se_3, the elevated process temperatures can act as an indirect annealing step for the underlying CdS layer, facilitating the out-diffusion of organic residues. This process can lead to the formation of voids and pinholes within the Sb_2Se_3 absorber layer. Conversely, in cases where the CdS films undergo prior thermal annealing (either in air or vacuum), the majority of these organic residues are effectively removed before the deposition of Sb_2Se_3. As a result, the annealed CdS layers provide a more stable and residue-free

interface, which promotes the growth of compact and pinhole-free Sb_2Se_3 absorber layers. These findings reinforce the significance of appropriate post-deposition treatment of the CdS ETL in determining the final morphology and structural integrity of the Sb_2Se_3 absorber.

3.1.3 The effect of CdS post-deposition annealing on CdS/Sb_2Se_3 solar cell properties

In this section, solar cells were fabricated using a superstrate device architecture consisting of glass/FTO/CdS/Sb_2Se_3/Au, and a systematic investigation was carried out to evaluate the influence of various CdS annealing conditions on the photovoltaic (PV) performance parameters. The PV parameters of the fabricated devices were extracted from current density-voltage (JV) characteristics, with representative curves under standard illumination shown in Figure 25a, and the corresponding average values are summarised in Figure 26.

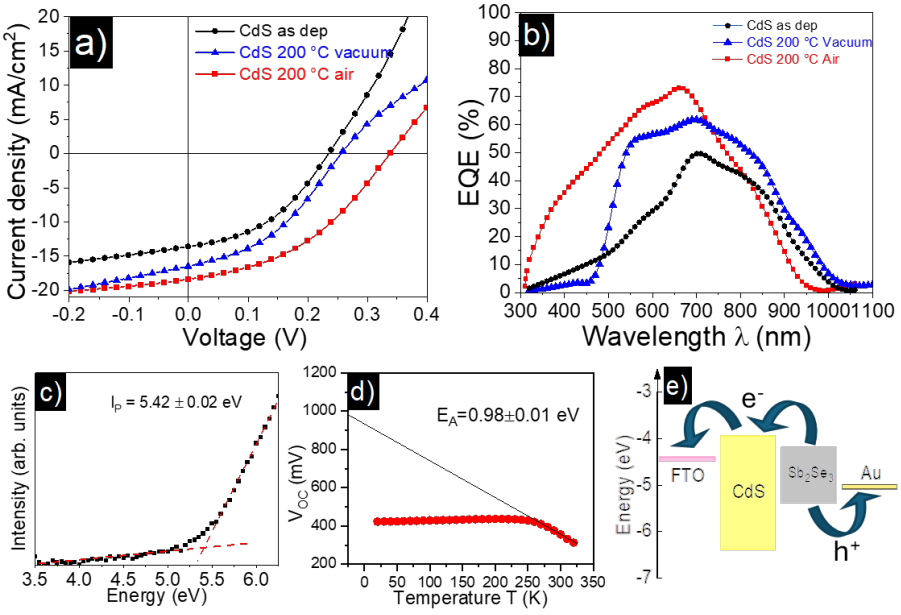

Figure 25. a) JV characteristics and b) EQE of CdS/Sb_2Se_3 solar cells with as-deposited, air and vacuum annealed CdS at 200 °C, c) Ionization potential of Sb_2Se_3 d) activation energy calculated from V_{OC}–T plot, e) band alignment of FTO/CdS/Sb_2Se_3/Au solar cell structure.

The analysis indicates that the devices incorporating as-deposited CdS films exhibited the lowest PCE of 1.2%. In contrast, significant improvements were observed in all key PV parameters, open circuit voltage (V_{OC}), short-circuit current density (J_{SC}), fill factor (FF), and PCE, when the CdS ETL was subjected to annealing at 200 °C in either vacuum or air. However, for annealing temperatures ≥250 °C, regardless of whether performed in vacuum or air, a decline in all PV parameters was observed (Figure 26). Among the tested conditions, annealing at 200 °C in air yielded the best device performance, with the top-performing solar cell achieving a PCE of 2.8%, accompanied by a V_{OC} of 350 mV, J_{SC} of 18.3 mA/cm^2, and FF of 43% (Table 4). This particular device also demonstrated the highest EQE response in the short-wavelength range (300–700 nm), as shown in Figure 25b.

Table 4. Photovoltaic parameters of the best performing CdS/Sb_2Se_3 solar cells with as-deposited, vacuum and air annealed at 200 °C, CdS films.

No.	CdS annealing condition	Photovoltaic parameters			
		V_{OC} (mV)	J_{SC} (mA/cm^2)	FF (%)	PCE (%)
1.	As deposited	230	13.7	39	1.2
2.	Vacuum 200 °C	260	16.4	44	1.8
3.	Air 200 °C	350	18.3	43	2.8

In comparison, the EQE response in the 300–700 nm region was substantially lower for the devices incorporating as-deposited and 200 °C vacuum-annealed CdS. This reduction in short-wavelength EQE has been previously reported in CdS/Sb_2Se_3 [4], [207] and CdTe/CdS [179], [219], [220] heterostructures, and is often attributed to intermixing between the CdS and the absorber layers (Sb_2Se_3 or CdTe), leading to the formation of a $CdS_{1-x}Se_x$ or $CdTe_{1-x}S_x$ solid solution at the heterojunction interface.

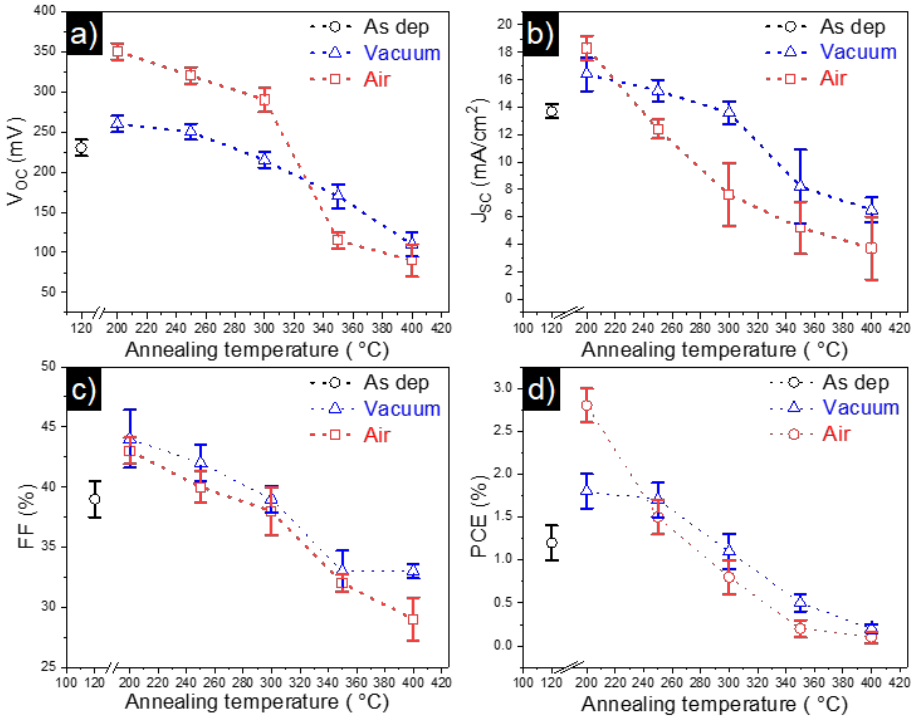

Figure 26. Main photovoltaic parameters, including a) open circuit voltage (V_{OC}), b) short circuit current density (J_{SC}), c) fill factor (FF), and d) photoconversion efficiency (PCE) with average values (marked as hollow squares) measured for Sb_2Se_3 devices.

In this research (publication I), the pronounced intermixing observed in the as-deposited and 200 °C vacuum-annealed CdS-based devices likely accounts for their diminished EQE in the 300–700 nm range. For the device with as-deposited CdS, this phenomenon may be linked to the film's morphology, which features small grains (Figures 20a and 21a) with high surface energy. These high-energy surfaces are prone to mass

transport via the gas phase during the CSS deposition of Sb_2Se_3 at 450 °C, thereby facilitating extensive alloy formation at the interface. Furthermore, the presence of organic residues, as discussed in previous studies [179], [200], [221], and the occurrence of large aggregates on the surface of as-deposited CdS may interfere with proper heterojunction formation. These issues collectively contribute to the reduced EQE and the relatively low PCE observed for these devices (Figures 25a and b). In contrast, devices fabricated using CdS layers annealed at 200 °C in vacuum exhibited a notable improvement in EQE and PCE relative to their as-deposited counterparts. This enhancement suggests a more favourable CdS/Sb_2Se_3 interface, which can be attributed to the removal of organic residues during the vacuum annealing process. The resulting cleaner and more thermally stable CdS films facilitate improved absorber morphology and enhanced junction quality. The most pronounced enhancement was observed for the devices employing 200 °C air-annealed CdS, which exhibited the highest EQE and best overall device performance. This indicates that the intermixing at the CdS/Sb_2Se_3 interface in these devices was minimal.

For the top-performing device, the ionisation potential (I_P) values for both the Sb_2Se_3 absorber and CdS ETLs were determined through linear extrapolation from the valence band edge photoemission to 0 eV. A representative fitting for the Sb_2Se_3 layer is shown in Figure 25c, yielding an I_P of 5.42$\pm$0.02 eV, which is consistent with values reported in the literature [97]. Further analysis of the resulting energy band diagram (Figure 25e) reveals that the conduction band minimum of CdS lies above that of Sb_2Se_3, producing a spike-like conduction band offset of approximately 0.2 eV at the main interface. While this type of band alignment may assist in preventing carrier recombination, it can also act as a barrier to electron transport, thereby contributing to a reduction in J_{SC}, as suggested in previous studies [222]. The temperature-dependent open-circuit voltage (V_{OC}–T) characteristics were analysed by linear extrapolation to 0 K, yielding an activation energy E_A of 0.98$\pm$0.01 eV (Figure 25d), which is lower than the optical bandgap of Sb_2Se_3 (~1.2 eV). This discrepancy indicates that significant recombination occurs at or near the CdS/Sb_2Se_3 interface, thereby limiting device performance.

Based on these results, the PDT conditions for the CdS films were optimized and fixed at 200 °C air annealing. Subsequently, new strategies were adopted to further enhance the absorber and ETL properties, including the incorporation of chlorine into the CdS layer and the implementation of the VTD technique for Sb_2Se_3 film fabrication, with the aim of improving the overall performance of the solar cells.

3.2 Impact of In-situ chlorine incorporation in CdS films on its properties and CdS/Sb_2Se_3 solar cells.

In this section, the detailed results regarding the impact of in situ chlorine incorporation into CdS films, achieved by introducing NH_4Cl into the CBD solution, on the properties of CdS film, as well as on the performance of CdS/Sb_2Se_3 solar cells, are presented and discussed. Furthermore, the deposition method for Sb_2Se_3 thin films was transitioned from CSS to VTD. This modification was implemented to overcome the fixed source-to-substrate distance limitation inherent in the CSS setup available at the institute, and to explore the scalability potential of the VTD technique for future device fabrication. These findings have been published in publication II.

3.2.1 The effect of in situ chlorine incorporation on CdS film properties

Structural and morphological properties

To evaluate the impact of chlorine incorporation on the structural and morphological properties of CdS thin films, a series of CdS layers were deposited on glass substrates via CBD, incorporating varying concentrations of NH_4Cl at 0, 1, 2, 4, and 8 mM in the precursor solution. The resulting films were subsequently characterized using XRD and SEM techniques.

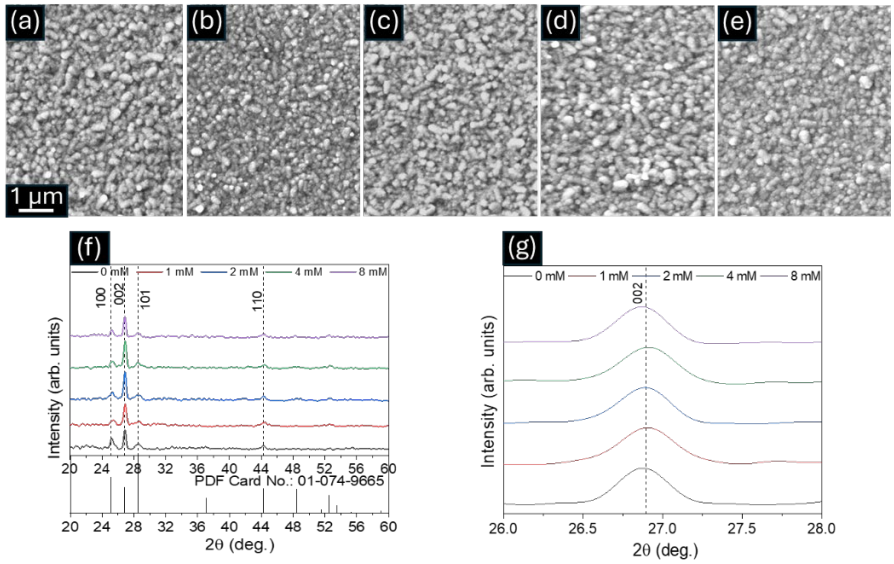

Figure 27. (a-e) Surface SEM images of CdS films prepared with 0, 1, 2, 4, and 8 mM NH_4Cl in the CBD precursor, (f) XRD pattern of CdS with different NH_4Cl concentration, (g) Variation of (002) peak of CdS films with different NH_4Cl concentration.

The surface morphology of the CdS films was examined using SEM, as shown in Figures 27a-e. All samples exhibited compact, uniform grain structures without visible cracks, and no substantial variations in surface morphology were observed across the different NH_4Cl concentrations. This morphological stability suggests that the relatively low concentration of NH_4Cl employed in the present study did not significantly disrupt the growth dynamics of the CdS films. Although previous reports have demonstrated changes in CdS morphology upon doping with chloride ions [6] or silver ions [223], the current findings indicate that the low Cl^- concentrations used here maintained the integrity of the film morphology.

The XRD pattern of CdS films with different NH_4Cl concentrations was compared with standard reference data (PDF Card No. 01-074-9665) [133], as shown in Figure 27f. The results confirmed the formation of hexagonal phase CdS, with prominent diffraction peaks observed at 25.2°, 26.8°, 28.5°, and 44.3°, corresponding to the (100), (002), (101), and (110) crystallographic planes, respectively. Importantly, no secondary phases such as $CdCl_2$ or other chlorine-related compounds were detected, indicating that Cl incorporation did not lead to the formation of extrinsic crystalline phases. This observation is consistent with findings by Sivaraman et al. [224], who similarly reported an absence of chlorine-related diffraction peaks in CdS films doped with Cl via spray coating, even at higher Cl concentrations than those used in the present study.

A detailed analysis of the 002 reflection was carried out to elucidate the effect of NH_4Cl incorporation on lattice structure (Figure 27g). The 002 peak appeared at nearly the same 2θ position, indicating minimal structural variation within the NH_4Cl concentration range. However, the sample with 8 mM NH_4Cl exhibited a shift of the 002 peak toward a lower 2θ angle compared to the 4 mM NH_4Cl sample, implying a lattice expansion possibly due to enhanced Cl incorporation. Notably, as the NH_4Cl concentration increased from 0 to 4 mM, a slight shift of the 002 peak toward higher 2θ values was observed. This peak displacement was observed in CdS films subjected to different annealing environments (Publication I) and is attributed to the lattice disorders, particularly hydroxide (OH^-) and chloride (Cl^-) species during film formation. The observed shift in the 002 reflection serves as indirect evidence of chlorine incorporation into the CdS lattice structure.

Optical and electrical properties

In continuation with the methodology adopted in publication I, the optical and electrical properties of CdS thin films with varying concentrations of NH_4Cl were systematically investigated. The optical band gap of the CdS films deposited on FTO substrate was determined using Tauc plot analysis derived from UV-Vis absorption spectra, and the electrical properties of the CdS films deposited on glass substrate were examined through Hall effect measurements.

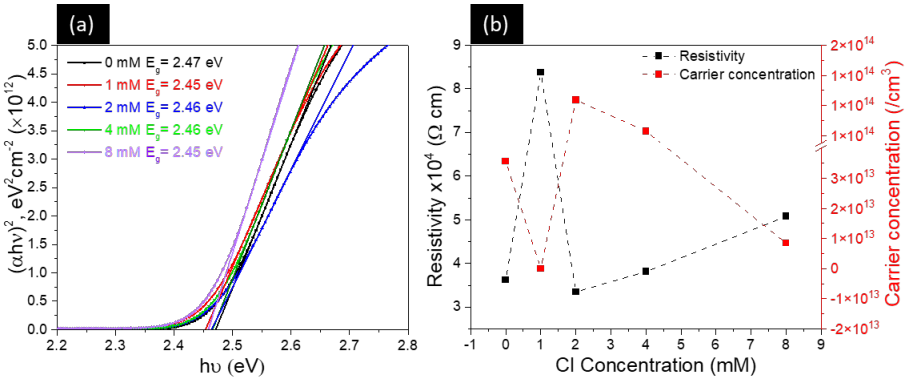

Figure 28. (a) Tauc plots, showing the variation in bandgap of CdS films processed with 0–8 mM NH_4Cl concentration (b) electrical properties (carrier concentration and resistivity) of CdS films with different NH_4Cl concentration.

The band gap results (Figure 28a) indicate a slight decrease in the optical band gap from 2.47 eV to 2.45 eV with the initial introduction of NH_4Cl at a concentration of 1 mM. As the NH_4Cl concentration was further increased beyond 1 mM, the band gap remained nearly constant, exhibiting only marginal variations on the order of 0.1 eV. It is important to note that these changes are relatively minor when compared to previous studies [224] involving high levels of chlorine doping, where more pronounced band gap modifications were reported.

The electrical properties of the CdS films, specifically carrier concentration and resistivity as a function of NH_4Cl concentration are presented in Figure 28b. All films exhibited resistivity on the order of 10^4 Ω cm, consistent with values previously reported by Hiie et al. [225]. A notable increase in resistivity was observed upon the introduction of 1 mM NH_4Cl, rising from 3.6×10^4 to 8.3×10^4 Ω cm. However, a sharp reduction in resistivity occurred when the NH_4Cl concentration was increased to 2 mM, dropping to

$3.3\times10^4\ \Omega$ cm. Beyond this point, as the concentration of NH_4Cl was further increased to 4 mM and 8 mM, the resistivity exhibited only a moderate increase, ranging from 3.3×10^4 to $5.0\times10^4\ \Omega$ cm. This abrupt reduction in resistivity from 1 mM to 2 mM NH_4Cl may be attributed to the incorporation of Cl^- ions into the CdS lattice, although no distinct Cd or Cl phases were detected in the XRD patterns (Figure 27f). An alternative explanation involves sulfur vacancies: the introduced Cl atoms may occupy these vacancies, thereby increasing the free carrier concentration and consequently reducing the resistivity. Such mechanisms have also been reported in literature addressing sulfur-deficient CdS films [226].

The carrier concentration exhibited significant variation with NH_4Cl concentration. The highest carrier density of 1.3×10^{14} cm^{-3} was recorded for CdS films containing 2 mM NH_4Cl. Increasing the NH_4Cl concentration to 4 mM resulted in a similar carrier concentration, while a further increase to 8 mM led to a two-order-of-magnitude drop in carrier density to 8.4×10^{12} cm^{-3}. Notably, the CdS film with 2 mM NH_4Cl exhibited both the highest carrier concentration (1.3×10^{14} cm^{-3}) and the lowest resistivity ($3.3\times10^4\ \Omega$ cm), whereas the film with 1 mM NH_4Cl showed the highest resistivity ($8.3\times10^4\ \Omega$ cm) and the lowest carrier concentration (3.4×10^{10} cm^{-3}). These pronounced variations in electrical properties provide strong evidence for the successful incorporation of chlorine into the CdS lattice.

The reason for the changes in electrical properties in CdS films is due to two concomitant processes (both hydroxyl group and chlorine incorporation) occurring in the lattice.

$$nCdS + Cd(OH)_2 \rightarrow Cd_{n+1}S_n2(OH)_2V_{Cd} \quad (3)$$
$$2NH_4Cl + CdSO_4 \leftrightarrow CdCl_2 + (NH_4)_2SO_4 \quad (4)$$
$$nCdS + CdCl_2 \rightarrow Cd_{n+1}S_n2Cl_2V_{Cd} \quad (5)$$

According to equation 3, as a result of the chemical reaction during CBD process, cadmium hydroxysulfide is formed, and the OH group occupies the sulfur site in the CdS lattice, behaving as a shallow donor. On another hand, according to equation 4, the presence of NH_4Cl in the CBD precursor solution promotes the formation of $CdCl_2$, leading to the incorporation of Cl into the CdS lattice and generating one V_{Cd} per every pair of incorporated Cl_S. Depending on the concentration of both hydroxyl group and chlorine in CdS, the generated V_{Cd}^{2-} can compensate the $(OH)_S^+$ and Cl_S^+, resulting in a low electron density of CdS.

Thus, at 0 mM NH_4Cl, the electron concentration in CdS film is entirely determined by the concentration of OH group which is incorporated into CdS on sulfur sites, generating an electron density of ~3×10^{13} cm^{-3} (Figure 28b). An incorporation of 1 mM NH_4Cl in the CBD precursor seems to be a relatively low concentration to generate enough Cl_S^+ which would enhance the electron density. At such moderate Cl concentration and considering the incorporated $(OH)_S^+$, the concentration of double charged acceptor $(V_{Cd})^{2-}$ (which is generated by incorporation of both, and $Cd(OH)_2$ (equation 3), $CdCl_2$ (equation 5)) appears to be high enough to compensate the shallow donors, resulting in enhanced resistivity and reduced electron density (Figure 28b). An increase in the electron density of the films processed with 2 mM NH_4Cl in the CBD precursor is due to the enhanced concentration of Cl_S^+ shallow donor defects which seems to be in higher concentration compared to $(V_{Cd})^{2-}$ at the given incorporated $CdCl_2$ amount. As the amount of NH_4Cl in the CBD precursor increases further, the electron density in CdS gradually drops (Figure 28b) because of the high Cl incorporation into the CdS lattice. Under these conditions,

there is a high probability for Cl to occupy the interstitial states (acting as a *p*-type defect) in the CdS lattice, promoting a high degree of compensation effect. Thus, these results indicate that depending on the amount of the NH_4Cl in the CBD precursor, the balance between $(OH)_S^+$ and Cl_S^+ is always shifted, governing resistivity, electron density and work function in CdS films.

To gain deeper insight into the energy level alignment and surface electronic behavior of the CdS films, and to understand the modifications induced by the in situ incorporation of NH_4Cl, the work function (WF) of the films was analyzed under a dark–light–dark–light–dark illumination cycle. Spatially resolved WF mapping was also conducted to assess the homogeneity of the electronic structure across the film surface. Figure 29a-e displays the WF maps of CdS films with 0, 1, 2, 4, and 8 mM NH_4Cl measured under dark conditions, whereas Figures 29f-j present the corresponding WF maps of the same samples under illumination. Figure 29k illustrates the variation in average WF values and surface photovoltage (SPV) as a function of NH_4Cl concentration.

In the case of the CdS film with 0 mM NH_4Cl, the WF fluctuated between 4.42 and 4.55 eV in the dark. Upon illumination, a decrease in WF by approximately 0.10 eV was observed, resulting in a WF range of 4.32–4.42 eV (Figure 29f). This light-induced WF reduction indicates a positive photovoltage, signifying the generation of photogenerated holes at the surface. With the incorporation of 1 mM NH_4Cl, the WF increased significantly, ranging from 4.50 to 4.60 eV in the dark (Figure 29b), and again exhibited a positive photovoltage under illumination (Figure 29g). Notably, the CdS film with 1 mM NH_4Cl displayed a more uniform surface charge distribution compared to the other samples. For the film with 2 mM NH_4Cl, the WF range in the dark was between 4.42 and 4.45 eV Figure 29c), with minor fluctuations likely influenced by local surface morphology. Similarly, the 4 mM NH_4Cl-CdS film exhibited WF values within the same 4.42–4.45 eV range (Figure 29d), and a light-induced decrease of approximately 0.15 eV was recorded, again indicating a positive SPV. The 8 mM NH_4Cl-CdS film showed WF values between 4.46 and 4.56 eV under dark conditions (Figure 29e), which decreased under illumination by about 0.20 eV to a range of 4.32–4.36 eV (Figure 29j). Overall, the maximum WF of 4.63 eV was observed for the film containing 1 mM NH_4Cl, indicating a 0.12 eV increase relative to the undoped film. For higher NH_4Cl concentrations, the WF values remained relatively stable, with variations confined within a narrow 0.02 eV window. Spatial mapping revealed that, except for the 1 mM NH_4Cl-CdS sample, the CdS films exhibited comparable and uniform work function distributions in both dark and illuminated states. The 1 mM NH_4Cl-CdS film uniquely demonstrated localised regions of higher work function.

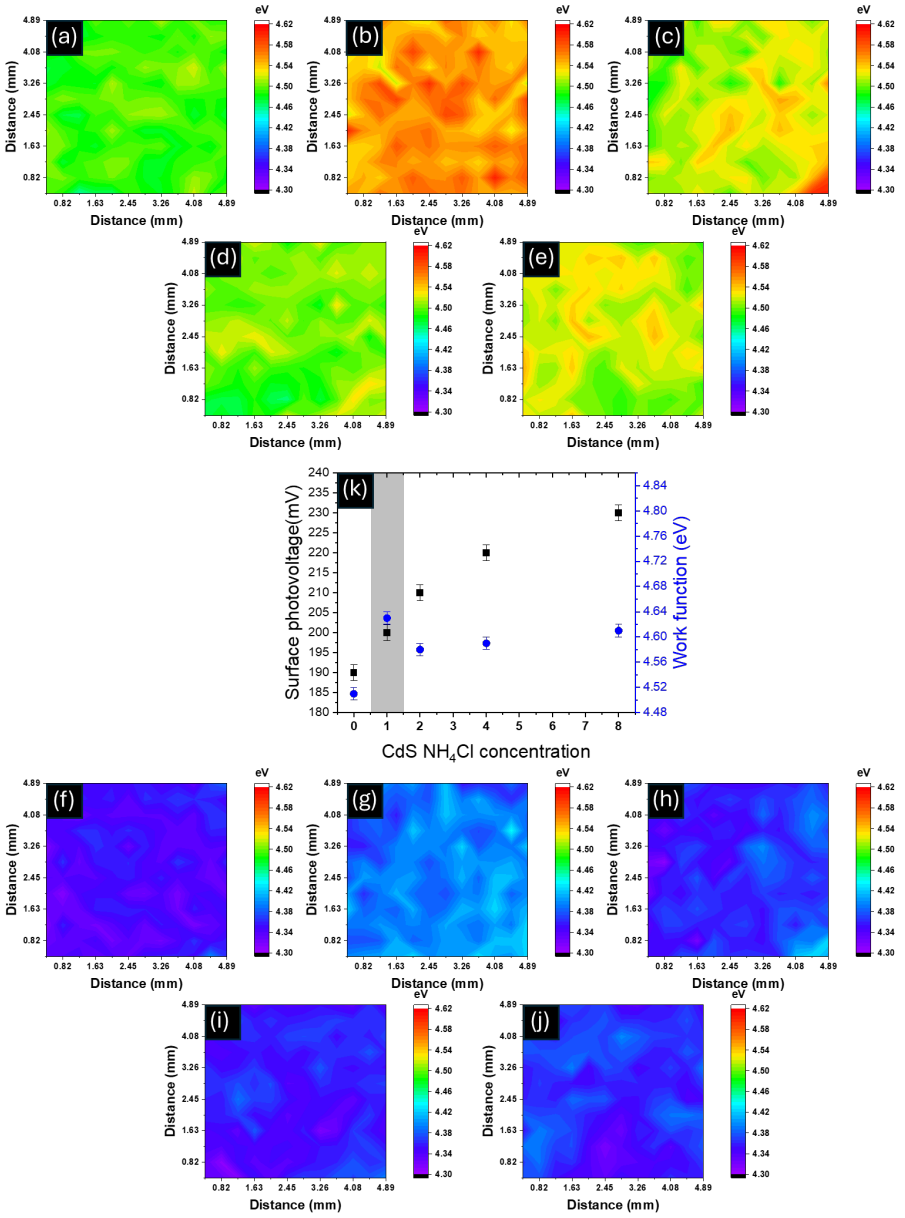

Figure 29. (a, b, c, d, e) dark and (f, g, h, i, j) light condition work function distribution of CdS films at 0, 1, 2, 4, and 8 mM NH_4Cl in order (k) Variation of work function (WF) and surface photovoltage (SPV) with the change in NH_4Cl concentration.

This observed WF trend aligns with the electrical characterization results, where a substantial increase in carrier concentration was recorded as NH_4Cl concentration increased from 1 mM to 2 mM (Figure 28b). This abrupt rise in carrier concentration suggests effective Cl^- incorporation into the CdS lattice, acting as donor species. However, further increases in NH_4Cl concentration from 2 mM to 8 mM resulted in a marked decline in carrier concentration, which may be attributed to compensation effects. These could arise from the formation of electrically neutral Cl-containing complexes, as well as

the incorporation of hydroxide (OH^-) species during deposition. Despite this, a consistent and monotonic increase in SPV was observed, rising from 190 eV to 240 eV with increasing NH_4Cl concentration from 0 to 8 mM (Figure 29k), indicating enhanced surface photovoltage response and suggesting improved charge separation characteristics at the film surface with higher dopant levels.

3.2.2 The effect of in situ chlorine incorporation in CdS films on Sb_2Se_3 film properties

As a continuation toward complete solar cell fabrication, Sb_2Se_3 absorber layers with an average thickness of approximately 1 µm were deposited on glass/FTO/CdS substrates by VTD method. These substrates included CdS ETLs synthesized with varying NH_4Cl concentrations during CBD, enabling an investigation of how the modifications in the CdS layer influence the structural and morphological characteristics of the overlying Sb_2Se_3 absorber films.

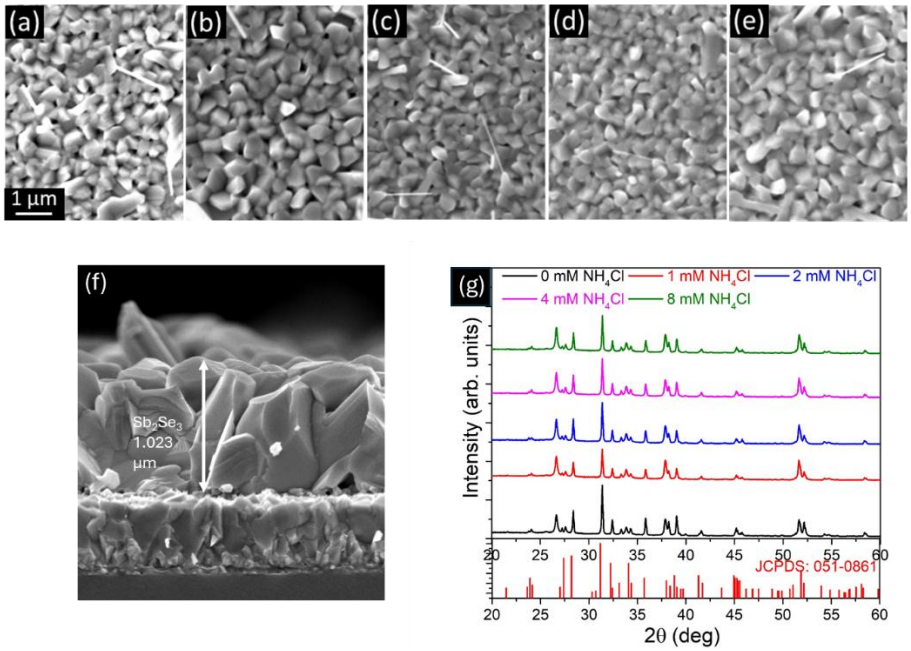

Figure 30. (a-e) Surface SEM images of Sb_2Se_3 films prepared on CdS layers with 0, 1, 2, 4, and 8 mM NH_4Cl in the CBD precursor, (f) Cross-section SEM image of 1 mM NH_4Cl-CdS/Sb_2Se_3 structure (g) XRD pattern of Sb_2Se_3 on CdS with 1 mM NH_4Cl concentration.

The SEM images of Sb_2Se_3 films (Figure 30a-e) exhibited compact morphology with no apparent porosity, indicating continuous and dense film coverage. However, the grain size and shape were not entirely uniform across the samples. Some grains appeared irregular in shape, while others exhibited tower-like vertical grain structures. These morphological deviations are likely attributable to localised substrate temperature fluctuations during the VTD growth process, which can impact the nucleation and grain growth dynamics. No significant changes in the surface morphology of the Sb_2Se_3 films were observed due to the Cl incorporation in the CdS films. This suggests that the Cl-modified CdS layer has a minimal impact on the surface growth features of the

absorber material under the current deposition conditions. The cross-sectional SEM image of the Sb_2Se_3 film deposited on the 1 mM NH_4Cl-CdS substrate (Figure 30f) confirms the presence of well-defined, vertically aligned columnar grains. Such a columnar microstructure is typically favourable for efficient charge transport in thin-film solar cell absorbers.

The XRD data of Sb_2Se_3 films, regardless of the NH_4Cl concentration used in the CdS precursor layer, exhibited identical diffraction patterns. The complete set of XRD patterns for all samples is shown in Figure 30g. The diffraction peaks observed at 15.03°, 16.87°, 23.9°, 27.02°, 28.2°, 31.16°, 32.22°, 34.08°, 37.98°, 39.08°, 41.35°, 44.95°, 45.57°, and 54.88° correspond to the (020), (120), (130), (021), (211), (221), (301), (240), (041), (411), (250), (431), (002), and (061) crystallographic planes of orthorhombic Sb_2Se_3, in good agreement with the standard JCPDS card No. 15-0861 [5]. Among these reflections, the (221) and (211) peaks were particularly intense, indicating a preferential growth orientation along these planes. This observation aligns with the columnar grain structure visible in the cross-sectional SEM image (Figure 30f), suggesting a tilted columnar alignment characteristic of high-quality Sb_2Se_3 films suitable for photovoltaic applications.

3.2.3 Elemental composition of Cl incorporated CdS and CdS/Sb_2Se_3 interface

To elucidate the elemental composition CdS films deposited with varying NH_4Cl concentrations, both X-ray Photoelectron Spectroscopy (XPS) and Energy Dispersive X-ray Spectroscopy (EDX) analyses were conducted. The XPS spectra revealed distinct peaks corresponding to Cd 3d, specifically at binding energies of 405.8 eV and 412.5 eV, which are characteristic of Cd^{2+} in CdS. However, no significant Cl 2p signal was detected within the typical Cl 2p binding energy range of 190–210 eV. This absence of surface Cl signal suggests that chlorine introduced during the CBD process is not predominantly located at the surface of the CdS films. Instead, the incorporated chlorine atoms are likely distributed within the bulk of the film, which is beyond the detection depth of XPS.

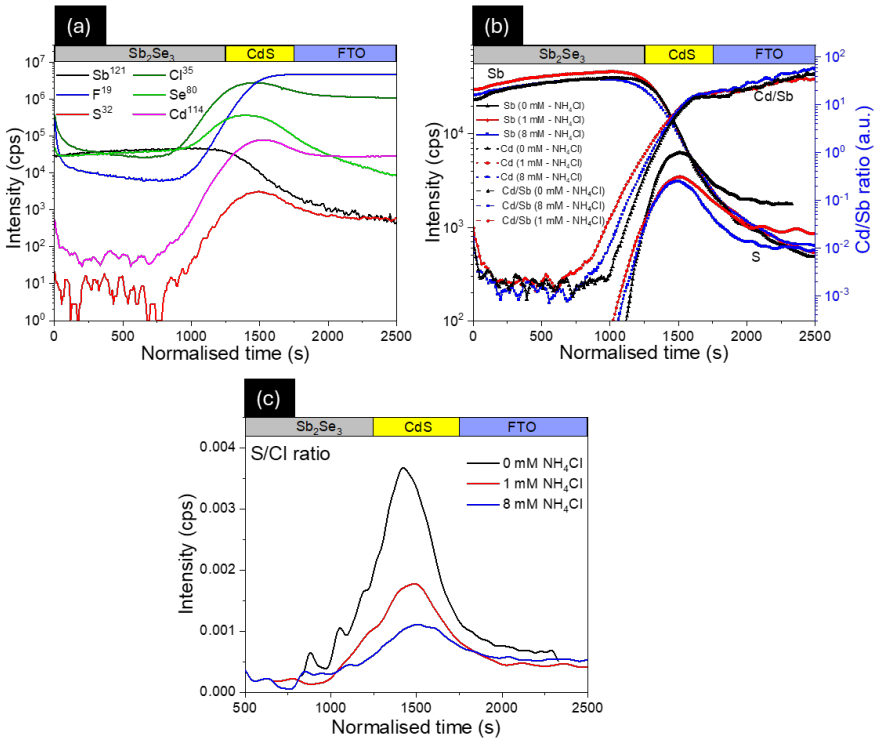

Figure 31. Secondary ion mass Spectroscopy (SIMS) depth profiles, a) Sb, Se, Cd, S, Cl, and F elemental distribution in 1 mM NH_4Cl-CdS samples b) Cd/Sb ratio at NH_4Cl-CdS/Sb_2Se_3 interface c) S/Cl ratio of 0, 1, 8 mM NH_4Cl-CdS samples.

The elemental distribution and interfacial interdiffusion within the CdS/Sb_2Se_3 heterojunction solar cells were analysed through SIMS method, performed on samples employing CdS ETLs prepared with 0, 1, and 8 mM NH_4Cl concentrations. Figure 31a illustrates the depth profiles of key elemental species Sb^{121}, Se^{80}, Cl^{35}, Cd^{114}, S^{32}, and F^{19} for the solar cell incorporating 1 mM NH_4Cl-CdS. The depth-resolved profiles confirm the distinct presence of constituent elements corresponding to the Sb_2Se_3 absorber and CdS ETLs. Notably, the Cl^{35} signal detected within the 1 mM NH_4Cl-CdS sample provides strong evidence of successful Cl incorporation into the CdS layer. The S/Cl ratio derived from SIMS data (Figure 31c) was highest in the Cl-free (0 mM NH_4Cl) sample and progressively decreased with increasing NH_4Cl concentration. This trend confirms the effective incorporation of chlorine into the CdS films as the NH_4Cl concentration in the chemical bath is increased.

To further investigate possible intermixing at the CdS/Sb_2Se_3 interface, the Sb/Cd intensity ratio was calculated from SIMS data for all three NH_4Cl concentrations (0, 1, and 8 mM), as shown in Figure 31b. The samples prepared with 1 mM and 8 mM NH_4Cl exhibited a more gradual slope at the CdS leading edge compared to the 0 mM sample, indicating enhanced Cd diffusion into the Sb_2Se_3 absorber. Interestingly, this interdiffusion does not appear to scale linearly with Cl concentration; the 1 mM NH_4Cl-CdS sample displayed the most pronounced intermixing, suggesting optimal Cl-induced lattice modification occurs at this concentration. Such interdiffusion can promote the formation of a CdSe transition layer at the interface, potentially improving the heterojunction

quality. Compared with earlier reports, Wen et al. [85] have reported a remarkable PCE of 7.6% using a similar Sb_2Se_3 absorber deposited by the VTD method and have attributed their result to improved lattice matching and defect passivation due to interfacial intermixing. Similarly, Liang et al. [188] reported a 7.4% efficiency in substrate-configuration CdS/Sb_2Se_3 solar cells utilising VTD followed by post-selenization. However, other studies [4], [124], [207] employing the CSS method have reported a detrimental impact on device performance from excessive intermixing, underscoring the deposition technique dependence of this effect. These contradictory results highlight that the extent and nature of intermixing at the CdS/Sb_2Se_3 interface and its subsequent influence on solar cell performance are strongly dependent on multiple interrelated factors. In particular, PDT of the CdS films, the degree of chlorine incorporation into the CdS layer, and the specific process conditions employed during absorber deposition (e.g., optimized VTD or CSS methods) all play critical roles in determining whether such interfacial interdiffusion yields beneficial or detrimental effects on device efficiency.

3.2.4 The effect of in situ chlorine incorporation in CdS films on CdS/Sb_2Se_3 solar cell properties

As the next step, Sb_2Se_3-based solar cells were fabricated in a superstrate configuration (glass/FTO/CdS/Sb_2Se_3/Au), wherein the CdS ETL was deposited with varying concentrations of NH_4Cl to investigate the influence of in situ chlorine incorporation on the device performance.

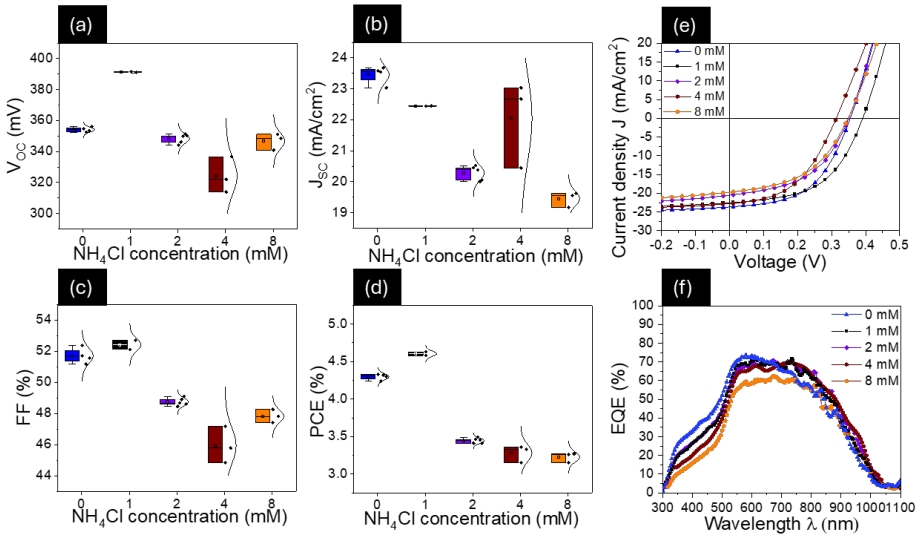

Figure 32. (a) open circuit voltage (V_{OC}), (b) short circuit current density (J_{SC}), (c) fill factor (FF), (d) power conversion efficiency (PCE), (e) JV characteristics and (f) external quantum efficiency (EQE) of CdS/Sb_2Se_3 solar cells with a change in NH_4Cl concentration in the CBD-CdS.

The device parameters, such as V_{OC}, FF, and PCE (Figure 32), extracted from the JV curve (Figure 32e) of the solar cells, were increased when 1 mM of NH_4Cl was introduced to the CdS films. The V_{OC} increases to 391 mV from 354 mV, FF increases to 52.4% from 51.7%, and PCE increases to 4.6% from 4.2%. The highest PCE of 4.6% was also obtained for the cells using a CdS ETL with 1 mM NH_4Cl (Figure 32d). As the NH_4Cl concentration in the CdS film increases after 1 mM all the solar cell properties go down. The lowest PCE of

2.2% was obtained for the solar cells with 8 mM NH_4Cl CdS ETLs. The incorporated Cl has affected the solar cell parameters. The cells with maximum resistivity and minimum carrier concentration (1 mM NH_4Cl) CdS as ETL, resulted in the best performance.

The improved performance of the solar cells with 1 mM NH_4Cl-CdS depends on several mechanisms that happen to the CdS as well as the CdS/Sb_2Se_3 interface during the VTD deposition. In general, during this process, the underlying CdS ETL experiences thermal annealing, particularly during the temperature ramp-up phase of the substrate and source. This thermal exposure induces a recrystallisation of the CdS layer, wherein the initially small grains with high surface energy undergo grain growth. This recrystallisation not only modifies the microstructure of CdS but also facilitates the decomposition and out-diffusion of incorporated species such as chlorine and hydroxyl (OH) groups. Along with that the SIMS analysis of the CdS/Sb_2Se_3 interface shown in Figure 31b has revealed notable elemental interdiffusion. This plays a critical role in determining the structural and electronic properties of the *n–p* heterojunction by affecting interface defect formation and the overall quality of the junction. Specifically, the SIMS results of the 1mM NH_4Cl-CdS/Sb_2Se_3 sample confirmed an extensive diffusion of Cd atoms into the Sb_2Se_3 absorber compared to the other samples. This latter observation is particularly noteworthy, as previous reports have only speculated on Cd diffusion without providing direct experimental evidence. Certain studies have hypothesised that Cd incorporation into Sb_2Se_3 may act as a donor defect, potentially generating a rectifying junction within the space charge region [209]. This dual effect appears to enhance the quality of the heterojunction and, in turn, the overall device performance.

The EQE response (Figure 32f) of the solar cells shows steady efficiency in the 550–750 nm range. The solar cells with CdS ETL deposited with 0 and 1 mM NH_4Cl have ~70% response in the 550-750 nm region. As the concentration of the NH_4Cl in the CdS films increases, the response steadily decreases, and the lowest efficiency of ~50% was obtained for the cells using CdS films with 8 mM NH_4Cl. At the lower wavelength of the EQE spectra, a clear reduction in the response can be observed. This is one of the peculiar trends that has been reported by other researchers due to the intermixing effect between CdS and Sb_2Se_3 occurring as result of higher temperature deposition of Sb_2Se_3 absorber film. In our investigation, we observed a reduction in the EQE spectral response at lower wavelengths (400–550 nm) for solar cells fabricated using 8 mM NH_4Cl-CdS compared to those utilising 1 mM NH_4Cl. This agrees well with the SIMS results (Figure 31a), where a higher degree of interdiffusion is revealed for the 1 mM NH_4Cl concentration. This intermixing process may contribute to a reduction in the effective thickness of the CdS ETL, thereby decreasing parasitic absorption at the lower wavelengths.

The better performance of the cell also depends on the best heterojunction between the ETL and the absorber films. CdS films are known for intermixing with the Sb_2Se_3 films; different research groups are trying to overcome these problems through different methods. There are reports on the incorporation of Al^{3+} [7], [82] heterojunction annealing [107] and $CdCl_2$ thin-layer deposition [205], [214], [227] which resulted in better performance in the devices. The introduction of thin films such as TiO_2 also improved the efficiencies of the Sb_2Se_3 solar cell. In our case, it was the simple incorporation of Cl in the bath at 1 mM concentration that resulted in tremendously improved solar cell performance.

Based on the optimisation of the CdS ETL through PDT as discussed in Section 3.1, and the favourable chlorine incorporation observed at 1 mM NH_4Cl concentration, the CdS

deposition parameters were fixed for subsequent device fabrication. With these optimised CdS conditions established, the focus of the research was then directed towards optimising the VTD process for the Sb_2Se_3 absorber, specifically by adjusting the source-to-substrate distance and incorporating argon (Ar) as a carrier gas.

3.3 Impact of Sb_2Se_3 growth rate via VTD on defect formation and PV performance of CdS/Sb_2Se_3 solar cells

In this section, the key findings obtained from the optimisation of the source-to-substrate distance ($D_{So\text{-}Sub}$) and the incorporation of argon (Ar) carrier gas to control the growth rate of Sb_2Se_3 during the deposition via VTD are presented and analysed. To ensure a consistent basis for comparison, solar cells were fabricated using both chloride-processed and non-processed CdS ETLs. Given the previously established optimal condition for NH_4Cl treatment at a concentration of 1 mM (as discussed in Section 3.2), this concentration was selected for the present investigation. For clarity and consistency, CdS films processed with and without NH_4Cl are hereafter referred to as chloride-processed and non-chloride-processed CdS films, respectively, denoted as Cl-CdS and Non-Cl-CdS. Similarly, solar cells incorporating these respective ETLs are denoted as Cl-CdS SCs and Non-Cl-CdS SCs.

3.3.1 The influence of $D_{So\text{-}Sub}$ and growth rate during VTD on Sb_2Se_3 film properties

Structure and morphological properties

In the preceding study (Section 3.2), the VTD of Sb_2Se_3 was carried out with a fixed $D_{So\text{-}Sub}$ of 10 cm, yielding a moderate and reproducible deposition rate of approximately 0.16 μm/min. Building upon these initial findings, this section's study aims to further optimise the VTD growth rate while maintaining a constant Sb_2Se_3 absorber thickness of 0.8±0.1 μm. To this end, the $D_{So\text{-}Sub}$ parameter was systematically varied across four values: 3 cm, 4 cm, 6 cm, and 10 cm, corresponding to deposition rates of approximately 1.0, 0.8, 0.4, and 0.16 μm/min, respectively.

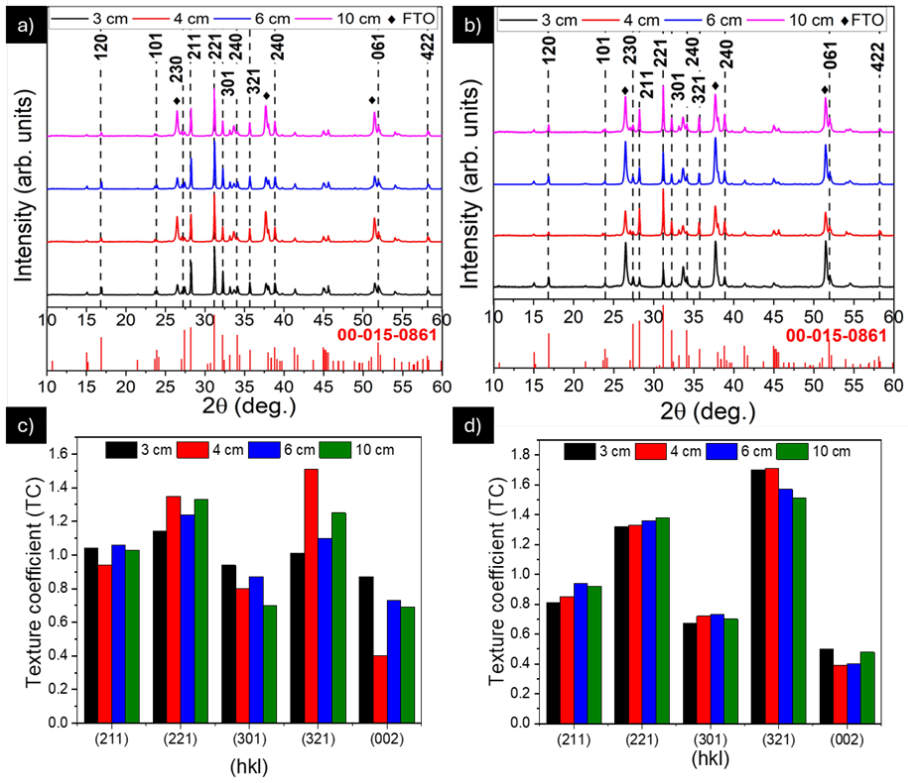

Figure 33. a) & c) XRD pattern and Texture coefficient of Sb_2Se_3 films (constant thickness of ~0.8 µm) deposited on Non-Cl-CdS films at 3, 4, 6 and 10 source to substrate VTD distance ($D_{So\text{-}Sub}$), b) & d) XRD pattern and Texture coefficient of Sb_2Se_3 films deposited on Cl-CdS films at 3, 4, 6 and 10 $D_{So\text{-}Sub}$.

The XRD patterns, shown in Figure 33 a and b, indicate that all films exhibit crystalline features characteristic of orthorhombic Sb_2Se_3, as confirmed by comparison with the standard PDF reference card (00-015-0861). Notably, prominent diffraction peaks corresponding to the (221) and (211) planes were observed at 2θ positions of 31.16° and 28.2°, respectively. These reflections are commonly associated with preferentially oriented columnar grain growth and have been widely reported in the literature as indicative of high-quality absorber layers with vertically aligned ribbon-like grains [4], [90]. The (321) peak exhibited the highest TC values (Figure 33d), followed by the (221) and (211) peaks, confirming the hk1 orientation of Sb_2Se_3 films deposited via VTD, regardless of the employed Cl-CdS, Non-Cl-CdS, or the $D_{So\text{-}Sub}$. Notably, the Sb_2Se_3 films deposited on Cl-CdS films displayed more consistent TC values across varying $D_{So\text{-}Sub}$ compared to films deposited on Non-Cl-CdS films, suggesting enhanced uniformity in the structural properties.

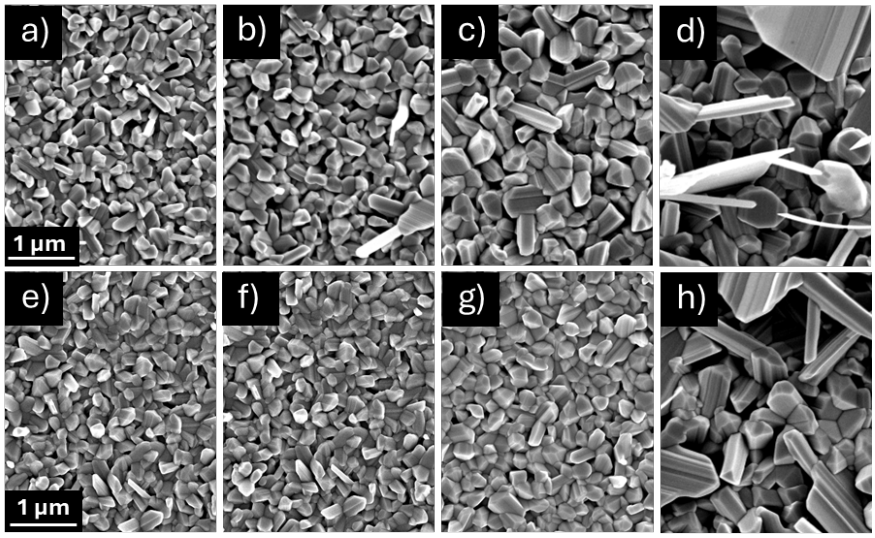

Figure 34. a-d) Surface SEM images of Sb_2Se_3 films deposited on Non-Cl-CdS films at 3, 4, 6 and 10 cm D_{So-Sub} (e-h) Surface SEM images of Sb_2Se_3 films deposited on Cl-CdS films at 3, 4, 6 and 10 cm D_{So-Sub}.

The crystallographic orientation of Sb_2Se_3 thin films plays a critical role in determining the overall PV performance of the solar cell. Specifically, the presence of preferential growth along the (hk1) planes has been shown to enhance charge carrier transport along the quasi-one-dimensional ribbons of Sb_2Se_3, thereby facilitating efficient charge extraction and improving device performance [216]. In contrast, orientations aligned along (hk0) planes are associated with increased recombination losses due to the unfavourable charge transport pathways, which detrimentally affect the PCE of the devices. Furthermore, the surface morphology, particularly grain compactness and the absence of pinholes, is equally essential for minimising recombination sites and ensuring optimal charge collection.

The surface morphology of Sb_2Se_3 films deposited on non-Cl-CdS substrates at varying D_{So-Sub} is shown in Figure 34a-d. At a D_{So-Sub} of 3 cm (Figure 34a), the Sb_2Se_3 film exhibited a compact and relatively uniform morphology. Increasing the D_{So-Sub} to 4 cm (Figure 34b) resulted in improved grain size and enhanced film compactness. However, further increasing the D_{So-Sub} to 6 cm (Figure 34c) led to the emergence of irregular grain growth, and at 10 cm (Figure 34d), the films displayed a pronounced degree of morphological disorder, characterised by both random grain orientations and variable grain sizes. In contrast, Sb_2Se_3 films deposited on Cl-CdS substrates demonstrated progressively enhanced morphological quality with increasing D_{So-Sub} up to 6 cm. As seen in Figure 34e-g, the films became increasingly uniform and compact, with larger and more well-defined grains. Notably, at a D_{So-Sub} of 6 cm (Figure 34g), the Sb_2Se_3 film exhibited significantly better compactness and surface uniformity compared to its non-Cl-CdS counterpart under the same deposition conditions. Nevertheless, at a D_{So-Sub} of 10 cm (Figure 34h), morphological degradation was again evident, with the films showing random grain orientation and diminished uniformity, irrespective of the chloride treatment applied to the CdS layer. It is important to note that for very short D_{So-Sub} values (1–2 cm), significant re-evaporation effects were observed, resulting in drastic reductions in film thickness to approximately 200 nm. This underscores the critical importance of optimising the D_{So-Sub} to balance deposition/growth rate and film quality.

3.3.2 The effect of $D_{So\text{-}Sub}$ and growth rate during VTD on CdS/Sb_2Se_3 solar cells

The Sb_2Se_3 solar cells were fabricated in a superstrate configuration with Cl-CdS and Non-Cl-CdS at different $D_{So\text{-}Sub}$ to study the effect of both changes on the device parameters (Figure 35 and Table 5).

Table 5. PV parameters from JV measurement of champion solar cells with and without chlorine-processed CdS ETL at different $D_{So\text{-}Sub}$.

No.	Solar cell	$D_{So\text{-}Sub}$ (cm)	Device parameters			
			V_{OC} (mV)	J_{SC} (mA/cm^2)	FF (%)	PCE (%)
1.	SC with non-Cl-CdS	3	360	22.7	53.9	4.4
		4	350	23.0	55.1	4.4
		6	364	23.9	53.1	4.6
		10	355	23.5	51.7	4.3
2.	SC with Cl-CdS	3	353	19.6	55.4	3.8
		4	351	19.8	53.8	3.7
		6	376	24.9	52.8	5.0
		10	391	22.4	52.7	4.6

In the case of solar cells fabricated with Non-Cl-CdS ETLs (Non-Cl-CdS SCs), the V_{OC} exhibited a non-linear dependence on the $D_{So\text{-}Sub}$ during the VTD growth of Sb_2Se_3. The lowest V_{OC} value of 346 mV was recorded for devices with an absorber deposited at a $D_{So\text{-}Sub}$ of 4 cm, while a maximum V_{OC} of 364 mV was achieved at 6 cm. Upon further increasing the distance to 10 cm, V_{OC} decreased slightly to 352.4 mV. A similar trend was observed for other photovoltaic parameters, including J_{SC}, FF, and PCE, as illustrated in Figure 35b-d. These parameters improved progressively with increasing $D_{So\text{-}Sub}$ up to 6 cm, beyond which a decline was noted. The optimal device performance was obtained at a $D_{So\text{-}Sub}$ of 6 cm, with the highest J_{SC} of 24 mA/cm^2, FF of 56.4%, and a corresponding PCE of 4.6%. At a $D_{So\text{-}Sub}$ of 10 cm, the efficiency declined marginally to 4.2%, indicating suboptimal growth conditions.

In contrast, devices incorporating Cl-CdS ETLs (Cl-CdS SCs) demonstrated a more pronounced and consistent enhancement in performance metrics with increasing $D_{So\text{-}Sub}$. The V_{OC} increased steadily from 345 mV at 3 cm to 391 mV at 10 cm, indicating improved junction quality likely due to the synergistic effects of Cl incorporation and optimised absorber growth. However, for J_{SC} and PCE, peak values were achieved at an intermediate $D_{So\text{-}Sub}$ of 6 cm, recording 25 mA/cm^2 and 5.0%, respectively. These values declined slightly at 10 cm, suggesting a deterioration in film quality or increased recombination losses at lower deposition rates. The enhanced performance observed for the Cl-CdS/Sb_2Se_3 device at 6 cm is attributed to the improved morphological characteristics of the absorber layer, as confirmed by SEM analysis (Figure 34g), which revealed compact, uniform, and pinhole-free grain conditions favourable for efficient carrier transport and reduced interface recombination.

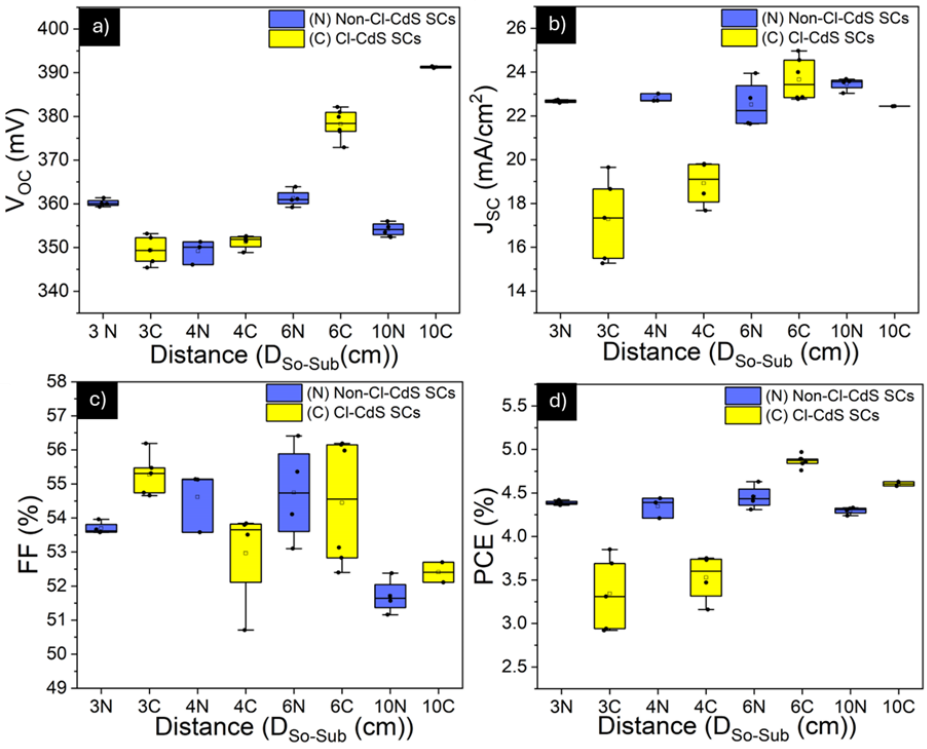

Figure 35. Variation of PV parameters cell a) V_{OC}, b) J_{SC}, c) FF and d) PCE of Non-Cl-CdS and Cl-CdS SCs at different D_{So-Sub} during VTD deposition.

A notable decline in PCE was observed for Cl-CdS/Sb_2Se_3 SCs in comparison to their Non-Cl-CdS counterparts, particularly at D_{So-Sub} of 3 and 4 cm. This reduction in device performance can be primarily attributed to the presence of chlorine within the CdS layer and its interaction with the thermal environment during Sb_2Se_3 deposition. At shorter D_{So-Sub} values (1–2 cm), significant re-evaporation of the Sb_2Se_3 was observed from the substrate, leading to severely reduced thickness and a deterioration in grain compactness. Although re-evaporation effects were less pronounced at D_{So-Sub} of 3 and 4 cm, the elevated substrate temperatures during VTD are likely to affect the CdS layer. This heating effect can be considered as a PDT step in a vacuum condition, inadvertently altering the material properties and thus adversely affecting device performance.

In section 3.1, the effects of PDT under high-vacuum conditions on similarly processed Cl-treated CdS films were discussed. It was revealed that vacuum annealing of Cl-CdS films at temperatures near 400 °C led to a degradation in all key photovoltaic parameters, which correlates well with the diminished PCE observed in Cl-CdS/Sb_2Se_3 devices at D_{So-Sub} of 3 and 4 cm. Although the earlier investigation utilised the CSS method for Sb_2Se_3 deposition, the deposition conditions (such as substrate temperatures and D_{So-Sub} (3 and 4 cm)) were comparable to the VTD process. The primary reason for the degradation is due to the thermal decomposition of $Cd(OH)_2$, resulting in the formation of CdO within the CdS layer. This significantly reduces the carrier concentration of the CdS films, thereby affecting their function as an ETL. On the other hand, the comparative performance data suggest that non-Cl-CdS-based devices are less prone to performance deterioration under the same VTD conditions, indicating more thermal stability of the non-Cl-CdS films.

Despite this, it is important to emphasise that Cl-CdS films and the corresponding Cl-CdS/Sb_2Se_3 solar cells demonstrated higher PCE values when processed under optimised conditions. This indicates that, while Cl incorporation introduces sensitivity to thermal treatment, it also offers potential performance advantages when the thermal influence is carefully controlled.

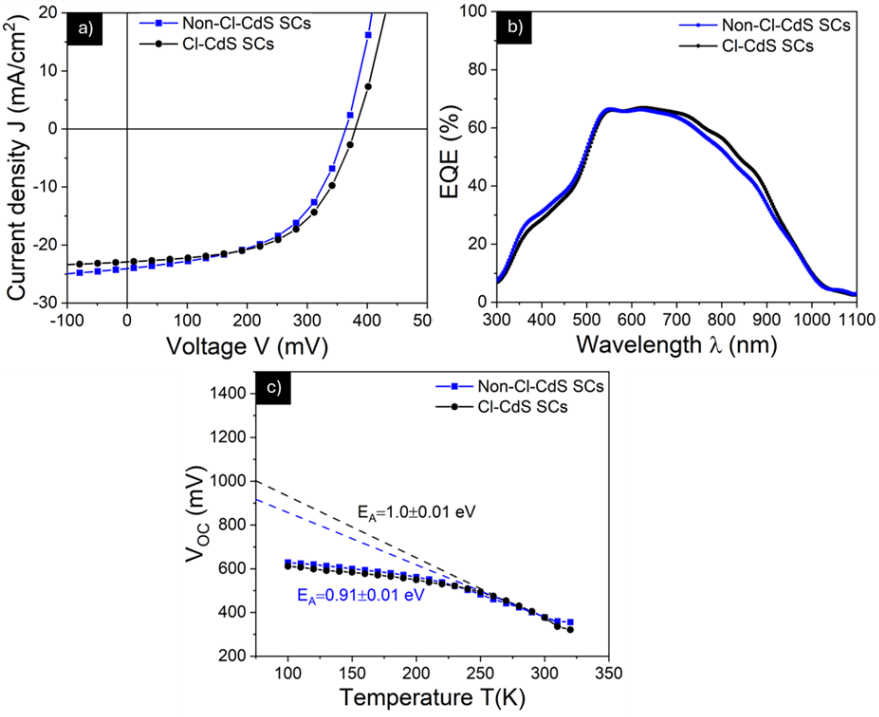

Figure 36. a) JV characteristics and b) EQE spectra of the best-performing Non-Cl-CdS and Cl-CdS SCs. Voc - temperature dependence for Non-Cl-CdS SC (c) and Cl-CdS (d) SCs.

Figures 36a and 36b show the JV characteristics and EQE spectra of the best-performing Cl-CdS and Non-Cl-CdS SCs, respectively. The Cl-CdS device exhibited a modest enhancement in the EQE response within the 500-800 nm wavelength range. The integrated J_{SC}, calculated from the EQE data, correlated well with those obtained from the JV measurements. Despite this, both device types displayed a notable dip in EQE near 500 nm, indicative of parasitic absorption losses, which are commonly associated with the use of CdS as an ETL in Sb_2Se_3 solar cells. In the lower wavelength range (300–550 nm), the EQE intensity was substantially reduced when compared to devices utilising TiO_2 as the ETL, as reported by Hobson et al.[97]. This is likely attributable to two primary factors. Firstly, the lower bandgap of CdS (~2.4 eV), relative to that of TiO_2 (~3.2 eV), leads to increased parasitic absorption of incoming photons. Secondly, interfacial intermixing at the CdS/Sb_2Se_3 junction frequently observed in prior studies, may contribute to additional recombination losses, thereby suppressing carrier collection in the short-wavelength region. Alternative ETL such as TiO_2 offers superior optical transparency; its practical implementation in Sb_2Se_3 solar cells, particularly those fabricated via VTD, remains challenging. TiO_2-based devices fabricated using alternative deposition techniques, such as CSS for Sb_2Se_3 film deposition, have demonstrated

promising performance. Notably, Don et al. [110] achieved a PCE of 8.12% by incorporating a seed layer and utilising RF sputtered TiO_2. However, VTD-processed Sb_2Se_3 devices incorporating TiO_2 as the ETL have shown comparatively lower efficiencies, typically ranging from 4.8% [90] to 5.33% [228]. These limitations are often attributed to issues such as poor surface energy compatibility, increased interfacial defect densities, and lattice mismatch between Sb_2Se_3 and TiO_2.

To further investigate the defect states in the devices, temperature-dependent V_{OC} measurements were conducted for both best Cl-CdS and non-Cl-CdS-based Sb_2Se_3 solar cells (Figures 36c). In both cases, the V_{OC} exhibited a temperature-independent plateau below 200 K, a feature typically associated with defect-induced carrier freeze-out or Fermi-level pinning. Above this threshold, the V_{OC} showed a linear temperature dependence, allowing for the extraction of the activation energy (E_A) by extrapolating the linear portion of the V_{OC}-T curve to 0 K. The extracted E_A values were approximately 0.91 eV for the Non-Cl-CdS devices and 1.0 eV for the Cl-CdS devices. These values are in good agreement with the reported optical bandgap of Sb_2Se_3 (~1.2 eV) [216], as well as the bandgap values derived from the EQE measurements. However, the deviation of E_A from the intrinsic bandgap provides insight into the dominant recombination pathways in the devices. In particular, the E_A value for Cl-CdS devices being closer to the bandgap suggests that recombination is more likely to occur within the bulk of the Sb_2Se_3 absorber, rather than at the interface. Conversely, the lower E_A observed in Non-Cl-CdS devices implies that interface recombination is more significant in these cells. This conclusion is further supported by the JV characteristics (Figure 36a), where the Cl-CdS solar cells consistently exhibited higher V_{OC} values than their non-Cl-CdS counterparts. The relatively higher E_A and improved V_{OC} observed in Cl-CdS devices suggest that chlorine treatment, while introducing some bulk recombination, may simultaneously suppress interface-related losses, thereby enhancing the overall voltage output. These results also emphasise the importance of interface engineering strategies to mitigate recombination losses at the heterojunction, which is essential for further improving the efficiency of Sb_2Se_3-based solar cells.

3.3.3 Influence of thermodynamic conditions and VTD system geometry in Sb_2Se_3 film growth and device performance

The thermodynamic parameters associated with the VTD process significantly influence the structural and morphological quality of Sb_2Se_3 thin films, thereby affecting the PV performance of the resulting devices. In the research study of publication III, a fixed absorber thickness of 0.8 μm was maintained across all depositions to isolate the effect of $D_{So\text{-}Sub}$ on film properties. Despite the constant thickness, variations in deposition conditions, including growth rate, vapour supersaturation, and thermal gradient arising from different $D_{So\text{-}Sub}$ configurations, introduced significant changes in the crystallographic and morphological characteristics of the Sb_2Se_3 absorber layers. These changes, in turn, impacted the device performance, underscoring the complex interdependence between process thermodynamics and film quality.

An important consideration in this context is the specific geometry of the custom-built VTD setup employed in this work (Figure 16, Chapter 2). The deposition process tube, which is a coaxial, quasi-closed quartz tube (length: 20 cm, inner diameter: 2.7 cm, volume: ~46.3 cm^3) inserted into a larger horizontal quartz furnace tube (length: 102 cm, inner diameter: 5.5 cm, volume: ~460.5 cm^3). This configuration facilitates the film deposition at a working pressure ~1×10^{-3} mbar (0.1 Pa), establishing a regime

approximating free molecular (Knudsen) flow. The applied carrier gas flow (0.05 LPM of Ar) was optimised to enable adequate vapour refresh without significantly diluting the vapour density. The small volume of the inner quartz tube contributes to stabilised thermal and vapour gradients, reducing losses due to sidewall deposition and maintaining steady-state supersaturation conditions. This controlled environment enhances the sensitivity of deposition dynamics to $D_{So\text{-}Sub}$ variations, enabling fine-tuned regulation of local supersaturation levels across the substrate surface.

At a constant source temperature (T_{So}) of 520 °C during the VTD deposition, the equilibrium vapor pressure of Sb_2Se_3 was estimated using a well-established empirical relation (equation 6):

$$\log_{10}(p_{Torr}) = {}^{9566}/_{T} + 10.632 \quad (6)$$

Applying this relation yields a vapor pressure of approximately 0.037 Torr (~5 Pa) at 520 °C. In contrast, at the substrate temperature (T_{Sub}) of 420 °C, the vapor pressure ranges between 0.003–0.005 Torr (0.4–0.7 Pa). The supersaturation ratio can be calculated using equation 7,

$$S = {}^{P_v}/_{P_{eq}} \quad (7)$$

This ratio for VTD deposition of the Sb_2Se_3 was found to be 7–12 during the deposition process. This level of supersaturation is sufficient to exert a strong influence on nucleation kinetics and crystal growth mechanisms.

At larger $D_{So\text{-}Sub}$ values (e.g., 10 cm), vapor flux becomes more diluted with the inert Ar carrier gas and subject to partial sidewall deposition losses, which reduces the local supersaturation and leads to sparse nucleation. As a consequence, the films display irregular grain morphologies and non-uniform grain orientation (Figures 34d, 34h). In contrast, for intermediate $D_{So\text{-}Sub}$ values (3–6 cm), the vapor transfer rate and supersaturation are more balanced (S ≈ 2–5), and an optimal growth rate of ~0.4 µm/min was achieved at 6 cm $D_{So\text{-}Sub}$. These conditions promote the formation of well-sintered, large-grained Sb_2Se_3 films with improved grain size distribution and preferred crystallographic orientation.

Furthermore, the use of Cl-treated CdS (Cl-CdS) substrates enhanced interfacial quality and grain growth. The Cl-CdS interface facilitates balanced interdiffusion of Cd into the Sb_2Se_3 layer, as verified by SIMS in earlier work (publication II). This controlled interdiffusion enhances the density of nucleation sites and contributes to the growth of larger, more uniform grains. The improvements in film microstructure and interfacial properties correlate with the observed enhancements in optoelectronic performance, including a peak power conversion efficiency of 5% for devices fabricated at a $D_{So\text{-}Sub}$ of 6 cm using Cl-CdS as the ETL.

In summary, this study demonstrates that vapor supersaturation, growth rate, and source-to-substrate distance are critically interconnected through the geometrical and operational parameters of the VTD system. The optimization of these parameters is essential for achieving high-quality absorber films and improved photovoltaic performance. These findings highlight the importance of precise control over deposition thermodynamics and system design in the scalable manufacturing of high-efficiency Sb_2Se_3-based solar cells.

3.3.4 The defect analysis of non-Cl-CdS and Cl-CdS based Sb_2Se_3 solar cells

In this section, a detailed investigation of defect characteristics in Sb_2Se_3 solar cells fabricated with and without chloride-processed CdS ETL is presented. To facilitate this analysis, the best-performing devices from each group, Cl-CdS/Sb_2Se_3 and Non-Cl-CdS/Sb_2Se_3 were selected as representative samples. Two complementary characterization techniques were employed to probe the defect states: (i) dark JV measurement presented in a log–log scale to analyze charge transport and recombination mechanisms, and (ii) temperature-dependent admittance spectroscopy (TAS), performed under varying bias voltages, to identify and quantify defect activation energies and their energetic distribution within the bandgap. The results and their implications are discussed in detail in the following subsections.

Dark JV characteristics (log J-log V curve)

The logarithmic current density versus voltage (log J–log V) analysis is an essential characterization technique for evaluating charge transport mechanisms in PV devices, particularly under dark conditions. Unlike standard illuminated JV measurements, this method provides deeper insights into the defect density in the thin-film solar cells by distinguishing different conduction regimes that are otherwise indistinguishable. Typically, the log J–log V curve is divided into three distinct regions:

- **Ohmic Region**: At low applied voltages, the current increases linearly with voltage (slope ~1), indicating that the current is governed by thermally generated free carriers and follows Ohm's law. In this regime, charge transport is not significantly hindered by traps or defects.
- **Trap-Filled Limited Region (TFL)**: As the voltage increases, the injected carrier density rises, and the traps within the absorber material begin to fill. This results in a steep increase in current, often showing a slope greater than 2. The slope in this region is strongly influenced by the trap density and energy distribution. This region reflects the transition from ohmic behavior to space-charge-limited conduction.
- **Space-Charge-Limited Conduction (SCLC) Region (Child)**: At even higher voltages, the traps are completely filled, and the current is dominated by space-charge effects. The slope typically returns to a value around 2 (or slightly higher), indicating that current transport is limited by the buildup of space charge due to the imbalance of injected carriers. In this region, analysis of the slope and onset voltage allows estimation of key parameters such as trap density and mobility.

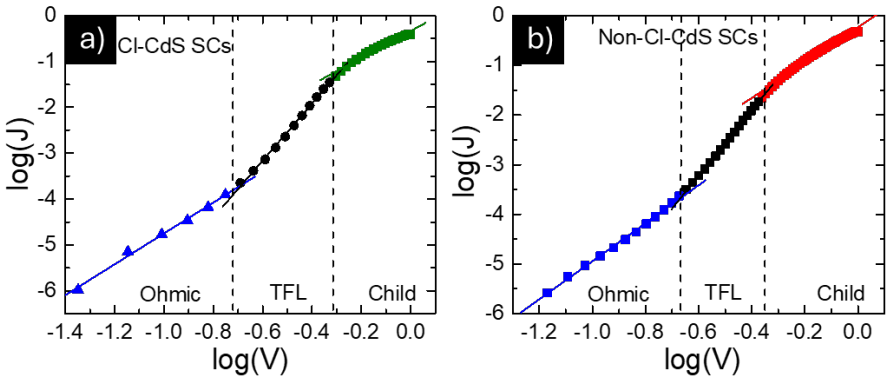

Figure 37. Log(J)-log(V) plots deduced from dark J-V curves of Cl-CdS SCs (a) and Non-Cl-CdS (b) SCs.

This multi-region behaviour in the log J–log V plot makes it an invaluable diagnostic tool for evaluating defect-related properties in absorber layers like Sb_2Se_3 and identifying limitations in device performance. By enabling the extraction of quantitative metrics such as trap density (N_T). N_T in this research work was subsequently calculated by using the V_{TFL} in the following Equation (8):

$$N_T = \frac{2\varepsilon\varepsilon_0 V_{TFL}}{qL^2} \quad (8)$$

where N_T trap density is in cm^{-3}, ε is the dielectric constant of Sb_2Se_3 (15.1), ε is the electric constant, V_{TFL} is the trap-filling-limit voltage in V, q is electric charge in C, and L is the Sb_2Se_3 absorber thickness. In publication III, the V_{TFL} values extracted from the log J–log V plots (Figure 37a,b) were found to be 0.68 V and 0.64 V for the Non-Cl-CdS and Cl-CdS Sb_2Se_3 SCs, respectively. A low V_{TFL} value (<0.2 V) is typically indicative of an exceptionally low trap density; however, it may also suggest limitations in charge injection or a reduced carrier concentration. In contrast, a high V_{TFL} (>1 V) often reflects a high density of trap states, increased recombination losses, and poor material or interfacial quality, commonly associated with deep-level defects. A moderate V_{TFL} range (0.2–1.0 V) is considered optimal for high-efficiency thin-film solar cells such as CdTe, CIGS, and perovskites [229], as it implies a manageable defect density and favourable charge transport characteristics. In the present case, both devices exhibit V_{TFL} values below 1.0 V, with the Cl-CdS SCs showing a slightly lower V_{TFL}, indicating a relatively low defect concentration and efficient charge transport compared to the non-Cl-CdS-based SCs. The N_T values were calculated to be 7×10^{14} cm^{-3} and 8×10^{14} cm^{-3} for the Non-Cl-CdS and Cl-CdS SCs, respectively. These values are in close agreement with previously reported results [212], [230], [231] and are notably lower than those documented by Chen et al. [232], signifying the superior quality of Sb_2Se_3 absorber films fabricated via the optimized VTD method. Interestingly, the slightly lower N_T value observed in the Non-Cl-CdS device suggests a reduced density of trap states, which may contribute to suppressed recombination losses both at the CdS/Sb_2Se_3 interface and within the bulk of the absorber layer. These findings further emphasize the importance of controlling deposition conditions and interface treatments in tailoring defect characteristics for improved photovoltaic performance.

Temperature-dependent admittance spectroscopy (TAS)

In publication III, we extended our analysis to elucidate the behaviour of the activation energies extracted from temperature-dependent admittance spectroscopy (TAS). In the case of deep-level defects residing within the bulk of the absorber, the activation energy obtained from TAS corresponds to the fixed energy separation between the defect level and the relevant band edge (either conduction or valence band), and thus remains largely invariant with changes in applied bias. By contrast, an activation energy that exhibits a systematic shift as a function of bias voltage is indicative of defect states located at or near the heterojunction interface, where the local electrostatic potential and hence the apparent defect level energy vary with the applied bias [233]. Such bias-dependent behaviour, therefore, serves as a diagnostic signature of interface-related recombination centres rather than intrinsic bulk defects.

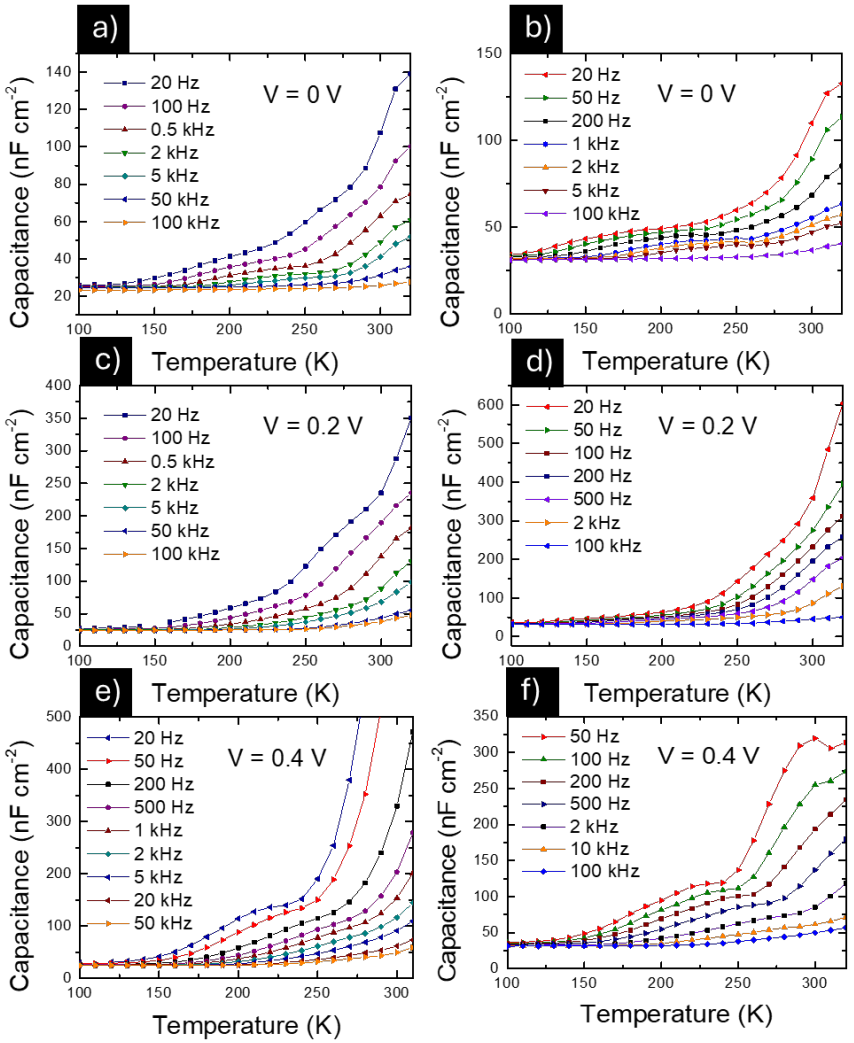

Figure 38. C-f-T curves of Cl-CdS SCs measured under 0 V (a), 0.2 V (c), and 0.4 V (e) and Non-Cl-CdS SCs measured at 0 V (b), 0.2 V (d), and 0.4 V (f).

Figure 38a-f presents the temperature and frequency-dependent capacitance (C-f-T) characteristics of Cl-CdS and non-Cl-CdS-based Sb_2Se_3 SCs, measured under three different bias voltages: 0.0 V, 0.2 V, and 0.4 V. The capacitance values were extracted from the real and imaginary parts of impedance Z (*f*, T) using an equivalent circuit model consisting of a capacitor in parallel with a resistor, both in series with an additional resistor, following the approach described by Levcenko et al. [234]. In both device types, the capacitance curves exhibit a plateau region in the temperature range near 100 K, with typical values ranging between 25–35 nF cm^{-2}. This plateau is consistent with the geometric capacitance of the devices, assuming a relative permittivity (dielectric constant) of $\varepsilon \approx 15$ for Sb_2Se_3, as reported in the literature. The observation of a well-defined single capacitance step in each C–f–T curve indicates the presence of a discrete defect-related transition that dominates the dielectric response over the measured temperature range. To quantitatively evaluate the activation energy associated with the detected defect level,

the inflection points of the capacitance steps were determined from the derivative of the capacitance with respect to frequency, i.e., from the maxima in the -fdC/df plots. The characteristic emission frequencies f_0, corresponding to these inflection points at various temperatures, were then used to construct Arrhenius plots. The activation energy (E_A) was extracted by fitting the temperature dependence of the emission frequency to the standard relation for thermally activated emission (equation 9) [235]:

$$\omega_0 = 2\pi f_0 = 2\xi_0 T^2 \exp\left(-\frac{E_A}{kT}\right) \quad (9)$$

Where ξ_0 is the thermal emission prefactor, k is the Boltzmann constant, and T is the temperature. This approach provides insight into the energetic depth and nature of the dominant defect states within the device structure.

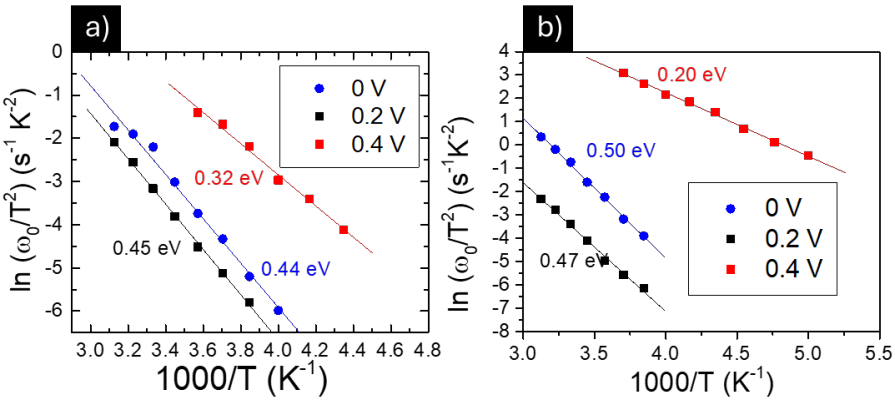

Figure 39. Arrhenius plot of the inflection frequencies of Cl-CdS SCs (a) and Non-Cl-CdS (b) SCs measured under 0 V, 0.2 V, and 0.4 V bias.

For the Cl-CdS-based Sb_2Se_3 SCs, the extracted E_A values from TAS measurements were found to be 0.44 eV, 0.45 eV, and 0.32 eV under applied forward bias voltages of 0 V, 0.2 V, and 0.4 V, respectively, as shown in Figure 39a. In comparison, the Non-Cl-CdS-based devices exhibited E_A values of 0.50 eV, 0.47 eV, and 0.20 eV under the same biasing conditions (Figure 39b). In both cases, a clear trend is observed: the activation energy decreases as the applied bias increases from 0 to 0.4 V. The relatively constant activation energy between 0 V and 0.2 V, followed by a notable reduction at 0.4 V, suggests a bias-dependent behaviour of the underlying defect state. This behaviour is typically indicative of interface-related defects rather than deep bulk states within the absorber layer. In particular, such bias dependence of E_A is often attributed to the modulation of band bending at the heterojunction interface under forward bias, which in turn alters the energetic alignment of defect states relative to the conduction or valence band edges [113], [233].

The reduction in E_A at higher forward bias could arise from the electric field-induced narrowing of the depletion region, which changes the local potential at the interface. This may allow defect states, which are otherwise energetically isolated, to interact more significantly with free carriers or with the band edges. Therefore, the observed activation energies are likely associated with trap states located either at the CdS/Sb_2Se_3 heterojunction or within the ETL near the interface. The dependence of these trap states on the applied voltage reinforces the hypothesis that they are not bulk traps but rather interface-localised defects whose energetic position is modulated by the applied electric

field. Such defects can act as recombination centres under operating conditions, thereby adversely impacting device performance parameters such as V_{OC} and FF.

To accurately attribute the origin of these defect states, it is essential to correlate experimental findings with theoretical studies, particularly those involving first-principles calculations of defect formation energies and electronic structure using density functional theory (DFT). Recent DFT investigations [87] have predicted a diverse array of intrinsic point defects in Sb_2Se_3, including vacancies, antisites, and interstitials. Among these, vacancy-type defects are often considered to be the most prevalent under typical synthesis conditions; however, the specific defect populations are highly sensitive to the vapor-phase stoichiometry and the structural characteristics of the resulting condensed phase. Notably, the antimony vacancy (V_{Sb}) has been associated with energy levels approximately 0.3–0.4 eV above the valence band maximum (VBM), while the selenium vacancy (V_{Se}) is positioned around 0.5–0.7 eV below the conduction band minimum (CBM), with the exact level depending on its charge state and local coordination environment [4], [87], [236]. In addition to vacancies, antisite defects such as Sb_{Se} and Se_{Sb} have also been predicted and experimentally inferred in Sb_2Se_3. These antisites are amphoteric in character, introducing deep-level states located at VBM + 0.494 eV and VBM + 0.697 eV, respectively. Due to their mid-gap positioning and substantial capture cross-sections for both electrons and holes, these defects are particularly detrimental to photovoltaic performance, as they can serve as efficient non-radiative recombination centres [4], [7], [87], [237].

In publication III, the activation energies extracted from TAS for both Cl-CdS and non-Cl-CdS-based solar cells fall within the range of 0.44–0.5 eV. These values are broadly consistent with those associated with either the V_{Sb} vacancy or the Sb_{Se} antisite defects. The close similarity in E_A values between the two device types, along with comparable defect densities as inferred from capacitance measurements, suggests the presence of a common dominant defect mechanism in both systems. Although these findings do not unambiguously confirm the chemical identity of the defect states, the consistency with DFT-predicted defect levels provides strong support for attributing the observed activation energies to intrinsic point defects, most likely V_{Sb} or Sb_{Se}, which are known to critically impact the optoelectronic properties of Sb_2Se_3 absorber layers.

These findings regarding the defects presented in publication III indicate that additional performance improvements in Sb_2Se_3-based solar cells may be attainable through more effective control or elimination of electrically active defect states. Recent literature highlights several promising strategies designed to mitigate interfacial and bulk defects, particularly those present at the CdS/Sb_2Se_3 junction. Among these, post-deposition selenium (Se) treatments have been shown to overcome the V_{Se} defect. In parallel, the incorporation of alkali metals such as lithium into the CdS layer has demonstrated potential in modulating the chemical environment at the interface. Liu et al. [238] reported that lithium doping, when combined with the deposition of a $CdCl_2$ monolayer between CdS and Sb_2Se_3, enhances interfacial quality by promoting chemical homogeneity and suppressing defect generation. Another strategy involves tellurium (Te) alloying within the Sb_2Se_3 absorber layer. This approach has been helpful in effectively modifying the Sb/Se ratio, thereby reducing the formation of Sb_{Se} defect. Ma et al. [98] demonstrated that Te incorporation can modulate defect formation energetics, resulting in improved crystallinity and reduced mid-gap defect density. Furthermore, photo-annealing has emerged as a particularly promising post-deposition treatment, which can facilitate lattice reordering and enhance epitaxial alignment at the interface.

Liang et al. [237] reported that such treatments significantly reduce the density of interfacial Sb_{Se} defects, which are known to act as efficient non-radiative recombination centres.

Irrespective of the precise dominant defect states identified in the solar cells, the improved device performance observed in Cl-CdS/Sb_2Se_3 solar cells achieving PCE approaching 5%, underscores the synergistic benefits of optimised VTD growth conditions for the Sb_2Se_3 absorber and the chloride treatment of the CdS ETL. These enhancements reflect a multifaceted improvement in both bulk and interfacial material quality. The SIMS analysis presented in Section 3.2 (Publication II) confirmed the diffusion of Cd into the Sb_2Se_3 absorber when deposited on Cl-treated CdS layers. This interdiffusion phenomenon has been widely reported in the literature and is often correlated with the passivation of deep-level defects, particularly vacancy and antisite-related states, located near the heterojunction interface [237]. It is likely that these deep states possess relatively high activation energies and, as such, may fall outside the detection window of the TAS techniques employed in publication III. Moreover, Cl-treatment of the CdS ETL appears to support a more balanced interdiffusion of Cd and Cl into the Sb_2Se_3 absorber during VTD growth. This process not only improves the quality of the interface but may also promote the enhanced diffusion of nucleation centres across the substrate, resulting in larger grains with improved crystallographic orientation. These microstructural improvements are known to reduce grain boundary density and enhance carrier collection efficiency, thereby contributing to superior optoelectronic properties of the absorber layer.

In summary, the combined insights from this study (publication III) underscore the critical influence of both optimised VTD parameters and chloride treatment of the CdS ETL on the performance of Sb_2Se_3-based thin-film photovoltaic devices. The synergistic effects of these approaches contribute significantly to improving the structural and optoelectronic quality of the Sb_2Se_3 absorber and enhancing the heterojunction interface, thereby mitigating recombination losses and boosting overall device efficiency. While these results represent a substantial step forward, further improvements in PCE are achievable through the integration of advanced defect mitigation strategies and more refined interface engineering techniques. Such efforts will be essential to approach the record efficiencies currently reported by only a few research groups worldwide. Collectively, these findings highlight the indispensable role of comprehensive process optimization and targeted materials engineering in the continued advancement of Sb_2Se_3 solar cell technology. As the field moves toward commercial viability, incorporating these methodologies into scalable and industrially compatible fabrication protocols will be pivotal in unlocking the full potential of Sb_2Se_3 as a sustainable, earth-abundant absorber material for high-efficiency thin-film photovoltaic applications.

Conclusions

This doctoral work comprised the development of CdS/Sb_2Se_3 thin-film solar cells by VTD, encompassing a fundamental study of the fabrication process, the effects of CdS processing and interfacial phenomena, as well as device optimization and defect characterization. The research aimed to elucidate the interrelation between CdS processing, CSS and VTD Sb_2Se_3 absorber properties, and device performance, providing a new and complementary knowledge for further material and device optimization. Based on the obtained results, the main conclusions are as follows:

1. The effect of annealing atmosphere and temperature on CBD-CdS films and CdS/Sb_2Se_3 device performance was investigated. Increasing the annealing temperature from 200 to 400 °C in both vacuum and air changed the CdS morphology from highly dispersed small grains to sintered dense grains, reduced the bandgap from 2.43 eV to 2.35 eV and drop the carrier concentration value from ~10^{18} to ~10^{11} cm^{-3} (vacuum) and ~10^{17} to ~10^{10} cm^{-3} (air). The changes observed in annealed CdS films were attributed to the influence of residual OH groups within the lattice and the formation of secondary phases affecting their structural and electronic properties.
2. The annealing conditions of CdS films strongly influenced the structural and morphological properties of the CSS Sb_2Se_3 absorber. Absorbers grown on vacuum-annealed CdS (200–400 °C) showed larger, compact grains, whereas those on as-deposited CdS were irregular and porous. XRD analysis indicated increased presence of (hk1) crystal planes for Sb_2Se_3 films grown on air-annealed CdS films.
3. Air annealing of CdS at 200 °C was identified as the optimal treatment, yielding a 2.8% PCE, a 60% boost compared to the cells with as-deposited CdS. However, intermixing between the CdS buffer and the CSS Sb_2Se_3 absorber, along with strong interfacial carrier recombination, remained major factors limiting device efficiency.
4. An alternative approach to the challenging $CdCl_2$ post-deposition treatment of CdS in CdS/Sb_2Se_3 devices has been proposed, involving controllable Cl incorporation in CdS films by systematically varying the NH_4Cl concentration in the CBD precursor solution from 1 to 8 mM.
5. Increasing the chlorine concentration maintained consistent structural and morphological properties of CdS films but significantly modified their electrical characteristics by changing carrier concentration from 10^{13} to 10^{12} cm^{-3}.
6. Sb_2Se_3 films deposited by VTD on CdS film with different Cl concentrations showed similar morphology, though irregular grain heights appeared due to temperature fluctuations from high vapor flow. All Sb_2Se_3 retained pronounced (221) orientation, independent of Cl content in CdS film.
7. SIMS provided clear evidence of Cl incorporation within the CdS lattice and enhanced Cd diffusion into the VTD Sb_2Se_3 absorber, representing one of the key insights of this work. Incorporation of 1 mM NH_4Cl as a Cl source in CBD-CdS significantly improved device PCE by ~20%, demonstrating an effective and controllable alternative to conventional $CdCl_2$ PDT.
8. An optimized growth protocol for Sb_2Se_3 absorber films deposited by VTD was established by introducing Ar gas to control the growth rate and adjusting the source-to-substrate distance $D_{So\text{-}Sub}$.

9. An optimal source-to-substrate distance of ~6 cm ensured an absorber growth rate of ~0.4 µm/min, yielding compact and uniform Sb_2Se_3 films with improved grain structure, while shorter or longer distances led to rough or inhomogeneous morphologies. XRD analysis showed increased presence of (hk1) crystal planes, largely independent of $D_{So\text{-}Sub}$.
10. Devices fabricated with Cl-processed CdS and Sb_2Se_3 deposited at the optimized $D_{So\text{-}Sub}$ achieved a 5% PCE, about 10% higher than those using non-chloride processed CdS, owing to improved absorber quality and reduced interface recombination.
11. Temperature-dependent V_{OC} and dark J–V analyses revealed decreased interface recombination and a lower trap density (~10^{14} cm^{-3}) in optimized devices, while admittance spectroscopy indicated the presence of deep defects in the absorber as the main factor limiting PCE.

Outline and future work

Building upon the findings of this doctoral research, several promising directions can be pursued to further enhance the performance of CdS/Sb_2Se_3 thin-film solar cells. A key future objective is to systematically investigate Cd doping of the Sb_2Se_3 absorber layer, to improve charge carrier density and carrier lifetimes. Another promising strategy involves the application of metal halide PDTs directly on Sb_2Se_3 films, such as $CdCl_2$, $MgCl_2$, or NaF, that have the potential to passivate surface bulk defects, grain boundaries, and enhance crystallinity. To further enhance electron extraction and reduce recombination at the front TCO-ETL interface, integration of dual or alternative ETLs should be explored. Combining CdS with TiO_2 or investigating alternative ETLs such as Zn(O, S), SnO_2, or $Zn_{1-x}Mg_xO$ could enable better band alignment, improved ETL transparency, and enhanced carrier collection. Finally, extending the study on VTD by examining the impact of different carrier gas environments, including pure Ar, N_2, and O_2 their mixtures, could provide valuable insights into further optimization of absorber thin film growth, defect formation, and stoichiometric control. Such investigations will be essential for optimizing large-area VTD deposition and achieving reproducible high-quality Sb_2Se_3 absorber films suitable for scalable PV manufacturing. Collectively, these future directions aim to build upon the foundation established in this thesis, advancing Sb_2Se_3-based solar cells toward higher efficiencies, improved stability, and sustainable commercialization.

References

[1] N. Juneja, "Development of Semi-Transparent Sb_2S_3 Solar Cells with Fluorene-based Compounds as Hole Transport Materials," 2024, doi: 10.23658/taltech.68/2024.

[2] P. Prabeesh, I. Packia Selvam, and S. N. Potty, "Structural properties of czts thin films on glass and mo coated glass substrates: A rietveld refinement study," Appl Phys A Mater Sci Process, vol. 124, no. 3, pp. 1–6, Mar. 2018, doi: 10.1007/s00339-018-1649-7.

[3] N. Juneja et al., "Dopant-free fluorene based dimers linked with thiophene units as prospective hole transport materials for Sb_2S_3 solar cells," Sustain Energy Fuels, vol. 8, no. 18, pp. 4324–4334, Jul. 2024, doi: 10.1039/d4se00472h.

[4] N. Spalatu et al., "Screening and optimization of processing temperature for Sb_2Se_3 thin film growth protocol: Interrelation between grain structure, interface intermixing and solar cell performance," Sol Ener Mater Sol Cells, vol. 225, Jun. 2021, doi: 10.1016/j.solmat.2021.111045.

[5] R. Krautmann et al., "Analysis of grain orientation and defects in Sb_2Se_3 solar cells fabricated by close-spaced sublimation," Sol Energy, vol. 225, pp. 494–500, 2021, doi: 10.1016/j.solener.2021.07.022.

[6] N. Maticiuc, J. Hiie, T. Raadik, A. Graf, and A. Gavrilov, "The role of Cl in the chemical bath on the properties of CdS thin films," Thin Solid Films, vol. 535, no. 1, pp. 184–187, May 2013, doi: 10.1016/j.tsf.2012.11.107.

[7] G. Chen et al., "Suppressing Buried Interface Nonradiative Recombination Losses Toward High-Efficiency Antimony Triselenide Solar Cells," Adv Mater, vol. 36, no. 5, Feb. 2024, doi: 10.1002/adma.202308522.

[8] J. Siim Eensalu, Deposition of Sb_2S_3 Thin Films by Ultrasonic Spray Pyrolysis for Photovoltaic Applications. Tallinn University of Technology, 2022.

[9] C. Yu, S. Xu, J. Yao, and S. Han, "Recent advances in and new perspectives on crystalline silicon solar cells with carrier-selective passivation contacts," Crystals, vol. 8, no. 11, Nov. 2018, doi: 10.3390/cryst8110430.

[10] Y. Lee, C. Park, N. Balaji, Y. J. Lee, and V. A. Dao, "High-efficiency Silicon Solar Cells: A Review," Isr J Chem, vol. 55, no. 10, pp. 1050–1063, Oct. 2015, doi: 10.1002/ijch.201400210.

[11] W. Shockley, "The Theory of p-n Junctions in Semiconductors and p-n Junction Transistors," Jul. 1949. doi: 10.1002/j.1538-7305.1949.tb03645.x.

[12] K. Yoshikawa et al., "Silicon heterojunction solar cell with interdigitated back contacts for a photoconversion efficiency over 26%," Nat Energy, vol. 2, no. 5, Mar. 2017, doi: 10.1038/nenergy.2017.32.

[13] M. Konagai, "Present status and future prospects of silicon thin-film solar cells," Jpn J Appl Phys, vol. 50, no. 3, Mar. 2011, doi: 10.1143/JJAP.50.030001.

[14] Q. Xu, Y. Zhao, and X. Zhang, "Light Management in Monolithic Perovskite/Silicon Tandem Solar Cells," Solar RRL, vol. 4, no. 2, Feb. 2020, doi: 10.1002/solr.201900206.

[15] I. Almansouri, A. Ho-Baillie, S. P. Bremner, and M. A. Green, "Supercharging Silicon Solar Cell Performance by Means of Multijunction Concept," IEEE J Photovolt, vol. 5, no. 3, pp. 968–976, May 2015, doi: 10.1109/JPHOTOV.2015.2395140.

[16] M. I. A. Arafa and E. S. S. A. Said, "A different vision for uninterruptible load using hybrid solar-grid energy," IJPEDS, vol. 10, no. 1, pp. 381–387, Mar. 2019, doi: 10.11591/ijpeds.v10.i1.pp381-387.

[17] F. Rahman, C. D. Farmer, N. P. Johnson, C. Schmidt, G. Pfaff, and C. R. Stanley, “High radiant flux photovoltaic cells for solar proximity missions,” Semicond Sci Technol, vol. 22, no. 7, pp. 695–700, Jul. 2007, doi: 10.1088/0268-1242/22/7/003.

[18] L. K. Sai, R. A. M. Osman, and M. S. Idris, “Modeling the effect of ARC and other parameters on the efficiency of GaAs solar cell using silvaco,” in Materials Science Forum, Trans Tech Publications Ltd, 2015, pp. 204–208. doi: 10.4028/www.scientific.net/MSF.819.204.

[19] A. Bermudez-Garcia, P. Voarino, and O. Raccurt, “Environments, needs and opportunities for future space photovoltaic power generation: A review,” Appl Energy, vol. 290, May 2021, doi: 10.1016/j.apenergy.2021.116757.

[20] P. S. Wijewarnasuriya, “Optimization of material/device parameters of CdTe photovoltaic for solar cells applications,” in Energy Harvesting and Storage: Materials, Devices, and Applications VII, SPIE, May 2016, p. 986503. doi: 10.1117/12.2229487.

[21] S. Sirohi, V. Kumar, and T. P. Sharma, “Optical, structural and electrical properties of CdTe sintered films,” Opt Mater, vol. 12, no. 1, pp. 121–125, May 1999, doi: 10.1016/S0925-3467(98)00053-6.

[22] A. Romeo and E. Artegiani, “CdTe-based thin film solar cells: Past, present and future,” Energies, vol. 14, no. 6, Mar. 2021, doi: 10.3390/en14061684.

[23] S. Surabhi, Kumaranurag, S. Rajpal, and S. R. Kumar, “A new route for preparing CdTe thin films by chemical bath deposition,” Mater Today Proc, vol. 44, pp. 1463–1467, 2021, doi: 10.1016/j.matpr.2020.11.635.

[24] X. Zhang et al., “Research Status of Recovery of Tellurium from Cadmium Telluride Photovoltaic Modules,” IOP Conf Ser Mater Sci Eng, vol. 782, no. 2, Apr. 2020, doi: 10.1088/1757-899X/782/2/022024.

[25] I. Visoly-Fisher, K. D. Dobson, J. Nair, E. Bezalel, G. Hodes, and D. Cahen, “Factors affecting the stability of CdTe/CdS solar cells deduced from stress tests at elevated temperature,” Adv Funct Mater, vol. 13, no. 4, pp. 289–299, Apr. 2003, doi: 10.1002/adfm.200304259.

[26] V. Fthenakis, C. Athias, A. Blumenthal, A. Kulur, J. Magliozzo, and D. Ng, “Sustainability evaluation of CdTe PV: An update,” Renew Sustain Energy Rev, vol. 123, May 2020, doi: 10.1016/j.rser.2020.109776.

[27] T. Dalibor, R. Reichel, C. H. Wu, P. Borowski, S. Peng, and J. Chen, “Cu(In,Ga)(Se, S)$_2$ thin-film technology: Aspects of historical development, current status, and future prospects,” Int J Appl Glass Sci, vol. 16, no. 2, Apr. 2025, doi: 10.1111/ijag.16696.

[28] A. Belghachi and N. Limam, “Effect of the absorber layer band-gap on CIGS solar cell,” Chin J Phys, vol. 55, no. 4, pp. 1127–1134, Aug. 2017, doi: 10.1016/j.cjph.2017.01.011.

[29] M. Alves, P. Anacleto, V. Teixeira, J. Carneiro, and S. Sadewasser, “Fabrication of Pre-Structured Substrates and Growth of CIGS Micro-Absorbers,” Nanomaterials, vol. 14, no. 6, Mar. 2024, doi: 10.3390/nano14060543.

[30] C. Helbig, A. M. Bradshaw, C. Kolotzek, A. Thorenz, and A. Tuma, “Supply risks associated with CdTe and CIGS thin-film photovoltaics,” Appl Energy, vol. 178, pp. 422–433, 2016, doi: 10.1016/j.apenergy.2016.06.102.

[31] Y. Li et al., “CZTSSe solar cells: insights into interface engineering,” J Mater Chem A Mater, vol. 11, no. 10, pp. 4836–4849, Feb. 2023, doi: 10.1039/d2ta09561k.

[32] W. Li et al., “Fabrication of Cu_2ZnSnS_4 thin film solar cells by annealing of reactively sputtered precursors,” J Alloys Compd, vol. 701, pp. 55–62, 2017, doi: 10.1016/j.jallcom.2016.12.285.

[33] P. Prabeesh, I. P. Selvam, and S. N. Potty, “Effect of annealing temperature on a single step processed Cu_2ZnSnS_4 thin film via solution method,” Thin Solid Films, vol. 606, pp. 94–98, May 2016, doi: 10.1016/j.tsf.2016.03.037.

[34] P. Prabeesh, V. G. Sajeesh, I. Packia Selvam, M. S. Divya Bharati, G. Mohan Rao, and S. N. Potty, “CZTS solar cell with non-toxic buffer layer: A study on the sulphurization temperature and absorber layer thickness,” Sol Energy, vol. 207, pp. 419–427, Sep. 2020, doi: 10.1016/j.solener.2020.06.103.

[35] C. Cui et al., “Heterojunction reconstruction via In doping towards high-efficiency CZTSSe solar cells,” Chem Engin J, vol. 476, Nov. 2023, doi: 10.1016/j.cej.2023.146701.

[36] P. Prabeesh, P. Saritha, I. P. Selvam, and S. N. Potty, “Fabrication of kesterite absorber films by spray pyrolysis: Effect of annealing temperature on the phase formation,” Adv Mater Proc, vol. 2, no. 1, pp. 46–50, Dec. 2021, doi: 10.5185/amp.2017/111.

[37] M. P. Suryawanshi et al., “CZTS based thin film solar cells: A status review,” Mater Tech, vol. 28, no. 1–2, pp. 98–109, Mar. 2013, doi: 10.1179/1753555712Y.0000000038.

[38] M. S. Rana, M. M. Islam, and M. Julkarnain, “Enhancement in efficiency of CZTS solar cell by using CZTSe BSF layer,” Sol Energy, vol. 226, pp. 272–287, Sep. 2021, doi: 10.1016/j.solener.2021.08.035.

[39] K. B. Cheon, S. K. Hwang, S. W. Seo, J. H. Park, M. A. Park, and J. Y. Kim, “Roughness-Controlled $Cu_2ZnSn(S,Se)_4$ Thin-Film Solar Cells with Reduced Charge Recombination,” ACS Appl Mater Interfaces, vol. 11, no. 27, pp. 24088–24095, Jul. 2019, doi: 10.1021/acsami.9b05852.

[40] J. H. Yum, P. Chen, M. Grätzel, and M. K. Nazeeruddin, “Recent developments in solid-state dye-sensitized solar cells,” ChemSusChem, vol. 1, no. 8–9, pp. 699–707, Sep. 2008, doi: 10.1002/cssc.200800084.

[41] D. Wei, “Dye sensitized solar cells,” Int J Mol Sci, vol. 11, no. 3, pp. 1103–1113, Mar. 2010, doi: 10.3390/ijms11031103.

[42] G. M. Lana et al., “One-Dimensional TiO_2 Nanocomposite-based Photoanode for Dye-Sensitized solar Cells: A review,” Sol Energy, vol. 279, Sep. 2024, doi: 10.1016/j.solener.2024.112850.

[43] N. Tomar, A. Agrawal, V. S. Dhaka, and P. K. Surolia, “Ruthenium complexes based dye sensitized solar cells: Fundamentals and research trends,” Sol Energy, vol. 207, pp. 59–76, Sep. 2020, doi: 10.1016/j.solener.2020.06.060.

[44] S. Athithya, S. Harish, H. Ikeda, M. Navaneethan, and J. Archana, “Controlled synthesis of monodispersed ZnO nanospindle decorated TiO_2 mesospheres for enhanced charge transport in dye-sensitized solar cells,” CrystEngComm, vol. 25, no. 21, pp. 3198–3209, May 2023, doi: 10.1039/d3ce00031a.

[45] C. K. Kim, H. Zhou, T. Kowalewski, K. Matyjaszewski, and H. K. Kim, “Soft-Templated Tellurium-Doped Mesoporous Carbon as a Pt-Free Electrocatalyst for High-Performance Dye-Sensitized Solar Cells,” ACS Appl Mater Interfaces, vol. 11, no. 2, pp. 2093–2102, Jan. 2019, doi: 10.1021/acsami.8b19223.

[46] H. S. Jung and J. K. Lee, “Dye sensitized solar cells for economically viable photovoltaic systems,” J Phys Chem Let, vol. 4, no. 10, pp. 1682–1693, May 2013, doi: 10.1021/jz400112n.

[47] C. Anrango-Camacho, K. Pavón-Ipiales, B. A. Frontana-Uribe, and A. Palma-Cando, “Recent Advances in Hole-Transporting Layers for Organic Solar Cells,” Nanomaterials, vol. 12, no. 3, Feb. 2022, doi: 10.3390/nano12030443.

[48] A. R. Murad, A. Iraqi, S. B. Aziz, S. N. Abdullah, and M. A. Brza, “Conducting polymers for optoelectronic devices and organic solar cells: A review,” Polymers, vol. 12, no. 11, pp. 1–47, Nov. 2020, doi: 10.3390/polym12112627.

[49] J. Yi, G. Zhang, H. Yu, and H. Yan, “Advantages, challenges and molecular design of different material types used in organic solar cells,” Jan. 01, 2024, Nature Research. doi: 10.1038/s41578-023-00618-1.

[50] X. Zhang et al., “Recent Progress in Hole-Transporting Layers of Conventional Organic Solar Cells with p–i–n Structure,” Adv Funct Mater, vol. 32, no. 44, Oct. 2022, doi: 10.1002/adfm.202205398.

[51] Z. Zhou, Z. Yuan, Z. Yin, Q. Xue, N. Li, and F. Huang, “Progress of semitransparent emerging photovoltaics for building integrated applications,” GEE, vol. 9, no. 6, pp. 992–1015, Jun. 2024, doi: 10.1016/j.gee.2023.05.006.

[52] C. Li et al., “Achieving Record-Efficiency Organic Solar Cells upon Tuning the Conformation of Solid Additives,” J Am Chem Soc, vol. 144, no. 32, pp. 14731–14739, Aug. 2022, doi: 10.1021/jacs.2c05303.

[53] K. Kawano, R. Pacios, D. Poplavskyy, J. Nelson, D. D. C. Bradley, and J. R. Durrant, “Degradation of organic solar cells due to air exposure,” Sol Energy Mater Sol Cells, vol. 90, no. 20, pp. 3520–3530, Dec. 2006, doi: 10.1016/j.solmat.2006.06.041.

[54] N. Bristow and J. Kettle, “Outdoor performance of organic photovoltaics: Diurnal analysis, dependence on temperature, irradiance, and degradation,” J Renew and Sustain Energy, vol. 7, no. 1, Jan. 2015, doi: 10.1063/1.4906915.

[55] N. Bristow and J. Kettle, “Outdoor organic photovoltaic module characteristics: Benchmarking against other PV technologies for performance, calculation of Ross coefficient and outdoor stability monitoring,” Sol Energy Mater Sol Cells, vol. 175, pp. 52–59, Feb. 2018, doi: 10.1016/j.solmat.2017.10.008.

[56] M. R. Kim and D. Ma, “Quantum-dot-based solar cells: Recent advances, strategies, and challenges,” J Phys Chem Lett, vol. 6, no. 1, pp. 85–99, Jan. 2015, doi: 10.1021/jz502227h.

[57] J. Singh, R. Thareja, and P. Malik, “Exploring the Potential of Quantum Dot-Sensitized Solar Cells: Innovation and Insights,” ChemPhysChem, vol. 26, no. 10, May 2025, doi: 10.1002/cphc.202400800.

[58] Best Research-Cell Efficiency Chart. Photovoltaic Research, “https://www.nrel.gov/pv/cell-efficiency,” NREL, 2025.

[59] I. Mora-Seró, “Current Challenges in the Development of Quantum Dot Sensitized Solar Cells,” Adv Energy Mater, vol. 10, no. 33, Sep. 2020, doi: 10.1002/aenm.202001774.

[60] N. Suresh Kumar and K. Chandra Babu Naidu, “A review on perovskite solar cells (PSCs), materials and applications,” J Materiomics, vol. 7, no. 5, pp. 940–956, Sep. 2021, doi: 10.1016/j.jmat.2021.04.002.

[61] J. Pastuszak and P. Węgierek, “Photovoltaic Cell Generations and Current Research Directions for Their Development,” Materials, vol. 15, no. 16, Aug. 2022, doi: 10.3390/ma15165542.

[62] P. Roy, N. Kumar Sinha, S. Tiwari, and A. Khare, “A review on perovskite solar cells: Evolution of architecture, fabrication techniques, commercialization issues and status,” Sol Energy, vol. 198, pp. 665–688, Mar. 2020, doi: 10.1016/J.SOLENER.2020.01.080.

[63] X. Jiang et al., “Isomeric diammonium passivation for perovskite–organic tandem solar cells,” Nature, vol. 635, no. 8040, pp. 860–866, Nov. 2024, doi: 10.1038/s41586-024-08160-y.

[64] S. Bhattarai et al., “A detailed review of perovskite solar cells: Introduction, working principle, modelling, fabrication techniques, future challenges,” Micro Nanostruc, vol. 172, p. 207450, Dec. 2022, doi: 10.1016/J.MICRNA.2022.207450.

[65] B. G. Krishna, D. Sundar Ghosh, and S. Tiwari, “Progress in ambient air-processed perovskite solar cells: Insights into processing techniques and stability assessment,” Sol Energy, vol. 224, pp. 1369–1395, Aug. 2021, doi: 10.1016/j.solener.2021.07.002.

[66] S. A. Moiz and A. N. M. Alahmadi, “Design of dopant and lead-free novel perovskite solar cell for 16.85% efficiency,” Polymers, vol. 13, no. 13, Jul. 2021, doi: 10.3390/polym13132110.

[67] Y. Pan et al., “Vapor Transport Deposition of $Sb_2(S,Se)_3$ Solar Cells with Continuously Tunable Band Gaps,” ACS Appl Energy Mater, vol. 5, no. 6, pp. 7240–7248, Jun. 2022, doi: 10.1021/acsaem.2c00790.

[68] N. Ali et al., „Antimony sulphide, an absorber layer for solar cell application,” Appl Phys A Mater Sci Process, vol. 122, no. 1, pp. 1–7, Jan. 2016, doi: 10.1007/s00339-015-9542-0.

[69] R. Krautmann et al., “Low processing temperatures explored in Sb_2S_3 solar cells by close-spaced sublimation and analysis of bulk and interface related defects,” Sol Energy Mater Sol Cells, vol. 251, Mar. 2023, doi: 10.1016/j.solmat.2022.112139.

[70] G. J. Chen et al., “Crystal Growth Promotion and Defect Passivation by Hydrothermal and Selenized Deposition for Substrate-Structured Antimony Selenosulfide Solar Cells,” ACS Appl Mater Interfaces, vol. 14, no. 28, pp. 31986–31997, Jul. 2022, doi: 10.1021/acsami.2c06805.

[71] A. Bosio, G. Foti, S. Pasini, and D. Spoltore, “A Review on the Fundamental Properties of Sb_2Se_3-Based Thin Film Solar Cells,” Energies, vol. 16, no. 19, Oct. 2023, doi: 10.3390/en16196862.

[72] Y. Zhou et al., “Thin-film Sb_2Se_3 photovoltaics with oriented one-dimensional ribbons and benign grain boundaries,” Nat Photonics, vol. 9, no. 6, pp. 409–415, Jun. 2015, doi: 10.1038/nphoton.2015.78.

[73] Y. Zhao et al., “Regulating deposition kinetics via a novel additive-assisted chemical bath deposition technology enables fabrication of 10.57%-efficiency Sb_2Se_3 solar cells,” Energy Environ Sci, vol. 15, no. 12, pp. 5118–5128, Oct. 2022, doi: 10.1039/d2ee02261c.

[74] S. Wang et al., “A Novel Multi-Sulfur Source Collaborative Chemical Bath Deposition Technology Enables 8%-Efficiency Sb_2S_3 Planar Solar Cells,” Adv Mater, vol. 34, no. 41, Oct. 2022, doi: 10.1002/adma.202206242.

[75] Y. Zhao et al., “Regulating Energy Band Alignment via Alkaline Metal Fluoride Assisted Solution Post-Treatment Enabling $Sb_2(S,Se)_3$ Solar Cells with 10.7% Efficiency,” Adv Energy Mater, vol. 12, no. 1, Jan. 2022, doi: 10.1002/aenm.202103015.

[76] A. A. F. Husain, W. Z. W. Hasan, S. Shafie, M. N. Hamidon, and S. S. Pandey, “A review of transparent solar photovoltaic technologies,” Renew Sustain Energy Rev, vol. 94, pp. 779–791, Oct. 2018, doi: 10.1016/j.rser.2018.06.031.

[77] J. S. Eensalu, A. Katerski, E. Kärber, I. O. Acik, A. Mere, and M. Krunks, “Uniform Sb_2S_3 optical coatings by chemical spray method,” Beilstein J Nanotechnol, vol. 10, no. 1, pp. 198–210, 2019, doi: 10.3762/bjnano.10.18.

[78] J. S. Eensalu et al., “Semitransparent Sb_2S_3 thin film solar cells by ultrasonic spray pyrolysis for use in solar windows,” Beilstein J Nanotechnolo, vol. 10, pp. 2396–2409, 2019, doi: 10.3762/bjnano.10.230.

[79] J. Han et al., “Synergistic Effect through the Introduction of Inorganic Zinc Halides at the Interface of TiO_2 and Sb_2S_3 for High-Performance Sb_2S_3 Planar Thin-Film Solar Cells,” ACS Appl Mater Interfaces, vol. 12, no. 39, pp. 44297–44306, Sep. 2020, doi: 10.1021/acsami.0c11550.

[80] J. Rodriguez-Castro, P. Dale, M. F. Mahon, K. C. Molloy, and L. M. Peter, “Deposition of antimony sulfide thin films from single-source antimony thiolate precursors,” Chem Mater, vol. 19, no. 13, pp. 3219–3226, Jun. 2007, doi: 10.1021/cm070405j.

[81] E. Zimmermann et al., “Toward High-Efficiency Solution-Processed Planar Heterojunction Sb_2S_3 Solar Cells,” Adv Sci, vol. 2, no. 5, May 2015, doi: 10.1002/advs.201500059.

[82] Y. Luo et al., “Carrier Transport Enhancement Mechanism in Highly Efficient Antimony Selenide Thin-Film Solar Cell,” Adv Funct Mater, 2023, doi: 10.1002/adfm.202213941.

[83] K. Li et al., “One-dimensional Sb_2Se_3 enabling ultra-flexible solar cells and mini-modules for IoT applications,” Nano Energy, vol. 86, Aug. 2021, doi: 10.1016/j.nanoen.2021.106101.

[84] Z. Li et al., “9.2%-efficient core-shell structured antimony selenide nanorod array solar cells,” Nat Commun, vol. 10, no. 1, Dec. 2019, doi: 10.1038/s41467-018-07903-6.

[85] X. Wen et al., “Vapor transport deposition of antimony selenide thin film solar cells with 7.6% efficiency,” Nat Commun, vol. 2179, no. 9, May 2018, doi: 10.1038/s41467-018-04634-6.

[86] S. Wang et al., “A Novel Multi-Sulfur Source Collaborative Chemical Bath Deposition Technology Enables 8%-Efficiency Sb_2S_3 Planar Solar Cells,” Adv Mater, vol. 34, no. 41, Oct. 2022, doi: 10.1002/adma.202206242.

[87] C. N. Savory and D. O. Scanlon, “The complex defect chemistry of antimony selenide,” J Mater Chem A Mater, vol. 7, no. 17, pp. 10739–10744, 2019, doi: 10.1039/c9ta02022e.

[88] M. Huang, P. Xu, D. Han, J. Tang, and S. Chen, “Complicated and Unconventional Defect Properties of the Quasi-One-Dimensional Photovoltaic Semiconductor Sb 2 Se 3,” ACS Appl Mater Interfaces, vol. 11, no. 17, pp. 15564–15572, May 2019, doi: 10.1021/acsami.9b01220.

[89] J. Otavio Mendes, A. Merenda, K. Wilson, A. Fraser Lee, E. Della Gaspera, and J. van Embden, “Substrate Morphology Directs (001) Sb_2Se_3 Thin Film Growth by Crystallographic Orientation Filtering,” Small, vol. 20, no. 39, Sep. 2024, doi: 10.1002/smll.202302721.

[90] R. Juškėnas, A. Naujokaitis, A. Drabavičius, V. Pakštas, D. Vainauskas, and R. Kondrotas, "Seed Layer Optimisation for Ultra-Thin Sb_2Se_3 Solar Cells on TiO_2 by Vapour Transport Deposition," Materials, vol. 15, no. 23, Dec. 2022, doi: 10.3390/ma15238356.

[91] R. Tang et al., "Highly efficient and stable planar heterojunction solar cell based on sputtered and post-selenized Sb_2Se_3 thin film," Nano Energy, vol. 64, Oct. 2019, doi: 10.1016/j.nanoen.2019.103929.

[92] V. Kumar, E. Artegiani, A. Kumar, G. Mariotto, F. Piccinelli, and A. Romeo, "Effects of post-deposition annealing and copper inclusion in superstrate Sb_2Se_3 based solar cells by thermal evaporation," Sol Energy, vol. 193, pp. 452–457, Nov. 2019, doi: 10.1016/j.solener.2019.09.069.

[93] V. Kumar et al., "Analysis of Se Co-evaporation and Post-selenization for Sb_2Se_3-Based Solar Cells," ACS Appl Energy Mater, vol. 4, no. 11, pp. 12479–12486, Nov. 2021, doi: 10.1021/acsaem.1c02301.

[94] J. Zhou et al., "Dual-function of $CdCl_2$ treated SnO_2 in Sb_2Se_3 solar cells," Appl Surf Sci, vol. 534, Dec. 2020, doi: 10.1016/j.apsusc.2020.147632.

[95] C. Chen et al., "Optical properties of amorphous and polycrystalline Sb_2Se_3 thin films prepared by thermal evaporation," Appl Phys Lett, vol. 107, no. 4, Jul. 2015, doi: 10.1063/1.4927741.

[96] M. Birkett et al., "Band gap temperature-dependence of close-space sublimation grown Sb_2Se_3 by photo-reflectance," APL Mater, vol. 6, no. 8, Aug. 2018, doi: 10.1063/1.5027157.

[97] T. D. C. Hobson et al., "Isotype Heterojunction Solar Cells Using n-Type Sb_2Se_3 Thin Films," Chemistry of Materials, vol. 32, no. 6, pp. 2621–2630, Mar. 2020, doi: 10.1021/acs.chemmater.0c00223.

[98] Y. Ma et al., "Efficient defect passivation of Sb_2Se_3 film by tellurium doping for high performance solar cells," J Mater Chem A Mater, vol. 8, no. 14, pp. 6510–6516, Apr. 2020, doi: 10.1039/d0ta00443j.

[99] K. Y. Rajpure and C. H. Bhosale, "Preparation and characterization of spray deposited photoactive Sb_2S_3 and Sb_2Se_3 thin films using aqueous and non-aqueous media," Mater Chem Phys, vol. 73, no. 1, pp. 6–12, Jan. 2002, doi: 10.1016/S0254-0584(01)00350-9.

[100] D. Liu et al., "Direct Hydrothermal Deposition of Antimony Triselenide Films for Efficient Planar Heterojunction Solar Cells," ACS Appl Mater Interfaces, vol. 13, no. 16, pp. 18856–18864, Apr. 2021, doi: 10.1021/acsami.1c02393.

[101] S. Barthwal, R. Kumar, and S. Pathak, "Present Status and Future Perspective of Antimony Chalcogenide (Sb_2X_3) Photovoltaics," ACS Appl Energy Mater, vol. 5, no. 6, pp. 6545–6585, Jun. 2022, doi: 10.1021/acsaem.2c00420.

[102] K. J. Tiwari et al., "Efficient Sb_2Se_3/CdS planar heterojunction solar cells in substrate configuration with (hk0) oriented Sb_2Se_3 thin films," Sol Energy Mater Sol Cells, vol. 215, Sep. 2020, doi: 10.1016/j.solmat.2020.110603.

[103] B. Ríos-Ramirez and P. K. Nair, "On the Stability of Operation of Antimony Sulfide Selenide Thin Film Solar Cells Under Solar Radiation," Phys Status Solidi (A) Appl Mater Sci, vol. 215, no. 24, Dec. 2018, doi: 10.1002/pssa.201800479.

[104] K. Li et al., "Orientation Engineering in Low-Dimensional Crystal-Structural Materials via Seed Screening," Adv Mater, vol. 31, no. 44, Nov. 2019, doi: 10.1002/adma.201903914.

[105] R. Tang et al., “Controlled sputtering pressure on high-quality Sb_2Se_3 thin film for substrate configurated solar cells,” Nanomaterials, vol. 10, no. 3, Mar. 2020, doi: 10.3390/nano10030574.

[106] Y. Di Luo et al., “An effective combination reaction involved with sputtered and selenized Sb precursors for efficient Sb_2Se_3 thin film solar cells,” Chem Engine J, vol. 393, Aug. 2020, doi: 10.1016/j.cej.2020.124599.

[107] R. Tang et al., “Heterojunction Annealing Enabling Record Open-Circuit Voltage in Antimony Triselenide Solar Cells,” Adv Mater, vol. 34, no. 14, Apr. 2022, doi: 10.1002/adma.202109078.

[108] K. Yang, B. Li, and G. Zeng, “Effects of substrate temperature and SnO_2 high resistive layer on Sb_2Se_3 thin film solar cells prepared by pulsed laser deposition,” Sol Energy Mater Sol Cells, vol. 208, May 2020, doi: 10.1016/j.solmat.2019.110381.

[109] R. Krautmann, Development of Sb_2Se_3 and Sb_2S_3 Thin Film Solar Cells by Close-Spaced Sublimation. Tallinn University of Technology, 2023.

[110] C. H. Don et al., “Multi-Phase Sputtered TiO_2-Induced Current–Voltage Distortion in Sb_2Se_3 Solar Cells,” Adv Mater Interfaces, vol. 10, no. 20, Jul. 2023, doi: 10.1002/admi.202300238.

[111] L. Guo et al., “Stable and efficient Sb_2Se_3 solar cells with solution-processed NiO_x hole-transport layer,” Sol Energy, vol. 218, pp. 525–531, Apr. 2021, doi: 10.1016/j.solener.2021.02.063.

[112] R. Kondrotas, J. Zhang, C. Wang, and J. Tang, “Growth mechanism of Sb_2Se_3 thin films for photovoltaic application by vapor transport deposition,” Sol Energy Mater Sol Cells, vol. 199, pp. 16–23, Sep. 2019, doi: 10.1016/j.solmat.2019.04.024.

[113] T. P. Weiss et al., “Post-deposition annealing and interfacial atomic layer deposition buffer layers of Sb_2Se_3/CdS stacks for reduced interface recombination and increased open-circuit voltages,” Prog Photovolt Res Appl, 2022, doi: 10.1002/pip.3625.

[114] W. Wang et al., “Promising $Sb_2(S,Se)_3$ Solar Cells with High Open Voltage by Application of a TiO2/CdS Double Buffer Layer,” Solar RRL, vol. 2, no. 11, Nov. 2018, doi: 10.1002/solr.201800208.

[115] X. Wen et al., “Magnetron sputtered ZnO buffer layer for Sb_2Se_3 thin film solar cells,” Sol Energy Mater Sol Cells, vol. 172, pp. 74–81, Dec. 2017, doi: 10.1016/j.solmat.2017.07.014.

[116] A. N. Kulkarni, S. A. Arote, H. M. Pathan, and R. S. Patil, “Sb_2Se_3 sensitized heterojunction solar cells,” Mater Renew Sustain Energy, vol. 4, no. 3, Sep. 2015, doi: 10.1007/s40243-015-0058-5.

[117] V. Hernández-Calderón et al., “CdS/ZnS Bilayer Thin Films Used As Buffer Layer in 10%-Efficient $Cu_2ZnSnSe_4$ Solar Cells,” ACS Appl Energy Mater, vol. 3, no. 7, pp. 6815–6823, Jul. 2020, doi: 10.1021/acsaem.0c00937.

[118] S. Chen et al., “Simultaneous Band Alignment Modulation and Carrier Dynamics Optimization Enable Highest Efficiency in Cd-Free Sb_2Se_3 Solar Cells,” Adv Funct Mater, vol. 34, no. 40, Oct. 2024, doi: 10.1002/adfm.202403934.

[119] K. Li et al., “Improved efficiency by insertion of $Zn_{1-x}Mg_xO$ through sol-gel method in ZnO/Sb_2Se_3 solar cell,” Sol Energy, vol. 167, pp. 10–17, Jun. 2018, doi: 10.1016/j.solener.2018.03.081.

[120] J. Lindahl, J. T. Wätjen, A. Hultqvist, T. Ericson, M. Edoff, and T. Törndahl, "The effect of $Zn_{1-x}Sn_xO_y$ buffer layer thickness in 18.0% efficient Cd-free Cu(In,Ga)Se_2 solar cells," Prog Photovolt: Res Appl, vol. 21, no. 8, pp. 1588–1597, Dec. 2013, doi: 10.1002/pip.2239.

[121] M. Terheggen, H. Heinrich, G. Kostorz, D. Baetzner, A. Romeo, and A. N. Tiwari, "Analysis of Bulk and Interface Phenomena in CdTe/CdS Thin-Film Solar Cells," Interface Sci, vol. 12, pp. 259–266, 2004, doi: 10.1023/B:INTS.0000028655.11608.c7.

[122] A. Mavlonov et al., "A review of Sb_2Se_3 photovoltaic absorber materials and thin-film solar cells," Sol Energy, vol. 201, pp. 227–246, May 2020, doi: 10.1016/j.solener.2020.03.009.

[123] J. M. Burst et al., "CdTe solar cells with open-circuit voltage breaking the 1V barrier," Nat Energy, vol. 1, no. 4, 2016, doi: 10.1038/NENERGY.2016.15.

[124] X. Liu et al., "Improving the performance of Sb_2Se_3 thin film solar cells over 4% by controlled addition of oxygen during film deposition," Prog Photovolt: Res Appl, vol. 23, no. 12, pp. 1828–1836, Dec. 2015, doi: 10.1002/pip.2627.

[125] L. Wang et al., "Stable 6%-efficient Sb_2Se_3 solar cells with a ZnO buffer layer," Nat Energy, vol. 2, no. 4, Mar. 2017, doi: 10.1038/nenergy.2017.46.

[126] C. Cheng, L. Wang, and J. Yu, "CdS-based S-scheme photocatalyst," Interface Sci Technology, vol. 35, pp. 175–199, Jan. 2023, doi: 10.1016/B978-0-443-18786-5.00001-9.

[127] B. G. An, H. R. Kim, Y. W. Chang, J. G. Park, and J. C. Pyun, "Photosensors-based on cadmium sulfide (CdS) nanostructures: a review," J Korean Ceram Soc, vol. 58, no. 6, pp. 631–644, Nov. 2021, doi: 10.1007/s43207-021-00141-5.

[128] J. Mao, W. Xu, and S. Seo, "Exploring the dual phases of cadmium sulfide: synthesis, properties, and applications of hexagonal wurtzite and cubic zinc blende crystal structures," Jul. 25, 2024, Royal Society of Chemistry. doi: 10.1039/d4ta03496a.

[129] A. H. Alkhayattomran and M. R. Ahmed, "Impact of reaction temperature on the structural, surface morphology and antibacterial activity of hydrothermally synthesized CdS nanoparticles," J Phys Conf Ser, vol. 1879, no. 3, May 2021, doi: 10.1088/1742-6596/1879/3/032091.

[130] Z. Ping et al., "First-principle study of phase stability, electronic structure and thermodynamic properties of cadmium sulfide under high pressure," J Phys Chem Solids, vol. 75, no. 5, pp. 662–669, May 2014, doi: 10.1016/j.jpcs.2014.01.021.

[131] V. Lahariya and S. K. Gupta, "Enhanced photoluminescence from CdS nanocrystals encapsulated by PVP and SHMP," Optoelectron Lett, vol. 18, no. 5, pp. 257–262, May 2022, doi: 10.1007/s11801-022-1162-2.

[132] N. Maticiuc et al., "Comparative study of CdS films annealed in neutral, oxidizing and reducing atmospheres," in Energy Procedia, 2014, pp. 77–84. doi: 10.1016/j.egypro.2013.12.012.

[133] N. Maticiuc, J. Hiie, V. Mikli, T. Potlog, and V. Valdna, "Structural and optical properties of cadmium sulfide thin films modified by hydrogen annealing," Mater Sci Semicond Process, vol. 26, no. 1, pp. 169–174, 2014, doi: 10.1016/j.mssp.2014.04.031.

[134] N. Maticiuc, A. Katerski, M. Danilson, M. Krunks, and J. Hiie, "XPS study of OH impurity in solution processed CdS thin films," Sol Energy Mater Sol Cells, vol. 160, pp. 211–216, Feb. 2017, doi: 10.1016/j.solmat.2016.10.040.

[135] N. Spalatu et al., “Postdeposition Processing of SnS Thin Films and Solar Cells: Prospective Strategy to Obtain Large, Sintered, and Doped SnS Grains by Recrystallization in the Presence of a Metal Halide Flux,” ACS Appl Mater Interfaces, vol. 11, no. 19, pp. 17539–17554, May 2019, doi: 10.1021/acsami.9b03213.

[136] P. A. Bozkurt and B. Derkuş, “Synthesis and characterization of CdS nanorods by combined sonochemical-solvothermal method,” Materials Science- Poland, vol. 34, no. 3, pp. 684–690, Sep. 2016, doi: 10.1515/msp-2016-0089.

[137] R. M. Abdelhameed and I. M. El Radaf, “Self-cleaning lanthanum doped cadmium sulfide thin films and linear/nonlinear optical properties,” Mater Res Express, vol. 5, no. 6, Jun. 2018, doi: 10.1088/2053-1591/aac638.

[138] R. Aggarwal and R. Kumar, “Optimization of Thermal Annealing Effect on Sol-Gel-Driven Spin-Coated CdS Thin Films,” J Appl Spectrosc, vol. 91, no. 1, pp. 246–252, Mar. 2024, doi: 10.1007/s10812-024-01712-0.

[139] S. Chander and M. S. Dhaka, “Optical and structural constants of CdS thin films grown by electron beam vacuum evaporation for solar cells,” Thin Solid Films, vol. 638, pp. 179–188, Sep. 2017, doi: 10.1016/j.tsf.2017.07.048.

[140] M. Sharma, S. Kumar, L. M. Sharma, T. P. Sharma, and M. Husain, “CdS sintered films: Growth and characteristics,” Physica B Condens Matter, vol. 348, no. 1–4, pp. 15–20, May 2004, doi: 10.1016/j.physb.2003.08.129.

[141] A. Vera-Marquina et al., “Optical properties of annealed CdS-nanostructured films for solar cells,” Frontiers in Optics, 2014, doi: 10.1364/FIO.2014.FW2B.6.

[142] L. Geng et al., “Electron beam evaporated cadmium sulphide thin films for solar cell applications,” J Renew Sustain Energy, vol. 4, no. 4, Jul. 2012, doi: 10.1063/1.4730616.

[143] B. Barman, K. V. Bangera, and G. K. Shivakumar, “Effect of substrate temperature on the suitability of thermally deposited cadmium sulfide thin films as window layer in photovoltaic cells,” Superlattices Microstruct, vol. 123, pp. 374–381, Nov. 2018, doi: 10.1016/j.spmi.2018.09.030.

[144] L. Fang et al., “Electron beam evaporation deposition of cadmium sulphide and cadmium telluride thin films: Solar cell applications,” Chinese Physics B, vol. 22, no. 9, Sep. 2013, doi: 10.1088/1674-1056/22/9/098802.

[145] G. W. C. Kumarage, R. P. Wijesundera, E. Comini, and B. S. Dassanayake, “Enhancing the Photovoltaic Performance of $Cd_{(1-x)}Zn_xS$ Thin Films Using Seed Assistance and EDTA Treatment,” Micro, vol. 3, no. 4, pp. 867–878, Dec. 2023, doi: 10.3390/micro3040059.

[146] A. Kumar, V. Kumar, R. Chandra, and Y. K. Gautam, “Effect of sputtering process parameters on structural and optical properties of CdS thin films,” Mater Res Express, vol. 6, no. 10, Sep. 2019, doi: 10.1088/2053-1591/ab4334.

[147] A. Romeo et al., “Properties of CIGS solar cells developed with evaporated II-VI buffer layers,” in Technical Digest of the International PVSEC-14, 2004.

[148] N. Spalatu et al., “Properties of the $CdCl_2$ air-annealed CSS CdTe thin films,” Energy Procedia, vol. 44, pp. 85–95, 2014, doi: 10.1016/j.egypro.2013.12.013.

[149] A. I. Oliva, O. Solís-Canto, R. Castro-Rodríguez, and P. Quintana, “Formation of the band gap energy on CdS thin films growth by two different techniques,” Thin Solid Films, vol. 391, no. 1, pp. 28–35, Jul. 2001, doi: 10.1016/S0040-6090(01)00830-6.

[150] J. Han et al., “Annealing effects on the chemical deposited CdS films and the electrical properties of CdS/CdTe solar cells,” Mater Res Bull, vol. 46, no. 2, pp. 194–198, Feb. 2011, doi: 10.1016/j.materresbull.2010.11.014.

[151] S. Salam et al., “The effect of processing conditions on the structural morphology and physical properties of ZnO and CdS thin films produced via sol-gel synthesis and chemical bath deposition techniques,” Adv Nat Sci: Nanosci Nanotechnol, vol. 2, no. 4, 2011, doi: 10.1088/2043-6262/2/4/045001.

[152] G. Pérez-Hernández et al., “A comparative study of CdS thin films deposited by different techniques,” in Thin Solid Films, May 2013, pp. 154–157. doi: 10.1016/j.tsf.2012.11.092.

[153] B. S. Moon, J. H. Lee, and H. Jung, “Comparative studies of the properties of CdS films deposited on different substrates by R.F. sputtering,” Thin Solid Films, vol. 511–512, pp. 299–303, Jul. 2006, doi: 10.1016/J.TSF.2005.11.080.

[154] N. K. Das et al., “Effect of substrate temperature on the properties of RF sputtered CdS thin films for solar cell applications,” Results Phys, vol. 17, Jun. 2020, doi: 10.1016/j.rinp.2020.103132.

[155] N. H. Kim, S. H. Ryu, H. S. Noh, and W. S. Lee, “Electrical and optical properties of sputter-deposited cadmium sulfide thin films optimized by annealing temperature,” Mater Sci Semicond Process, vol. 15, no. 2, pp. 125–130, Apr. 2012, doi: 10.1016/j.mssp.2011.09.001.

[156] C. Doroody et al., “A comparative study of CdS thin films grown on ultra-thin glass substrates by RF magnetron sputtering and chemical bath deposition,” Mater Sci Semicond Process, vol. 133, Oct. 2021, doi: 10.1016/j.mssp.2021.105935.

[157] Y. Park, E. K. Kim, S. Lee, and J. Lee, “Growth and characterization of CdS thin films on polymer substrates for photovoltaic applications,” J Nanosci Nanotechnol, vol. 14, no. 5, pp. 3880–3883, 2014, doi: 10.1166/jnn.2014.8132.

[158] L. V. Garcia et al., “Structure and properties of CdS thin films prepared by pulsed laser assisted chemical bath deposition,” Mater Res Bull, vol. 83, pp. 459–467, Nov. 2016, doi: 10.1016/j.materresbull.2016.06.027.

[159] M. F. Rahman, J. Hossain, and A. B. M. Ismail, “Structural, surface morphological and optical properties and their correlation with the thickness of spin coated superior quality CdS thin film synthesized using a novel chemical route,” SN Appl Sci, vol. 2, no. 12, Dec. 2020, doi: 10.1007/s42452-020-03836-2.

[160] N. Ahmad et al., “Cadmium-Free Kesterite Thin-Film Solar Cells with High Efficiency Approaching 12%,” Advanced Science, vol. 10, no. 26, Sep. 2023, doi: 10.1002/advs.202302869.

[161] S. Karthikeyan, A. E. Hill, and R. D. Pilkington, “Low temperature pulsed direct current magnetron sputtering technique for single phase β-In_2S_3 buffer layers for solar cell applications,” Appl Surf Sci, vol. 418, pp. 199–206, Oct. 2017, doi: 10.1016/j.apsusc.2017.01.147.

[162] D. Oyetunde, M. Afzaal, M. A. Vincent, I. H. Hillier, and P. O’Brien, “Cadmium sulfide and cadmium phosphide thin films from a single cadmium compound,” Inorg Chem, vol. 50, no. 6, pp. 2052–2054, Mar. 2011, doi: 10.1021/ic102309r.

[163] D. Barreca et al., “Cadmium O-alkylxanthates as CVD precursors of CdS: A chemical characterization,” Appl Organomet Chem, vol. 19, no. 1, pp. 59–67, Jan. 2005, doi: 10.1002/aoc.833.

[164] G. Ojeda-Barrero, A. I. Oliva-Avilés, A. I. Oliva, R. D. Maldonado, M. Acosta, and G. M. Alonzo-Medina, “Effect of the substrate temperature on the physical properties of sprayed-CdS films by using an automatized perfume atomizer,” Mater Sci Semicond Process, vol. 79, pp. 7–13, Jun. 2018, doi: 10.1016/j.mssp.2018.01.018.

[165] A. A. Yadav and E. U. Masumdar, “Photoelectrochemical investigations of cadmium sulphide (CdS) thin film electrodes prepared by spray pyrolysis,” J Alloys Compd, vol. 509, no. 17, pp. 5394–5399, Apr. 2011, doi: 10.1016/j.jallcom.2011.02.061.

[166] V. K. Jain and A. Verma, Eds., Physics of Semiconductor Devices. in Environmental Science and Engineering. Cham: Springer International Publishing, 2014. doi: 10.1007/978-3-319-03002-9.

[167] M. G. Faraj, H. H. Karim, A. F. Qader, I. N. Qader, and R. T. Ali, “Effect of molarity on the optical and structural properties of CdS thin films deposited by spray pyrolysis on flexible plastic substrates,” J Mater Sci: Mater Electron, vol. 35, no. 32, Nov. 2024, doi: 10.1007/s10854-024-13839-z.

[168] H. Y. R. Atapattu, D. S. M. De Silva, K. A. S. Pathiratne, O. I. Olusola, and I. M. Dharmadasa, “Necessity and relevance of precipitate free clear electrolytes for electrodeposition of CdS semiconductor materials with enhanced photovoltaic properties,” J Mater Sci: Mater Electron, vol. 28, no. 24, pp. 18592–18602, Dec. 2017, doi: 10.1007/s10854-017-7808-3.

[169] A. U. Yimamu, S. Z. Werta, F. T. Maremi, B. F. Dejene, and O. K. Echendu, “Effect of deposition voltage on the physico-chemical properties of electrodeposited Mg-doped CdS thin films for Opto-electronic application,” Mater Today Commun, vol. 42, Jan. 2025, doi: 10.1016/j.mtcomm.2024.111410.

[170] H. Hu, S. C. Kung, L. M. Yang, M. E. Nicho, and R. M. Penner, “Photovoltaic devices based on electrochemical-chemical deposited CdS and poly3-octylthiophene thin films,” Solar Energy Materials and Solar Cells, vol. 93, no. 1, pp. 51–54, Jan. 2009, doi: 10.1016/j.solmat.2008.03.011.

[171] S. Z. Werta, O. K. Echendu, and F. B. Dejene, “Optical and Morphological Studies of Electrodeposited CdS Thin Film Grown at Different Deposition Times from Acetate Precursor,” ECS J Solid State Sci Technol, vol. 8, no. 2, pp. P112–P118, 2019, doi: 10.1149/2.0151902jss.

[172] J. Nishino, S. Chatani, Y. Uotani, and Y. Nosaka, “Electrodeposition method for controlled formation of CdS films from aqueous solutions,” J Electroanal Chem, vol. 473, no. 1–2, pp. 217–222, Sep. 1999, doi: 10.1016/S0022-0728(99)00250-8.

[173] Y. J. Chang, Y. W. Su, D. H. Lee, S. O. Ryu, and C. H. Chang, “Investigate the reacting flux of chemical bath deposition by a continuous flow microreactor,” Electrochem Solid-State Let, vol. 12, no. 7, 2009, doi: 10.1149/1.3117211.

[174] N. Maticiuc, “Mechanism of Changes in the Properties of Chemically Deposited CdS Thin Films Induced by Thermal Annealing,” Tallinn University of Technology, 2015.

[175] M. A. Martínez, C. Guillén, and J. Herrero, “Morphological and structural studies of CBD-CdS thin films by microscopy and diffraction techniques,” Appl Surf Sci, vol. 136, no. 1–2, pp. 8–16, Oct. 1998, doi: 10.1016/S0169-4332(98)00331-6.

[176] P. Roy and S. K. Srivastava, “A new approach towards the growth of cadmium sulphide thin film by CBD method and its characterization,” Mater Chem Phys, vol. 95, no. 2–3, pp. 235–241, Feb. 2006, doi: 10.1016/j.matchemphys.2005.06.010.

[177] M. B. Ortuño-López, M. Sotelo-Lerma, A. Mendoza-Galván, and R. Ramírez-Bon, “Optical band gap tuning and study of strain in CdS thin films,” in Vacuum, Nov. 2004, pp. 181–184. doi: 10.1016/j.vacuum.2004.07.038.

[178] H. Guo et al., “Highly efficient and thermally stable Sb_2Se_3 solar cells based on a hexagonal CdS buffer layer by environmentally friendly interface optimization,” J Mater Chem C Mater, vol. 8, no. 48, pp. 17194–17201, Dec. 2020, doi: 10.1039/d0tc04017g.

[179] N. Maticiuc, N. Spalatu, V. Mikli, and J. Hiie, “Impact of CdS annealing atmosphere on the performance of CdS-CdTe solar cell,” Appl Surf Sci, vol. 350, pp. 14–18, Sep. 2015, doi: 10.1016/j.apsusc.2015.01.172.

[180] Q. Lin et al., “Influence of the Ammonia Concentration in Chemical Bath Deposition and Selenourea Concentration in Hydrothermal Process on the Properties of CdS and $Sb_2S_{3-y}Se_y$ Thin Films and the Photovoltaic Performance of the Corresponding Solar Cells,” Energy Technol, vol. 11, no. 7, Jul. 2023, doi: 10.1002/ente.202201478.

[181] X. Wang et al., “Interfacial engineering for high efficiency solution processed Sb_2Se_3 solar cells,” Sol Energy Mater Sol Cells, vol. 189, pp. 5–10, Jan. 2019, doi: 10.1016/j.solmat.2018.09.020.

[182] Z. Li et al., “Sb_2Se_3 thin film solar cells in substrate configuration and the back contact selenization,” Sol Energy Mater Sol Cells, vol. 161, pp. 190–196, Mar. 2017, doi: 10.1016/J.SOLMAT.2016.11.033.

[183] J. Zhang et al., “Improving the performance of Sb_2Se_3 thin-film solar cells using n-type MoO_3 as the back contact layer,” Sol Energy, vol. 214, pp. 231–238, Jan. 2021, doi: 10.1016/j.solener.2020.11.074.

[184] C. Yuan, L. Zhang, W. Liu, and C. Zhu, “Rapid thermal process to fabricate Sb_2Se_3 thin film for solar cell application,” Sol Energy, vol. 137, pp. 256–260, Nov. 2016, doi: 10.1016/j.solener.2016.08.020.

[185] C. Chen et al., “6.5% Certified Efficiency Sb_2Se_3 Solar Cells Using PbS Colloidal Quantum Dot Film as Hole-Transporting Layer,” ACS Energy Lett, vol. 2, no. 9, pp. 2125–2132, Sep. 2017, doi: 10.1021/acsenergylett.7b00648.

[186] Z. Feng et al., “Efficiency enhancement of a Sb_2Se_3 solar cell after adding a Si3N4 interface layer,” Mater Lett, vol. 314, May 2022, doi: 10.1016/j.matlet.2022.131796.

[187] C. Chen et al., “Efficiency Improvement of Sb_2Se_3 Solar Cells via Grain Boundary Inversion,” ACS Energy Lett, vol. 3, no. 10, pp. 2335–2341, Oct. 2018, doi: 10.1021/acsenergylett.8b01456.

[188] G. Liang et al., “Crystal Growth Promotion and Defects Healing Enable Minimum Open-Circuit Voltage Deficit in Antimony Selenide Solar Cells,” Adv Sci, vol. 9, no. 9, Mar. 2022, doi: 10.1002/advs.202105142.

[189] K. Li et al., “7.5% n-i-p Sb_2Se_3 solar cells with CuSCN as a hole-transport layer,” J Mater Chem A Mater, vol. 7, no. 16, pp. 9665–9672, 2019, doi: 10.1039/c9ta01773a.

[190] J. Tao et al., „Solution-processed SnO_2 interfacial layer for highly efficient Sb_2Se_3 thin film solar cells,” Nano Energy, vol. 60, pp. 802–809, Jun. 2019, doi: 10.1016/j.nanoen.2019.04.019.

[191] L. Guo et al., “Improved stability and efficiency of CdSe/Sb_2Se_3 thin-film solar cells,” Sol Energy, vol. 188, pp. 586–592, Aug. 2019, doi: 10.1016/j.solener.2019.06.042.

[192] A. Amin et al., “Solution-processed vanadium oxides as a hole-transport layer for Sb_2Se_3 thin-film solar cells,” Sol Energy, vol. 231, pp. 1–7, Jan. 2022, doi: 10.1016/j.solener.2021.11.009.

[193] L. Guo et al., “Interface Engineering via Sputtered Oxygenated CdS:O Window Layer for Highly Efficient Sb_2Se_3 Thin-Film Solar Cells with Efficiency Above 7%,” Solar RRL, vol. 3, no. 10, Oct. 2019, doi: 10.1002/solr.201900225.

[194] G. X. Liang et al., “Facile preparation and enhanced photoelectrical performance of Sb_2Se_3 nano-rods by magnetron sputtering deposition,” Sol Energy Mater Sol Cells, vol. 160, pp. 257–262, Feb. 2017, doi: 10.1016/j.solmat.2016.10.042.

[195] G. X. Liang et al., “Sputtered and selenized Sb_2Se_3 thin-film solar cells with open-circuit voltage exceeding 500 mV,” Nano Energy, vol. 73, Jul. 2020, doi: 10.1016/j.nanoen.2020.104806.
[196] S. Rijal et al., “Templated Growth and Passivation of Vertically Oriented Antimony Selenide Thin Films for High-Efficiency Solar Cells in Substrate Configuration,” Adv Funct Mater, vol. 32, no. 10, Mar. 2022, doi: 10.1002/adfm.202110032.
[197] G. Liang et al., “Ion doping simultaneously increased the carrier density and modified the conduction type of Sb_2Se_3 thin films towards quasi-homojunction solar cell,” J Materiomics, vol. 7, no. 6, pp. 1324–1334, Nov. 2021, doi: 10.1016/j.jmat.2021.02.009.
[198] H. El Maliki, J. C. Bernède, S. Marsillac, J. Pinel, X. Castel, and J. Pouzet, “Study of the influence of annealing on the properties of CBD-CdS thin films,” Appl Surf Sci, vol. 205, no. 1–4, pp. 65–79, Jan. 2003, doi: 10.1016/S0169-4332(02)01082-6.
[199] S. A. Tomás et al., “Influence of thermal annealings in different atmospheres on the band-gap shift and resistivity of CdS thin films,” J Appl Phys, vol. 78, no. 4, pp. 2204–2207, 1995, doi: 10.1063/1.360136.
[200] A. Graf et al., “Electrical characterization of annealed chemical-bath-deposited CdS films and their application in superstrate configuration CdTe/CdS solar cells,” Thin Solid Films, vol. 582, pp. 351–355, May 2015, doi: 10.1016/j.tsf.2014.11.003.
[201] A. A. Dakhel, “Electrical and optical properties of iron-doped CdO,” Thin Solid Films, vol. 518, no. 6, pp. 1712–1715, Jan. 2010, doi: 10.1016/j.tsf.2009.11.026.
[202] H. Kim and D. Kim, “Influence of CdS heat treatment on the microstructure of CdS and the performance of CdS/CdTe solar cells,” Solar Energy Materials & Solar Cells, vol. 67, pp. 297–304, Mar. 2001, doi: 10.1016/S0927-0248(00)00295-6.
[203] L. M. Fraas, W. P. Bleha, and P. Braatz, “Recrystallization of thermally evaporated CdS films via an H_2S heat-treatment process,” J Appl Phys, vol. 46, no. 2, pp. 491–495, 1975, doi: 10.1063/1.321671.
[204] J. Hiie, K. Muska, V. Valdna, V. Mikli, A. Taklaja, and A. Gavrilov, “Thermal annealing effect on structural and electrical properties of chemical bath-deposited CdS films,” Thin Solid Films, vol. 516, no. 20, pp. 7008–7012, Aug. 2008, doi: 10.1016/J.TSF.2007.12.008.
[205] L. Wang et al., “Ambient $CdCl_2$ treatment on CdS buffer layer for improved performance of Sb2Se3 thin film photovoltaics,” Appl Phys Lett, vol. 107, no. 14, Oct. 2015, doi: 10.1063/1.4932544.
[206] D. B. Li et al., “Stable and efficient CdS/Sb_2Se_3 solar cells prepared by scalable close space sublimation,” Nano Energy, vol. 49, pp. 346–353, Jul. 2018, doi: 10.1016/j.nanoen.2018.04.044.
[207] L. J. Phillips et al., “Current Enhancement via a TiO_2 Window Layer for CSS Sb 2 Se 3 Solar Cells: Performance Limits and High V oc,” IEEE J Photovolt, vol. 9, no. 2, pp. 544–551, Mar. 2019, doi: 10.1109/JPHOTOV.2018.2885836.
[208] J. Tao et al., “Investigation of electronic transport mechanisms in Sb_2Se_3 thin-film solar cells,” Sol Energy Mater Sol Cells, vol. 197, pp. 1–6, Aug. 2019, doi: 10.1016/j.solmat.2019.04.003.
[209] Y. Zhou et al., “Buried homojunction in CdS/Sb_2Se_3 thin film photovoltaics generated by interfacial diffusion,” Appl Phys Lett, vol. 111, no. 1, Jul. 2017, doi: 10.1063/1.4991539.

[210] P. Fan et al., "Quasi-Vertically Oriented Sb_2Se_3 Thin-Film Solar Cells with Open-Circuit Voltage Exceeding 500 mV Prepared via Close-Space Sublimation and Selenization," ACS Appl Mater Interfaces, vol. 13, no. 39, pp. 46671–46680, Oct. 2021, doi: 10.1021/acsami.1c13223.

[211] Z. Li et al., "Efficiency enhancement of Sb_2Se_3 thin-film solar cells by the co-evaporation of Se and Sb_2Se_3," Appl Phys Exp, vol. 9, no. 5, May 2016, doi: 10.7567/APEX.9.052302.

[212] S. Chen et al., "An effective engineering with simultaneous carrier density enhancement and interface optimization enables efficient Sb_2Se_3 solar cells," Appl Surf Sci, vol. 619, May 2023, doi: 10.1016/j.apsusc.2023.156783.

[213] Z. Duan et al., "Sb_2Se_3 Thin-Film Solar Cells Exceeding 10% Power Conversion Efficiency Enabled by Injection Vapor Deposition Technology," Adv Mater, vol. 34, no. 30, Jul. 2022, doi: 10.1002/adma.202202969.

[214] H. Cai et al., "Interfacial Engineering towards Enhanced Photovoltaic Performance of Sb_2Se_3 Solar Cell," Adv Funct Mater, vol. 32, no. 46, Nov. 2022, doi: 10.1002/adfm.202208243.

[215] X. Hu et al., "Investigation of electrically-active defects in Sb_2Se_3 thin-film solar cells with up to 5.91% efficiency via admittance spectroscopy," Sol Energy Mater Sol Cells, vol. 186, pp. 324–329, Nov. 2018, doi: 10.1016/j.solmat.2018.07.004.

[216] C. Chen et al., "Characterization of basic physical properties of Sb_2Se_3 and its relevance for photovoltaics," Front Optoelectron, vol. 10, no. 1, pp. 18–30, Mar. 2017, doi: 10.1007/s12200-017-0702-z.

[217] A. Kylner, "Effect of impurities in the CdS buffer layer on the performance of the Cu(In, Ga)Se_2 thin film solar cell," J Appl Phys, vol. 85, no. 9, pp. 6858–6865, May 1999, doi: 10.1063/1.370204.

[218] J. B. Varley and V. Lordi, "Electrical properties of point defects in CdS and ZnS," Appl Phys Lett, vol. 103, no. 10, Sep. 2013, doi: 10.1063/1.4819492.

[219] T. Potlog et al., "Structural reproducibility of CdTe thin films deposited on different substrates by close space sublimation method," Phys Status Solidi (A) Appl Mater Sci, vol. 209, no. 2, pp. 272–276, Feb. 2012, doi: 10.1002/pssa.201127123.

[220] N. Spalatu et al., "Effect of $CdCl_2$ annealing treatment on structural and optoelectronic properties of close spaced sublimation CdTe/CdS thin film solar cells vs deposition conditions," Thin Solid Films, vol. 582, pp. 128–133, May 2015, doi: 10.1016/j.tsf.2014.11.066.

[221] M. Koltsov et al., "A post-deposition annealing approach for organic residue control in TiO_2 and its impact on Sb_2Se_3/TiO_2 device performance," Faraday Discuss, vol. 239, pp. 273–289, Apr. 2022, doi: 10.1039/d2fd00064d.

[222] H. Shiel et al., "Natural Band Alignments and Band Offsets of Sb_2Se_3 Solar Cells," ACS Appl Energy Mater, vol. 3, no. 12, pp. 11617–11626, Dec. 2020, doi: 10.1021/acsaem.0c01477.

[223] S. R. Ferrá-González et al., "Optical and structural properties of CdS thin films grown by chemical bath deposition doped with Ag by ion exchange," Optik, vol. 125, no. 4, pp. 1533–1536, Feb. 2014, doi: 10.1016/j.ijleo.2013.08.035.

[224] T. Sivaraman, V. Narasimman, V. S. Nagarethinam, and A. R. Balu, "Effect of chlorine doping on the structural, morphological, optical and electrical properties of spray deposited CdS thin films," Prog Nat Sci: Mater Int, vol. 25, no. 5, pp. 392–398, Oct. 2015, doi: 10.1016/j.pnsc.2015.09.010.

[225] J. Hiie, T. Dedova, V. Valdna, and K. Muska, “Comparative study of nano-structured CdS thin films prepared by CBD and spray pyrolysis: Annealing effect,” Thin Solid Films, vol. 511–512, pp. 443–447, Jul. 2006, doi: 10.1016/j.tsf.2005.11.070.

[226] O. De Melo, L. Hernández, O. Zelaya-Angel, R. Lozada-Morales, M. Becerril, and E. Vasco, “Low resistivity cubic phase CdS films by chemical bath deposition technique,” Appl Phys Lett, vol. 65, no. 10, pp. 1278–1280, 1994, doi: 10.1063/1.112094.

[227] M. Azam et al., “Organic Chloride Salt Interfacial Modified Crystallization for Efficient Antimony Selenosulfide Solar Cells,” ACS Appl Mater Interfaces, vol. 14, no. 3, pp. 4276–4284, Jan. 2022, doi: 10.1021/acsami.1c20779.

[228] W. Wang, Z. Cao, H. Wang, J. Luo, and Y. Zhang, “Remarkable Cd-free Sb_2Se_3 solar cell yield achieved by interface band-alignment and growth orientation screening,” J Mater Chem A Mater, vol. 9, no. 47, pp. 26963–26975, Dec. 2021, doi: 10.1039/d1ta08404f.

[229] Z. Feng et al., “Buried Interface Modulation Using Self-Assembled Monolayer and Ionic Liquid Hybrids for High-Performance Perovskite and Perovskite/$CuInGaSe_2$ Tandem Photovoltaics,” Adv Mater, vol. 37, no. 8, Feb. 2025, doi: 10.1002/adma.202412692.

[230] C. Duan et al., “Plasma etching-Induced surface modification and interfacial defect passivation for antimony triselenide thin film solar cells,” Ceram Int, vol. 50, no. 7, pp. 12253–12262, Apr. 2024, doi: 10.1016/j.ceramint.2024.01.129.

[231] J. Lin et al., “Crystallographic orientation control and defect passivation for high-efficient antimony selenide thin-film solar cells,” Mater Today Phys, vol. 27, Oct. 2022, doi: 10.1016/j.mtphys.2022.100772.

[232] S. Chen et al., “Improved Open-Circuit Voltage of Sb_2Se_3 Thin-Film Solar Cells Via Interfacial Sulfur Diffusion-Induced Gradient Bandgap Engineering,” Solar RRL, vol. 5, no. 10, Oct. 2021, doi: 10.1002/solr.202100419.

[233] T. P. Weiss, S. Nishiwaki, B. Bissig, S. Buecheler, and A. N. Tiwari, “Voltage dependent admittance spectroscopy for the detection of near interface defect states for thin film solar cells,” Phys Chem Chem Phys, vol. 19, no. 45, pp. 30410–30417, 2017, doi: 10.1039/c7cp05236g.

[234] S. Levcenko et al., “Deep Defects in $Cu_2ZnSn(S,Se)_4$ Solar Cells with Varying Se Content,” Phys Rev Appl, vol. 5, no. 2, Feb. 2016, doi: 10.1103/PhysRevApplied.5.024004.

[235] T. Walter, R. Herberholz, C. Müller, and H. W. Schock, “Determination of defect distributions from admittance measurements and application to $Cu(In,Ga)Se_2$ based heterojunctions,” J Appl Phys, vol. 80, no. 8, pp. 4411–4420, Oct. 1996, doi: 10.1063/1.363401.

[236] M. Chen et al., “Interface optimization and defects suppression via NaF introduction enable efficient flexible Sb_2Se_3 thin-film solar cells,” J Energy Chem, vol. 90, pp. 165–175, Mar. 2024, doi: 10.1016/j.jechem.2023.10.059.

[237] X. Liang et al., “Reduction of bulk and interface defects via photo-annealing treatment for high-efficiency antimony selenide solar cells,” Energy Environ Sci, Oct. 2024, doi: 10.1039/d4ee02877e.

[238] C. Liu et al., “Heterojunction lithiation engineering and diffusion-induced defect passivation for highly efficient $Sb_2(S,Se)_3$ solar cells,” Energy Environ Sci, Oct. 2024, doi: 10.1039/d4ee03135k.

Acknowledgements

First and foremost, I would like to express my sincere gratitude to my supervisors, Prof. Dr. Nicolae Spalatu and Dr. Atanas Katerski, for granting me the opportunity to pursue my doctoral studies in the Laboratory for Thin Film Energy Materials at Tallinn University of Technology. Their unwavering guidance, support, and patience have been instrumental throughout the course of this research. I am also deeply thankful to the head of the laboratory, Prof. Dr. Ilona Oja Acik, for her encouragement and support, and to Prof. Dr. Malle Krunks for her insightful suggestions and assistance during article revisions and presentation preparations. My heartfelt thanks go to my colleagues in the laboratory, whose camaraderie and collaboration made this journey both intellectually rewarding and personally enriching.

On a personal note, I am immensely grateful to my parents, Gopi V. and Jalaja A. S., my brother, Sanish V. G., my sister-in-law, Karthika M., and my niece, Noumika S., for their unwavering love and support throughout this journey. I am also thankful to my dear friend Sijo and his family, who stood by me from my very first day in Estonia. My sincere appreciation also goes to my Malayali friends in Estonia, whose support during challenging times was invaluable. I would also like to thank the TalTech Badminton Club and badminton friends and partners for providing a welcome outlet for recreation and balance during my studies.

I gratefully acknowledge the contributions of my co-authors and collaborators, whose involvement significantly enriched the quality of this research. Special thanks to Prof. Dr. Bohuslav Rezek (Czech Technical University), Prof. Dr. Guillaume Zoppi (Northumbria University), Prof. Dr. Aivars Vembris (University of Latvia), and Raavo Josepson (TalTech) for their generous collaboration and support in the characterisation aspects of this thesis.

This research would not have been possible without the financial support from various funding sources. I gratefully acknowledge the support from the Estonian Research Council through the projects PRG2676 (“All Inorganic Semi-Transparent Thin Film Solar Cells for Solar Windows and Indoor Photovoltaics”) and PSG689 (“Bismuth Chalcogenide Thin-Film Disruptive Green Solar Technology for Next Generation Photovoltaics”), as well as the project TK210 (“TK210U8: Centre of Excellence in Sustainable Green Hydrogen and Energy Technologies”) funded by the Estonian Ministry of Education and Research. I also thank the EU Horizon 2020 project 5GSOLAR (952509), and the Clean Energy Transition Partnership (CETPartnership) under the 2022 joint call for research proposals, co-funded by the European Commission (GA No. 101069750) and the Estonian Research Council (agreement No. MOB3PRT2). Finally, I am grateful for the support and international networking opportunities provided by the COST Action RENEW-PV (CA21148) – Research and International Networking on Emerging Inorganic Chalcogenides for Photovoltaics, supported by COST (European Cooperation in Science and Technology).

To everyone who has been part of this journey, directly or indirectly, I extend my sincere thanks.

Abstract

Development of CdS/Sb_2Se_3 Thin Film Solar Cells: Implications of CdS Processing on Absorber Layer Properties and Device Performance

Antimony selenide (Sb_2Se_3) has emerged as a promising absorber material for next-generation thin-film solar cells owing to its non-toxicity, elemental abundance, near-optimal bandgap (~1.2 eV), and high absorption coefficient (~10^5 cm^{-1} in the visible region). Its pseudo-one-dimensional orthorhombic crystal structure, composed of $(Sb_4Se_6)_n$ ribbons weakly bound by van der Waals forces, minimizes dangling bonds at grain boundaries, leading to excellent defect tolerance compared to other thin-film technologies such as CdTe, CIGS, and CZTS, which face issues of elemental scarcity, toxicity, and secondary phase formation. As a simple binary compound, Sb_2Se_3 offers ease of synthesis and deposition using scalable vacuum techniques like close-spaced sublimation (CSS) and vapour transport deposition (VTD). In particular, VTD provides precise control of deposition parameters such as substrate-to-source distance (D_{So-Sub}), temperature, and time, enabling the growth of vertically oriented columnar grains that enhance carrier transport and device efficiency. Cadmium sulfide (CdS), with its wide bandgap (~2.42 eV) and *n*-type conductivity, serves as an effective electron transport layer (ETL) for Sb_2Se_3 solar cells, typically deposited via chemical bath deposition (CBD) due to its simplicity and excellent film uniformity. Theoretical studies predict a maximum power conversion efficiency (PCE) of 32.74% for Sb_2Se_3 solar cells, while recent experimental reports have achieved PCE of ~10.5% for superstrate-type devices, underscoring Sb_2Se_3's strong potential for sustainable photovoltaic applications. This gap between the theoretical and experimental PCE indicates that there is still room for improvement.

The main aim of the thesis is to develop CdS/Sb_2Se_3 solar cells by VTD, from a fundamental study of the fabrication process, implication of CdS processing and related interface, to the fabrication of complete device, their optimisation and defect characterization.

This thesis is based on three interconnected research publications. Publications I and II focus on the impact of CdS post-deposition treatment (PDT) and Cl incorporation via NH_4Cl during CBD on Sb_2Se_3 properties and solar cell performance, while Publication III investigates the effect of VTD D_{So-Sub} in Ar flow on Sb_2Se_3 and CdS/Sb_2Se_3 cells, comparing devices with and without Cl-processed CdS. The thesis comprises three chapters. Chapter 1 provides a detailed literature study of Sb_2Se_3 and CdS material properties and their deposition methods. Chapter 2 mainly provides an overview of the deposition methods and characterisation techniques used for CdS and Sb_2Se_3 films and devices used in the doctoral work. It includes descriptions on deposition parameters such as CSS, VTD, CBD, and thermal evaporation and characterisation techniques such as X-ray diffraction (XRD), UV-Vis spectroscopy, Hall measurement, secondary electron spectroscopy (SEM), Secondary ion mass spectroscopy (SIMS), Kelvin probe and TAS. Building upon the three core publications, Chapter 3 is divided into three main sections that collectively reflect their central findings. The first section investigates the effect of PDT of the CdS ETL on the film properties and the performance of CdS/Sb_2Se_3 solar cells. The second section examines the impact of chlorine incorporation in CdS films through precursor modification and its influence on the structural and electrical properties of CdS and

Sb_2Se_3, as well as on the properties of CdS-Sb_2Se_3 interface and CdS/Sb_2Se_3 device performance. The third section focuses on the optimisation of Sb_2Se_3 absorber growth via VTD, specifically the role of growth rate and deposition parameters (comparing structures with and without Cl-processed CdS) on the properties of Sb_2Se_3 and solar cells, with a strong emphasis on analysis of bulk and interface defects as the key limiting factors in these devices.

The results demonstrate that PDT of CdS films between 200–400 °C in vacuum and air led to notable changes in film properties. Annealing transformed the CdS morphology from fine dispersed grains to sintered, dense structures, reduced the band gap from 2.43 to 2.35 eV, and significantly lowered electron density from ~10^{18} to ~10^{11} cm^{-3} for vacuum annealed samples and ~10^{17} to ~10^{10} cm^{-3} for air annealed samples. These changes were attributed to the removal of OH groups. The annealing also influenced the morphology of the overlying Sb_2Se_3 absorber, promoting better grain structure and vertical growth, particularly on 200 °C air-annealed CdS. This condition yielded the best device performance, achieving a 2.8% PCE, representing a 60% improvement over devices with as-deposited CdS. Higher annealing temperatures, especially in air, led to CdO formation and performance degradation.

Investigation of the impact of chlorine in CdS films by incorporating low concentrations of NH_4Cl (0-8 mM) into the CdS chemical bath revealed that the structural and morphological properties of CdS remained mostly unaffected; significant changes were observed in the electrical properties, including a sharp decrease in carrier concentration and increased resistivity at 1 mM NH_4Cl. The bandgap slightly narrowed, and SIMS analysis confirmed Cl incorporation into CdS and Cd interdiffusion into the Sb_2Se_3 absorber. Devices with 1 mM NH_4Cl-treated CdS showed the best performance, achieving a 4.6% PCE, 20% improvement over untreated CdS devices. A spike-like band alignment was proposed, allowing efficient charge transfer at the CdS-Sb_2Se_3 interface. However, higher Cl concentrations negatively affected the performance and EQE response of the cells. These findings highlight the delicate balance of Cl incorporation and its critical role in optimising CdS/Sb_2Se_3 solar cell efficiency.

The growth rate of the Sb_2Se_3 by VTD was achieved by adjusting the $D_{So\text{-}Sub}$ and incorporating Ar gas. An optimal $D_{So\text{-}Sub}$ of 6 cm assured an absorber growth rate of 0.4 μm/min, which resulted in compact and uniform absorber films with improved grain structure. Devices using Cl-incorporated CdS and optimised Sb_2Se_3 showed enhanced performance, achieving a PCE of 5%, a ~10% improvement over devices without chloride-processed CdS. For the same device, structural analyses confirmed improved Sb_2Se_3 grain orientation along [001] crystal direction and improved morphology, while combination analysis of dark log-log JV plots and temperature-dependent V_{OC} revealed lower trap density (~10^{14} cm^{-3}) and slightly reduced interface recombination. Additionally, TAS was measured at different bias voltages, revealing the presence of deep defects that could be located close to the heterojunction interface. The extracted activation energies of 0.5 eV (non-Cl SCs) and 0.4 eV (Cl-CdS SCs) above the valence band maximum (VBM) fall in a range that aligns more closely with V_{Sb} and Sb_{Se} defects.

In conclusion, this doctoral thesis presents a comprehensive investigation into the development of CdS/Sb_2Se_3 thin-film solar cells fabricated by VTD, highlighting the strong interdependence between CdS ETL processing, CdS/Sb_2Se_3 interface formation, and Sb_2Se_3 absorber growth dynamics. Through systematic studies on CdS post-deposition treatments, chlorine incorporation, and optimisation of Sb_2Se_3 growth conditions,

the work demonstrates clear pathways for improving film quality, interface properties, and device performance.

The novelty of this thesis lies in its integrated approach to understanding and optimising the CdS/Sb_2Se_3 heterojunction through a combination of process engineering, defect analysis, and interface characterisation. A new method for chlorine incorporation via chemical bath deposition was developed and shown to strongly influence Cd interdiffusion and device efficiency. For the first time, Cl incorporation into the CdS lattice, Cd diffusion into the Sb_2Se_3 absorber, and interdiffusion processes at the CdS/Sb_2Se_3 interface were directly evidenced by SIMS analysis. The thesis also provides new insights into interface-related defect states through TAS analysis and identifies optimised VTD growth parameters that enhance Sb_2Se_3 properties and device performance. Together, these findings advance the fundamental understanding and technological development of emerging Sb_2Se_3-based thin film solar cells.

Kokkuvõte

CdS/Sb_2Se_3 õhukesekilelise päikesepatarei arendus: CdS kihi tehnoloogia mõju absorberkihi omadustele ja seadise efektiivsusele

Antimonseleniid (Sb_2Se_3) on kerkinud esile kui paljulubav absorbermaterjal uue põlvkonna õhukesekilelistes päikesepatareides, sest tegemist on mittetoksilise ühendiga, mille keemilisi elemente leidub maapõues rohkesti, tal on optimaalne keelutsooni laius (~1,2 eV) ning kõrge neeldumistegur (~10^5 cm^{-1} valguse nähtavas piirkonnas). Antimonseleniid omab kvaasi-ühemõõtmelist (Q-1D) ortorombilist kristallstruktuuri, mis koosneb nõrkade van der Waalsi jõududega seotud $(Sb_4Se_6)_n$ ahelatest. Lihtsa binaarse ühendina on Sb_2Se_3 süntees ja sadestamine lihtne ning sobib hästi skaleeritavate vaakummeetoditega, nagu lähidistants-sublimatsioon (ingl *close-spaced sublimation (CSS)*) ja aurutransport-sadestamine (ingl *vapor transport deposition (VTD)*). Sealjuures lubab just VTD täpselt kontrollida sadestamisparameetreid, nagu substraadi-lähteaine vahekaugus (D_{So-Sub}), temperatuur ja aeg, võimaldades kasvatada vertikaalselt orienteeritud kolonnilisi kristalliteri, mis hõlbustavad laengukandjate liikuvust ja parandavad seeläbi seadme kasutegurit. Kaadmiumsulfiid (CdS), millel on lai keelutsooni laius (~2,4 eV) ja n-tüüpi juhtivus, toimib tõhusa elektrontranspordikihina (ingl *electron transport layer (ETL)*). Sb_2Se_3 päikesepatareides sadestatakse CdS tavaliselt keemilise vanni meetodil (ingl *chemical bath deposition (CBD)*) selle lihtsuse ja saadud kile ühtluse tõttu. Teoreetilised uuringud ennustavad Sb_2Se_3 päikesepatareidele maksimaalset kasutegurit (ingl *power conversion efficiency (PCE)*) 32,7%, samas kui hiljutistes katsetes on superstraat-tüüpi seadiste PCE olnud ~10,5%, mis rõhutab Sb_2Se_3 tugevat potentsiaali kestlikes päikeseenergeetika (PV) lahendustes. Samas näitab teoreetilise ja eksperimentaalse kasuteguri erinevus, et arenguruumi veel on.

Doktoritöö eesmärk on arendada CdS/Sb_2Se_3 päikesepatareisid VTD meetodil, alates tootmisprotsessi põhjalikust uurimisest, CdS töötlemisest ja tema mõjust CdS/Sb_2Se_3 piirpinnale, kuni tervikliku seadme valmistamise, optimeerimise ja defektide karakteriseerimiseni.

Töö tugineb kolmele omavahel seotud teadusartiklile. Artiklid I ja II keskenduvad CdS kihi järeltöötluse (ingl *post-deposition treatment (PDT)*) ja Cl lisamise mõjule CBD protsessis. Sb_2Se_3 omadustele ja päikesepatarei efektiivsusele. III artikkel uurib VTD sadestamisel D_{So-Sub} mõju argooni (Ar) keskkonnas Sb_2Se_3 kihi ja CdS/Sb_2Se_3 päikesepatarei omadustele, võrreldakse seadiseid, millel on kloorita või klooriga töödeldud CdS elektrontranspordikiht. Doktoritöö koosneb kolmest peatükist. Esimene peatükk annab põhjaliku ülevaate Sb_2Se_3 ja CdS materjali omadustest ning nende sadestusmeetoditest. Teine peatükk annab ülevaate CdS ja Sb_2Se_3 kilede ning seadmete sadestus- ja karakteriseerimismeetoditest, näiteks CSS, VTD, CBD ja termiline aurustamine ning röntgendifraktsioon (XRD), UV-Vis spektroskoopia, Halli mõõtmine, skaneeriv elektronspektroskoopia (SEM), sekundaar-ioonmassispektroskoopia (SIMS), Kelvini sond ja kompleksjuhtivusspektroskoopia (ingl *temperature-dependent admittance spectroscopy (TAS)*). Kolmandas peatükis on kolm põhiosa, mis kajastavad kolme teadusartikli olulisimaid tulemusi: esimeses osas uuritakse CdS elektrontranspordikihi järeltöötluse mõju õhukeste kilede omadustele ja CdS/Sb_2Se_3 päikesepatareide jõudlusele; teises osas vaadeldakse kloori lisamise mõju CdS õhukestele kiledele lähteaine lahuse modifitseerimise kaudu ja selle mõju CdS ja Sb_2Se_3 struktuurilistele ning

elektrilistele omadustele, samuti CdS-Sb_2Se_3 piirpinnale ja seadme jõudlusele; kolmandas osas keskendutakse Sb_2Se_3 absorberkihi optimeerimisele VTD meetodil, vaadeldes kristallikasvu kiirusi ja sadestamisparameetreid (struktuurides, millel on kas kloorita või klooriga töödeldud CdS elektrontranspordikiht), ning läbi defektianalüüsi kiles ja kilede piirpinnal paiknevate defektide mõju päikesepatareide jõudlusele.

Tulemused näitavad, et CdS kilede järeltöötlus temperatuuridel 200–400 °C vaakumis ja õhus põhjustas märkimisväärseid muutusi kile omadustes. Kuumutamine muutis CdS morfoloogiat peeneteralistest hajutatud kristalliteradest tihedateks paakunud kilestruktuurideks, vähendas keelutsooni laiust 2,43 eV-lt 2,35 eV-le ning langetas oluliselt elektronide tihedust ~10^{18} cm^{-3}-lt ~10^{11} cm^{-3} -le vaakumis töödeldud proovides ja ~10^{17} cm^{-3}-lt ~10^{10} cm^{-3} -le õhus töödeldud proovides. Need muutused tulenesid OH^- rühmade eemaldamisest järeltöötluste protsessis. Kuumutamine mõjutas ka Sb_2Se_3 absorberkihi morfoloogiat soodustades tihedamat kristallistruktuuri ja vertikaalsemat kristallikasvu, eriti 200 °C õhus kuumutatud CdS kihi korral. See kuumtöötlus andis parima seadme kasuteguri, saavutades 2,8% efektiivsuse, mis oli 60% parem kui töötlemata CdS kihiga seadistes. Kõrgemad kuumutamistemperatuurid, eriti õhus, põhjustasid oksiidide moodustumist ja jõudluse halvenemist.

Kloori mõju uurimine CdS kiledes, mille käigus lisati keemilisse vanni madalaid NH_4Cl kontsentratsioone (0–8 mM), näitas, et CdS kihi struktuursed ja morfoloogilised omadused jäid enamasti muutumatuks, kuid elektrilised omadused muutusid oluliselt: vabade laengukandjate kontsentratsioon vähenes järsult ja eritakistus kasvas 1 mM NH_4Cl lahuse juures. Keelutsooni laius vähenes ning SIMS analüüs kinnitas kloori lisandumist CdS kihti ja kaadmiumi difundeerumist Sb_2Se_3 absorberkihti. Seadmed, mis kasutasid 1 mM NH_4Cl lahusega töödeldud CdS kihti, andsid parima, 4,6% efektiivsuse, mis oli 20% parem kui töötlemata CdS kihiga seadmetel. Seda selgitati läbi piik-tüüpi (ingl *spike-like*) energiatsoonide joondumise, mis võimaldab efektiivset vabade laengukandjate transporti CdS-Sb_2Se_3 piirpinnal. Suuremad kloorikontsentratsioonid jällegi halvendavad seadiste jõudlust ja kvantefektiivsust (ingl *external quantum efficiency (EQE)*). Need tulemused rõhutavad kloori lisamise tasakaalu olulisust ja selle kriitilist rolli CdS/Sb_2Se_3 päikesepatareide kasuteguri optimeerimisel.

Sb_2Se_3 kasvu kiirust VTD meetodiga optimeeriti $D_{So\text{-}Sub}$ vahekauguse ja argooni (Ar) gaasi lisamise abil. Optimaalne $D_{So\text{-}Sub}$ oli 6 cm, mis kindlustas absorberkihi kasvu kiiruseks 0,4 µm/min ja mis parandas absorberkihi kristallstruktuuri kompaktsust ja ühtlust. Seadised, kus kasutati klooriga töödeldud CdS kihti ja optimeeritud Sb_2Se_3 absorberit, näitasid paremat jõudlust, saavutades kasuteguri 5%, mis on ~10% parem kui ilma kloorita töödeldud CdS kihiga seadistel. Struktuurianalüüsid parimal seadmel kinnitasid Sb_2Se_3 kristallikasvu paranemist [001] suunas ja morfoloogia paranemist. Lisaks näitas voolu-pinge pimekõverate temperatuursõltuvus madalamat lõksutihedust (~10^{14} cm^{-3}) ja vähenenud piirpinna rekombinatsiooni. Erinevatel pingetel mõõdetud TAS paljastas sügavate defektide olemasolu, mis võivad paikneda heterosiirde piirpinna vahetus läheduses. Leitud aktivatsioonienergiad 0,5 eV (klooriga töötlemata CdS päikesepatareides) ja 0,4 eV (klooriga töödeldud CdS päikesepatareides) valentstsoonimaksimumi suhtes jäävad vahemikku, mis vastavad kõige paremini V_{Sb} ja Sb_{Se} defektidele Sb_2Se_3-s.

Kokkuvõttes esitleb käesolev doktoritöö põhjalikku uurimust VTD meetodil valmistatud CdS/Sb_2Se_3 õhukesekileliste päikesepatareide arendamisest, tuues esile tugevat ristsõltuvust CdS elektrontranspordikihi valmistamise, CdS/Sb_2Se_3 heterosiirde piirpinna kujunemise ja Sb_2Se_3 absorberkihi kasvu dünaamika vahel. Süsteemsed uuringud CdS kihi järeltöötluse, kloori lisamise sadestuslahusesse ja Sb_2Se_3 kasvu

tingimuste optimeerimise kohta näitavad selgeid võimalusi kilede kvaliteedi, piirpinna omaduste ja seadmete jõudluse parandamiseks.

Töö uudsus seisneb CdS/Sb_2Se_3 heterosiirde mõistmise ja optimeerimise integreeritud lähenemises, mis ühendab protsessitehnika, defektide analüüsi ja heterosiirde karakteriseerimise iseloomustamise. Antud töös arendati uus meetod kloori lisamiseks keemilise vanni sadestamise kaudu, mis mõjutab oluliselt kaadmiumi difusiooni ja seadme kasutegurit. Esmakordselt tõendati SIMS analüüsiga kloori lisandumist CdS kristallivõresse ning Cd difusiooni Sb_2Se_3 absorberkihti ning vastastikuseid difusiooniprotsesse CdS/Sb_2Se_3 piirpinnal. See töö annab uusi teadmisi heterosiirde piirpinnaga seotud defektidest TAS-analüüsi kaudu ning esitleb optimeeritud VTD kasvuparameetreid, mis parandavad Sb_2Se_3 kile omadusi ja seeläbi seadme jõudlust. Doktoritöö tulemused on olulised õhukesekileliste Sb_2Se_3 päikesepatareide fundamentaalsel mõistmisel ja panustavad seadise tehnoloogia arendamisele.

Appendix 1

Publication I

S. Vadakkedath Gopi, N. Spalatu, M. Basnayaka, R. Krautmann, A. Katerski, R. Josepson, *et al*., "Post deposition annealing effect on properties of CdS films and its impact on CdS/Sb_2Se_3 solar cells performance," Frontiers in Energy Research, vol. 11, 2023, Art. no. 1162576, DOI: 10.3389/fenrg.2023.1162576.

frontiers | Frontiers in Energy Research

TYPE Original Research
PUBLISHED 10 May 2023
DOI 10.3389/fenrg.2023.1162576

Check for updates

OPEN ACCESS

EDITED BY
Kok-Keong Chong,
Tunku Abdul Rahman University, Malaysia

REVIEWED BY
Soonmin Ho,
INTI International University, Malaysia
Guangxing Liang,
Shenzhen University, China

*CORRESPONDENCE
Sajeesh Vadakkedath Gopi,
sajeesh.vadakkedath@taltech.ee
Nicolae Spalatu,
nicolae.spalatu@taltech.ee

RECEIVED 16 February 2023
ACCEPTED 28 April 2023
PUBLISHED 10 May 2023

CITATION
Vadakkedath Gopi S, Spalatu N, Basnayaka M, Krautmann R, Katerski A, Josepson R, Grzibovskis R, Vembris A, Krunks M and Oja Acik I (2023), Post deposition annealing effect on properties of CdS films and its impact on CdS/Sb_2Se_3 solar cells performance.
Front. Energy Res. 11:1162576.
doi: 10.3389/fenrg.2023.1162576

COPYRIGHT
© 2023 Vadakkedath Gopi, Spalatu, Basnayaka, Krautmann, Katerski, Josepson, Grzibovskis, Vembris, Krunks and Oja Acik. This is an open-access article distributed under the terms of the Creative Commons Attribution License (CC BY). The use, distribution or reproduction in other forums is permitted, provided the original author(s) and the copyright owner(s) are credited and that the original publication in this journal is cited, in accordance with accepted academic practice. No use, distribution or reproduction is permitted which does not comply with these terms.

Post deposition annealing effect on properties of CdS films and its impact on CdS/Sb_2Se_3 solar cells performance

Sajeesh Vadakkedath Gopi[1]*, Nicolae Spalatu[1]*, Madhawa Basnayaka[1], Robert Krautmann[1], Atanas Katerski[1], Raavo Josepson[2], Raitis Grzibovskis[3], Aivars Vembris[3], Malle Krunks[2] and Ilona Oja Acik[1]

[1]Department of Materials and Environmental Technology, Tallinn University of Technology, Tallinn, Estonia, [2]Division of Physics, Tallinn University of Technology, Tallinn, Estonia, [3]Institute of Solid State Physics, University of Latvia, Riga, Latvia

Antimony selenide (Sb_2Se_3) is one of the emerging photovoltaic absorber materials possessing abundance and non-toxicity as the main attributes. Following CdTe technology, CdS is a widely used partner layer for Sb_2Se_3 solar cells. Related to CdS/Sb_2Se_3 device configuration, a number of studies reported findings and challenges regarding the intermixing phenomenon at the main interface and suitability of various annealing for CdS (and related interface) and still, significant room remains in developing strategies for interface optimization and understanding of the physiochemistry behind. In this perspective, this work provides a systematic investigation of the effect of vacuum and air annealing at temperatures between 200 and 400°C on the properties of CdS deposited by chemical bath deposition and combined with Sb_2Se_3 absorber obtained by close-spaced sublimation the direct impact of the CdS annealing on the device performance is illustrated. It is found that by varying the annealing temperature from 200 to 400°C in both, vacuum and air ambient, the morphology of CdS changes from highly dispersed small grain structure to sintered dense grains, the band gap decreases from 2.43 to 2.35 eV and the electron density drops from ~10^{18} to ~10^{11} cm^{-3}. These changes were correlated with the changes in the CdS lattice and connected with the mobility of the OH group and the presence of secondary phases in CdS layers. 200°C air annealing of CdS was found as an optimal treatment resulting in 2.8% Sb_2Se_3/CdS cell efficiency - a 60% boost compared to the 1.8% performance of the device with as-deposited CdS. Material and device characterization analysis is performed, providing complementary insights on the interrelation between the physicochemical mechanism of the CdS annealing processes and device functionality.

KEYWORDS

antimony selenide, close-spaced sublimation, cadmium sulfide, post deposition annealing, thin film solar cells

1 Introduction

Thin film photovoltaic (PV) devices based on antimony selenide (Sb_2Se_3) absorber materials have attracted intensive research in recent years due to their rapid Photo conversion efficiency (PCE) progress. Besides being composed of Earth-abundant and non-toxic elements, Sb_2Se_3 has a suitable band gap energy between 1.1–1.3 eV (Li Z. et al., 2019; Tang et al., 2022) and high absorption coefficient of $>10^4$ cm^{-1} in the visible light region (Zhou et al., 2015). These excellent properties make Sb_2Se_3 a viable addition to copper indium gallium selenide [Cu (In, Ga)Se_2] and cadmium telluride (CdTe) solar cells, which have shown PCEs reaching 22% (Green et al., 2021), but for which the scarcity of constituent elements (In, Ga, and Te) is seen as a potential future constraint. The single-phase structure and relatively low melting point at 611°C have enabled the deposition of Sb_2Se_3 by physical vapor techniques, such as magnetron sputtering (Tang et al., 2019; Chen et al., 2022), close-spaced sublimation (CSS) (Hobson et al., 2020; Spalatu et al., 2021) and vapor transport deposition (VTD) (Wen et al., 2018). To date, almost all the record PCEs for Sb_2Se_3 PV devices, including the record 9.2% (Li Z. et al., 2019), have been achieved with CSS and VTD fabrication techniques (Krautmann et al., 2023). Since Sb_2Se_3 is composed of quasi-one-dimensional ribbons, the charge transfer across the absorber film is strongly dependent on which crystal direction the Sb_2Se_3 ribbons align (Chen et al., 2015). Given that Sb-Se atoms form covalent bonds within ribbons, but adjacent ribbons only bond via weak van der Waals' forces, vertical (and vertically-tilted) Sb_2Se_3 ribbons have been deemed optimal for efficient charge transport (Li K. et al., 2019; Hobson et al., 2020; Krautmann et al., 2021). Thus, substantial research efforts have been dedicated to the development of Sb_2Se_3 absorber films, to deliver suitable processing conditions for optimal grain morphology and orientation [*hkl, l = 1*] and for efficient Sb_2Se_3 solar cells (Kumar et al., 2021; Büttner et al., 2022; Campbell et al., 2022; Weiss et al., 2022). Another big focus in the development chain of Sb_2Se_3-based solar cells has been the identification of a suitable heterojunction partner layer to the Sb_2Se_3 absorber, where various buffer layers, e.g., cadmium sulfide (CdS) (Weiss et al., 2022), titanium dioxide (TiO_2) (Phillips et al., 2019), zinc oxide (ZnO) (Wang et al., 2017), cadmium selenide (CdSe) (Guo et al., 2019), tin oxide (SnO_2) (Zhou et al., 2020) have already been tested. Among these, PV devices based on CdS/Sb_2Se_3 heterojunctions stand out as most prolific, having produced some of the highest PCEs of 8.6% and 7.9% for substrate and superstrate configurations, respectively (Liu et al., 2021; Tang et al., 2022). The choice for CdS, is derived from the fact that this is one of the most established n-type heterojunction (HTJ) partner layers in more mature thin film solar cell technologies such as CIGS (Carron et al., 2019), CdTe (Potlog et al., 2011; 2012) and CZTS (Hernández-Calderón et al., 2020; Punathil et al., 2021). Like in the aforementioned solar cell technologies, CdS (~2.4 eV) buffer films for Sb_2Se_3 PV devices are mostly fabricated by a simple and cost-efficient chemical bath deposition (CBD) method. This is particularly the case for state-of-the-art substrate CdS/Sb_2Se_3 solar cells (Li et al., 2017; Tiwari et al., 2020; Fan et al., 2021; Tang et al., 2022). In CdS/Sb_2Se_3 PV devices with superstrate configuration, however, various fabrication techniques aside from the CBD method, like magnetron sputtering (Ou et al., 2019; Guo et al., 2020), thermal evaporation (TE) (Kumar et al., 2021) and metal-organic solution coating method (MOSC) (Leng et al., 2021), have been successfully deployed. Another interesting aspect that distinguishes superstrate devices from substrate devices is the common use of post-deposition treatments (PDTs) on the deposited CdS films prior to the Sb_2Se_3 absorber deposition. Whereas the CdS films in the substrate configuration devices are not often subjected to any PDTs, some groups have tried it and demonstrated it in previous reports (Wen et al., 2018; Ou et al., 2019; Guo et al., 2020; Kumar et al., 2021; Leng et al., 2021; Wang et al., 2022). For instance, superstrate CdS/Sb_2Se_3 solar cells, with record PCEs of 7.6% (Wen et al., 2018) and 7.9% (Liu et al., 2021), both applied a PDT on CBD-deposited CdS films that involved cadmium chloride ($CdCl_2$) treatment and a following air annealing step at 400°C. Another study demonstrated a PDT on CBD-CdS buffer films involving ammonia etching, which helped achieve a superstrate CdS/Sb_2Se_3 device with a PCE of 7.5% (Wang et al., 2022). Reports of superstrate CdS/Sb_2Se_3 solar cells with PCEs of 5.9% (Leng et al., 2021) and 7.4% (Guo et al., 2020) applied air annealing on MOSC-made and sputtered CdS films, respectively. These studies with varying PDT approaches highlight the lack of understanding of the underlying physiochemical processes and optoelectronic properties that decide the quality of the CdS/Sb_2Se_3 HTJ. An additional issue which needs to be addressed in the scientific community is the need and role of oxygen in the PDT process of CdS and its impact on the CdS/Sb_2Se_3 hetero-interface formation and solar cell performance. The question stands for whether the presence of oxygen (air) in the PDT is needed or not, and if required, then what would be the optimal temperature of annealing. A number of recent studies reported that higher annealing temperatures (400°C–450°C) in air, combined with $CdCl_2$ treatment are beneficial for the formation of CdS/Sb_2Se_3 interface and solar cell PCEs. Whereas Tang's group concluded that during the PDT at 400°C in air, Cl^- traces from $CdCl_2$ treatment passivated surface defects on CdS grains, which was attributed to improved performance (Wang et al., 2015), another report (Spalatu et al., 2017) showed that cadmium oxychloride (CdO·$CdCl_2$) and cadmium hydroxide [Cd $(OH)_2$] residuals (Graf et al., 2015) resulting from $CdCl_2$ treatment impair the quality of the CdS/Sb_2Se_3 HTJ as well as the growth of the Sb_2Se_3 absorber. Until now, many factors that could affect CdS/Sb_2Se_3 HTJ include lattice mismatch, elemental diffusion, parasitic absorption, conduction band offset (CBO), and a large number of interface defects between CdS and Sb_2Se_3 have been mentioned. (Ou et al., 2019; Guo et al., 2020; Wang et al., 2022).

Considering the above aspects, the present study offers a systematic investigation into post-deposition treatments conducted on chemically deposited CdS films at various temperatures and in different atmospheres to identify conditions, which are optimal for subsequent Sb_2Se_3 growth and high-quality CdS/Sb_2Se_3 interface. With that, we reveal a novel post-deposition treatment approach for CdS buffer layers employed in superstrate CdS/Sb_2Se_3 solar cells. The physicochemical processes responsible for the changes in the CdS properties with respect to various annealing conditions are described and correlated with Sb_2Se_3 absorber growth, interface intermixing, and device performance. The results provide complementary knowledge on understanding the challenges and perspectives of the CdS/Sb_2Se_3 device.

2 Experimental

2.1 Fabrication of CBD CdS films and post-deposition annealing

CdS films were prepared on glass and glass/FTO (25 × 25 mm^2) substrates using the chemical bath deposition (CBD) technique. The substrates were cleaned by immersing them in a standard cleaning solution containing potassium dichromate, water, and sulfuric acid for half an hour to remove impurities from the surfaces, later they were boiled in distilled water followed by drying in hot air flow. The deposition was carried out on a closed jar containing $CdSO_4$ (1 mM), $(NH_4)_2SO_4$ (0.7 M), NH_4Cl (0.1 μM), NH_4OH (30 mM), and thiourea (10 mM) dissolved in de-ionized (DI) water at 85°C and 500 rpm. The deposition was carried out for 5 min to achieve the desired thickness of 60 nm. After the film deposition, the substrates were ultrasonicated in distilled water with a few drops of tri-ethanolamine (TEA). Then the films were rinsed with DI water and dried in airflow. These films are then annealed in a vacuum at 120°C for 15 min to remove impurities such as water, hydroxides, and organic compounds which may have stayed on the films. The resulting films are called "as deposited" CdS films and then they are divided into two batches. One batch is annealed in air and the other one in a vacuum at different temperatures (200, 250, 300, 350, and 400°C). The air annealing was carried out in a single-zone quartz tube furnace. The samples were loaded into the preheated quartz tube at the desired temperature and then kept there for 30 min. The samples were removed from the tube immediately after the annealing time for rapid cooling. The vacuum annealing was also carried out in the single-zone quartz tube furnace. The samples are loaded into the quartz tube at room temperature, then evacuated using a rotary pump up to ~10^{-5} mbar pressure. The quartz tube is placed in a single-zone furnace and the temperature was ramped to the set value. Once the temperature reaches the set value it is maintained for 30 min. After the annealing time, the samples are allowed to cool down gradually to room temperature while keeping the vacuum. Once it reaches room temperature the vacuum is released and the samples were taken out. The samples with glass/CdS samples are used for the CdS film characterization and the samples with glass/FTO/CdS samples were used for Sb_2Se_3 absorber deposition to study the growth of Sb_2Se_3 on different CdS films and for cell fabrication.

2.2 Fabrication of CdS/Sb_2Se_3 solar cell

The vacuum and air-annealed glass/FTO/CdS samples were used for the device preparation. The absorber Sb_2Se_3 was deposited using a close-spaced sublimation technique. Sb_2Se_3 granules of 5 N purity (Sigma—Aldrich) were used as source material and the substrate is kept at a 4 cm distance from the source material. The source material is kept at 490°C and the substrate at 460°C temperature during the deposition to maintain a deposition rate of 1 μm/min. A thickness of ~1.5 μm was optimized and then it was deposited on all the annealed buffer layers to study the effect of CdS annealing on the growth of the Sb_2Se_3 absorber. The superstrate configuration solar cell with glass/FTO/CdS/Sb_2Se_3/Au finished with deposition of Au thin film using the thermal evaporation method. Indium pads are used on Au and FTO layers to make a connection for the device performance measurements.

2.3 Characterization of thin films and solar cells

Structural properties of the CdS and Sb_2Se_3 films were characterized by X–ray diffraction spectra (XRD) with Rigaku Ultima IV system using monochromator Cu Kα radiation (λ = 1.54 Å, 40 kV, 40 mA) equipped with D/teX Ultra silicon line detector in the 2θ (Bragg-Brento) regime using a 2θ step of 0.04°, a counting time 2–10 s/step with sample rotation. The XRD patterns of the samples were compared with JCPDS 01-089-0440 and 01-074-9665 (for CdS) and JCPDS 15-0861 (for Sb_2Se_3). Top-view and cross-sectional images of films were made by Zeiss EVO-MA15 scanning electron microscope (SEM) equipped with a Zeiss HR FESEM Ultra 55 system. The electrical properties such as carrier concentration, mobility, and resistivity of CdS films were measured at room temperature using Hall and van der Pauw controller H-50. The band gap of the films was calculated from UV-VIS spectroscopy (Jasco V-670 in 200–2,500 nm wavelength range) using the Tauc plot. The crystal growth and morphology of Sb_2Se_3 thin films on CdS films were also characterized by XRD and SEM analysis.

The device performance of the cell was analyzed from the J-V curve [AUTOLAB PGSTAT 30 and Oriel class A solar simulator 91159 A (100 mW cm^{-2}, AM1.5)] measured at room temperature. The external quantum efficiency (EQE) was also measured for solar cells using a light source (Newport 300 W Xenon lamp, 69911), monochromator (Newport Cornerstone 260) detector (Merlin), calibrated Si reference detector combination in 300–1,000 nm wavelength range.

Temperature-dependent J-V characteristics under 100 mWcm^{-2} condition of CdS/Sb_2Se_3 solar cells were measured with KEITHLEY 2400 Source Meter, where the temperature in Janis closed cycle He cryostat was varied from 20 K to 320 K with a step of ΔT = 20 K. The ionization energies of the CBD CdS and CSS Sb_2Se_3 layers were determined by the photoelectron emission spectroscopy method, by measuring the dependence of photoelectron emission current on the photon energy.

3 Results and discussion

3.1 Structure and morphology of CBD CdS films depending on the post-deposition annealing conditions

As a first step, we investigated the impact of temperature and annealing ambient conditions on the structural properties of a CdS single layer deposited onto glass substrates by XRD analysis. Figures 1A, B shows the XRD patterns of CdS films annealed at 200°C–400°C in a vacuum and in air, for 30 min. The XRD patterns are compared with standard data (ICDD: 01-089-0440 and 01-074-9665) (Graf et al., 2015). The diffractograms of CdS samples annealed in air at 200°C–400°C show 100, 101, 110, 103, and 004 diffraction peaks corresponding to CdS crystal structure. However, the XRD pattern

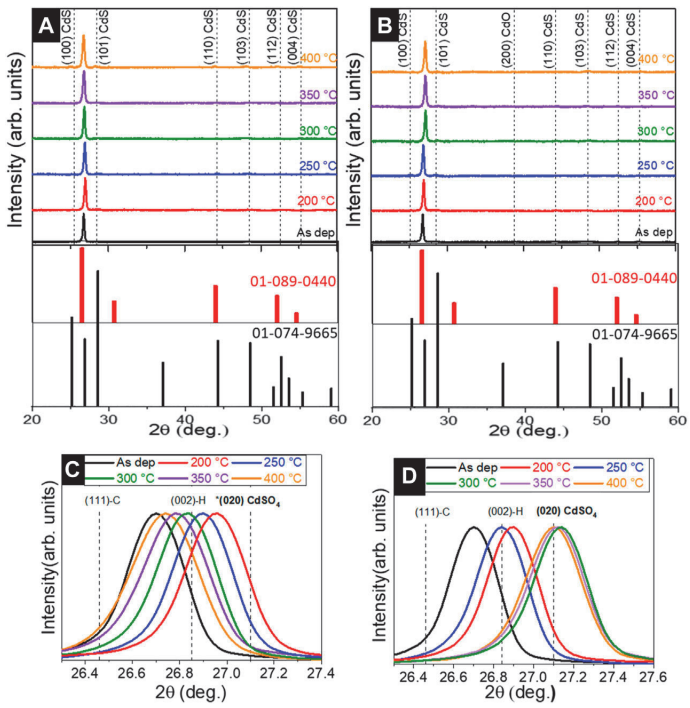

FIGURE 1
XRD pattern of **(A)** vacuum annealed and **(B)** air annealed CdS films, at 200°C–400°C temperatures for 30 min; displacement of dominant XRD peak depending on the **(C)** vacuum and **(D)** air annealing conditions.

of 400°C annealed samples displayed a 200 peak corresponding to the CdO phase (00-005-0640). The appearance of such a phase in the XRD patterns indicates oxidation of the CdS layer. On the other hand, the diffractogram of vacuum-annealed samples shows the presence of CdS phase, without any secondary phases, regardless of annealing temperature. To gain a deeper understanding of the impact of the annealing conditions on structural changes in CBD CdS layers, we further analyzed the XRD patterns (in Figures 1C, D) in the 2- theta region of 26°–27° at higher resolution. In this 2-theta region, the main 111 peak is located and has been attributed as belonging to both cubic and hexagonal modifications in the literature (Maticiuc et al., 2014; 2015). If we analyze the evolution of the 111 XRD peak for vacuum and air-annealed samples separately (Figures 1C, D) with the increase in temperature, it can be observed that there is a clear difference in the peak shift behavior in both cases. In the case of the vacuum annealed samples when the annealing was performed at 200°C there is a large shift of 111 peak towards higher 2-theta values (~27°) compared to the as-deposited CdS. As the annealing temperature was increased from 200°C to 400°C, the 111 peak shifted systematically towards lower 2-theta values and at 400°C annealing vacuum annealing reached the 2-theta position close to the as-deposited sample. In contrast, for the air-annealed samples, as the annealing temperature increases, the 111 peak shifts towards higher 2-theta values compared to the as-deposited samples. At 300, 350, and 400°C annealing temperatures, the peak position shifts close 020 peak corresponding to the $CdSO_4$ phase (ICDD: 00-014-0352) indicating there might be the possibility for other secondary phases at the higher air annealing temperature. However, in the XRD pattern (Figure 1B) no other peaks related to $CdSO_4$ were detected except the presence of CdO in 400°C air annealed CdS layers. It should be noted that the shift of 111 peak position was accompanied by the variation of the lattice parameter. (Figure 2A). The lattice parameter decreases with the increase of both vacuum and air annealing temperature.

The above observations related to the shift of the main XRD peak (corresponding changes in the lattice parameter), and appearance of oxide phases can be correlated considering the following aspects. First, the appearance of the CdO phase at higher annealing temperature (Figure 1B) has been observed previously in (Maticiuc et al., 2015) and explained by the decomposition of $CdSO_3$ which is usually formed in the CdS lattice when reacting with oxygen in the air (Kylner, 1999; Maticiuc et al., 2014). The shifting of the main peak as a result of vacuum annealing can be related to the decomposition of Cd $(OH)_2$ which naturally crystallized in the lattice during the deposition process of the CdS film. The presence of Cd $(OH)_2$ in the CdS lattice is also the main reason for the variation of lattice

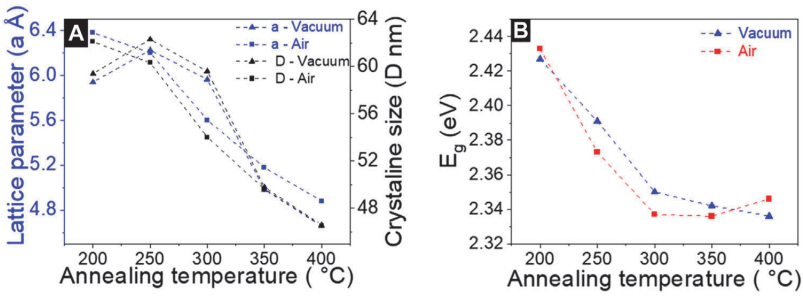

FIGURE 2
(A) variation of lattice parameter **(A)** and crystalline size (D) depending on the vacuum and air annealing temperatures. **(B)** variation in the bandgap of CdS films with vacuum and air annealing temperature.

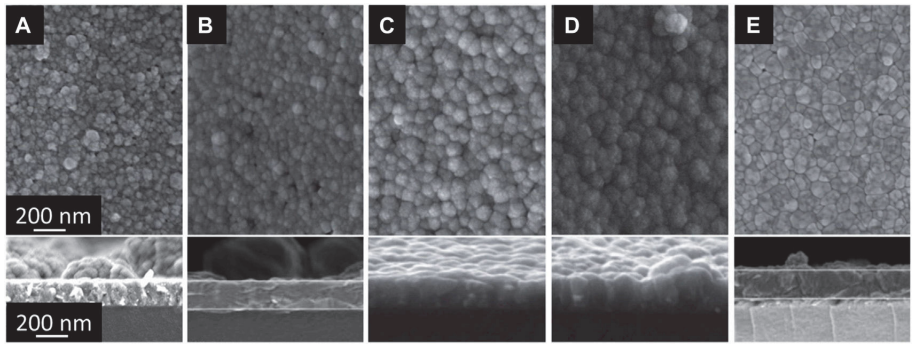

FIGURE 3
Surface and cross-section SEM images of CdS films deposited on glass substrates: **(A)** as deposited, **(B)** annealed in vacuum at 200°C, **(C)** annealed in air at 200°C, **(D)** annealed in vacuum at 400°C, **(E)** annealed in air at 400°C with an annealing duration of 30 min.

(correspondingly shift of the main XRD peak) between the hexagonal and cubic structures. The increase in the annealing temperature generates the dissociation of Cd $(OH)_2$ into CdO and water, and promotes the changes in the lattice parameters (Figure 3A). The reduction of lattice constants in both air and vacuum annealing conditions can be also explained due to mobility of $(OH)_s$ groups in the CdS lattice. A good indication of this effect is the decreasing of crystallite size as the temperature of vacuum and air annealing increased from 200°C to 400°C (Figure 2A). Although such a trend in the crystallite size with annealing temperature is an unexpected trend, the out-diffusion of OH impurity has such impact on the CdS lattice as explained in (Maticiuc et al., 2017). On the other hand, in the case of air-annealed samples, the position of the main XRD peak at 27.15° is very close to the 2-theta value of 020 diffraction peak position corresponding to the $CdSO_4$ phase. The overall presence of phase mixture in CdS can play important role in the optoelectronic properties of CdS and related CdS/Sb_2Se_3 solar cell performance.

The morphology of as-deposited and annealed CdS films was also investigated by SEM. Figure 3 shows the surface and cross-section SEM images of CdS films deposited on glass substrates. As deposited CdS layer (Figure 3A) has small grains with some particles agglomerated in clusters. Vacuum annealing at 200°C did not change the grain size and overall morphology of the layers (Figure 3B). However, the same annealing temperature in the air leads to more uniform grain size distribution (Figure 3C). While vacuum annealing at 400°C lead to the similar morphology observed for the 200°C air annealing (Figure 3D), the same annealing at 400°C in the air lead to the more densely packed grains in the films (Figure 3E). The latest observation indicates that 400°C air annealing generates conditions for re-crystallization and sintering of the CdS films.

Since the CdS is deposited on FTO for the solar cell fabrication, the morphology of the CdS deposited on FTO substrates was also analyzed (Figure 4). As can be seen in Figures 4A, B, both, as deposited and 200°C vacuum annealed CdS films grown on FTO exhibit similar morphology with CdS deposited on glass. In this case,

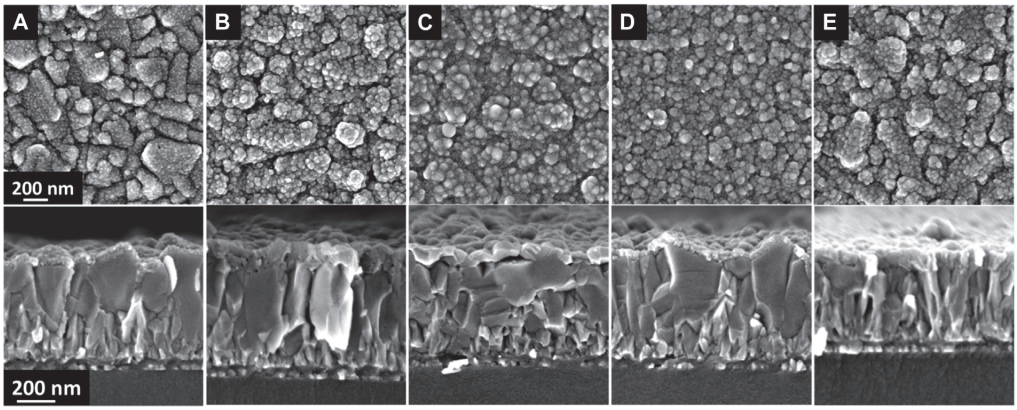

FIGURE 4
Surface and cross-section SEM images of CdS films deposited on FTO/glass substrates: **(A)** as deposited, **(B)** annealed in vacuum at 200°C, **(C)** annealed in air at 200°C, **(D)** annealed in vacuum at 400°C, **(E)** annealed in air at 400°C with an annealing duration of 30 min.

the porous layers comprising small grains and some grain conglomerates cover uniformly the relatively large FTO grains. Air annealing at 200°C and 400°C and as well as vacuum annealing at 400°C lead to significant densification of the CdS film (Figures 4C–E).

3.2 Impact of annealing conditions on CdS optoelectronic properties

The above results on the changes of structural and morphological properties of CdS films with annealing conditions will impact the optoelectronic properties of these layers and consequently will affect the solar cell performance. Thus, as a further step, a detailed analysis of changes in the electrical properties of the CdS layer depending on the annealing was performed.

Table 1 shows the variation of electrical properties (carrier concentration, mobility, and resistivity) of CdS films deposited on a glass substrate after post-deposition air and vacuum annealing at 200°C–400°C for 30 min. As deposited CdS films showed n-type conductivity with 4.4×10^{15} cm^{-3} carrier concentration, 5 cm^2/Vs. mobility, and 2.8×10^2 Ω cm resistivity. All the films maintain the same conductivity type independent of the annealing conditions. For both air and vacuum annealing conditions, the variation of electrical parameters in Table 1 can be divided into three distinct regions: i) 200°C–250°C annealing in which the resistivity decreases from 4.2 to 2.6 Ω cm and from 3.2 to 0.2 Ω cm while the electron concentration increases by one order magnitude, from 10^{17} to 10^{18} cm^{-3} and 10^{18} to 10^{19} cm^{-3} for air and vacuum annealing, respectively; ii) 300°C annealing where resistivity increases to 45 and 8.5 Ω cm while the electron concentration decreases by one order of magnitude, from 10^{18} to 10^{17} cm^{-3} and from 10^{19} to 10^{18} cm^{-3} for air and vacuum annealing, respectively; iii) 350°C–400°C annealing where the resistivity increases from 7.7×10^3 to 4.2×10^4 Ω cm and 4.6×10^1 to 1×10^4 Ω cm while the electron density reduces drastically by three and seven orders of magnitude for air and vacuum annealing, respectively. A similar trend in the electron concentration with the variation of air annealing temperature has been observed by Maticiuc et al. (Maticiuc et al., 2014) and correlated with the mobility of the hydroxide group (OH) in the CdS lattice. It has been proposed that the OH incorporated in the lattice of CdS, acting as a shallow donor (Varley and Lordi, 2013). At low annealing temperatures (200°C), the OH groups are quite unstable and decomposes by releasing water and generating sulfur vacancies (V_S). It is well established that the sulfur vacancies (V_S^{2+}) act as a donor defect and an increase in their concentration can explain the abrupt increase in electron density. The high annealing temperatures (350°C and 400°C) induces conditions for excessive removal of OH from the CdS lattice, which results in the reduction of electron density. Although such mechanism was described for hydrogen and air-annealed CdS layers, it is also valid for vacuum annealing in this study. In addition to this mechanism, specifically for air annealing at 400°C, the presence of CdO secondary phases (as detected from XRD in Figure 1B) in CdS could be responsible for the significant drop in electron concentration to ~10^{10} cm^{-3}. The low values of mobilities at 200°C–300°C annealing temperature can be explained by the scattering of carriers with ionized impurities in the lattice. At higher air and vacuum annealing temperatures (350°C and 400°C) these impurities are removed from the lattice which leads to higher values of mobility(Spalatu et al., 2019).

The band gap of CdS films deposited on glass substrates was determined from a Tauc plot based on the UV—VIS measurements and the effect of annealing temperature and conditions on the bandgap values were analyzed thoroughly. As deposited CdS, films exhibit a band gap value of ~2.42 eV. As the annealing temperature (200°C–400°C) in both air and vacuum increased a clear trend of band gap decrease was observed (Figure 2B). While for vacuum annealing this effect can be explained due to the

TABLE 1 Electrical properties of CdS films annealed at different annealing temperatures in air and vacuum.

Annealing temperature (°C)	Air			Vacuum		
	Carrier concentration (cm^{-3})	Mobility (cm^2/Vs)	Resistivity (Ω cm)	Carrier concentration (/cm^3)	Mobility (cm^2/Vs)	Resistivity (Ω cm)
No annealing	4.4×10^{15}	5	2.8×10^{2}	4.4×10^{15}	5	2.8×10^{2}
200	6.3×10^{17}	3.1	4.2	1.7×10^{18}	1.2	3.2
250	3×10^{18}	3.3	2.6	1.4×10^{19}	2.2	2×10^{-1}
300	2.1×10^{17}	0.7	4.5×10^{1}	8.5×10^{17}	0.9	8.5
350	1.6×10^{13}	6.1	7.7×10^{3}	1.2×10^{18}	1.0	4.6×10^{1}
400	1.2×10^{10}	12	4.2×10^{4}	5×10^{11}	13	1×10^{4}

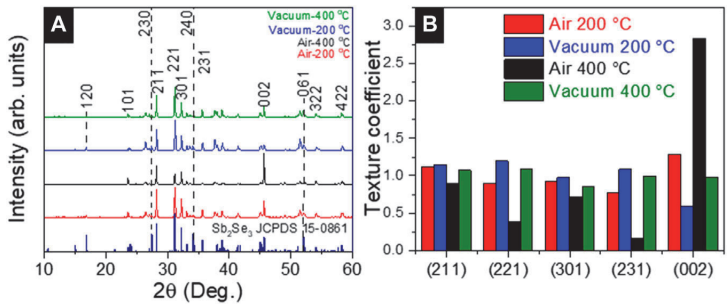

FIGURE 5
(A) XRD spectrum and **(B)** texture coefficient of Sb_2Se_3 on CdS annealed in vacuum and air at 200°C and 400°C.

decomposition of Cd $(OH)_2$ to CdO and water (Maticiuc et al., 2014), in air annealing the presence of CdO (as detected by XRD) narrows the band gap (Dakhel, 2010).

3.3 Structure and morphology of Sb_2Se_3 films deposited on annealed CdS layer

As a step towards the fabrication of a solar cell device, Sb_2Se_3 absorber films were deposited on a glass/FTO/CdS stack and the impact of the CdS air and vacuum annealing on structure and morphology of Sb_2Se_3 films was analyzed.

Figures 5A, B shows the XRD patterns and texture coefficients of Sb_2Se_3 films grown on as-deposited, 200°C and 400°C air annealed, and 200, 400°C vacuum annealed CdS samples. Texture coeficients were performed according to (Krautmann et al., 2021). Diffraction peaks at 28.2°, 31.1°, 32.2°, 45.1°, and 45.6° were detected and comparing the patterns with standard data (JCPDS 15-0861) in both annealing conditions, it belongs to 211, 221, 301, 151, and 002 planes of orthorhombic Sb_2Se_3 crystal structure (Krautmann et al., 2021). In the Sb_2Se_3 films deposited on air-annealed CdS films, the grains grow predominantly along the (002) plane. The intensity of the (002) peak is dominant over the others, especially being highlighted for Sb_2Se_3 grown on 400°C air annealed CdS. Meanwhile, the Sb_2Se_3 grown on the vacuum annealed samples always exhibit 221 orientation. These results indicate that the Sb_2Se_3 tends to grow more vertically on the air-annealed CdS film compared to the vacuum-annealed CdS samples. Generally, there is no clear evidence for a preferential orientation in any of the Sb_2Se_3 samples. Although the intensity of 221 reflection is slightly higher for the Sb_2Se_3 absorber grown onto 400°C vacuum annealed CdS, it can be concluded that the samples are randomly oriented.

One possible explanation for the 002 highlighted Sb_2Se_3 grain orientation deposited on 400°C air-annealed CdS might be related to the more compact grain morphology of CdS. As shown by SEM (Figure 3) these films with large sintered grains and higher surface energy can provide different nucleation sites favorable for the growth of Sb_2Se_3 in this direction. At the same time, oxidation of the layer (detection of CdO from XRD, Figure 1B) could also contribute to this effect, however, there is no direct proof for this hypothesis and specific investigation is required.

From a structural, optical, and morphological analysis of CdS, it was found that higher temperature (300°C–400°C) vacuum annealed CdS films have pin holes and lower band gap meanwhile in air annealed CdS films presence of impurities like CdO was detected in the film. Based on these findings a set of glass/FTO/CdS/Sb_2Se_3 heterostructures were analyzed by SEM. Figure 6 shows the surface

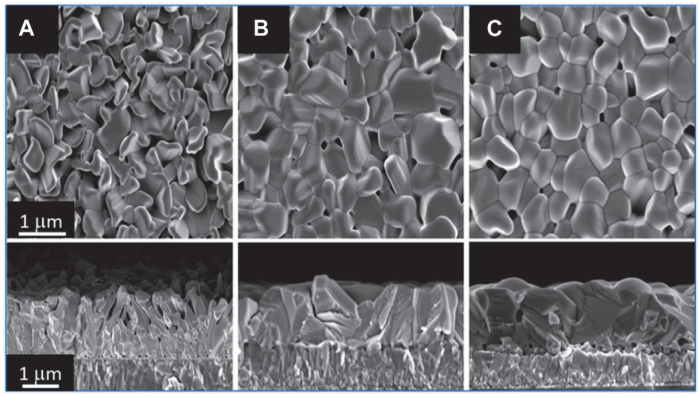

FIGURE 6
SEM images of superstrate configuration glass/FTO/CdS/Sb_2Se_3 stack with CSS Sb_2Se_3 absorber layer deposited at 460°C: **(A)** top-and cross-sectional view of absorber film deposited onto as deposited CdS, **(B)** top-and cross-sectional view of absorber deposited onto vacuum annealed CdS at 200°C and **(C)** top-and cross-sectional view onto air annealed CdS at 200°C.

and cross-section SEM images of CdS/Sb_2Se_3 with as-deposited, vacuum, and air annealed at 200°C CdS films. It can be seen that the absorber grown on as-deposited CdS (Figure 6A) exhibit more irregularly shaped grains with sharp edges and higher inner porosity compared to the Sb_2Se_3 films grown on annealed CdS. The absorber deposited on 200°C vacuum annealed CdS has larger, compact, and well-packed grains (Figure 6B). Air-annealed CdS at 200°C resulted in a similar well-packed absorber morphology with a more homogeneous distribution of grain shape and size. It is important to mention that the absorber deposited on both, 400°C vacuum and air-annealed CdS, displays similar morphology as seen in Figure 6C Overall the results of SEM analysis for the absorber are in good correlation with the above SEM and XRD results of CdS films. Thus, the reason for the higher inner porosity of the absorber in Figure 6A is related to the high concentration of organic residues in as-deposited CdS films. In this case, the subsequent CSS Sb_2Se_3 deposition process acts as an annealing process for the CdS films, resulting in the out-diffusion of organic residues from the films and making the absorber film porous and pinhole rich. On the other hand, in the annealed CdS films these residues are already removed from the CdS leading to more stable films which help the absorber to grow in a more pinhole-free compact manner.

3.4 Impact of the CdS annealing on the device performance

The solar cells were fabricated following the superstrate configuration of glass/FTO/CdS/Sb_2Se_3/Au and the impact of the CdS annealing conditions on the PV parameters was analyzed. The PV parameters of the devices were extracted from the J–V curve measurements (Figure 8A representative curves under illumination) and the average values are presented in Figure 7. The analysis shows that the solar cells with as-deposited CdS exhibit the lowest PCE, whereas the devices with 200°C vacuum and air-annealed CdS buffer layer, there is a clear improvement in all the PV parameters (V_{OC}, J_{SC}, FF, and PCE). Nevertheless, all the PV parameters decreased for the cells with CdS annealed in both, vacuum and air at T ≥ 250°C. So far, comparing the performance of all the devices in Figure 7, it is clear that annealing of CdS at 200°C in both vacuum and air resulted in the best solar cells PCE, with the top performance of 2.8% (V_{OC} of 350 mV, J_{SC} of 18.3 mA/cm^2 and fill factor of 43%) achieved for the cells processed with 200°C air annealed CdS (Table 2). The same best cell shows the highest EQE response in the short-wavelength region, 300–700 nm (Figure 8B). In caparison with the best cell, the EQE response in the 300–700 nm region is significantly reduced for the devices with as-deposited and 200°C vacuum annealed CdS. The reduced EQE response in the short-wavelength region has been previously observed for Sb_2Se_3/CdS (Phillips et al., 2019; Spalatu et al., 2021) and for CdTe/CdS devices (Potlog et al., 2012; Maticiuc et al., 2015; Spalatu et al., 2015) and explained by intermixing between CdS and Sb_2Se_3 (or CdTe) absorbers with the formation of $CdS_{1-x}Se_x$ (or $CdTe_{1-x}S_x$) solid alloy at the main interface. In the case of Sb_2Se_3 devices with as-deposited and 200°C vacuum annealed CdS this intermixing seems to be very pronounced resulting in low EQE response at 300–700 nm region. For the device with as-deposited CdS, this effect can be related to the morphology of CdS film, containing small grains (Figures 3A, 4A) with high surface energy, which are active for interdiffusion by mass transport through the gas phase, and resulting in a high degree of alloy formation at the interface during Sb_2Se_3 absorber deposition at 450°C. In addition to this effect, the presence of organic residuals (Graf et al., 2015; Maticiuc et al., 2015; Koltsov et al., 2022) and the presence of large segregates on the surface of as-deposited CdS can significantly alter the formation of the heterojunction interface resulting in reduced EQE and modest PCE of the corresponding solar cell (Figures 8A, B). On another hand, for the device with 200°C vacuum annealed CdS the improved EQE response (Figure 8B) and PCE (Figure 8A) (compared with as-deposited CdS-based cells) indicate the formation of better CdS-Sb_2Se_3 interface which can be

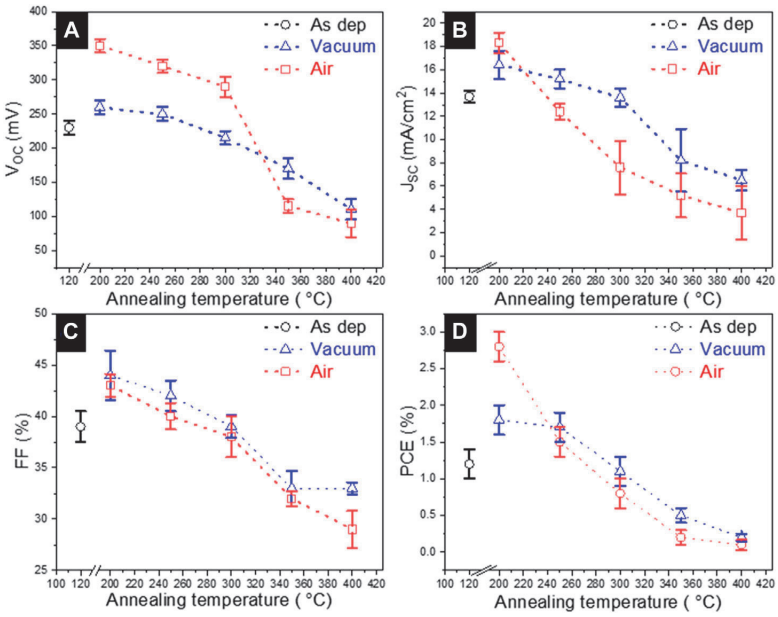

FIGURE 7
Main photovoltaic parameters including **(A)** open circuit voltage (V_{OC}), **(B)** short circuit current density (J_{SC}), **(C)** fill factor (FF), and **(D)** photoconversion efficiency (PCE) with average values (marked as hollow squares) measured for Sb_2S_3 devices with Sb_2S_3absorber deposited at substrate temperatures in the range of 240°C–400°C.

connected with the removal of the organic residuals from CdS as a result of vacuum annealing, leading to better absorber morphology and better-quality interface. Finally, 200°C air annealing of CdS films resulted in the best EQE response and maximum device performance implying that intermixing in the corresponding cell has the lowest extent. For the same best device, the energy-band diagram with the band alignment was drawn (Figure 8E) based on photoelectron emission spectroscopy. The ionization potential (I_p) of the Sb_2Se_3 and CdS layers was determined through the extrapolation of the linear fit from valence band edge photoemission to 0 eV. An example of fitting for the absorber is presented in Figure 8C, obtaining an I_p value of 5.42 ± 0.02 eV, in good correlation with the values reported in the literature (Hobson et al., 2020). Further analysis of the band diagram shows that the conduction band minima of CdS lie above the conduction band minima of Sb_2Se_3, forming a spike-like band offset (~0.2 eV) at the main interface. This spike-like band offset could act as a potential barrier for the electron flow which reduces the J_{SC} of the device (Shiel et al., 2020). Furthermore, the linear extrapolation fit to 0 K in the V_{OC}–T plot provides an activation energy of 0.98 ± 0.01 eV (Figure 8D), which is lower than the band gap of the absorber (~1.2 eV). This implies that the rate of the recombination processes at the main interface is high, which reduces the PV parameters of the solar cell device. There are several recent reports in which the recombination of the carriers was suppressed by different techniques such as the introduction of Al^{3+} cations in the CdS buffer layer (Luo et al., 2023), heterojunction annealing (Tang et al., 2022), and effective antimony selenide crystal engineering (Tang et al., 2022).

So far the best PCE of 2.8% in this study was obtained for the device processed with CdS annealed at 200°C. The obtained result is significant from one side, considering a 60% boost in PCE compared to the cell fabricated with as-deposited CdS (1.8%). With this achievement, we also demonstrated that annealing in air at a relatively low temperature can be a suitable PDT to improve the properties of CdS films and the efficiency of the related device. On another side, putting in the context of other reports, these results could provide some more debates as several reports on similar device configurations suggested that an annealing step at temperatures ≥400°C and in the presence of air and $CdCl_2$ treatment is a requirement for CdS to achieve PCE between 5%–7% (Wang et al., 2015; Li et al., 2018; Azam et al., 2022; Cai et al., 2022). Application of high air annealing temperature (400°C) in this study and attempts to perform post-deposition $CdCl_2$ treatment of CdS films in our previous investigation (Spalatu et al., 2021) show that the oxide phases (and oxy-chloride residuals) which inevitably are formed at the surface CdS have a detrimental impact on the formation of good quality heterojunction interface and can significantly decrease the device performance. In addition, most of the studies that report a reasonable 5%–7% PCE for CdS/Sb_2Se_3 devices use thermal evaporation (TE) for deposition of the Sb_2Se_3 absorber (Liu et al., 2014; Kumar et al., 2019). Better control of the intermixing between CdS and Sb_2Se_3 may lead to better interfaces and higher PCE cells. Compared to TE, CSS employed in this study, clearly provide the advantage of the rapid process and high-quality absorber, however, the

TABLE 2 Photovoltaic parameters of the best performing CdS/Sb_2Se_3 solar cells with as-deposited, vacuum and air annealed at 200°C, CdS films.

No	CdS annealing condition	Photovoltaic parameters			
		V_{OC} (mV)	J_{SC} (mA/cm^2)	FF (%)	PCE (%)
1	As deposited	230	13.7	39	1.2
2	Vacuum 200°C	260	16.4	44	1.8
3	Air 200°C	350	18.3	43	2.8

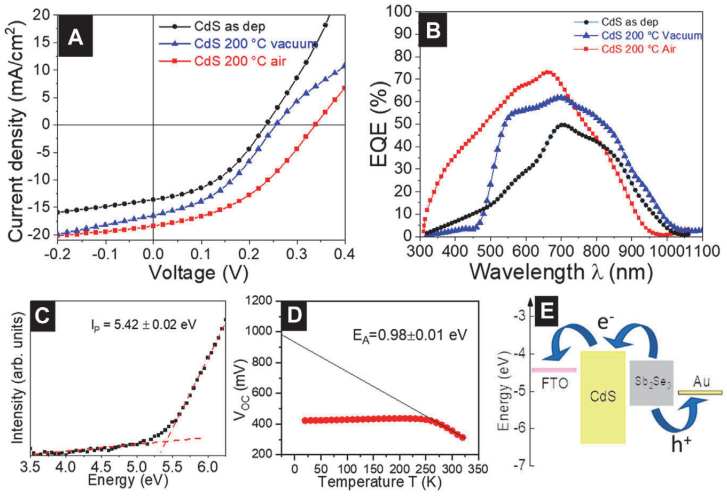

FIGURE 8
(A) J-V characteristics and **(B)** EQE of CdS/Sb_2Se_3 solar cells with as deposited, air and vacuum annealed CdS at 200°C, **(C)** Ionization potential of Sb_2Se_3 **(D)** activation energy calculated from V_{OC}–T plot, **(E)** band alignment of FTO/CdS/Sb_2Se_3/Au solar cell structure.

peculiarity of CSS with very close proximity between substrate and source (which implies high supersaturation of the vapor stream close to the substrate) can be a limitation for some device configuration which involve high reactivity of the underlayer components such as CdS. A prospective approach to overcome this challenge could be the implementation of various interfacial nanoscale layers such as TiO_2 (the feasibility of CSS being well proven for Sb_2Se_3/TiO_2 device configuration), which from one side, would imply more efforts for the interface engineering, and from a wider perspective, identification of other alternative partner layers with suitable band offsets for the emerging Sb_2Se_3 device.

4 Conclusion

In this study, we investigated the influence of air and vacuum annealing on the properties of CBD-deposited CdS films and find out the impact of these annealing conditions on the performance of CdS/Sb_2Se_3 solar cells. It was found that the increase of the annealing temperature from 200 to 400°C in both, vacuum and air ambient, changed the morphology of CdS from highly dispersed small grain structure to sintered dense grains, decreased the band gap from 2.43 to 2.35 eV and dropped the electron density from ~10^{18} to ~10^{11} cm^{-3}. The changes in the properties of annealed CdS films were explained via the mechanism of the OH group in the lattice as well as the presence of secondary phases. The annealing conditions of CdS layers significantly impact the structural and morphological properties of the Sb_2Se_3 absorber. While the Sb_2Se_3 absorber grown on as-deposited CdS exhibited irregularly shaped grains with sharp edges and higher inner porosity, the absorber layers deposited on 200°C and 400°C vacuum annealed CdS have larger, compact, and well-packed grains. XRD analysis showed that Sb_2Se_3 tends to grow more vertically on the air-annealed CdS film compared to the vacuum-annealed CdS samples. 200°C air annealing of CdS was found as an optimal treatment resulting in 2.8% Sb_2Se_3/CdS cell PCE—a 60% boost compared to the 1.8% performance of the device with as deposited CdS. The performance of the CdS/Sb_2Se_3 solar cells has reduced as the annealing temperature increase in both, air and vacuum conditions. The presence of oxide phases in CdS annealed in air at 400°C is detrimental to the device's performance. In addition, the extent of intermixing phenomenon between the CdS buffer layer and CSS Sb_2Se_3 absorber as well as intense carrier recombination at the main interface are the strong limiting factors for the PCE of CdS/Sb_2Se_3 solar cells.

Data availability statement

The raw data supporting the conclusion of this article will be made available by the authors, without undue reservation.

Author contributions

SV: Conceptualization, methodology, validation, formal analysis, investigation, writing—original draft, visualization. NS: Conceptualization, investigation, formal analysis, writing—review and editing, resources, supervision, project administration, funding acquisition. MB: Methodology, Investigation. RK: Writing—review and editing. AK: Investigation. RJ: Investigation, formal analysis. RG: Formal analysis, Investigation. AV: Formal analysis, Investigation. MK: Writing—review and editing. IO: Writing, reviewing and editing, project administration funding acquisition. All authors listed have made a substantial, direct, and intellectual contribution to the work and approved it for publication. All authors contributed to the article and approved the submitted version.

Funding

This study was funded by the Estonian Research Council projects PRG627 "Antimony chalcogenide thin films for next-generation semi-transparent solar cells applicable in electricity producing windows," PSG689 "Bismuth Chalcogenide Thin-Film Disruptive Green Solar Technology for Next-Generation Photovoltaics," the Estonian Centre of Excellence project TK141 (TAR16016EK) "Advanced materials and high-technology devices for energy recuperation systems," and the European Union's Horizon2020 programme under the ERA Chair project 5GSOLAR grant agreement No. 952509. The article/publication is based upon work from COST Action Research and International Networking on Emerging Inorganic Chalcogenides for Photovoltaics (RENEW-PV), CA21148, supported by COST (European Cooperation in Science and Technology). Institute of Solid-State Physics, University of Latvia has received funding from the European Union's Horizon 2020 Framework Programme H2020-WIDESPREAD-01-2016-2017-TeamingPhase2 under grant agreement No. 739508, project CAMART^2.

Conflict of interest

The authors declare that the research was conducted in the absence of any commercial or financial relationships that could be construed as a potential conflict of interest.

Publisher's note

All claims expressed in this article are solely those of the authors and do not necessarily represent those of their affiliated organizations, or those of the publisher, the editors and the reviewers. Any product that may be evaluated in this article, or claim that may be made by its manufacturer, is not guaranteed or endorsed by the publisher.

References

Azam, M., Luo, Y., Tang, R., Chen, S., Zheng, Z. H., Su, Z. H., et al. (2022). Organic chloride salt interfacial modified crystallization for efficient antimony selenosulfide solar cells. *ACS Appl. Mat. Interfaces* 14, 4276–4284. doi:10.1021/acsami.1c20779

Büttner, P., Scheler, F., Döhler, D., Barr, M. K. S., Bosch, M., Rey, M., et al. (2022). Continuous, crystalline Sb2S3 ultrathin light absorber coatings in solar cells based on photonic concentric p-i-n heterojunctions. *Nano Energy* 103, 107820. doi:10.1016/j.nanoen.2022.107820

Cai, H., Cao, R., Gao, J., Qian, C., Che, B., Tang, R., et al. (2022). Interfacial engineering towards enhanced photovoltaic performance of Sb2Se3 solar cell. *Adv. Funct. Mat.* 32, 2208243. doi:10.1002/adfm.202208243

Campbell, S., Phillips, L. J., Major, J. D., Hutter, O. S., Voyce, R., Qu, Y., et al. (2022). Routes to increase performance for antimony selenide solar cells using inorganic hole transport layers. *Front. Chem.* 10, 954588. doi:10.3389/fchem.2022.954588

Carron, R., Nishiwaki, S., Feurer, T., Hertwig, R., Avancini, E., Löckinger, J., et al. (2019). Advanced alkali treatments for high-efficiency Cu(in,Ga)Se2 solar cells on flexible substrates. *Adv. Energy. Mat.* 9, 1900408. doi:10.1002/AENM.201900408

Chen, C., Li, W., Zhou, Y., Chen, C., Luo, M., Liu, X., et al. (2015). Optical properties of amorphous and polycrystalline Sb2Se3 thin films prepared by thermal evaporation. *Appl. Phys. Lett.* 107, 043905. doi:10.1063/1.4927741

Chen, S., Liu, T., Chen, M., Ishaq, M., Tang, R., Zheng, Z., et al. (2022). Crystal growth promotion and interface optimization enable highly efficient Sb2Se3 photocathodes for solar hydrogen evolution. *Nano Energy* 99, 107417. doi:10.1016/j.nanoen.2022.107417

Dakhel, A. A. (2010). Electrical and optical properties of iron-doped CdO. *Thin Solid Films* 518, 1712–1715. doi:10.1016/j.tsf.2009.11.026

Fan, P., Chen, G. J., Chen, S., Zheng, Z. H., Azam, M., Ahmad, N., et al. (2021). Quasi-vertically oriented Sb2Se3thin-film solar cells with open-circuit voltage exceeding 500 mV prepared via close-space sublimation and selenization. *ACS Appl. Mat. Interfaces* 13, 46671–46680. doi:10.1021/ACSAMI.1C13223/ASSET/IMAGES/ACSAMI.1C13223.SOCIAL.JPEG_V03

Graf, A., Maticiuc, N., Spalatu, N., Mikli, V., Mere, A., Gavrilov, A., et al. (2015). "Electrical characterization of annealed chemical-bath-deposited CdS films and their application in superstrate configuration CdTe/CdS solar cells," in *Thin solid films* (Elsevier B.V.), 351–355. doi:10.1016/j.tsf.2014.11.003

Green, M. A., Dunlop, E. D., Hohl-Ebinger, J., Yoshita, M., Kopidakis, N., and Hao, X. (2021). Solar cell efficiency tables (Version 58). *Prog. Photovoltaics Res. Appl.* 29, 657–667. doi:10.1002/PIP.3444

Guo, H., Jia, X., Hadke, S. H., Zhang, J., Wang, W., Ma, C., et al. (2020). Highly efficient and thermally stable Sb 2 Se 3 solar cells based on a hexagonal CdS buffer layer by environmentally friendly interface optimization. *J. Mat. Chem. C Mat.* 8, 17194–17201. doi:10.1039/D0TC04017G

Guo, L., Grice, C., Zhang, B., Xing, S., Li, L., Qian, X., et al. (2019). Improved stability and efficiency of CdSe/Sb2Se3 thin-film solar cells. *Sol. Energy* 188, 586–592. doi:10.1016/j.solener.2019.06.042

Hernández-Calderón, V., Vigil-Galán, O., Guc, M., Carrillo-Osuna, A., Ramírez-Velasco, S., Sánchez-Rodríguez, F. J., et al. (2020). CdS/ZnS bilayer thin films used as buffer layer in 10%-efficient Cu2ZnSnSe4Solar cells. *ACS Appl. Energy Mat.* 3, 6815–6823. doi:10.1021/ACSAEM.0C00937/ASSET/IMAGES/ACSAEM.0C00937.SOCIAL.JPEG_V03

Hobson, T. D. C., Phillips, L. J., Hutter, O. S., Shiel, H., Swallow, J. E. N., Savory, C. N., et al. (2020). Isotype heterojunction solar cells using n-type Sb2Se3 thin films. *Chem. Mat.* 32, 2621–2630. doi:10.1021/acs.chemmater.0c00223

Koltsov, M., Krautmann, R., Katerski, A., Maticiuc, N., Krunks, M., Oja Acik, I., et al. (2022). A post-deposition annealing approach for organic residue control in TiO2 and its impact on Sb2Se3/TiO2 device performance. *Faraday Discuss.* 239, 273–286. doi:10.1039/d2fd00064d

Krautmann, R., Spalatu, N., Gunder, R., Abou-Ras, D., Unold, T., Schorr, S., et al. (2021). Analysis of grain orientation and defects in Sb 2 Se 3 solar cells fabricated by close-spaced sublimation. *Sol. Energy* 225, 494–500. doi:10.1016/j.solener.2021.07.022

Krautmann, R., Spalatu, N., Josepson, R., Nedzinskas, R., Kondrotas, R., Gržibovskis, R., et al. (2023). Low processing temperatures explored in Sb2S3 solar cells by close-spaced sublimation and analysis of bulk and interface related defects. *Sol. Energy Mat. Sol. Cells* 251, 112139. doi:10.1016/j.solmat.2022.112139

Kumar, V., Artegiani, E., Kumar, A., Mariotto, G., Piccinelli, F., and Romeo, A. (2019). Effects of post-deposition annealing and copper inclusion in superstrate Sb2Se3 based solar cells by thermal evaporation. *Sol. Energy* 193, 452–457. doi:10.1016/j.solener.2019.09.069

Kumar, V., Artegiani, E., Punathil, P., Bertoncello, M., Meneghini, M., Piccinelli, F., et al. (2021). Analysis of Se Co-evaporation and post-selenization for Sb2Se3-based solar cells. *ACS Appl. Energy Mat.* 4, 12479–12486. doi:10.1021/acsaem.1c02301

Kylner, A. (1999). Effect of impurities in the CdS buffer layer on the performance of the Cu(In, Ga)Se2 thin film solar cell. *J. Appl. Phys.* 85, 6858–6865. doi:10.1063/1.370204

Leng, M., Chen, C., Xue, D. J., Gong, J., Liu, Y., Li, K., et al. (2021). Sb2Se3 solar cells employing metal-organic solution coated CdS buffer layer. *Sol. Energy Mat. Sol. Cells* 225, 111043. doi:10.1016/J.SOLMAT.2021.111043

Li, D. B., Yin, X., Grice, C. R., Guan, L., Song, Z., Wang, C., et al. (2018). Stable and efficient CdS/Sb2Se3 solar cells prepared by scalable close space sublimation. *Nano Energy* 49, 346–353. doi:10.1016/j.nanoen.2018.04.044

Li, K., Chen, C., Lu, S., Wang, C., Wang, S., Lu, Y., et al. (2019a). Orientation engineering in low-dimensional crystal-structural materials via seed screening. *Adv. Mat.* 31, 1903914. doi:10.1002/adma.201903914

Li, Z., Chen, X., Zhu, H., Chen, J., Guo, Y., Zhang, C., et al. (2017). Sb2Se3 thin film solar cells in substrate configuration and the back contact selenization. *Sol. Energy Mat. Sol. Cells* 161, 190–196. doi:10.1016/J.SOLMAT.2016.11.033

Li, Z., Liang, X., Li, G., Liu, H., Zhang, H., Guo, J., et al. (2019b). 9.2%-efficient core-shell structured antimony selenide nanorod array solar cells. *Nat. Commun.* 10, 125. doi:10.1038/s41467-018-07903-6

Liu, D., Tang, R., Ma, Y., Jiang, C., Lian, W., Li, G., et al. (2021). Direct hydrothermal deposition of antimony triselenide films for efficient planar heterojunction solar cells. *ACS Appl. Mat. Interfaces* 13, 18856–18864. doi:10.1021/ACSAMI.1C02393/SUPPL_FILE/AM1C02393_SI_001.PDF

Liu, X., Chen, J., Luo, M., Leng, M., Xia, Z., Zhou, Y., et al. (2014). Thermal evaporation and characterization of Sb2Se3 thin film for substrate Sb2Se3/CdS solar cells. *ACS Appl. Mat. Interfaces* 6, 10687–10695. doi:10.1021/am502427s

Luo, Y., Chen, G., Chen, S., Ahmad, N., Azam, M., Zheng, Z., et al. (2023). Carrier transport enhancement mechanism in highly efficient antimony selenide thin-film solar cell. *Adv. Funct. Mat.* 33. doi:10.1002/adfm.202213941

Maticiuc, N., Katerski, A., Danilson, M., Krunks, M., and Hiie, J. (2017). XPS study of OH impurity in solution processed CdS thin films. *Sol. Energy Mat. Sol. Cells* 160, 211–216. doi:10.1016/j.solmat.2016.10.040

Maticiuc, N., Kukk, M., Spalatu, N., Potlog, T., Krunks, M., Valdna, V., et al. (2014). Comparative study of CdS films annealed in neutral, oxidizing and reducing atmospheres. *Energy Procedia* 44, 77–84. doi:10.1016/j.egypro.2013.12.012

Maticiuc, N., Spalatu, N., Mikli, V., and Hiie, J. (2015). "Impact of CdS annealing atmosphere on the performance of CdS-CdTe solar cell," in *Appl. Surf. Sci.* (Elsevier B.V.), 14–18. doi:10.1016/j.apsusc.2015.01.172

Ou, C., Shen, K., Li, Z., Zhu, H., Huang, T., and Mai, Y. (2019). Bandgap tunable CdS: O as efficient electron buffer layer for high-performance Sb2Se3 thin film solar cells. *Sol. Energy Mat. Sol. Cells* 194, 47–53. doi:10.1016/J.SOLMAT.2019.01.043

Phillips, L. J., Savory, C. N., Hutter, O. S., Yates, P. J., Shiel, H., Mariotti, S., et al. (2019). Current enhancement via a TiO 2 window layer for CSS Sb 2 Se 3 solar cells: Performance limits and high V oc. *IEEE J. Photovolt.* 9, 544–551. doi:10.1109/JPHOTOV.2018.2885836

Potlog, T., Spalatu, N., Fedorov, V., Maticiuc, N., Antoniuc, C., Botnariuc, V., et al. (2011). "The performance of thin film solar cells employing photovoltaic ZnSe/CdTe, CdS/CdTe and ZnTe/CdTe heterojunctions," in Conference Record of the IEEE Photovoltaic Specialists Conference, 001365–001370. doi:10.1109/PVSC.2011.6186211

Potlog, T., Spalatu, N., Maticiuc, N., Hiie, J., Valdna, V., Mikli, V., et al. (2012). Structural reproducibility of CdTe thin films deposited on different substrates by close space sublimation method. *Phys. Status Solidi (A) Appl. Mater. Sci.* 209, 272–276. doi:10.1002/pssa.201127123

Punathil, P., Zanetti, S., Artegiani, E., Kumar, V., and Romeo, A. (2021). Analysis of the drying process for precursors of Cu2ZnSn(S,Se)4 layers by low cost non vacuum fabrication technique. *Sol. Energy* 224, 992–999. doi:10.1016/J.SOLENER.2021.06.063

Shiel, H., Hutter, O. S., Phillips, L. J., Swallow, J. E. N., Jones, L. A. H., Featherstone, T. J., et al. (2020). Natural band alignments and band offsets of Sb2Se3Solar cells. *ACS Appl. Energy Mat.* 3, 11617–11626. doi:10.1021/acsaem.0c01477

Spalatu, N., Hiie, J., Kaupmees, R., Volobujeva, O., Krustok, J., Acik, I. O., et al. (2019). Postdeposition processing of SnS thin films and solar cells: Prospective strategy to obtain large, sintered, and doped SnS grains by recrystallization in the presence of a metal halide flux. *ACS Appl. Mat. Interfaces* 11, 17539–17554. doi:10.1021/acsami.9b03213

Spalatu, N., Hiie, J., Mikli, V., Krunks, M., Valdna, V., Maticiuc, N., et al. (2015). "Effect of CdCl2annealing treatment on structural and optoelectronic properties of close spaced sublimation CdTe/CdS thin film solar cells vs deposition conditions," in *Thin solid films* (Elsevier B.V.), 128–133. doi:10.1016/j.tsf.2014.11.066

Spalatu, N., Krautmann, R., Katerski, A., Karber, E., Josepson, R., Hiie, J., et al. (2021). Screening and optimization of processing temperature for Sb2Se3 thin film growth protocol: Interrelation between grain structure, interface intermixing and solar cell performance. *Sol. Energy Mat. Sol. Cells* 225, 111045. doi:10.1016/j.solmat.2021.111045

Spalatu, N., Krunks, M., and Hiie, J. (2017). Structural and optoelectronic properties of CdCl2 activated CdTe thin films modified by multiple thermal annealing. *Thin Solid Films* 633, 106–111. doi:10.1016/j.tsf.2016.09.042

Tang, R., Chen, S., Zheng, Z. H., Su, Z. H., Luo, J. T., Fan, P., et al. (2022). Heterojunction annealing enabling record open-circuit voltage in antimony triselenide solar cells. *Adv. Mat.* 34, 2109078. doi:10.1002/adma.202109078

Tang, R., Zheng, Z. H., Su, Z. H., Li, X. J., Wei, Y. D., Zhang, X. H., et al. (2019). Highly efficient and stable planar heterojunction solar cell based on sputtered and post-selenized Sb2Se3 thin film. *Nano Energy* 64, 103929. doi:10.1016/j.nanoen.2019.103929

Tiwari, K. J., Neuschitzer, M., Espíndola-Rodriguez, M., Sánchez, Y., Jehl, Z., Vidal-Fuentes, P., et al. (2020). Efficient Sb2Se3/CdS planar heterojunction solar cells in substrate configuration with (hk0) oriented Sb2Se3 thin films. *Sol. Energy Mat. Sol. Cells* 215, 110603. doi:10.1016/j.solmat.2020.110603

Varley, J. B., and Lordi, V. (2013). Electrical properties of point defects in CdS and ZnS. *Appl. Phys. Lett.* 103, 102103. doi:10.1063/1.4819492

Wang, L., Li, D. B., Li, K., Chen, C., Deng, H. X., Gao, L., et al. (2017). Stable 6%-efficient Sb2Se3 solar cells with a ZnO buffer layer. *Nat. Energy* 2, 17046. doi:10.1038/nenergy.2017.46

Wang, L., Luo, M., Qin, S., Liu, X., Chen, J., Yang, B., et al. (2015). Ambient CdCl2 treatment on CdS buffer layer for improved performance of Sb2Se3 thin film photovoltaics. *Appl. Phys. Lett.* 107, 143902. doi:10.1063/1.4932544

Wang, W., Cao, Z., Wu, L., Chen, G., Ao, J., Luo, J., et al. (2022). Interface etching leads to the inversion of the conduction band offset between the CdS/Sb 2 Se 3 heterojunction and high-efficient Sb 2 Se 3 solar cells. *ACS Appl. Energy Mat.* 5, 2531–2541. doi:10.1021/ACSAEM.1C04078/SUPPL_FILE/AE1C04078_SI_001.PDF

Weiss, T. P., Minguez-Bacho, I., Zuccalà, E., Melchiorre, M., Valle, N., el Adib, B., et al. (2022). Post-deposition annealing and interfacial atomic layer deposition buffer layers of Sb2Se3/CdS stacks for reduced interface recombination and increased open-circuit voltages. *Prog. Photovoltaics Res. Appl.* 31, 203–219. doi:10.1002/pip.3625

Wen, X., Chen, C., Lu, S., Li, K., Kondrotas, R., Zhao, Y., et al. (2018). Vapor transport deposition of antimony selenide thin film solar cells with 7.6% efficiency. *Nat. Commun.* 9, 2179–2210. doi:10.1038/s41467-018-04634-6

Zhou, J., Zhang, X., Chen, H., Tang, Z., Meng, D., Chi, K., et al. (2020). Dual-function of CdCl2 treated SnO2 in Sb2Se3 solar cells. *Appl. Surf. Sci.* 534, 147632. doi:10.1016/j.apsusc.2020.147632

Zhou, Y., Wang, L., Chen, S., Qin, S., Liu, X., Chen, J., et al. (2015). Thin-film Sb2Se3 photovoltaics with oriented one-dimensional ribbons and benign grain boundaries. *Nat. Photonics* 9, 409–415. doi:10.1038/nphoton.2015.78

Appendix 2

Publication II

S. V. Gopi, N. Spalatu, A. Katerski, J. Kuliček, B. Razek, E. Ukraintsev, M. Š. Bařinková, G. Zoppi, R. Grzibovskis, A. Vembris, and L. Ignatane, "An alternative chlorine-assisted optimization of CdS/Sb_2Se_3 solar cells: Towards understanding of chlorine incorporation mechanism," *Journal of Alloys and Compounds*, vol. 1005, p. 176175, Nov. 2024, DOI: 10.1016/j.jallcom.2024.176729.

Journal of Alloys and Compounds 1005 (2024) 176175

Contents lists available at ScienceDirect

Journal of Alloys and Compounds

journal homepage: www.elsevier.com/locate/jalcom

An alternative chlorine-assisted optimization of CdS/Sb_2Se_3 solar cells: Towards understanding of chlorine incorporation mechanism

Sajeesh Vadakkedath Gopi [a,*], Nicolae Spalatu [a,*], Atanas Katerski [a], Jaroslav Kuliček [b], Bohuslav Razek [b], Egor Ukraintsev [b], Markéta Šlapal Bařinková [b], Guillaume Zoppi [c], Raitis Grzibovskis [d], Aivars Vembris [d], Liga Ignatane [d], Malle Krunks [a], Ilona Oja Acik [a]

[a] Department of Materials and Environmental Technology, Tallinn University of Technology, Ehitajate tee 5, Tallinn, Estonia
[b] Faculty of Electrical Engineering, Czech Technical University in Prague, Technická 2, Prague 166 27, Czech Republic
[c] Department of Mathematics, Physics, and Electrical Engineering, Northumbria University, Newcastle-upon-Tyne NE1 8ST, United Kingdom
[d] Institute of Solid-State Physics, University of Latvia, Riga, Latvia

ARTICLE INFO

Keywords:
Vapor transport deposition
CdS chlorine assisted optimization
Secondary ion mass spectroscopy
Sb2Se3 thin film solar cell

ABSTRACT

The current strategies in the development of Sb_2Se_3 thin film solar cells involve fabrication and optimization of superstrate and substrate device architectures, with the preferable choice for TiO_2 and CdS heterojunction layers. For CdS-based superstrate cells, several studies reported the necessity to apply $CdCl_2$ or other metal halide-based post-deposition treatment (PDT), highlighting improvement of CdS/Sb_2Se_3 device efficiency. However, the need, effect, and mechanism of such PDT are very often not described. Additionally, the fact that many groups have not succeeded in demonstrating its benefits suggests that this strategy is not straightforward, requiring a deeper understanding towards a more unified concept. The present study proposes an alternative approach to the challenging $CdCl_2$ PDT of CdS in CdS/Sb_2Se_3 device, involving controllable Cl incorporation in CdS films by systematically varying the concentration of NH_4Cl in the CBD precursor solution from 1 to 8 mM. Structural and electrical characterizations are correlated with advanced measurements of Scanning Kelvin Probe, surface photovoltage, and atomic force microscopy to understand the impact of Cl incorporation on the properties of CdS films and CdS/Sb_2Se_3 devices. The validity of Cl incorporation in the CdS lattice and interdiffusion processes at the CdS-Sb_2Se_3 interface is confirmed by secondary ion mass spectrometry analysis. It is demonstrated that incorporation of 1 mM of NH_4Cl, as a Cl source in CBD CdS, can boost the PCE of CdS/Sb_2Se_3 by ~20 %. With this approach, we offer new perspectives on the optimization methodology for Cl-based CdS/Sb_2Se_3 device processing and complementary understanding of the physiochemistry behind these processes.

1. Introduction

Antimony selenide (Sb_2Se_3) - based thin film photovoltaics have gained a lot of interest due to its huge potential for the development of eco-friendly solar cells. This material boasts a range of appealing characteristics, including its non-toxicity, abundance, and cost-effectiveness. Additionally, it exhibits a favourable band gap (1.1–1.3 eV)[1,2] and a high absorption coefficient ($>10^4$ cm^{-1} in the visible part of the spectrum)[3], positioning Sb_2Se_3 as a top contender among emerging thin film absorber materials. Given that Sb_2Se_3 is a binary compound with a single-phase structure, the potential for secondary phase formation, which was observed in quaternary compounds like copper indium gallium selenide (CIGS)[4] or copper zinc tin sulfide (CZTS)[5,6], can now be readily mitigated. This makes the material easy to deposit as thin films using different techniques such as radio frequency sputtering (RF)[7,8], thermal evaporation (TE)[9], close-spaced sublimation (CSS)[10,11], and vapour transport deposition (VTD)[12]. Among these deposition techniques, VTD provides clear advantages with increased controllability of the deposition conditions and a very high deposition rate at high temperatures resulting in a columnar structure, an essential feature for charge transport in devices [13] with power conversion efficiency (PCE) up to 7.6 % in superstrate configuration using VTD method [14].

Over the past decades, there has been a growing interest in Sb_2Se_3 solar cell research, leading to notable improvements in their efficiency. Fig. 1a illustrates the advancements in Sb_2Se_3 solar cell efficiencies over

* Corresponding authors.
E-mail addresses: sajeesh.vadakkedath@taltech.ee (S.V. Gopi), nicolae.spalatu@taltech.ee (N. Spalatu).

https://doi.org/10.1016/j.jallcom.2024.176175
Received 10 June 2024; Received in revised form 12 August 2024; Accepted 25 August 2024
Available online 26 August 2024
0925-8388/© 2024 The Authors. Published by Elsevier B.V. This is an open access article under the CC BY-NC license (http://creativecommons.org/licenses/by-nc/4.0/).

the years, utilizing different buffer layers such as CdS, $CdCl_2$-treated CdS, and TiO_2. The corresponding highest reported efficiencies are 10.1 %, 8.4 %, and 7.6 %, respectively. This data indicates that highly efficient Sb_2Se_3 solar cells have been achieved with both untreated and $CdCl_2$-treated CdS buffer layers. From 2009–2024, there have been approximately 59 publications focusing on the use of CdS alone and 26 publications utilizing $CdCl_2$-treated CdS buffer layers in Sb_2Se_3 solar cells (Fig. 1b). These publications specifically include those that have completed the solar cell fabrication and reported their efficiencies. It is important to note that numerous other publications concentrate solely on the material aspects of the research and are excluded from this database. This comprehensive analysis highlights the significant progress made in Sb_2Se_3 solar cell research and underscores the ongoing efforts to optimize buffer layers for enhanced device performance.

Among various explored heterojunction partner/buffer layers such as TiO_2 [15,16], ZTO [17], ZnO [18], and SnO_2 [19] many research groups set the choice for CdS in developing Sb_2Se_3 solar cells. This is often justified by its easy deposition through the well-established chemical bath deposition (CBD) method, suitable band gap of ~2.5 eV, n-type conductivity, and optimum band alignment with Sb_2Se_3[11]. Z. Duan et al. [20] and X. Wen et al. [14] reported PCE's as high as 10.1 % and 7.6 % using substrate and superstrate configurations employing CdS as the buffer layer. It is worth mentioning that these remarkable PCE results were achieved using CBD-deposited CdS films, without the employment of additional post-deposition treatments (PDTs). However, many studies reported the necessity of PDTs, especially the need for $CdCl_2$ treatment in air at temperatures $\geq$ 400 °C for 5–10 min [21]. Such a PDT is very often reported by many groups as a key step for achieving reasonable PCE for superstrate configuration CdS/Sb_2S_3 thin film devices. Nevertheless, the provided mechanisms behind this PTD step are often ambiguous and mainly justified as a taken standardized step – transferred from CdTe thin film technology [21,22]. Independent of the employed PDTs strategy for CdS, several studies raised the concerns about intermixing phenomenon, occurring at the CdS-Sb_2Se_3 interface and being identified as one major limitation for the PCE of the CdS/Sb_2Se_3 device configuration [10]. It has been shown that this intermixing, primarily driven by the diffusion of Cd to Sb_2Se_3 or Se to CdS, leads to the formation of CdSe at the interface [23]. The role of CdSe at the interface remains contentious, with contradictory reports suggesting its beneficial effect on carrier transport or detrimental impact – as the formation of a barrier at the main heterojunction interface [14,15]. In this context, the role of $CdCl_2$ PDT in the presence of air ambient conditions has been also justified as a necessary step to control the extent of the intermixing effect at the interface [24]. In particular, the beneficial effect of oxygen during the PDT (without $CdCl_2$) has been proven, even at moderate annealing temperatures of 200 °C, by improving the stability of CBD CdS and thus, preventing the formation of excessive intermixing at absorber-buffer interface [25]. The impact of various metal halide-based PDTs (such as $CdCl_2$ and $AlCl_3$) on the properties of CdS and CdS/Sb_2Se_3 thin film solar cells properties has been investigated, aiming the control and optimization of both, intermixing as well as passivation of interface defects [21,26,27].

However, there is no consensus yet in the community on the beneficial or detrimental effects of these metal halide-based PDTs and if this processing step should be employed as a PDT or as a controllable chlorine incorporation at the stage of CBD CdS deposition followed by annealing in various environmental conditions. Related to chlorine incorporation into the CdS lattice, it is well established that this impurity acts as a n-type shallow dopant and depending on its concentration, can significantly impact the electron concentration in the n-type CdS deposited by any physical or chemical methods [28]. The validity of chlorine as an n-type dopant in Sb_2Se_3 was also confirmed by the synthesis of intrinsic Sb_2Se_3 crystals from metallic precursors and subsequent deliberate n-type doping by the addition of $MgCl_2$ [29]. It has been also reported that during the intermixing between CdS and Sb_2Se_3, Cd diffusion can convert p-type Sb_2Se_3 into n-type by introducing a donor defect [30].

On one hand, all these results suggest that the extent of intermixing (alloy formation at the CdS-Sb_2Se_3 interface) and diffusivity of Cl or Cd depends on the employed deposition techniques and processing temperatures of both, CdS and Sb_2Se_3 films in the thin film solar stack. On the other hand, it is suggested that metal halide-based PDTs have an important role in the intermixing/alloy formation at the interface and hence, in the formation of the n-n isotype or n-p type heterojunction at CdS-Sb_2Se_3 interface. The latter phenomenon will significantly impact the recombination processes at this interface and consequently, affect the PV parameters and final PCE of the device. Based on the literature analysis, it can be also depicted that there is no unified answer yet on whether the metal halide-based PDTs (in air at $\geq$400 °C) and/or chlorine doping of CdS are needed and effective for the CdS-Sb_2Se_3 interface and PCE of the final device. Although such a statement might raise tumultuous debates, it is based on the following justifications: (i) According to Fig. 1b a significant number of studies do not report either successful or unsuccessful results of $CdCl_2$ PDT (or any other metal halide-based PDT) on the CdS properties and PCE of CdS/Sb_2S_3 devices; this finding is valid, independent of the employed superstrate or substrate CdS-based Sb_2Se_3 cell configuration. (ii) On the other hand, a several studies report findings on the suitability and beneficial effect of

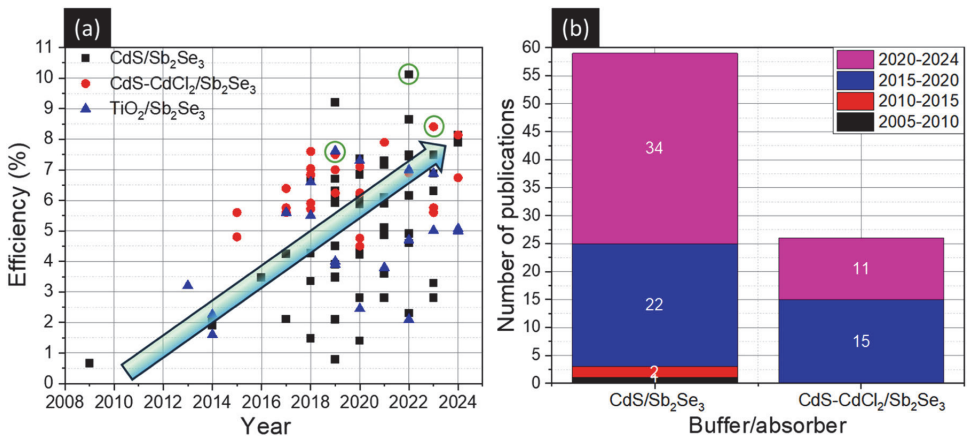

Fig. 1. Evolution of Sb_2Se_3 solar cell efficiency with CdS, $CdCl_2$-CdS and TiO_2 buffer layers and b) the corresponding number of publications.

$CdCl_2$-treated CdS on the PCE of Sb_2Se_3 solar cells.

At the same time, the developed knowledge on $CdCl_2$ PDT of CdS in CdTe demonstrated that this processing step promotes strong recrystallization (especially for CBD-deposited CdS) and improves the chemical stability of CdS towards the formation of suitable $CdS_{1-y}Te_y$ and $CdTe_{1-x}S_x$ alloy formation[31,32]. In one of our recent studies, we showed that standard $CdCl_2$ PDT of CBD CdS in the air at 400 °C is not a suitable approach for boosting the PCE of CdS/Sb_2Se_3 solar cells [10]. Therein close spaced sublimation was employed for the deposition of Sb_2Se_3 onto CBD CdS/FTO/glass and a very pronounced intermixing effect at the CdS-Sb_2Se_3 interface has been observed, limiting the final PCE of the device. Based on these cumulative results and considering the available knowledge on PDT $CdCl_2$ in CdTe, the transferability of the $CdCl_2$ processing step in air at 400°C to CdS (and consequently to the CdS-Sb_2Se_3 interface) is highly debatable and necessitates further systematic investigation and comprehensive understanding.

In this context, the present study proposes an alternative approach to the challenging $CdCl_2$ treatment of CdS in CdS/Sb_2Se_3 superstrate configuration cells. This approach involves incorporating Cl in a controllable manner into the CdS films by systematically varying the concentrations of NH_4Cl in the CBD precursor solution from 1 to 8 mM. Based on this precursor, a large series of CdS thin films were deposited onto both glass and glass/FTO substrates, and the impact of Cl incorporation on the properties of CdS films and CdS/Sb_2Se_3 was investigated. The incorporation of 1 mM of NH_4Cl, as a controllable chlorine source in CBD CdS, demonstrates a boost in the final PCE of CdS/Sb_2Se_3 by ~20 %. Routine structural and electrical characterization techniques are correlated with advanced measurements of Scanning Kelvin Probe, surface photovoltage, and atomic force microscopy to demonstrate and understand the impact of Cl incorporation on the properties of both CdS films and CdS/Sb_2Se_3 solar cells. We reveal that NH_4Cl introduced during the deposition does not change the CdS films structurally or morphologically but affects the film's electrical properties and energy levels resulting in a noticeable improvement in the solar cell performance. The validity of Cl incorporation into the CdS lattice and interdiffusion processes at the CdS-Sb_2Se_3 interface is confirmed by comprehensive secondary ion mass spectrometry depth profiles analysis of the CdS/Sb_2Se_3 heterostructure. Based on these systematic measurements, we provide a comprehensive discussion and analysis of the physicochemical processes responsible for the changes in the properties of CdS and CdS/Sb_2Se_3 solar cells, contributing with complementary knowledge on potential adjustments to methodologies for further development and optimization of emerging Sb_2Se_3-based thin film solar cells.

2. Experimental

2.1. Deposition of the CdS layer

CdS films were deposited on Flourine doped tin oxide (FTO) coated glass substrates (18 ×18 mm^2) by CBD. The substrates were cleaned using the standard procedure explained in the previously published article [25]. The deposition was carried out in a closed jar containing $CdSO_4$ (1 mM), $(NH_4)_2SO_4$ (0.7 M), NH_4Cl (0, 1, 2, 4 and 8 mM), NH_4OH (30 mM), and thiourea (10 mM) dissolved in de-ionized (DI) water at 79°C and stirred at 500 rpm. The chlorine content in the precursor was changed by the addition of different concentrations of NH_4Cl during the deposition. The deposition duration was optimized to be 10 min to get a 100 nm thick CdS layer. After deposition, the films were ultrasonicated in distilled water with a few drops of triethanolamine followed by washing again in distilled water and dried with a hot(100–150 °C) air gun. The prepared CdS samples were kept in a vacuum chamber and only taken outside for characterizations and deposition of Sb_2Se_3 by VTD.

2.2. Fabrication of CdS/Sb_2Se_3 solar cells

Sb_2Se_3 films were deposited on the glass/FTO/CdS substrates with different chlorine concentrations by VTD using a three-zone tubular furnace (Carbolite). Sb_2Se_3 granules of 5 N purity (Sigma Aldrich) were used as source materials. Initially, the quartz tube was evacuated using a combination of rotary and turbomolecular pumps (Pfeiffer vacuum) down to 10^{-5} mbar. The substrate-to-source distance was kept at 10 cm. The temperature of the source and substrate were ramped at 20 °C/min until it reached 500°C and 400°C, respectively. This temperature was kept for 5 min to obtain the desired thickness of 1 μm. After deposition, the furnace lid was opened, exposing the quartz tube to the ambient air. The vacuum pump was promptly shifted from turbo to rotary reducing the vacuum level to 10^{-2} mbar to stop the deposition of Sb_2Se_3 films. The superstrate configuration solar cells with glass/FTO/CdS/Sb_2Se_3/Au structure were completed by deposition of Au using thermal evaporation. Indium pads are used on top of the Au films during the device measurements.

2.3. Material and device characterizations

Structural properties of the CdS films and Sb_2Se_3 films were analyzed from X-ray diffraction (XRD) data measured by Rigaku Ultima IV using monochromator Cu Kα radiation (λ = 1.54 Å, 40 kV, 40 mA) equipped with D/teX silicon line detector in the 2Θ (Bragg-Bento) regime using 2Θ step of 0.04°, a counting time 2–10 s/step with sample rotation. The XRD patterns are then compared with JCPDS 01–074–9665 (CdS) and 015–0861 (Sb_2Se_3). The electrical properties (resistivity and carrier concentration) of CdS films were carried out at room temperature by Hall and Van der Paw controller H-50. The band gap of CdS films was calculated from UV vis spectroscopy (Jasco V-670 in 200–2500 nm) using a Tauc plot.

The contact potential difference (CPD) in the dark and under illumination of CdS and Sb_2Se_3 films was measured by a Scanning Kelvin Probe (SKP) system from KP Technology. The CPD data were recalculated to the work function values using the equation:

$$WF_{sample} = (CPD_{sample} - \quad CPD_{ref}) \times 10^{-3} + \quad WF_{ref} \tag{1}$$

As the WF reference (WF_{ref}), the Au reference sample from KP Technology was used. SKP measurements were done in a glove box using a grounded steel probe tip of 2 mm diameter. The CPD was measured in the dark-light-dark-light-dark cycle by switching solar simulator illumination (AM1.5 G filter, class AAA solar simulator HAL-C100, Asahi Spectra, Japan). CPD was measured as a function of time for 13.75 minutes (1250 data points). Multiple locations were tested on each sample. The surface photovoltage (SPV) was determined as the difference between WF_{light} and WF_{dark}. The second part of the SKP experiment was the mapping of WF across the scanned area of 4.89 × 4.89 mm^2 using a matrix of 12 × 12 points (hence 0.4075 mm per point). WF mapping was also performed in the dark and under the solar simulator illumination.

Topography of the CdS and CdS/Sb_2Se_3 films was measured by atomic force microscopy (AFM) using a NT-MDT Ntegra Prima instrument. Several Pt/Ir coated cantilevers with a resonance frequency of 75 KHz were used. The amplitude of the oscillation was 30 nm, with a setpoint of 65 %. The scan sizes were 1 × 1 and 2.5 × 2.5 μm^2 with scan speeds of 0.1 and 0.05 Hz respectively.

The surface morphology of the films was obtained using a scanning electron microscope (SEM) Zeiss EVO 10. The SEM images were acquired at 10 kV, magnification of 20 kX and working distance (WD) of 7.55 mm in the regime of secondary electrons (SE) using an off-beam detector.

The X-ray photoelectron spectroscopy (XPS) measurements were done using a Thermo Fisher ESCALAB Xi XPS/UPS system equipped with Al Kα radiation (hυ = 1486.6 eV) X-ray source.

Elemental depth profiling was acquired via secondary ion mass spectroscopy (SIMS). Positive and negative ion profiles were recorded using a hidden analytical IG20 gas ion gun and EQS1000 quadrupole detector. Samples were bombarded with Ar^+ ions (5 keV and 200 nA on the sample surface) and the beam was rastered over an area of 500 × 500 mm^2. A data gating of 10 % was applied for the analysis.

The superstate configuration solar cell performance was analyzed from the JV curve (AUTOLAB PGSTAT 30 and Oriel class A solar simulator 91159 A (100 mW/cm^2, AM1.5 G). The external quantum efficiency measurements were also carried out on the solar cells in the 300–1000 nm wavelength range using a light source (Newport 300 W Xenon lamp 69911), monochromator (Newport Cornerstone 260), and Si-calibrated detector (Merlin).

3. Results and discussions

As stated in the introduction part, in one of our recent studies, we showed that standard $CdCl_2$ PDT of CBD CdS in air at 400 °C is not a suitable approach for boosting the PCE of CdS/Sb_2Se_3 solar cells[10]. Therein, close-spaced sublimation (CSS) was employed for the deposition of Sb_2Se_3 onto glass/FTO/CBD - CdS and a very pronounced intermixing effect at the CdS-Sb_2Se_3 interface has been observed, limiting the final PCE of the device. At the same time, this might be the limitation of CSS technique in which a very close proximity between substrate and source (~10 mm) graphite blocks implies a very high supersaturated vapour phase near the samples. This effect combined with a high deposition rate (~0.5 μm/min) promotes conditions for a high chemical reactivity between CdS and Sb_2Se_3 and the formation of unfavourable alloy at the CdS-Sb_2Se_3 interface. This phenomenon appears to be less prominent when Sb_2Se_3 is deposited onto CdS using thermal vacuum evaporation and VTD techniques [33]. However, even for these techniques the effectiveness of $CdCl_2$ PDT of CdS buffer layer, in the air at 400 °C is still debatable. In this sense, we initially performed a series of experiments in which the $CdCl_2$ PDT in air at 400 °C was applied to CBD CdS followed by deposition of Sb_2Se_3 absorber by VTD. The impact of $CdCl_2$ PDT annealing duration on the solar cell performance is shown in fig S1 supplementary material. The results show that the longer the annealing time, the lower the solar cell performance. Independent of the annealing time the PCE is always lower compared to reference cell – without $CdCl_2$ treatment of CdS. We also investigated the impact of $CdCl_2$ PDT annealing temperature on the CdS/Sb_2Se_3 solar cells performance. The results are depicted in fig. S2 of supplementary material and it shows that regardless of the annealing temperature the PCE of the cells does not improve and the devices processed without $CdCl_2$ PDT of CdS still exhibit the highest PCE. Based on these results, we come with an alternative approach, proposing to incorporate chlorine in a controllable manner into the CdS films by systematically varying the concentrations of NH_4Cl in the CBD precursor solution from 1 to 8 mM. In this sense, we first analysed the impact of such processing approach on the properties of CdS films as described in Section 3.1 below.

3.1. Structural and morphological properties of CBD CdS films processed with different chlorine concentrations

To assess the influence of the incorporation of NH4Cl on the structural and morphological properties of CBD-deposited CdS films XRD, SEM, and AFM analysis were carried out on CdS films with 0, 1, 2, 4, and 8 mM NH4Cl concentrations. Fig. 1(a-e) shows the surface SEM images of the various CdS films. All films exhibited uniform and densely packed grains without any cracks and no significant changes in the CdS film morphology. There are reports on the modification of the morphology of CdS films due to doping of CdS with Cl- [28] as well as Ag ions [34] but here, since the concentration of the NH4Cl is rather small, a stable morphology was obtained for all the films.

The structural properties of the CdS films with different NH_4Cl concentrations were analyzed using XRD patterns, compared with standard pdf card 01–074–9665 [35] (Fig. 1f). The films exhibit hexagonal structure with distinct diffraction peaks at 25.2°, 26.8°, 28.5°, and 44.3° angles corresponding to the reflections from (100), (002), (101), and (110) planes, respectively. No discernible peaks associated with chlorine compounds, such as $CdCl_2$, were observed in the X-ray diffraction (XRD) pattern. This observation aligns with findings reported by Sivaraman et al. [36], who investigated the doping of chlorine into CdS and developed films via a spray coating method. Despite the lower chlorine concentration employed in our study compared to theirs, a similar trend was evident.

To investigate the effect of the NH_4Cl on the structural properties, the main (002) peak was separately analyzed (Fig. 2g). The films prepared with 0, 1, 2, and 4 mM NH_4Cl in the precursor had (002) peaks at nearly identical angles. In contrast, the CdS films with 8 mM NH_4Cl had a deviation to the lower 2Θ angle compared to that of 4 mM NH_4Cl CdS. In addition an interesting effect has been observed in which the (002) XRD peak is shifted towards higher 2Θ value as the NH_4Cl concentration increases from 0 to 4 mM. This effect has been observed previously in CdS films annealed in various ambient conditions [25] and can be explained by the presence of disorders in the lattice caused by incorporation of both Hydroxide group (OH) and chlorine into the CdS lattice during the deposition process. The displacement of (002) peak indicates that the chlorine was incorporated into the CdS lattice.

Fig. S3 (supplementary material) shows the AFM image of CdS deposited with 1 mM NH_4Cl in the precursor. Like the SEM images, the film has very uniform and well-packed grains.

3.2. Opto-electronic properties of CdS films processed with different chlorine concentrations

The bandgap of the CdS films deposited on the glass/FTO substrate with different NH_4Cl concentrations was calculated from Tauc plots based on UV-Vis measurements (Fig. 3a). The results reveal that there is a subtle decrease in the bandgap from 2.47 eV to 2.45 eV with the introduction of NH_4Cl and the concentration increases from 0 to 1 mM.

The band gap remains almost constant with the increase in the NH_4Cl concentration with slight changes of 0.1 eV. It is essential to emphasize that the observed changes in the bandgap were relatively small compared to the previous works involving high Cl^- doping levels.

The electrical properties (carrier concentration and resistivity) of the CdS films were obtained from hall measurements and the changes in these properties with an increase in NH_4Cl were investigated (Fig. 2b). All the films exhibit resistivity at the order of 10^4 Ω cm which was also reported by Hiie et al. [37]. Intriguingly, the resistivity of the CdS films had a pronounced surge from 3.6 $\times 10^4$ to 8.3 $\times 10^4$ Ω cm upon the introduction of 1 mM NH_4Cl in the bath. But then the resistivity sharply reduced to 3.3 $\times 10^4$ Ω cm when 2 mM NH_4Cl was used. After this, as the NH_4Cl concentration increases to 4 and 8 mM there is only a small step increase in the resistivity (3.3 $\times 10^4$ to 5.0 $\times 10^4$ Ω cm). The sharp decrease in the resistivity from 1 mM to 2 mM NH_4Cl might be due to the introduction of Cl^- ions into the CdS structure (not detected in XRD pattern (Fig. 2 f)), similarly, this can be also attributed to the sulfur deficiencies [38]. The incorporation of the added Cl atoms to the unoccupied sulfur vacancies increases the carriers which results in the decrease in resistivity.

Meanwhile, the carrier concentration of the CdS films has large variations corresponding to the change in NH_4Cl concentration. The maximum carrier concentration of 1.3 $\times 10^{14}$ /cm^3 was achieved for the films with 2 mM NH_4Cl. As the NH_4Cl concentration increases to 4 mM the carrier concentration remains almost similar but as the NH_4Cl concentration doubles to 8 mM the carrier concentration drops two orders of magnitude to 8.4 $\times 10^{12}$ /cm^3. The CdS films with 2 mM NH_4Cl have a maximum carrier concentration (1.318 $\times$ 10^{14} /cm^3) and the lowest resistivity (3.35 Ω cm) in the same way the CdS films 1 mM NH_4Cl have a maximum resistivity (8.37 Ω cm) and the lowest carrier concentration (3.4 $\times 10^{10}$ /cm^3). These significant changes in the electrical properties

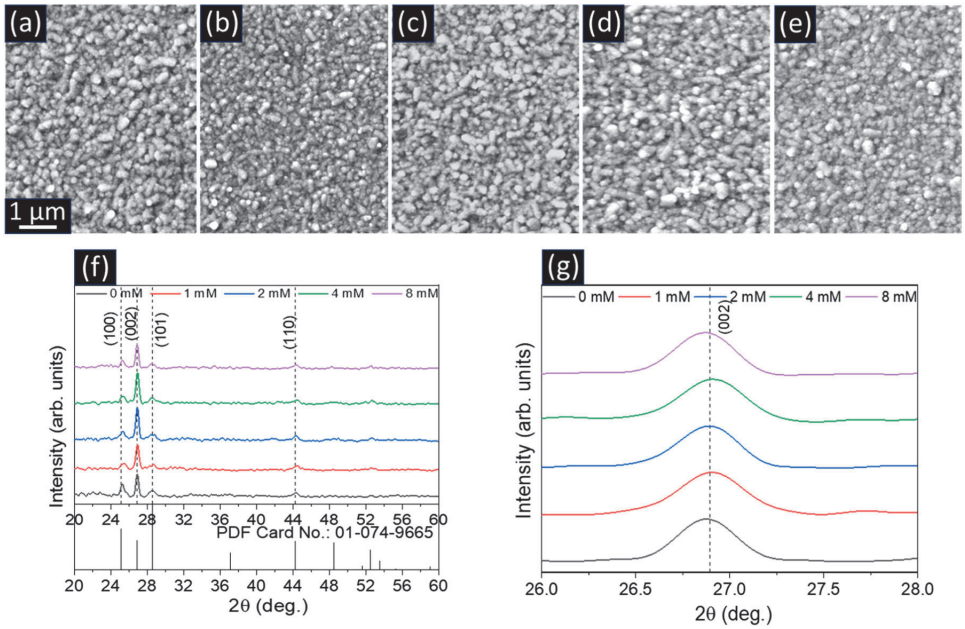

Fig. 2. (a-e) Surface SEM images of CdS films prepared with 0, 1, 2, 4, and 8 mM NH_4Cl in the CBD precursor, (f) XRD pattern of CdS with different NH_4Cl concentration, (g) Variation of (002) peak of CdS films with different NH_4Cl concentration.

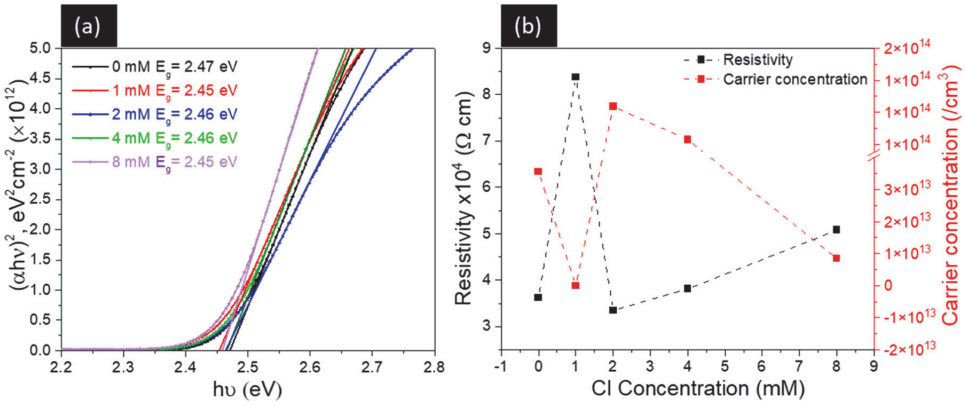

Fig. 3. (a) Tauc plots, showing the variation in bandgap of CdS films processed with 0–8 mM NH_4Cl concentration (b) electrical properties (carrier concentration and resistivity) of CdS films with different NH_4Cl concentration.

are good evidence of the incorporation of Cl into the CdS lattice. The more detailed explanation of the mechanism of chlorine incorporation on the electrical as well as on the device performance is explained in the later part of this paper.

As a step forward to better understand the energy levels of CdS films and the changes due to the introduction of NH_4Cl into it, the WF of the CdS films was measured in the dark-light-dark-light-dark cycle and the WF mapping was done in the dark and under the light across the 4.89 × 4.89 mm^2 area. Fig. 4(a, b, c, d, e) shows the WF maps of the CdS with 0, 1, 2, 4, and 8 mM NH_4Cl in the dark and Fig. 4(f, g, h, i, j) W.F. maps of same samples in order measured under the light. Fig. 4k shows the variation of WF and SPV with the change of NH_4Cl concentration, where WF is calculated as the average value from WF maps, and SPV is calculated from time-resolved measurements (Fig. S4 in the Supplementary material).

In Fig. 4a, WF for CdS with 0 mM NH_4Cl fluctuated between 4.42 and 4.55 eV in the dark, while WF decreased by ≈ 0.10 eV under illumination and fluctuated between 4.32 and 4.42 eV (Fig. 3f). A decrease in WF under light means positive photovoltage, thus generating holes on the surface. With the addition of 1 mM NH_4Cl, WF increased by 0.15 eV and fluctuated in the range of 4.50–4.60 eV (Fig. 4b). The WF values decreased under illumination and generated positive photovoltage (Fig. 3g). Furthermore, the surface charge is more homogenous compared to other samples. The sample CdS with 2 mM NH_4Cl WF range is 4.42–4.45 eV (Fig. 3c). Charge fluctuations can be partially influenced by sample morphology. Fig. 3d shows the WF map for CdS with 4 mM

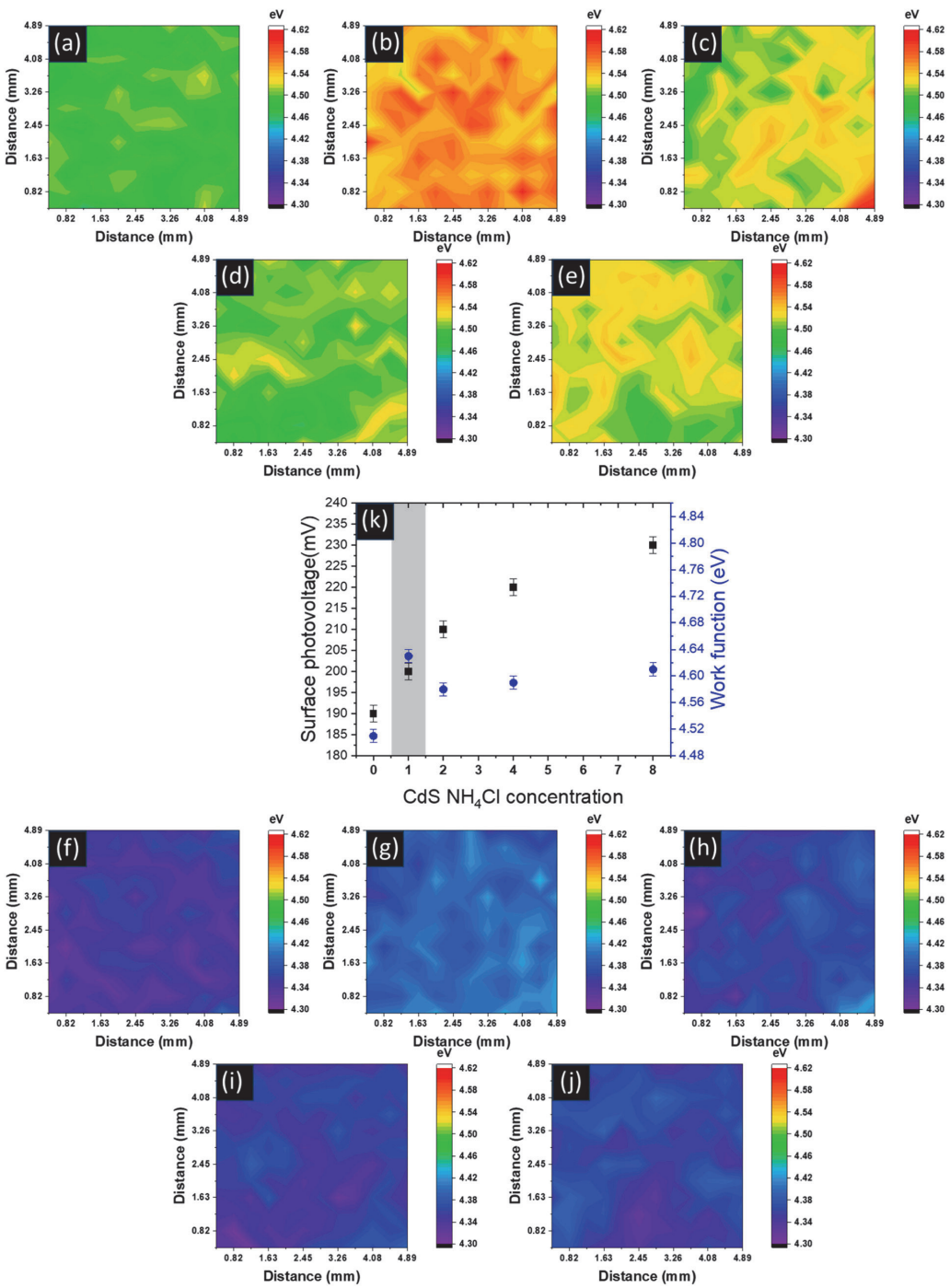

Fig. 4. (a, b, c, d, e) dark and (f, g, h, i, j) light condition work function distribution of CdS films at 0, 1, 2, 4, and 8 mM NH_4Cl in order (k) Variation of work function (WF) and surface photovoltage (SPV) with the change in NH_4Cl concentration.

NH_4Cl, where fluctuations of WF are in the similar range 4.42–4.45 eV as for CdS with 2 mM NH_4Cl. WF decreased under illumination for 0.15 eV, generating again positive SPV. The sample CdS with 8 mM NH_4Cl shows WF fluctuations between 4.46 and 4.56 eV (Fig. 3e). WF decreased under light by 0.20 eV to the range of 4.32–4.36 eV. In the overall trend we can see that the work function peaks at 4.63 eV when 1 mM NH_4Cl is introduced (increase by 0.12 eV). For higher NH_4Cl concentrations the values are similar, with small changes within 0.02 eV. The spatial distribution of work function across the sample surface is similar and uniform among the CdS films measured in the dark and under illumination, except for the CdS with 1 mM NH_4Cl which exhibits regions of higher work function compared to the other samples.

With the increase in the NH_4Cl concentration (1 mM to 2 mM) there was an abrupt increase in the carrier concentration (Fig. 2b). This is an indication of the incorporation of chlorine as a donor into the CdS lattice. From 2 mM to 8 mM NH_4Cl the carrier concentration decreases. It indicates that there is a compensation effect of chlorine by the creation of neutral complexes along with the side contribution of the OH impurities. Nevertheless, the surface photovoltage (Fig. 3k) of the CdS films increases steadily from 190 eV to 240 eV with an increase in the NH_4Cl concentration from 0 to 8 mM.

3.3. Elemental composition properties of CdS and CdS/Sb_2Se_3

The elemental characteristics of CdS films were investigated using X-ray Photoelectron Spectroscopy (XPS) and Energy Dispersive X-ray Spectroscopy (EDX) at varying NH_4Cl concentrations. The XPS spectra (depicted in Fig. S5a, b, and c) exhibited prominent Cd 3d peaks at 405.8 eV and 412.5 eV binding energies. Notably, there was no discernible detection of Cl 2p within the 190–210 eV range, suggesting that the chlorine incorporated during deposition is distributed deep within the film rather than residing on the surface. The peaks corresponding to Cd 3d and S 2p exhibited no significant variations with increasing NH_4Cl concentration. Similarly, Natalia et al. [39] also reported the non-varying XPS of CdS films with OH impurities.

Further confirmation was sought through EDX analysis performed on CdS films prepared with an NH_4Cl concentration of 8 mM (fig. S5 d). The peaks corresponding to O, S, Cd, and Sn were detected meanwhile Sn and O indicated the presence of oxygen and tin originating from the FTO substrate. Consequently, the elemental analysis corroborates the minimal chlorine content within the CdS film lattice. These results suggest that chlorine is either present in very low concentrations deep within the film or falls below the detection limit of the analytical instruments.

To investigate the elemental distribution and interdiffusion in the CdS/Sb_2Se_3 heterojunction solar cells, SIMS analysis was carried out on solar cells with 0, 1, and 8 mM NH_4Cl-CdS as buffer layers. Fig. 4a shows the distribution of Sb^{121}, Se^{80}, Cl^{35}, Cd^{114}, S^{32}, and F^{19} elements inside the solar cell structure with 1 mM-NH_4Cl. The distribution of constituents elements of the absorber (Sb_2Se_3) and buffer layer (CdS) was detected (Fig. 5a). The detection signals corresponding to Cl^{35} inside 1 mM NH_4Cl-CdS samples also confirm the incorporation of Cl inside the films, which was below the detection limit of EDX. To get insight into the possible intermixing of CdS and Sb_2Se_3 the Sb/Cd ratio (Fig. 5b) was calculated from the SIMS data for 0, 1, and 8 mM NH_4Cl-CdS samples.

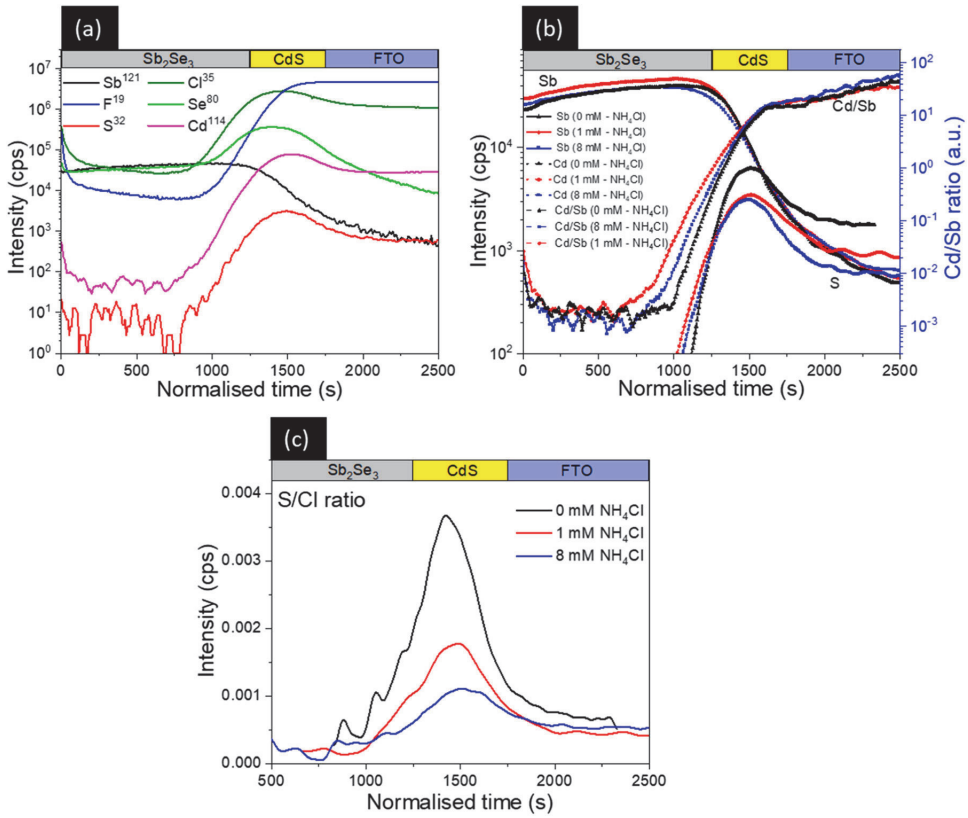

Fig. 5. Secondary ion mass Spectroscopy (SIMS) depth profiles, a) Sb, Se, Cd, S, Cl, and F elemental distribution in 1 mM NH_4Cl-CdS samples b) Cd/Sb ratio at NH_4Cl-CdS/Sb_2Se_3 interface c) S/Cl ratio of 0, 1, 8 mM NH_4Cl-CdS samples.

Both 1 mM and 8 mM samples showed a gentler slope at the CdS leading edge indicating Cd interdiffusion into the absorber when Cl is used. Interdiffusion appears not to be linearly correlated with the amount of Cl with the 1 mM NH_4Cl-CdS showing the largest intermixing. So clearly the CdS with 1 mM NH_4Cl has more interdiffusion of Cd to the absorber side which leads to more probability for intermixing and formation of CdSe at the interface. This might affect the solar cell performance, Wen X. et al.[14] reported that this intermixing leads to better lattice matching and lower defects, leading to an efficiency of 7.6 % using VTD as the deposition method for the Sb_2Se_3 deposition. Liang et al.[40] have also achieved an efficiency of 7.4 % through effective Sb_2Se_3 layer growth through VTD deposition followed by a post-selenisation procedure in substrate configuration CdS/Sb_2Se_3 solar cells. Meanwhile, other groups [10,15,41] have reported a detrimental effect on solar cell performance while depositing Sb_2Se_3 by CSS method. The impact of the Cl addition during the CBD process is shown in Fig. 5c where the S/Cl ratio is plotted. The S/Cl ratio is highest for 0 mM NH_4Cl-CdS and reduces with an increase in the NH_4Cl concentration, confirming the effective incorporation of Cl in the CdS films.

3.4. *Structural and morphological properties of Sb_2Se_3 deposited on CdS films processed with various chlorine concentrations*

As a step forward to solar cell preparation, the Sb_2Se_3 absorber films with a thickness of 1.023 μm were deposited by VTD on glass/FTO/CdS substrates, with varying NH_4Cl concentrations in the CdS films. The structural and morphological properties of the Sb_2Se_3 films were analyzed to study the effect of the change in CdS film on the absorber film. Fig. 6(a-e) shows the surface SEM images of Sb_2Se_3 films. It can be observed that the Sb_2Se_3 films are arranged very compactly without any porosity. However, the grains are not uniform, some with irregular size while others show a tower-like structure. This might be due to the substrate temperature irregularity obtained during VTD deposition. No significant changes in the morphology were observed for Sb_2Se_3 films due to changes in NH_4Cl concentration. The cross-section SEM image (Fig. 6 f) of 1 mM NH_4Cl-CdS/Sb_2Se_3 interface, confirms the columnar growth Sb_2Se_3 grains. The structural properties of the Sb_2Se_3 do not change with the difference in CdS films and all XRD spectra were identical to the example shown in Fig. 6 g for 1 mM NH_4Cl-CdS/Sb_2Se_3. The XRD pattern of Sb_2Se_3 deposited on CdS processed with various NH_4Cl concentration is presented in fig.S8 in the supporting material. The diffraction patterns were compared with standard data (JCPDS 15–0861) [13]. The diffraction peaks at 15.03°, 16.87°, 23.9°, 27.02°, 28.2°, 31.16°, 32.22°, 34.08°, 37.98°, 39.08°, 41.35°, 44.95°, 45.57° and 54.88° were detected corresponding to (020), (120), (130), (021), (211), (221), (301), (240), (041), (411), (250), (431), (002) and (061) planes. The XRD patterns have more intense (221) and (211) peaks indicating the tilted columnar grain growth of the Sb_2Se_3 films which was observed in the cross-section SEM image (Fig. 6 f) of the same sample.

Fig. S6 (supplementary material) presents the AFM image of the Sb_2Se_3 absorber film grown on CdS film with 1 mM NH_4Cl in the CBD bath. As with the SEM images, this gives a clear view of the overgrown grains in the film. The irregularities observed in the grain growth can be attributed to several factors, including non-uniform substrate temperature during rapid Sb_2Se_3 deposition. Additionally, the VTD deposition of the Sb_2Se_3 is happening at 400 °C. This could act as a post-deposition vacuum annealing process for the CdS films which leads to the out-diffusion of the residues and delay the growth of some grains.

3.5. *Impact of the chlorine concentration in the CBD CdS precursor on the device performance*

The Sb_2Se_3 solar cells with superstrate configuration (glass/FTO/CdS/Sb_2Se_3/Au) were fabricated and the changes in the device performance with a change in NH_4Cl concentration during the CdS deposition were analyzed. The solar cell parameters open circuit voltage (V_{OC}), short circuit current density (J_{SC}), fill factor (FF), and power conversion

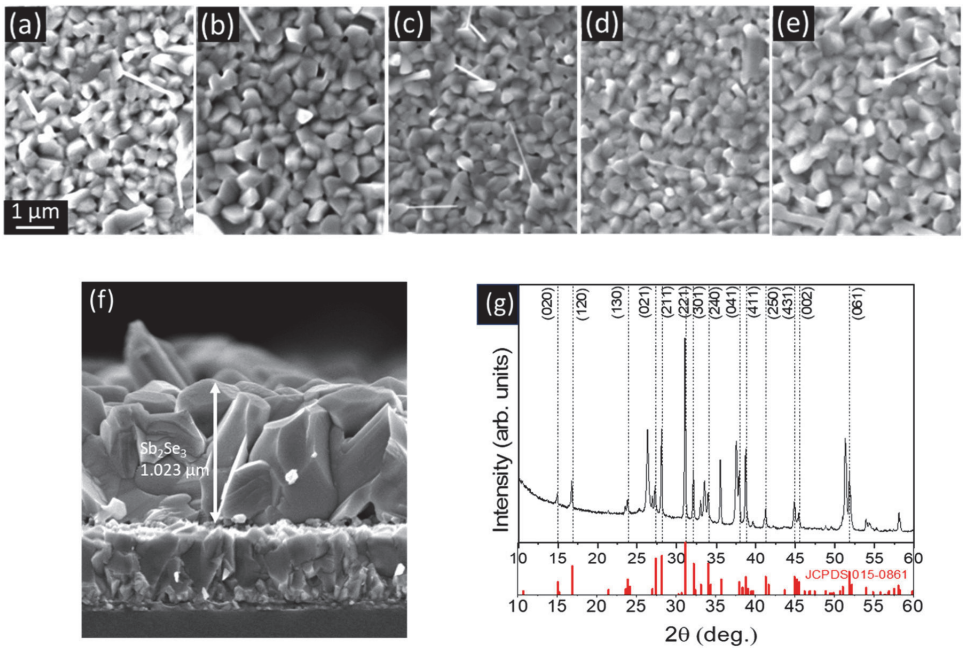

Fig. 6. (a-e) Surface SEM images of Sb_2Se_3 films prepared on CdS layers with 0, 1, 2, 4, and 8 mM NH_4Cl in the CBD precursor, (f) Cross-section SEM image of 1 mM NH_4Cl-CdS/Sb_2Se_3 structure (g) XRD pattern of Sb_2Se_3 on CdS with 1 mM NH_4Cl concentration.

efficiency (PCE) were extracted from the J-V characteristics (Fig. 7a-e).

The device parameters are influenced by the change in NH_4Cl concentration in the precursor during the CdS deposition. The V_{OC}, FF, and PCE of the solar cells were increased when 1 mM of NH_4Cl was introduced to the CdS films. The V_{OC} increases to 391.27 mV from 354.15 mV, FF increases to 52.4 % from 51.7 % and PCE increases to 4.6 % from 4.2 %. The highest PCE of 4.6 % was also obtained for the cells using a CdS layer buffer layer with 1 mM NH_4Cl. As the NH_4Cl concentration increases after 1 mM all the solar cell properties go down. The lowest PCE of 2.2 % was obtained for the solar cells with 8 mM NH_4Cl CdS buffer layers. The incorporated Cl has affected the solar cell parameters. The cells with maximum resistivity and minimum carrier concentration (1 mM NH_4Cl) CdS as buffer layer resulted in the best performance.

Similar to Fig. 4, WF maps and photovoltage were measured by SKP on the complete glass/FTO/CdS/Sb_2Se_3 devices. In this case on top Au contact and nearby bare Sb_2Se_3 surface. The results are summarized in fig. S7 and fig. S8 in the supplementary material. The most important observation is that the samples with 1 mM NH_4Cl show the largest photovoltage response and that the Au contact enhances this response, i.e., it significantly helps extract holes from the prepared solar cell.

The EQE response (Fig. 7 f) of solar cells shows steady efficiency in the 550 – 750 nm range. The integrated current density was also calculated from EQE and the values are in good agreement with those obtained from JV curves. The values of integrated J_{SC} are illustrated in fig. S9 in the supplementary material. The solar cells with CdS buffer layer deposited with 0 and 1 mM NH_4Cl have ~ 70 % response in the 550–750 nm region. As the concentration of the NH_4Cl in the CdS films increases the response steadily decreases, and the lowest efficiency of ~ 50 % was obtained for the cells using CdS films with 8 mM NH_4Cl. At the lower wavelength of the EQE spectra, a clear reduction in the response can be observed. This is one of the peculiar trends that has been reported by other researchers due to the intermixing effect between CdS and Sb_2Se_3 occurring as result of higher temperature deposition of Sb_2Se_3 absorber film. In our investigation, we observed a reduction in the EQE spectral response at lower wavelength (400–550 nm) for solar cells fabricated using 8 mM NH_4Cl-CdS/Sb_2Se_3 compared to those utilizing 1 mM NH_4Cl. The decrease in the EQE response at shorter wavelengths can be related with the greater stability of the CdS layer, and therefore to a greater parasitic absorption. This also agrees well with the SIMS results (Fig. 5a), where a higher degree of interdiffusion is revealed for the 1 mM NH_4Cl concentration. The mixing probably leads to a reduction of the CdS layer thickness and consequently of the parasitic absorption.

The better performance of the cell also depends on the best heterojunction between the buffer and the absorber films. CdS films are known for intermixing with the Sb_2Se_3 films, different research groups are trying to overcome these problems through different methods. There are reports on the incorporation of Al^{3+} [27,42], heterojunction annealing [43], and $CdCl_2$ thin-layer deposition [21,44,45] which resulted in better performance in the devices. The introduction of thin films such as TiO_2 also improved the efficiencies of the Sb_2Se_3 solar cell. In our case, it was the simple incorporation of Cl in the precursor/bath at 1 mM concentration that resulted in tremendously improved solar cell performance. This opens prospects for further fine-tuning and optimization of the CdS/Sb_2Se_3 heterojunction.

3.6. *Mechanism of chlorine incorporation in CdS and interrelation with CdS/Sb_2Se_3 device performance*

Based on the above observed systematic changes in the properties of CdS, Sb_2Se_3 films and solar cells, the following physicochemical processes are proposed:

(i) At the stage of CBD CdS processing: During the CBD deposition of CdS films, two concomitant processes occur in which both,

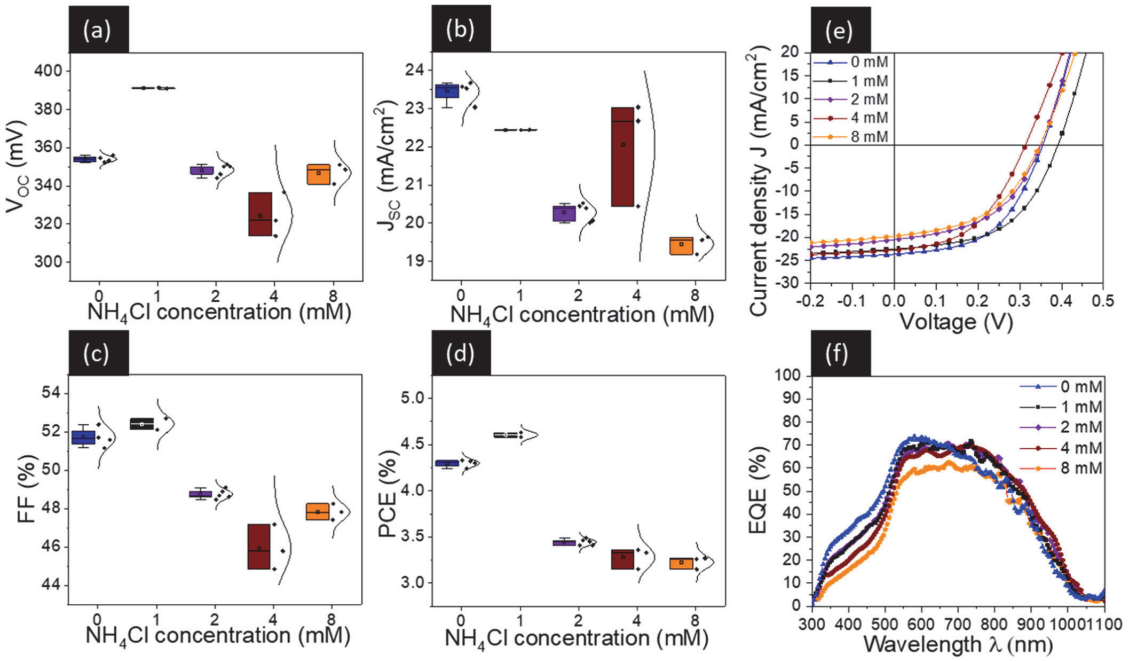

Fig. 7. (a) open circuit voltage (V_{OC}), (b) short circuit current (J_{SC}), (c) fill factor (FF), (d) power conversion efficiency (PCE), (e) JV characteristics and (f) external quantum efficiency (EQE) of CdS/Sb_2Se_3 solar cells with a change in NH_4Cl concentration in the precursor.

hydroxyl group and chlorine are incorporated into the CdS lattice according to the Eqs. 1–3:

$$nCdS + Cd(OH)_2 \rightarrow Cd_{n+1}S_n2(OH)_2V_{Cd} \quad (1)$$

$$2NH_4Cl + CdSO_4 \leftrightarrow CdCl_2 + (NH_4)_2SO_4 \quad (2)$$

$$nCdS + CdCl_2 \rightarrow Cd_{n+1}S_n2Cl_2V_{Cd} \quad (3)$$

According to Eq. 1, as a result of the chemical reaction, cadmium hydroxysulfide as a solid solution of cadmium hydroxide into CdS is formed and the OH group occupies the sulphur site into the CdS lattice, behaving as a shallow donor. On another hand, according to Eq. 2, the presence of NH_4Cl in the CBD precursor solution promotes formation of $CdCl_2$, leading to the incorporation of Cl into the CdS lattice and generating one V_{Cd} per every pair of incorporated Cl_S. Depending on the concentration of both hydroxyl group and chlorine in CdS, the generated V_{Cd}^{2-} can compensate the $(OH)_S^+$ and Cl_S^+, resulting in a low electron density of CdS.

Thus, at 0 mM NH_4Cl, the electron concentration in CdS film is entirely determined by the concentration of OH group which is incorporated into CdS on sulphur sites, generating an electron density of ~3 × 10^{13} cm^{-3} (Fig. 3b). An incorporation of 1 mM NH_4Cl in the CBD precursor seems to be a relatively low concentration to generate enough Cl_S^+ which would enhance the electron density. At such moderate Cl concentration and considering the incorporated $(OH)_S^+$, the concentration of double charged acceptor $(V_{Cd})^{2-}$ (which is generated by incorporation of both, and $Cd(OH)_2$ – Eq. 1, $CdCl_2$ – Eq. 3) appears to be high enough to compensate the shallow donors, resulting in enhanced resistivity and reduced electron density (Fig. 3b). An increase in the electron density of the films processed with 2 mM NH_4Cl in the CBD precursor can be explained by enhanced concentration of Cl_S^+ shallow donor defects which seems to be in higher concentration compared to $(V_{Cd})^{2-}$ at the given incorporated $CdCl_2$ amount. As the amount of NH_4Cl in the CBD precursor increases further, the electron density in CdS gradually drops (Fig. 3b) which can be related with the high Cl incorporation into the CdS lattice. Under these conditions, there is a high probability for Cl to occupy the interstitial states (acting as a p-type defect) into the CdS lattice, promoting high degree of compensation effect. Thus, these results indicate that depending on the amount of the NH_4Cl in the CBD precursor, the balance between $(OH)_S^+$ and Cl_S^+ is always shifted, governing, resistivity, electron density and work function in CdS films. However, this mechanism involves additional processes occurring during the stage of the Sb_2Se_3 absorber depositions by VTD, as follows.

At the stage of VTD Sb_2Se_3 absorber processing: During the Sb_2Se_3 absorber deposition at 400 °C (especially considering the time for ramping up the VTD source and substrate temperatures), CdS undergoes an annealing process, wherein the small CdS grains with high surface energy, undergoes intensive recrystallization by mass transport. On one hand, this recrystallization process induces decomposition and out diffusion of both chlorine and OH, resulting in their redistribution into the CdS lattice with a final impact on defect density and thus electrical properties of CdS buffer. On the other hand, according to SIMS analysis an interdiffusion of the elements at the main interfaces occurs, having a critical impact on the interface formation, including formation of interface defects and the quality of the n-p heterojunction. SIMS result confirms incorporation of Cl into the CdS and diffusion of Cd into Sb_2Se_3 absorber. The latest effect (of Cd diffusion into absorber) represent a major finding as many reports provided speculative hypothesis regarding Cd diffusion but without direct measurements proof. Some studies proposed the hypothesis that Cd act as donor defect in Sb_2Se_3 generating a rectifying junction in the spatial charge region [30]. Interestingly, in our case, for the device processed with 1 mM NH_4Cl CdS the diffusion of Cd was more pronounced (Fig. 5b). The same device showed the highest PCE suggesting that at 1 mM NH_4Cl the concentration of incorporated Cl into the CdS promotes a set of suitable condition for the formation of both, electrical properties of CdS as well as of the interdiffusion at the interface, resulting in the improved quality of the heterojunction and thus, device performance. It is worth mentioning that as an unexpected result, the SIMS analysis did not show any diffusion of chlorine into the absorber. So far, these results demonstrate that to achieve a beneficial impact of chlorine on the performance of CdS/Sb_2Se_3 device, the concentration of Cl should be relatively low, requiring careful incorporation control at both deposition stages, of CdS and Sb_2Se_3 absorber.

4. Conclusions

Exploring the influence of adding low concentration (1–8 mM NH_4Cl) of chlorine inside the CBD precursor on the characteristics of CdS films and CdS/Sb_2Se_3 solar cell device performance showed that the increase in chlorine concentrations does not affect the structural and morphological properties of CdS films whereas it significantly affects the electrical properties by changing carrier concentration and resistivity. There was an abrupt decrease in carrier concentration and an increase in resistivity with the introduction of 1 mM NH_4Cl. Additionally, bandgap of the CdS sample decreased with chlorine introduction from 2.47 eV to 2.45 eV. Photovoltage showed hole diffusion on CdS surface, on complete cells it showed pronounced positive effect of Au contact on effective charge collection. SIMS experiments detected increasing chlorine concentration and a higher interdiffusion of Cd into the absorber side was confirmed for devices with 1 mM NH_4Cl-CdS buffer layers. The morphology of Sb_2Se_3 films deposited via VTD on the CdS films with different NH_4Cl concentrations remained unchanged but an irregular grain height was observed in all films, this might be because of the irregular substrate temperature that occurred due to high vapor flow during the fast deposition. The Sb_2Se_3 films were (221) oriented regardless of CdS chlorine concentration. The devices with 1 mM NH_4Cl-CdS buffer layer had the best performance with 4.6 % PCE. A 20 % boost compared to the devices with 0 mM NH_4Cl-CdS. The performance of the devices decreases with an increase in chlorine concentration from 1 to 8 mM NH_4Cl. EQE measurements show a steady decrease in the spectral response in 500–800 nm region with an increase in NH_4Cl concentration. A detailed insight to the complex mechanism of the chlorine inside the CdS films and its effects on the device performance was provided opening new possibilities for the refinements in the methodologies of chlorine-assisted development and optimization of emerging CdS/Sb_2Se_3 solar cells.

Funding

All of the sources of funding for the work described in this publication are acknowledged below:

- Estonian Research Council project PRG627 “Antimony chalcogenide thin films for next-generation semi-transparent solar cells applicable in electricity producing windows”
- Estonian Research Council project PSG689 “Bismuth Chalcogenide Thin-Film Disruptive Green Solar Technology for Next Generation Photovoltaics”
- Estonian Ministry of Education and Research project (TK210; TK210U8) „Center of Excellence in Sustainable Green Hydrogen and Energy Technologies“,
- Engineering and Physical Sciences Research Council (UK) for funding through Reimagining Photovoltaics Manufacturing (EP/W010062/1)
- The European Union’s H2020 programme under the ERA Chair project 5GSOLAR grant agreement No 952509.
- COST Action Research and International Networking on Emerging Inorganic Chalcogenides for Photovoltaics (RENEW-PV), CA21148, supported by COST (European Cooperation in Science and Technology)

CRediT authorship contribution statement

Bohuslav Rezek: Writing – review & editing, Visualization, Validation, Supervision, Funding acquisition, Formal analysis, Data curation. **Markéta Šlapal Bařinková:** Formal analysis, Data curation. **Atanas Katerski:** Methodology, Formal analysis, Data curation. **Jaroslav Kuliček:** Writing – review & editing, Visualization, Validation, Formal analysis, Data curation. **Ilona Oja Acik:** Validation, Supervision, Project administration, Funding acquisition. **Nicolae Spalatu:** Writing – review & editing, Writing – original draft, Validation, Supervision, Methodology, Funding acquisition, Conceptualization. **Liga Ignatane:** Visualization, Formal analysis, Data curation. **Sajeesh Vadakkedath Gopi:** Writing – review & editing, Writing – original draft, Visualization, Validation, Investigation, Formal analysis, Data curation, Conceptualization. **Malle Krunks:** Writing – review & editing, Validation. **Raitis Grzibovskis:** Formal analysis, Data curation. **Aivars Vembris:** Formal analysis, Data curation. **Egor Ukraintsev:** Visualization, Formal analysis, Data curation. **Guillaume Zoppi:** Writing – review & editing, Visualization, Validation, Formal analysis, Data curation.

Declaration of Competing Interest

No conflict of interest exists.

Data availability

Data will be made available on request.

Acknowledgements

This study was funded by the Estonian Research Council projects PRG627 “Antimony chalcogenide thin films for next-generation semi-transparent solar cells applicable in electricity producing windows”, PSG689 “Bismuth Chalcogenide Thin-Film Disruptive Green Solar Technology for Next Generation Photovoltaics”, the Estonian Ministry of Education and Research project (TK210; TK210U8) „Center of Excellence in Sustainable Green Hydrogen and Energy Technologies“, and the European Union’s Horizon 2020 programme under the ERA Chair project 5GSOLAR grant agreement No 952509. The article is based upon work from COST Action Research and International Networking on Emerging Inorganic Chalcogenides for Photovoltaics (RENEW-PV), CA21148, supported by COST (European Cooperation in Science and Technology). The authors also acknowledge the Engineering and Physical Sciences Research Council (UK) for funding through Reimagining Photovoltaics Manufacturing (EP/W010062/1).

Intellectual property

We confirm that we have given due consideration to the protection of intellectual property associated with this work and that there are no impediments to publication, including the timing of publication, with respect to intellectual property. In so doing we confirm that we have followed the regulations of our institutions concerning intellectual property.

Appendix A. Supporting information

Supplementary data associated with this article can be found in the online version at doi:10.1016/j.jallcom.2024.176175.

References

[1] R. Tang, Z.H. Zheng, Z.H. Su, X.J. Li, Y.D. Wei, X.H. Zhang, Y.Q. Fu, J.T. Luo, P. Fan, G.X. Liang, Highly efficient and stable planar heterojunction solar cell based on sputtered and post-selenized Sb_2Se_3 thin film, Nano Energy 64 (2019), https://doi.org/10.1016/j.nanoen.2019.103929.

[2] Z. Li, X. Liang, G. Li, H. Liu, H. Zhang, J. Guo, J. Chen, K. Shen, X. San, W. Yu, R.E. I. Schropp, Y. Mai, 9.2%-efficient core-shell structured antimony selenide nanorod array solar cells, Nat. Commun. 10 (2019), https://doi.org/10.1038/s41467-018-07903-6.

[3] Y. Zhou, L. Wang, S. Chen, S. Qin, X. Liu, J. Chen, D.J. Xue, M. Luo, Y. Cao, Y. Cheng, E.H. Sargent, J. Tang, Thin-film Sb2Se3 photovoltaics with oriented one-dimensional ribbons and benign grain boundaries, Nat. Photonics 9 (2015) 409–415, https://doi.org/10.1038/nphoton.2015.78.

[4] Y.C. Lin, J.T. Huang, L.C. Wang, H.R. Hsu, Effect of Cu/(In+Ga) ratios on the secondary phases and the performance of Cu2InGa(S,Se)4thin film solar cells, J. Alloy. Compd. 690 (2017) 152–159, https://doi.org/10.1016/j.jallcom.2016.08.127.

[5] P. Prabeesh, I. Packia Selvam, S.N. Potty, Structural properties of czts thin films on glass and mo coated glass substrates: a rietveld refinement study, Appl. Phys. A Mater. Sci. Process. 124 (2018) 1–6, https://doi.org/10.1007/s00339-018-1649-7.

[6] P. Prabeesh, V.G. Sajeesh, I. Packia Selvam, M.S. Divya Bharati, G. Mohan Rao, S. N. Potty, CZTS solar cell with non-toxic buffer layer: a study on the sulphurization temperature and absorber layer thickness, Sol. Energy 207 (2020) 419–427, https://doi.org/10.1016/j.solener.2020.06.103.

[7] A. Dutta, R. Singh, S.K. Srivastava, T. Som, Tunable optoelectronic properties of radio frequency sputter-deposited Sb_2Se_3 thin films: role of growth angle and thickness, Sol. Energy 194 (2019) 716–723, https://doi.org/10.1016/j.solener.2019.11.016.

[8] A. Shongalova, M.R. Correia, J.P. Teixeira, J.P. Leitão, J.C. González, S. Ranjbar, S. Garud, B. Vermang, J.M.V. Cunha, P.M.P. Salomé, P.A. Fernandes, Growth of Sb_2Se_3 thin films by selenization of RF sputtered binary precursors, Sol. Energy Mater. Sol. Cells 187 (2018) 219–226, https://doi.org/10.1016/j.solmat.2018.08.003.

[9] X. Liu, J. Chen, M. Luo, M. Leng, Z. Xia, Y. Zhou, S. Qin, D.J. Xue, L. Lv, H. Huang, D. Niu, J. Tang, Thermal evaporation and characterization of Sb_2Se_3 thin film for substrate Sb_2Se_3/CdS solar cells, ACS Appl. Mater. Interfaces 6 (2014) 10687–10695, https://doi.org/10.1021/am502427s.

[10] N. Spalatu, R. Krautmann, A. Katerski, E. Karber, R. Josepson, J. Hiie, I.O. Acik, M. Krunks, Screening and optimization of processing temperature for Sb2Se3 thin film growth protocol: interrelation between grain structure, interface intermixing and solar cell performance, Sol. Energy Mater. Sol. Cells 225 (2021), https://doi.org/10.1016/j.solmat.2021.111045.

[11] H. Shiel, O.S. Hutter, L.J. Phillips, J.E.N. Swallow, L.A.H. Jones, T.J. Featherstone, M.J. Smiles, P.K. Thakur, T.L. Lee, V.R. Dhanak, J.D. Major, T.D. Veal, Natural Band Alignments and Band Offsets of Sb2Se3Solar Cells, ACS Appl. Energy Mater. 3 (2020) 11617–11626, https://doi.org/10.1021/acsaem.0c01477.

[12] R. Juškėnas, A. Naujokaitis, A. Drabavičius, V. Pakštas, D. Vainauskas, R. Kondrotas, Seed Layer Optimisation for Ultra-Thin Sb_2Se_3 Solar Cells on TiO2 by Vapour Transport Deposition, Materials 15 (2022), https://doi.org/10.3390/ma15238356.

[13] R. Krautmann, N. Spalatu, R. Gunder, D. Abou-Ras, T. Unold, S. Schorr, M. Krunks, I.O. Acik, Analysis of grain orientation and defects in Sb 2 Se 3 solar cells fabricated by close-spaced sublimation, Sol. Energy 225 (2021) 494–500, https://doi.org/10.1016/j.solener.2021.07.022.

[14] X. Wen, C. Chen, S. Lu, K. Li, R. Kondrotas, Y. Zhao, W. Chen, L. Gao, C. Wang, J. Zhang, G. Niu, J. Tang, Vapor transport deposition of antimony selenide thin film solar cells with 7.6% efficiency, (2021). https://doi.org/10.1038/s41467-018-04634-6.

[15] L.J. Phillips, C.N. Savory, O.S. Hutter, P.J. Yates, H. Shiel, S. Mariotti, L. Bowen, M. Birkett, K. Durose, D.O. Scanlon, J.D. Major, Current enhancement via a TiO 2 window layer for CSS Sb 2 Se 3 solar cells: performance limits and high V oc, IEEE J. Photo 9 (2019) 544–551, https://doi.org/10.1109/JPHOTOV.2018.2885836.

[16] M. Koltsov, R. Krautmann, A. Katerski, N. Maticiuc, M. Krunks, I. Oja Acik, N. Spalatu, A post-deposition annealing approach for organic residue control in TiO2 and its impact on Sb_2Se_3/TiO_2 device performance, Faraday Discuss. (2022), https://doi.org/10.1039/d2fd00064d.

[17] S. Chen, Y.A. Ye, M. Ishaq, D.Lou Ren, P. Luo, K.W. Wu, Y.J. Zeng, Z.H. Zheng, Z. H. Su, G.X. Liang, Simultaneous band alignment modulation and carrier dynamics optimization enable highest efficiency in Cd-Free Sb_2Se_3 solar cells, Adv. Funct. Mater. (2024), https://doi.org/10.1002/adfm.202403934.

[18] L. Wang, D.B. Li, K. Li, C. Chen, H.X. Deng, L. Gao, Y. Zhao, F. Jiang, L. Li, F. Huang, Y. He, H. Song, G. Niu, J. Tang, Stable 6%-efficient Sb_2Se_3 solar cells with a ZnO buffer layer, Nat. Energy 2 (2017), https://doi.org/10.1038/nenergy.2017.46.

[19] Z. Chen, H. Guo, C. Ma, X. Wang, X. Jia, N. Yuan, J. Ding, Efficiency improvement of Sb2Se3 solar cells based on La-doped SnO2 buffer layer, Sol. Energy 187 (2019) 404–410, https://doi.org/10.1016/j.solener.2019.05.026.

[20] Z. Duan, X. Liang, Y. Feng, H. Ma, B. Liang, Y. Wang, S. Luo, S. Wang, R.E. I. Schropp, Y. Mai, Z. Li, Sb_2Se_3 thin-film solar cells exceeding 10% power conversion efficiency enabled by injection vapor deposition technology, Adv. Mater. 34 (2022), https://doi.org/10.1002/adma.202202969.

[21] L. Wang, M. Luo, S. Qin, X. Liu, J. Chen, B. Yang, M. Leng, D.J. Xue, Y. Zhou, L. Gao, H. Song, J. Tang, Ambient CdCl2 treatment on CdS buffer layer for improved performance of Sb2Se3 thin film photovoltaics, Appl. Phys. Lett. 107 (2015), https://doi.org/10.1063/1.4932544.

[22] D.B. Li, X. Yin, C.R. Grice, L. Guan, Z. Song, C. Wang, C. Chen, K. Li, A.J. Cimaroli, R.A. Awni, D. Zhao, H. Song, W. Tang, Y. Yan, J. Tang, Stable and efficient CdS/Sb_2Se_3 solar cells prepared by scalable close space sublimation, Nano Energy 49 (2018) 346–353, https://doi.org/10.1016/j.nanoen.2018.04.044.

[23] T.P. Weiss, I. Minguez-Bacho, E. Zuccalà, M. Melchiorre, N. Valle, B. El Adib, T. Yokosawa, E. Spiecker, J. Bachmann, P.J. Dale, S. Siebentritt, Post-deposition

annealing and interfacial atomic layer deposition buffer layers of Sb_2Se_3/CdS stacks for reduced interface recombination and increased open-circuit voltages, Prog. Photovolt.: Res. Appl. (2022), https://doi.org/10.1002/pip.3625.
[24] J. Tao, X. Hu, J. Xue, Y. Wang, G. Weng, S. Chen, Z. Zhu, J. Chu, Investigation of electronic transport mechanisms in Sb_2Se_3 thin-film solar cells, Sol. Energy Mater. Sol. Cells 197 (2019) 1–6, https://doi.org/10.1016/j.solmat.2019.04.003.
[25] S. Vadakkedath Gopi, N. Spalatu, M. Basnayaka, R. Krautmann, A. Katerski, R. Josepson, R. Grzibovskis, A. Vembris, M. Krunks, I. Oja Acik, Post deposition annealing effect on properties of CdS films and its impact on CdS/Sb_2Se_3 solar cells performance, Front Energy Res 11 (2023), https://doi.org/10.3389/fenrg.2023.1162576.
[26] J. Zhou, X. Zhang, H. Chen, Z. Tang, D. Meng, K. Chi, Y. Cai, G. Song, Y. Cao, Z. Hu, Dual-function of $CdCl_2$ treated SnO_2 in Sb_2Se_3 solar cells, Appl. Surf. Sci. 534 (2020), https://doi.org/10.1016/j.apsusc.2020.147632.
[27] Y. Luo, G. Chen, S. Chen, N. Ahmad, M. Azam, Z. Zheng, Z. Su, M. Cathelinaud, H. Ma, Z. Chen, P. Fan, X. Zhang, G. Liang, Carrier transport enhancement mechanism in highly efficient antimony selenide thin-film solar cell, Adv. Funct. Mater. (2023), https://doi.org/10.1002/adfm.202213941.
[28] N. Maticiuc, J. Hiie, T. Raadik, A. Graf, A. Gavrilov, The role of Cl in the chemical bath on the properties of CdS thin films, Thin Solid Films (2013) 184–187, https://doi.org/10.1016/j.tsf.2012.11.107.
[29] T.D.C. Hobson, L.J. Phillips, O.S. Hutter, H. Shiel, J.E.N. Swallow, C.N. Savory, P. K. Nayak, S. Mariotti, B. Das, L. Bowen, L.A.H. Jones, T.J. Featherstone, M. J. Smiles, M.A. Farnworth, G. Zoppi, P.K. Thakur, T.L. Lee, H.J. Snaith, C. Leighton, D.O. Scanlon, V.R. Dhanak, K. Durose, T.D. Veal, J.D. Major, Isotype Heterojunction Solar Cells Using n-Type Sb_2Se_3 Thin Films, Chem. Mater. 32 (2020) 2621–2630, https://doi.org/10.1021/acs.chemmater.0c00223.
[30] Y. Zhou, Y. Li, J. Luo, D. Li, X. Liu, C. Chen, H. Song, J. Ma, D.J. Xue, B. Yang, J. Tang, Buried homojunction in CdS/Sb_2Se_3 thin film photovoltaics generated by interfacial diffusion, Appl. Phys. Lett. 111 (2017), https://doi.org/10.1063/1.4991539.
[31] I.O. Oladeji, L. Chow, C.S. Ferekides, V. Viswanathan, Z. Zhao, Metal/CdTe/CdS/Cd1−xZnxS/TCO/glass: a new CdTe thin film solar cell structure, Sol. Energy Mater. Sol. Cells 61 (2000) 203–211, https://doi.org/10.1016/S0927-0248(99)00114-2.
[32] A. Graf, N. Maticiuc, N. Spalatu, V. Mikli, A. Mere, A. Gavrilov, J. Hiie, Electrical characterization of annealed chemical-bath-deposited CdS films and their application in superstrate configuration CdTe/CdS solar cells. Thin Solid Films, Elsevier B.V., 2015, pp. 351–355, https://doi.org/10.1016/j.tsf.2014.11.003.
[33] H. Guo, Z. Chen, X. Wang, Q. Cang, X. Jia, C. Ma, N. Yuan, J. Ding, Enhancement in the efficiency of Sb2Se3 thin-film solar cells by increasing carrier concertation and inducing columnar growth of the grains, Sol. RRL 3 (2019), https://doi.org/10.1002/solr.201800224.
[34] S.R. Ferrá-González, D. Berman-Mendoza, R. García-Gutiérrez, S.J. Castillo, R. Ramírez-Bon, B.E. Gnade, M.A. Quevedo-López, Optical and structural properties of CdS thin films grown by chemical bath deposition doped with Ag by ion exchange, Opt. (Stuttg.) 125 (2014) 1533–1536, https://doi.org/10.1016/j.ijleo.2013.08.035.
[35] N. Maticiuc, J. Hiie, V. Mikli, T. Potlog, V. Valdna, Structural and optical properties of cadmium sulfide thin films modified by hydrogen annealing, Mater. Sci. Semicond. Process 26 (2014) 169–174, https://doi.org/10.1016/j.mssp.2014.04.031.
[36] T. Sivaraman, V. Narasimman, V.S. Nagarethinam, A.R. Balu, Effect of chlorine doping on the structural, morphological, optical and electrical properties of spray deposited CdS thin films, Prog. Nat. Sci.: Mater. Int. 25 (2015) 392–398, https://doi.org/10.1016/j.pnsc.2015.09.010.
[37] J. Hiie, T. Dedova, V. Valdna, K. Muska, Comparative study of nano-structured CdS thin films prepared by CBD and spray pyrolysis: annealing effect, Thin Solid Films 511–512 (2006) 443–447, https://doi.org/10.1016/j.tsf.2005.11.070.
[38] O. De Melo, L. Hernández, O. Zelaya-Angel, R. Lozada-Morales, M. Becerril, E. Vasco, Low resistivity cubic phase CdS films by chemical bath deposition technique, Appl. Phys. Lett. 65 (1994) 1278–1280, https://doi.org/10.1063/1.112094.
[39] N. Maticiuc, A. Katerski, M. Danilson, M. Krunks, J. Hiie, XPS study of OH impurity in solution processed CdS thin films, Sol. Energy Mater. Sol. Cells 160 (2017) 211–216, https://doi.org/10.1016/j.solmat.2016.10.040.
[40] G. Liang, M. Chen, M. Ishaq, X. Li, R. Tang, Z. Zheng, Z. Su, P. Fan, X. Zhang, S. Chen, Crystal growth promotion and defects healing enable minimum open-circuit voltage deficit in antimony selenide solar cells, Adv. Sci. 9 (2022), https://doi.org/10.1002/advs.202105142.
[41] X. Liu, C. Chen, L. Wang, J. Zhong, M. Luo, J. Chen, D.J. Xue, D. Li, Y. Zhou, J. Tang, Improving the performance of Sb_2Se_3 thin film solar cells over 4% by controlled addition of oxygen during film deposition, Prog. Photovolt.: Res. Appl. 23 (2015) 1828–1836, https://doi.org/10.1002/pip.2627.
[42] G. Chen, Y. Luo, M. Abbas, M. Ishaq, Z. Zheng, S. Chen, Z. Su, X. Zhang, P. Fan, G. Liang, Suppressing buried interface nonradiative recombination losses toward high-efficiency antimony triselenide solar cells, Adv. Mater. 36 (2024), https://doi.org/10.1002/adma.202308522.
[43] R. Tang, S. Chen, Z.H. Zheng, Z.H. Su, J.T. Luo, P. Fan, X.H. Zhang, J. Tang, G. X. Liang, Heterojunction annealing enabling record open-circuit voltage in antimony triselenide solar cells, Adv. Mater. 34 (2022), https://doi.org/10.1002/adma.202109078.
[44] M. Azam, Y.Di Luo, R. Tang, S. Chen, Z.H. Zheng, Z.H. Su, A. Hassan, P. Fan, H. L. Ma, T. Chen, G.X. Liang, X.H. Zhang, Organic chloride salt interfacial modified crystallization for efficient antimony selenosulfide solar cells, ACS Appl. Mater. Interfaces 14 (2022) 4276–4284, https://doi.org/10.1021/acsami.1c20779.
[45] H. Cai, R. Cao, J. Gao, C. Qian, B. Che, R. Tang, C. Zhu, T. Chen, Interfacial Engineering towards Enhanced Photovoltaic Performance of Sb2Se3 Solar Cell, Adv. Funct. Mater. (2022), https://doi.org/10.1002/adfm.202208243.

Journal of Alloys and Compounds 1008 (2024) 176729

Contents lists available at ScienceDirect

Journal of Alloys and Compounds

journal homepage: www.elsevier.com/locate/jalcom

Corrigendum

Corrigendum to "An alternative chlorine-assisted optimization of CdS/Sb_2Se_3 solar cells: Towards understanding of chlorine incorporation mechanism" [J. Alloy. Compd. 1005 (2024) 176175]

Sajeesh Vadakkedath Gopi [a,*], Nicolae Spalatu [a,*], Atanas Katerski [a], Jaroslav Kuliček [b], Bohuslav Rezek [b], Egor Ukraintsev [b], Markéta Šlapal Bařinková [b], Guillaume Zoppi [c], Liga Ignatane [d], Raitis Grzibovskis [d], Malle Krunks [a], Ilona Oja Acik [a]

[a] Department of Materials and Environmental Technology, Tallinn University of Technology, Ehitajate tee 5, Tallinn, Estonia
[b] Faculty of Electrical Engineering, Czech Technical University in Prague, Technická 2, 166 27, Prague, Czech Republic
[c] Department of Mathematics, Physics, and Electrical Engineering, Northumbria University, Newcastle-upon-Tyne NE1 8ST, United Kingdom
[d] Institute of Solid-State Physics, University of Latvia, Riga, Latvia

The authors regret to request to do two major changes in the published article

1. In the PDF version of the article, there is a typographical error in the name of one coauthor. The name '**Bohuslav Razek**' should be corrected to '**Bohuslav Rezek**.'
2. Additionally, an important project was inadvertently omitted from the acknowledgements. The following project should be included: **'MEYS project No. CZ.02.01.01/00/22_008/0004617 ("The Energy Conversion and Storage") under the Programme Johannes Amos Comenius, call Excellent Research'**

The authors would like to apologise for any inconvenience caused.

DOI of original article: https://doi.org/10.1016/j.jallcom.2024.176175.
* Corresponding authors.
E-mail addresses: sajeesh.vadakkedath@taltech.ee (S. Vadakkedath Gopi), nicolae.spalatu@taltech.ee (N. Spalatu), atanas.katerski@taltech.ee (A. Katerski), kulicjar@fel.cvut.cz (J. Kuliček), rezekboh@fel.cvut.cz (B. Rezek), ukraiego@fel.cvut.cz (E. Ukraintsev), barinmar@fel.cvut.cz (M.Š. Bařinková), guillaume.zoppi@northumbria.ac.uk (G. Zoppi), liga.ignatane@cfi.lu.lv (L. Ignatane), raitis.g@cfi.lu.lv (R. Grzibovskis), malle.krunks@taltech.ee (M. Krunks), ilona.oja@taltech.ee (I.O. Acik).

https://doi.org/10.1016/j.jallcom.2024.176729

Available online 2 October 2024
0925-8388/© 2024 The Author(s). Published by Elsevier B.V. All rights are reserved, including those for text and data mining, AI training, and similar technologies.

Appendix 3

Publication III

S. V. Gopi, R. Krautmann, A. Katerski, R. Josepson, D. Untila, J. Hiie, M. Krunks, I. Oja Acik, N. Spalatu, "Optimization of VTD Sb_2Se_3 absorber growth rate in CdS/Sb_2Se_3 thin film solar cells: A defect perspective on chloride vs non-chloride based devices", Solar Energy Materials and Solar Cells, vol. 293, 2025, DOI: 10.1016/j.solmat.2025.113856.

Solar Energy Materials & Solar Cells 293 (2025) 113856

Contents lists available at ScienceDirect

Solar Energy Materials and Solar Cells

journal homepage: www.elsevier.com/locate/solmat

Optimization of VTD Sb_2Se_3 absorber growth rate in CdS/Sb_2Se_3 thin film solar cells: A defect perspective on chloride vs non-chloride based devices

Sajeesh Vadakkedath Gopi [a,**], Robert Krautmann [a], Atanas Katerski [a], Raavo Josepson [b], Dumitru Untila [a], Jaan Hiie [a], Malle Krunks [a], Ilona Oja Acik [a], Nicolae Spalatu [a,*]

[a] Department of Materials and Environmental Technology, Tallinn University of Technology, Ehitajate tee 5, 19086, Tallinn, Estonia
[b] Division of Physics, Tallinn University of Technology, Ehitajate tee 5, 19086, Tallinn, Estonia

ARTICLE INFO

Keywords:
CdS/Sb2Se3 thin film solar cells
Vapor transport deposition
Chloride processed CdS
Admittance spectroscopy
interface defects

ABSTRACT

Control of source-to-substrate distance ($D_{So\text{-}Sub}$) and carrier gas in vapor transport deposition (VTD) of thin-film chalcogenide absorbers is crucial for ensuring uniform deposition and high film quality in solar cells. While well-optimized for large-scale CdTe, identifying a suitable VTD growth protocol for Sb_2Se_3 remains challenging due to its pseudo-1D ribbon-like structure. This challenge becomes even more complex for the CdS/Sb_2Se_3 device platform, where issues such as excessive intermixing and elemental diffusion at the CdS/Sb_2Se_3 interface must be mitigated to achieve a high-quality heterojunction and, consequently, a highly efficient solar cell. In this work, we address this challenge by investigating the impact of VTD $D_{So\text{-}Sub}$ in an Ar gas flow on the properties of Sb_2Se_3 and CdS/Sb_2Se_3 cells, comparing devices with and without chloride-processed CdS. It was found that at $D_{So\text{-}Sub} \leq$ 3 cm, a high growth rate with excessive oversaturation resulted in rough Sb_2Se_3 films with small grains. $D_{So\text{-}Sub} \approx$ 6 cm provided a balanced growth rate, leading to larger grains and a uniform surface, whereas $D_{So\text{-}Sub} \geq$ 10 cm resulted in a low growth rate and a highly dispersed structure. Solar cells with VTD $D_{So\text{-}Sub} \approx$ 6 cm and chloride-processed CdS reached 5 % efficiency, ~10 % higher than unprocessed counterparts. A comprehensive comparative analysis between these two device architectures is provided, highlighting the interrelation between absorber quality at different $D_{So\text{-}Sub}$, cell performance, defects, and recombination processes, contributing to a better understanding and optimization of CdS/Sb_2Se_3 solar cells.

1. Introduction

Over the past decade, antimony selenide (Sb_2Se_3) solar cells have achieved significant advancements in power conversion efficiency (PCE) and increased research interest. The material's exceptional properties, including a suitable band gap (~1.2 eV), high absorption coefficient (~10^4 cm^{-1}), and the possibility to control both n-type and p-type conductivity, position it as a promising candidate for the development of non-toxic and earth-abundant solar cells [1,2]. Notable features such as a low probability of secondary phase formation, low melting point, and unique 1D crystal structure facilitate the fabrication of thin films using cost-effective and scalable methods, such as close-spaced sublimation (CSS) and vapor transport deposition (VTD) [3,4]. All these material advantages have enabled rapid progress in achieving solar cell devices with a PCE of ~11 %, yet there remains considerable room for further improvement toward the 30 % theoretical limit predicted by the Shockley–Queisser (SQ) theory [5]. Key challenges in advancing Sb_2Se_3 solar cell performance include achieving columnar grain growth, selecting suitable partner layers, and mitigating interface and bulk defects [4,6,7]. Researchers have successfully addressed the challenge of columnar grain growth through rapid high-temperature deposition and the incorporation of seed layers, which have led to higher-quality photovoltaic-grade Sb_2Se_3 films, particularly using CSS and VTD methods [3,8]. Moreover, VTD offers additional control parameters, such as source-to-substrate distance ($D_{So\text{-}Sub}$) and the incorporation of carrier gases (e.g., Ar or N_2), providing greater flexibility to fine-tune film properties compared to CSS, further enhancing film quality and device performance.

Cadmium sulfide (CdS) has traditionally been utilized as an electron transport layer (ETL) for Sb_2Se_3 solar cells due to its well-established properties and optimized performance in cadmium telluride (CdTe) and copper indium gallium selenide (CIGS) solar cells [9–11]. CdS

* Corresponding author.
** Corresponding author.
E-mail addresses: sajeesh.vadakkedath@taltech.ee (S. Vadakkedath Gopi), nicolae.spalatu@taltech.ee (N. Spalatu).

https://doi.org/10.1016/j.solmat.2025.113856
Received 12 March 2025; Received in revised form 16 July 2025; Accepted 17 July 2025
Available online 23 July 2025
0927-0248/© 2025 The Authors. Published by Elsevier B.V. This is an open access article under the CC BY-NC license (http://creativecommons.org/licenses/by-nc/4.0/).

provides suitable band alignment with Sb_2Se_3, facilitating efficient carrier separation. Alternative, wider band gap ETL layers such as TiO_2 [12], ZnO [13], Zn_2SnO_4 (ZTO) [45], and SnO_2 [15] have been explored to enhance the performance of Sb_2Se_3 solar cells. Among these, TiO_2 has emerged as a promising candidate, particularly for overcoming transparency limitations and minimizing intermixing which has been reported in some cases for CdS-based Sb_2Se_3 cells. TiO_2 films, developed through techniques such as spin coating [16], spray deposition [17], and direct current (DC) sputtering [6], have demonstrated noticeable performance.

Independent of the ETL used, researchers have investigated various strategies to optimize the ETL-absorber interface properties and reduce interface defects, further enhancing the overall performance of Sb_2Se_3 solar cells. In this context, key strategies that have been intensively applied in recent years for both CdS and TiO_2-based device platforms include the application of $CdCl_2$ post-deposition treatments (PDTs) for the ETL in air at 380–420 °C and/or the incorporation of an intermediate interface layer between ETL and absorber [16,18].

Several studies have reported that these approaches can effectively reduce CdSe formation at the main interface and limit Cd diffusion into the absorber layer [12]. However, the impact of CdSe formation and/or Cd diffusion on the conductivity type and defect states in the Sb_2Se_3 absorber remains debatable, with some reports indicating a beneficial effect, while others suggest a detrimental one. An extensive analysis of reports published between 2005 and 2024 on the defect formation in Sb_2Se_3 within CdS/Sb_2Se_3 solar cells, comparing devices with and without $CdCl_2$ PDT for the CdS ETL indicates that in CdS/Sb_2Se_3 solar cells without $CdCl_2$ treatment, the predominant defect is selenium vacancy (V_{Se}), whereas in devices incorporating $CdCl_2$-treated CdS, antimony substitution by selenium (Se_{Sb}) emerges as the most dominant defect, accounting for approximately 50 % of the reported absorber defects. Several researchers, including [19–21], [2], [22–24], have reported Se_{Sb} defects in interface-modified CdS/Sb_2Se_3 solar cells. Notably [22], identified a Se_{Sb} defect with an activation energy of 0.11 eV and a defect density of 10^{16} cm^{-3}. These findings indicate that post deposition treatments of the ETL layer with interface engineering and selenium treatments have improved the performance of Sb_2Se_3 solar cells by mitigating the effects of V_{Se} defects.

Previous studies have presented mixed interpretations regarding the impact of $CdCl_2$ treatment on the properties of CdS/Sb_2Se_3 solar cells. Several reports indicate that $CdCl_2$ treatment effectively reduces deep-level defects and interface trap states, thereby minimizing non-radiative recombination losses. This reduction in defect density contributes to an increase in carrier lifetime and open-circuit voltage (V_{OC}), ultimately enhancing overall device performance [25]. Additionally, some studies suggest that $CdCl_2$ treatment improves band alignment and promotes the formation of a more uniform and compact grain structure in Sb_2Se_3 films, which facilitates charge transport while reducing recombination losses at grain boundaries [15]. Furthermore, $CdCl_2$ treatment has been shown to enhance Cd interdiffusion into the absorber layer, leading to a graded interface that mitigates interface recombination and defect trap formation [19]. Conversely, other reports highlight potential challenges associated with $CdCl_2$ treatment, particularly the increased likelihood of CdSe formation at the CdS/Sb_2Se_3 interface, which may act as a barrier to efficient carrier transport [8]. In order to bring more insight into this part, in our previous work, we systematically investigated various post-deposition treatments and their effectiveness in addressing these challenges [26]. Notably, we introduced an ‘‘*in situ* chlorine’’ incorporation method, which had not been previously explored for CdS/Sb_2Se_3 solar cells. Through this novel approach, we optimized the chlorine concentration in the CdS films by systematically varying the concentration of NH_4Cl in the chemical bath deposition (CBD) precursor solution, resulting in a 20 % enhancement in solar cell PCE [27]. This improvement was primarily attributed to modifications in the electrical properties of the CdS films, including increased carrier concentration, reduced resistivity, and an altered work function, while preserving the morphology and structural integrity of the films. Within the same study, a key finding was the detection of Cd diffusion from CdS to Sb_2Se_3 by SIMS analysis. Although our previous research has improved the performance of NH_4Cl-treated CdS/Sb_2Se_3 solar cells, a detailed study of the defect states and the mechanisms behind this improvement is still lacking. In particular, the effect of chlorine incorporation in the CdS layer on interface recombination, as well as how VTD parameters, like growth rate, influence grain growth and defect formation in Sb_2Se_3, remain poorly understood. This work addresses these unexplored areas, revealing important knowledge gaps and offering new insights into the factors that limit the efficiency of these promising solar cells.

Thus, in this study, the CdS/Sb_2Se_3 solar cells were optimized by fine-tuning the deposition of VTD Sb_2Se_3 films through variations in the $D_{So\text{-}Sub}$ (3, 4, 6, and 10 cm) and incorporating inert gas (Ar) to control the growth rate and achieved more columnar and compact grain structures in the Sb_2Se_3 films. The CdS ETL layers were processed with chloride, incorporating 1 mM NH_4Cl into the chemical bath solution, as optimized in the previous study [27]. The structural properties and morphology of Sb_2Se_3 films grown on both with and without chloride-processed CdS layers were systematically analyzed using X-ray diffraction (XRD) and scanning electron microscopy (SEM). Solar cells were fabricated in a superstrate configuration (glass/-FTO/CdS/Sb_2Se_3/Au) with VTD-deposited Sb_2Se_3 films prepared at varying $D_{So\text{-}Sub}$ on CdS ETL with and without the chloride-process. The optimization of the VTD process resulted in an 8 % improvement in the PCE of the solar cells compared to our previous studies, with the final PCE of 5 %. Furthermore, a comprehensive defect analysis was performed using admittance spectroscopy and temperature-dependent I-V measurements, providing deeper insights into the performance enhancements and underlying device physics.

2. Experimental

2.1. Chemical bath deposition (CBD) of CdS films

CdS films were deposited on precleaned glass substrates (18 × 18 mm^2) using CBD technique as described in our previously published articles [27]. The NH_4Cl (1 mM) was added to the bath solution to incorporate chlorine into the CdS films. The deposition time was fixed to be 10 min at 79 °C to achieve a fixed thickness of ~100 nm. The CdS films without and with NH_4Cl are referred to as non-chloride and chloride-processed CdS films.

2.2. Deposition of CdS/Sb_2Se_3 solar cells

Sb_2Se_3 films were deposited on the glass/FTO/CdS substrate with/without NH_4Cl using VTD deposition. A three-zone furnace (Carbolite, Germany) was used for the film deposition with 5N pure Sb_2Se_3 granules purchased from Sigma Aldrich as source material (0.02 g). The quartz tube was evacuated up to 10^{-6} mbar using a combination of both a rotary pump and turbo molecular pump (Pfeiffer, Germany). $D_{So\text{-}Sub}$ distance was varied (3, 4, 6, and 10 cm), and Ar gas was introduced to the quartz tube at a flow rate of 0.05 l/min to reduce the vacuum to 1–1.3 × 10^{-3} mbar. The substrate and source temperatures were fixed at 420 and 520 °C, and the ramping rate and the deposition time were fixed at 20 °C/min and 1 min, respectively. After the deposition time, the furnace lid was opened, at the same time the vacuum pump was shifted from turbo to the rotary pump and the Ar flow was stopped. At this time, the vacuum level dropped to 10^{-2} mbar, which resulted in a rapid stoppage for the Sb_2Se_3 film deposition. The samples were kept inside the quartz tube at the same conditions till the temperature of the furnace reached 30 °C or less. Later, the quartz tube was vented, and the samples were taken out. The solar cells (glass/FTO/CdS/Sb_2Se_3/Au) with superstrate configuration were finished with the deposition of Au contacts using the thermal evaporation method. The completed solar cell

stacks were annealed in air on a hot plate at 120 °C for 10 min for better alignment of the films. Indium pads are added on top of the Au contacts before the admittance measurements for better contacts and protection for the device from damage.

2.3. Material and device characterizations

The structural properties of CdS and Sb_2Se_3 films were analyzed from X-ray diffraction (XRD) data. The measurements were performed using Rigaku Ultima IV system with Cu Kα radiation, equipped with D/tex Ultra silicon detector in the 2Θ step of 0.04° at 2–10s/step and sample rotation. The measured XRD patterns were compared with the standard data, JCPDS 01-074-9665 for CdS films and JCPDS 00-015-0861 for Sb_2Se_3 films.

The morphology, along with the thickness of the CdS and Sb_2Se_3 films, was obtained from scanning electron microscope (SEM) images from Zeiss EVO-MA15 equipped with a Zeiss HR FESEM Ultra 55 system.

The performance of the glass/FTO/CdS/Sb_2Se_3/Au solar cells was analyzed from the J-V data measured by AUTOLAB PGSTAT 30 and Oriel class A solar simulator 91159 A (100 mW/cm^2, AM 1.5G) at room temperature. The external quantum efficiency (EQE) of the solar cells was measured using a custom setup with Newport 300 W Xenon lamp 6911 as light source, Newport cornerstone 260 as monochromator and Si calibrated Merlin detector at 300–1000 nm wavelength range.

Temperature-dependent J-V characteristics under 100 mW/cm^2 condition of CdS/Sb_2Se_3 solar cells were measured with KEITHLEY 2400 Source Meter, where the temperature in Janis closed-cycle He cryostat was varied from 20 K to 320 K with a step of $\Delta T = 10$ K.

Temperature-dependent admittance spectroscopy measurements were made at 20 K–320 K with a temperature step of $\Delta T = 10$ K using a Wayne Kerr 6500B impedance analyzer. Impedance Z and phase angle θ were measured as a function of frequency f and temperature T. Frequency f was varied from 20 Hz to 10 MHz, and a minimum AC voltage of 30 mV was applied to remove the background noise. To get more understanding of the defects, dark measurements were carried out at 0, 0.2 and 0.4V forward DC bias conditions.

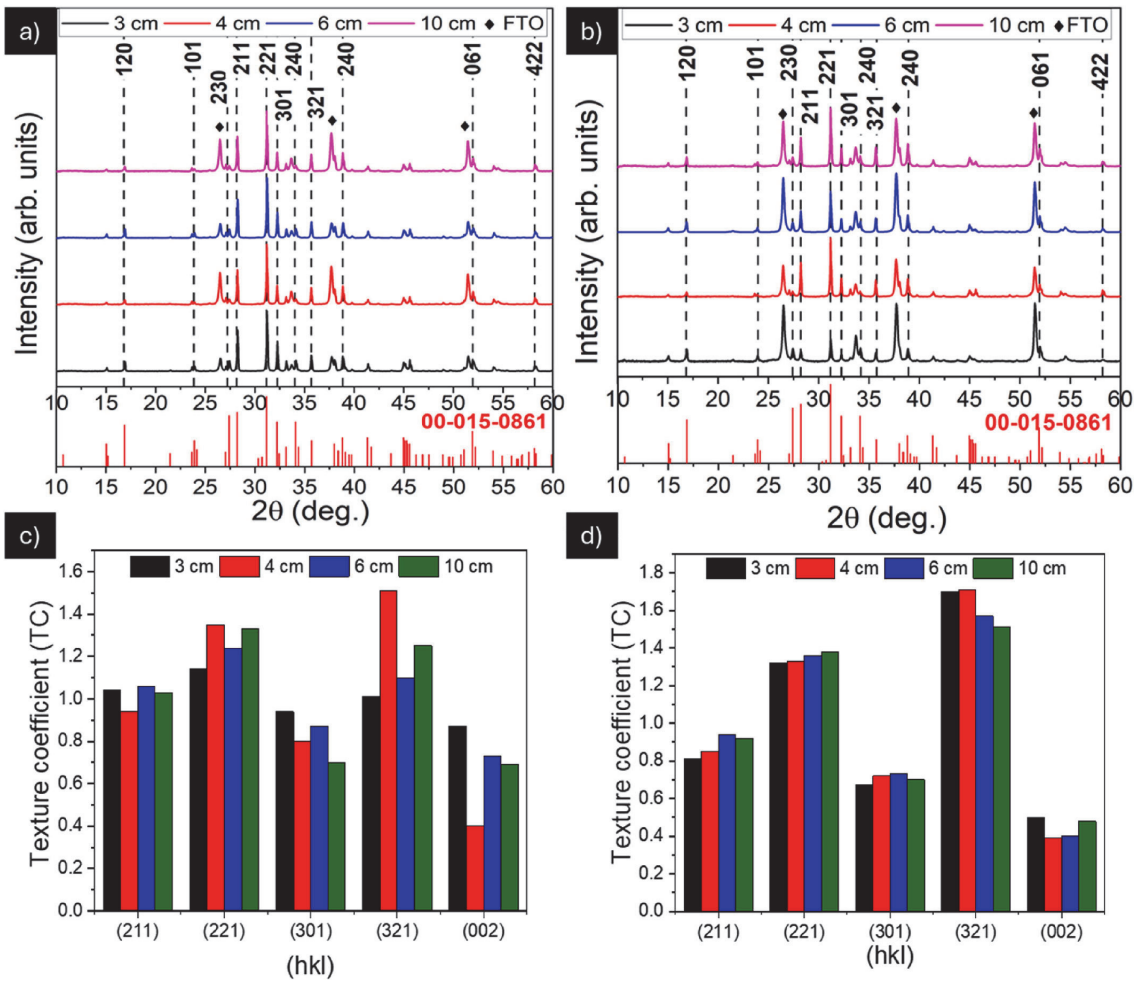

Fig. 1. a) & c) XRD pattern and Texture coefficient of Sb_2Se_3 films (constant thickness of ~0.8 μm) deposited on Non-Cl-CdS films at 3, 4, 6 and 10 source to substrate VTD distance ($D_{So\text{-}Sub}$), b) & d) XRD pattern and Texture coefficient of Sb_2Se_3 films deposited on Cl-CdS films at 3, 4, 6 and 10 $D_{So\text{-}Sub}$.

3. Results and discussion

3.1. Structural morphological properties of Sb_2Se_3 films

As mentioned in the introduction, our previous study proposed an alternative approach to the challenging $CdCl_2$ post-deposition treatment (PDT) of CdS in CdS/Sb_2Se_3 devices. This approach involved controllable Cl incorporation into CdS films by systematically varying the concentration of NH_4Cl in the chemical bath deposition (CBD) precursor solution. We found that incorporating 1 mM of NH_4Cl as a Cl source in CBD CdS was the optimal concentration, leading to a remarkable ~20 % enhancement in the PCE of CdS/Sb_2Se_3 devices. For simplicity, we labeled CdS films processed with and without NH_4Cl as chloride and non-chloride-processed CdS films (short abbreviation: Cl-CdS, Non-Cl-CdS) and for the solar cells (SCs) with these CdS layers as 'devices with/without chloride-processed CdS ETL', respectively (Cl-CdS SCs, Non-Cl-CdS SCs). It is important to note that in the same study, during VTD of Sb_2Se_3, the $D_{So\text{-}Sub}$ was maintained at 10 cm, ensuring a reasonable deposition rate of 0.16 μm/min. Building on these results, the first key step in this study was to further optimize the VTD growth rate while maintaining a constant Sb_2Se_3 absorber thickness of 0.8 ± 0.1 μm. This was achieved by systematically varying the $D_{So\text{-}Sub}$ at 3 cm, 4 cm, 6 cm, and 10 cm, corresponding to deposition rates of 1.0, 0.8, 0.4, and 0.16 μm/min, respectively. The deposition conditions are summarized in a table format in the supplementary information (Table S1). The impact of the VTD $D_{So\text{-}Sub}$ on the structural and morphological properties of Sb_2Se_3 deposited onto CdS/FTO/glass was analyzed by SEM and XRD. Fig. 1a and b present the XRD patterns of Sb_2Se_3 films deposited at $D_{So\text{-}Sub}$ of 3, 4, 6, and 10 cm. The XRD patterns were compared with the standard PDF card (00-015-0861). The patterns reveal prominent (221) and (211) peaks at 31.16° and 28.2° (2θ), correspondingly, which are consistently reported in the literature and very often linked with favorable columnar grain growth [3,8]. The texture coefficient (TC) of Sb_2Se_3 films grown on CdS buffer layers, both without (Fig. 1c) and with (Fig. 1d) NH_4Cl treatment, was calculated using the methodology described in previous reports [4]. The TC values were calculated using an equation,

$$TC = \frac{I(hkl)}{I_0(hkl)} \times \left[\frac{1}{N} \sum_{i=0}^{n} \frac{I(h_i k_i l_i)}{I_0(h_i k_i l_i)} \right]^{-1} \quad (1)$$

where I(*hkl*) is the experimentally obtained intensity of a given reflection with Miller indices (hkl), I_0 (*hkl*) is the corresponding reference intensity taken from the JCPDS Card No. 15–0861, and N is the total number of reflections considered in the calculation. The (321) peak exhibited the highest TC values, followed by the (221) and (211) peaks, confirming the hk1 orientation of Sb_2Se_3 films deposited via VTD, regardless of the employed Cl-CdS, Non-Cl-CdS, or the $D_{So\text{-}Sub}$. Notably, the Sb_2Se_3 films deposited on Cl-CdS films displayed more consistent TC values across varying $D_{So\text{-}Sub}$ compared to films deposited on Non-Cl-CdS films, suggesting enhanced uniformity in the structural properties.

The hk1 orientation of Sb_2Se_3 films plays a crucial role in determining device performance. This orientation facilitates improved carrier transport through the lattice, enhancing charge extraction [22]. In contrast, the hk0 orientation can result in increased carrier recombination, which negatively impacts the PCE of the device. Along with that, the Sb_2Se_3 grains should be more compact and pinhole-free. To analyze these aspects, the surface morphology of Sb_2Se_3 films deposited via the VTD method on Non-Cl-CdS (Fig. 2a–d) and Cl-CdS (Fig. 2e–h) ETL was analyzed from SEM images. For Sb_2Se_3 films deposited on Non-Cl-CdS, the film appeared compact and uniform at a $D_{So\text{-}Sub}$ of 3 cm (Fig. 2a). As the $D_{So\text{-}Sub}$ increased to 4 cm (Fig. 2b), the grain size and compactness improved. At $D_{So\text{-}Sub}$ 6 cm (Fig. 2c), irregular grain growth was observed, while a further increase of $D_{So\text{-}Sub}$ to 10 cm (Fig. 2d) resulted in a high degree of irregularity in both grain growth direction and size.

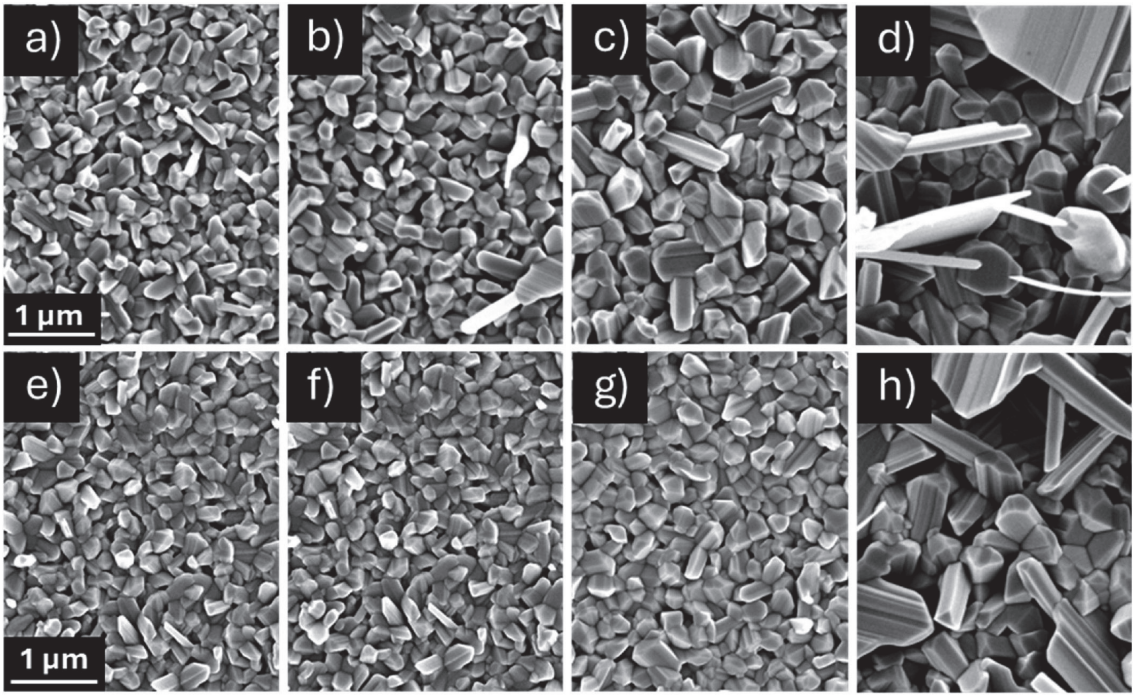

Fig. 2. (a–d) Surface SEM images of Sb_2Se_3 films deposited on Non-Cl-CdS films at 3, 4, 6 and 10 cm $D_{So\text{-}Sub}$ (e–h) Surface SEM images of Sb_2Se_3 films deposited on Cl-CdS films at 3, 4, 6 and 10 cm $D_{So\text{-}Sub}$.

This observation is further supported by the grain size distribution analysis (Fig. S2, supplementary information), derived from the SEM image presented in Fig. 2. In contrast, for Sb_2Se_3 films deposited on Cl-CdS films, the grain size, compactness, and uniformity improved progressively from 3 to 6 cm $D_{So\text{-}Sub}$ (Fig. 2e–g). Notably, at $D_{So\text{-}Sub}$ 6 cm, the Sb_2Se_3 film grown on the Cl-CdS substrate exhibited greater compactness and uniformity compared to the corresponding film deposited on Non-Cl-CdS. However, at a $D_{So\text{-}Sub}$ of 10 cm (Fig. 2h), the Sb_2Se_3 films were non-uniform and exhibited random grain orientations regardless of the Chloride treatment of CdS layer. Detailed cross-sectional SEM images of the Cl-CdS/Sb_2Se_3 heterojunction at different $D_{So\text{-}Sub}$ distances are provided in supplementary information (Fig. S1). As shown in Fig. S1a and S1f, significant re-evaporation of the Sb_2Se_3 films is evident at $D_{So\text{-}Sub}$ = 1–2 cm, resulting in a reduced film thickness of approximately 200 nm.

3.2. Device characteristics

The Sb_2Se_3 solar cells were fabricated in superstrate configuration with Cl-CdS and Non-Cl-CdS at different $D_{So\text{-}Sub}$ to study the effect of both changes on the device parameters (Fig. 3 and Table 1). The main solar cell parameters, such as open circuit voltage (V_{OC}), short circuit current (J_{SC}), fill factor (FF), and PCE, were extracted from the J-V characteristics of Non-Cl-CdS and Cl-CdS SCs (Fig. 3a–d and Table 1). In the case of Non-Cl-CdS SCs, the lowest V_{OC} of 346 mV was obtained with absorber processed at $D_{So\text{-}Sub}$ of 4 cm and the highest value of 364 mV was obtained at $D_{So\text{-}Sub}$ 6 cm. As the $D_{So\text{-}Sub}$ to 10 cm, the value again decreased to 352.4 mV. In the case of other parameters such as J_{SC}, FF and PCE (Fig. 3b, c and d), the values increase till 6 cm and then drop at $D_{So\text{-}Sub}$ of 10 cm. The highest J_{SC} of 24 mA/cm^2, PCE of 4.6 % and FF of 56.4 % for Non-Cl-CdS SCs were obtained at 6 cm $D_{So\text{-}Sub}$. At $D_{So\text{-}Sub}$ of 10 cm, the PCE value decreased from 4.6 % to 4.2 %. In the case of Cl-CdS SCs, the V_{OC} value increases from 345.4 mV to 391.5 mV as the $D_{So\text{-}Sub}$ increases from 3 to 10 cm. Meanwhile, the J_{SC} and PCE values increase till 6 cm distance and record their maximum (25 mA/cm^2 and 5 %), then decrease at 10 cm $D_{So\text{-}Sub}$. The highest PCE of 5 % was recorded for Cl-CdS SCs at $D_{So\text{-}Sub}$ of 6 cm during Sb_2Se_3-VTD deposition. The

Table 1
PV parameters from JV measurement of champion solar cells with and without chlorine processed CdS ETL at different $D_{So\text{-}Sub}$.

No.	Solar cell	$D_{So\text{-}Sub}$ (cm)	Device parameters			
			V_{OC} (mV)	J_{SC} (mA/cm^2)	FF (%)	PCE (%)
1.	SC with non-Cl-CdS	3	360.12	22.74	53.96	4.42
		4	350.09	23.02	55.13	4.44
		6	363.89	23.95	53.1	4.63
		10	354.74	23.58	51.71	4.33
2.	SC with Cl-CdS	3	353.17	19.65	55.47	3.85
		4	351.45	19.81	53.8	3.75
		6	376.91	24.97	52.83	4.97
		10	391.07	22.45	52.7	4.63

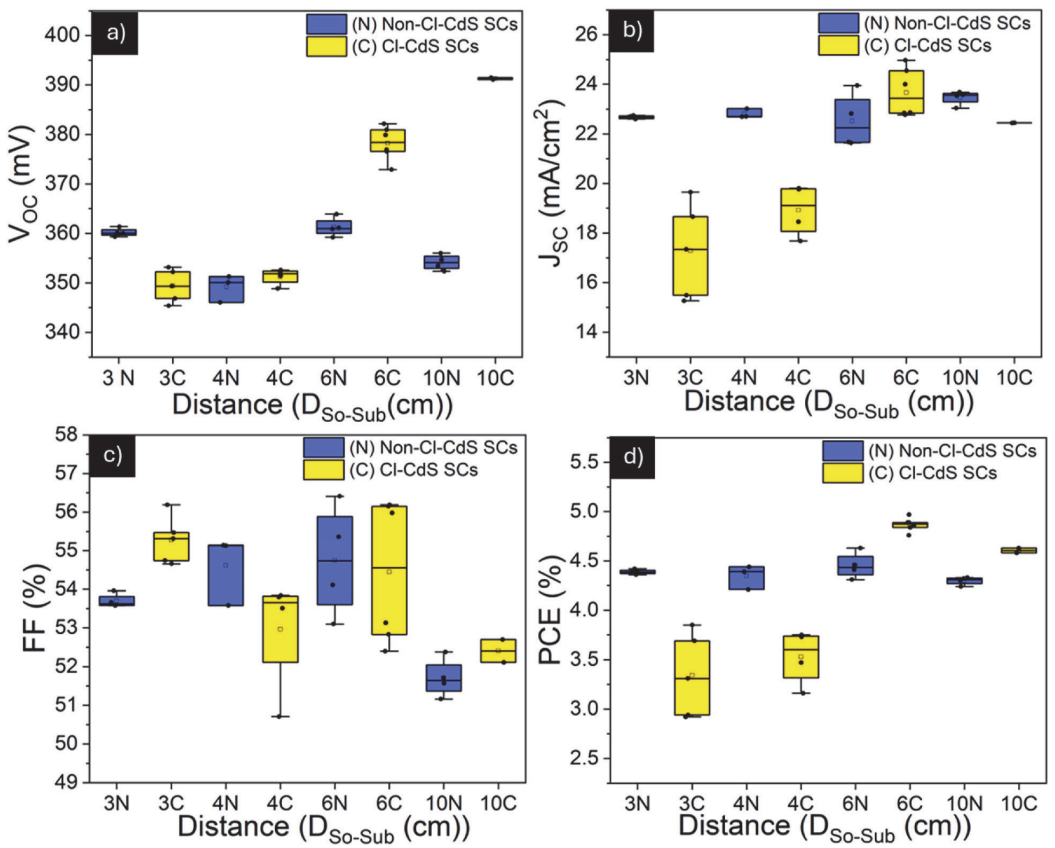

Fig. 3. Variation of PV parameters cell a) V_{OC}, b) J_{SC}, c) FF and d) PCE of Non-Cl-CdS and Cl-CdS SCs at different $D_{So\text{-}Sub}$ during VTD deposition. (N) and (C) stand for Non-Cl-CdS SCs and C-CdS SCs, while the numbers on the x-axis indicate the source-to-substrate distance ($D_{So\text{-}Sub}$).

superior performance of the Cl-CdS/Sb_2Se_3 solar cells at the optimal D_{So-Sub} of 6 cm is attributed to the enhanced compactness and uniformity of the Sb_2Se_3 grains, as evidenced by the surface morphology observed in the SEM images (Fig. 2g).

A significant reduction in PCE was observed for the Cl-CdS/Sb_2Se_3 solar cells compared to the non-Cl-CdS/Sb_2Se_3 at $D_{Sou-Sub}$ of 3 and 4 cm. It can primarily be attributed to the presence of chlorine content in the CdS layer. At shorter distances of 1–2 cm, we observed significant re-evaporation effects, which adversely impacted the Sb_2Se_3 absorber layer in terms of reduced thickness and compromised grain compactness (Fig. S1 in supplementary information). Although these issues appear to be mitigated at $D_{Sou-Sub}$ distances of 3 and 4 cm, the deposition of the absorber layer at 400 °C may act as a post-deposition annealing step for CdS, affecting the structural (for instance an intensive recrystallization of CdS can occur as well as interdiffusion of elements at the main interface) and optoelectronic properties of the CdS ETL and thus impacting the final device performance. Such effect has been observed in our previous study, where vacuum annealing of Cl-processed CdS at elevated temperatures (particularly around 400 °C) led to a degradation of all solar cell parameters [26]. This degradation trend is consistent with the performance reduction observed in the Cl-CdS/Sb_2Se_3 devices in the present study and may provide a plausible explanation for the lower PCE observed under these conditions. Although the earlier study employed closed space sublimation (CSS) for Sb_2Se_3 film deposition, the $D_{Sou-Sub}$ used was comparable to that in the current work. The main reason for this was attributed to the formation of CdO through the dissociation of $Cd(OH)_2$, which significantly reduces the carrier concentration of the CdS film, consequently affecting the formation of the heterojunction interface. So far, these results indicate that depending on the processing conditions of CdS ETL (Cl-vs non-Cl-processed) and the annealing temperature and environment (dictated in this case by the VTD deposition of the absorber), different conditions are established for achieving balanced optoelectronic properties in both the CdS and Sb_2Se_3 layers, as well as at their interface. It is evident that at $D_{Sou-Sub}$ distances between 1 and 4 cm, achieving this balance is particularly challenging. However, for the optimized $D_{Sou-Sub}$ distance of 6 cm, the resulting device performance suggests that a favorable trade-off between absorber-CdS quality and interface formation can be achieved, enabling higher PCE. Further study employing complementary analyses of this interface is needed to better understand the underlying mechanisms and to guide future device optimization.

Regardless of the employed Cl-CdS/Non-Cl-CdS the best device performance was achieved at 6 cm D_{So-Sub}. The J-V characteristics and EQE response of the best Cl-CdS and Non-Cl-CdS SCs are shown in Fig. 4a

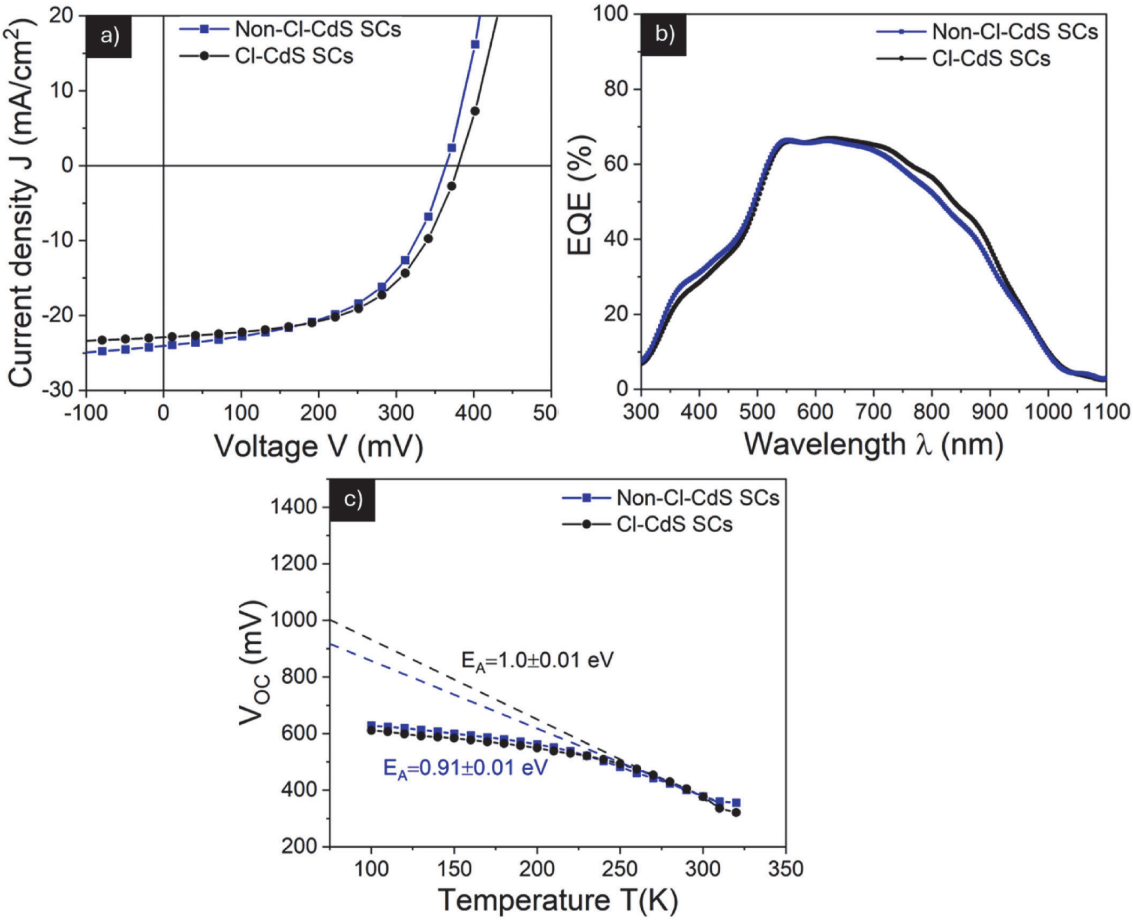

Fig. 4. (a) J–V characteristics and (b) EQE spectra of the best-performing Non-Cl-CdS and Cl-CdS SCs (c) Voc - temperature dependence for Non-Cl-CdS SCs and Cl-CdS SCs.

and b, respectively. The Cl-CdS SC exhibits a slightly enhanced EQE response in the 500–800 nm region. The parasitic absorption loss, which is inherent in the CdS/Sb_2Se_3 solar cells, still persists in both solar cells at ~500 nm wavelength. The integrated J_{SC} values have been calculated from the EQE data (Fig. S3) and found to be in good correlation with the values obtained from the J-V curve. In the lower wavelength region (300–550 nm) of the EQE spectra, the intensity is notably reduced compared to solar cells employing TiO_2 buffer layers (Hobson et al., 2020). This reduction can be attributed, on one hand, to parasitic absorption in the CdS layer, due to its lower bandgap (2.4 eV) relative to TiO_2 (~3.2 eV). On the other hand, the potential intermixing at the CdS/Sb_2Se_3 interface, previously reported in the literature, may also contribute to the low EQE response in the short wavelength region. Utilizing TiO_2 as a buffer layer can effectively reduce parasitic absorption in Sb_2Se_3 solar cells. However, despite its beneficial opto-electronic characteristics, TiO_2 poses considerable difficulties as a buffer/ETL for the deposition of Sb_2Se_3 films, especially in contrast to the more commonly used CdS layers. Although CSS has been successful in depositing Sb_2Se_3 on TiO_2, achieving an impressive PCE of 8.12 % [6] through the incorporation of a seed layer and RF sputtering, applying VTD in this scenario remains problematic and limited. Fewer studies report efficiencies of 4.8 % [3] and 5.33 % [28] indicating persistent challenges when utilizing TiO_2, prepared through either physical or chemical methods, as the ETL in VTD-processed Sb_2Se_3 devices. This issue correlates with differences in surface energy, defects, and the lattice matching of Sb_2Se_3 films prepared by VTD with those of TiO_2 films. Addressing these challenges will require more detailed investigations into the interfacial chemistry and crystallographic compatibility between TiO_2 and Sb_2Se_3, as well as potential surface treatments to enhance nucleation and grain growth.

Various strategies, such as introducing Al^{3+} or $CdCl_2$ treatment to the CdS layers [14,19,21], have been employed to address the intermixing effect. In our earlier study [27], the interface of CdS/Sb_2Se_3 device with Cl-CdS was thoroughly analyzed using secondary ion mass spectrometry (SIMS), which revealed significant Cd diffusion into the Sb_2Se_3 absorber layer. This diffusion, combined with the improved structural properties of the absorber layer achieved via VTD deposition, led to Cl-CdS/Sb_2Se_3 solar cells with a peak PCE of 4.6 %. In the present study, fine-tuning the absorber growth rate by adjusting the $D_{So\text{-}Sub}$ distance and introducing an Ar carrier gas further enhanced device performance, achieving a PCE of 5.0 %. This represents an approximate 10 % relative improvement over previously reported Cl-CdS/Sb_2Se_3 solar cells.

These results naturally lead to the consideration of the underlying physicochemical factors, including thermodynamic aspects, that govern the enhanced properties of the VTD-grown Sb_2Se_3 absorber and the corresponding CdS/Sb_2Se_3 interface. These factors also have important implications for overall device functionality. As emphasized in Section 3.1, the duration of the VTD process was adjusted for each source-to-substrate distance ($D_{So\text{-}Sub}$) to maintain a constant Sb_2Se_3 absorber thickness of 0.8 μm across all depositions. However, deposition conditions, such as growth rate and supersaturation, varied significantly with $D_{So\text{-}Sub}$. This, in turn, led to differences in the morphological and structural properties of the films and influenced the resulting device performance. In addition to these factors, the geometry of the VTD setup also plays a critical role in controlling the vapor flux and supersaturation. According to our experimental VTD setup (Fig. S5), the deposition process occurs inside a quasi-closed, coaxial inner quartz tube (length: 20 cm, inner diameter: 2.7 cm; volume: ~46.3 cm^3), inserted into a larger horizontal VTD furnace tube (length: 102 cm, inner diameter: 5.5 cm; volume: ~460.5 cm^3). Within this compact deposition space, it is reasonable to approximate the system operation like in the Knudsen (free molecular) flow regime under a working pressure of ~1×10^{-3} mbar (0.1 Pa), where vapor transport is dominated by line-of-sight molecular gas transport. The applied low carrier gas flow rate (0.05 LPM Ar) provides sufficient vapor refresh while avoiding dilution, and the small tube volume helps stabilize vapor density and thermal gradients. This controlled configuration minimizes vapor losses to sidewalls, ensures steady-state growth conditions, and enhances the effectiveness of source-to-substrate distance in regulating local supersaturation. Considering all these aspects, at the fixed source temperature T_{So} of 520 °C, the vapor pressure of Sb_2Se_3 was recalculated using the experimentally validated sublimation relation: $\log_{10}(p_{Torr}) = {}^{9566}/_{T} + 10.632$ [29,30], giving an estimated equilibrium vapor pressure of ~0.037 Torr (~5 Pa) at 520 °C. At the substrate temperature T_{Sub} of 420 °C, the equilibrium vapor pressure is much lower, between ~0.003 and 0.005 Torr (~0.4–0.7 Pa). This yields a supersaturation ratio of $S = {}^{P_v}/_{P_{eq}}$ of approximately 7–12 during deposition, a range high enough to affect film nucleation and growth behavior. At large $D_{So\text{-}Sub}$ (10 cm), vapor dilution and partial loss to sidewalls reduce supersaturation, leading to sparse nucleation and consequently, to a high degree of irregularity in both grain growth direction and size (Fig. 2d–h and Fig. S1). At $D_{So\text{-}Sub}$ between 3 and 6 cm, vapor arrival and supersaturation are balanced (S ≈ 2–5), with a balanced optimal 0.4 μm/min growth rate at 6 cm $D_{So\text{-}Sub}$, promoting larger, well-sintered grains with improved size distribution and uniformity and orientation. These improvements are further sustained by deposition onto Cl-CdS films, implying balanced interdiffusion (Cl, Cd) at the interface, as proved by SIMS [27], having also contributed to increased diffusion of nucleation centers (leading to the formation of larger Sb_2Se_3 grains). All these optimized features contribute to optoelectronic properties and CdS/Sb_2Se_3 interface quality, resulting in the enhanced 5 % device performance. On a practical note, these results show that source-to-substrate distance, growth rate, and vapor supersaturation are strongly interlinked through the VTD system geometry. These factors critically influence film quality and device performance, underscoring the need for careful system design and process control in VTD scalable Sb_2Se_3 solar cell manufacturing.

To explore the impact of defects on device performance, the variation of V_{OC} with temperature was analyzed for Cl-CdS and Non-Cl-CdS SCs (Fig. 4c). In both cases, the V_{OC} exhibited a plateau below a temperature of 200 K. The linear region of the V_{OC}-temperature curve was extrapolated to determine the activation energy (E_A), which was found to be approximately 0.91 eV for Non-Cl-CdS SCs solar cells and 1.0 eV for Cl-CdS SCs. These values are consistent with the reported bandgap of Sb_2Se_3 (~1.2 eV) [22] as well as the bandgap extracted from EQE (Fig. S4), indicating that interface recombination plays a significant role in limiting the V_{OC} of these devices. The E_A of the Cl-CdS SCs is closer to the bandgap of Sb_2Se_3 compared to the Non-Cl-CdS SCs. This suggests a higher degree of bulk recombination in the chlorinated devices, which could explain their relatively higher V_{OC} compared to the Non-Cl-CdS SCs, which have lower E_A values indicating higher interface recombination. This observation aligns with the J-V characteristics of the best-performing solar cells (Fig. 4a), where the Cl-CdS SCs exhibited a higher V_{OC} than Non-Cl-CdS SCs. These results underscore the critical role of interface engineering in enhancing the performance of Sb_2Se_3--based solar cells.

3.3. Defect analysis of the CdS/Sb_2Se_3 devices

Sb_2Se_3 devices continue to be hampered by a large concentration of bulk and interface defects. Distinguishing between the two types of defects is not an easy task and requires a combination of defect analyses to gain a more sophisticated understanding. First, we attempt to quantify the trap defect density from the dark J-V curves. Log-log plots of the dark J-V curves, as shown in Fig. 5a and b, enable the separation of three linear regions: Ohmic, Trap-filling-limit (TFL), and Cloud [31]. Linear extrapolation of the Ohmic and TFL regions provides an intersecting point, which is the TFL voltage (V_{TFL}) at which the trap states are expected to be filled. Trap density can be subsequently calculated by using the V_{TFL} in the following Equation (2):

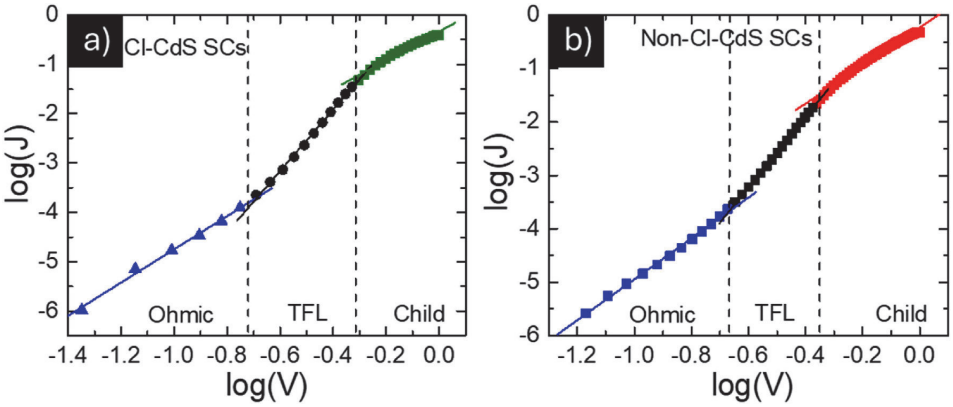

Fig. 5. Log(J)-log(V) plots deduced from dark J-V curves of Cl-CdS SCs (a) and Non-Cl-CdS (b) SCs.

$$N_T = \frac{2\varepsilon\varepsilon_0 V_{TFL}}{qL^2} \quad (2)$$

where N_T is trap density in cm^{-3}, ε is the dielectric constant of Sb_2Se_3 (15.1), ε is the electric constant, V_{TFL} is the trap-filling-limit voltage in V, q is electric charge in C, and L is the Sb_2Se_3 absorber thickness.

In this study, the V_{TFL} values obtained from Fig. 5a and b were 0.68 V and 0.64 V for Non-Cl-CdS and Cl-CdS SCs, respectively. A low V_{TFL} value (<0.2 V) is often interpreted as an indication of very low trap density; however, in some cases, it may also suggest poor charge injection or low carrier concentration. Conversely, a high V_{TFL} (>1 V) can be a sign of excessive traps and recombination losses, often associated with poor material quality, unoptimized interfaces, or deep-level defects. A moderate V_{TFL} (0.2–1.0 V) is generally desirable for high-efficiency thin-film solar cells, such as CdTe, CIGS, and perovskites [32], as it indicates controlled defect density and reasonable charge transport properties. In our case, both values are below 1.0 V (with a slightly lower V_{TFL} for the Cl-CdS SCs), suggesting a relatively low defect density and, consequently, an efficient charge transport.

The N_T values were calculated to be 7×10^{14} and 8×10^{14} cm^{-3}, for Non-Cl-CdS and Cl-CdS SCs, respectively. These trap density values are similar to the reported values of [33–35] and lower than those reported by Ref. [31]. This suggests that the optimized Sb_2Se_3 films deposited via the VTD method exhibit superior quality. Notably, the N_T value for the Non-Cl-CdS SCs is lower, indicating fewer trap sites and defect centers in the Sb_2Se_3 films. This observation suggests that the Sb_2Se_3 films grown on Non-Cl-CdS layers contain a lower density of trap centers, which may reduce the recombination of charge carriers at the interface and in the bulk of Sb_2Se_3.

To get more insights on the defects in Non-Cl-CdS and Cl-CdS SCs, temperature-dependent admittance (TAS) analysis was performed, as a powerful, proven technique for unveiling defects in the bulk Sb_2Se_3 [4,8]. In this study, we went one step further and attempted to identify the nature of the extracted activation energies. In the case of deep defects located in the absorber, the activation energy derived from admittance measurement usually corresponds to the energy difference between the defect level and a specific band edge (e.g., conduction or valence band). This energy is typically fixed and does not shift significantly with applied bias.

If the activation energy of a deep defect observed in TAS shifts with voltage bias, it is often an indication of an interface-related defect rather than a bulk defect in the absorber [36]. This is a common signature of interface states or defects near the junction, where the local potential varies with applied bias, altering the apparent activation energy.

Fig. 6a–f shows C-*f*-T curves of Cl-CdS and Non-Cl-CdS SCs measured at 0.0, 0.2, and 0.4 V. Capacitance was derived from the real and imaginary parts of impedance Z (*f*, T) signal and calculated using an equivalent circuit model, which comprises of a capacitor, a series and a parallel resistor [37]. It can be observed that the capacitance reaches a plateau value of 25–35 nF cm^{-2} near 100 K. Given that the reported value of the dielectric constant (ε) of Sb_2Se_3 is 15, the plateau corresponds well to the geometric capacitance of these devices.

Generally, a single capacitance step could be seen in the C-f-T curves. Determining the inflection points of the derivative plot of the capacitance (-*f*d*C*/d*f*) allows extraction of thermal activation energies from the Arrhenius plots via Equation. (3) [38],

$$\omega_0 = 2\pi f_0 = 2\xi_0 T^2 \exp\left(-\frac{E_A}{kT}\right) \quad (3)$$

where ξ_0 is the thermal emission prefactor, k is Boltzmann constant, T is temperature and E_A is activation energy.

For Cl-CdS SCs, the extracted E_A values were 0.44 eV, 0.45 eV, and 0.32 eV for 0 V, 0.2 V, and 0.4 V forward bias conditions, respectively (Fig. 7a). Similarly, for Non-Cl-CdS SCs, the E_A values were 0.50 eV, 0.47 eV, and 0.20 eV at 0 V, 0.2 V, and 0.4 V forward bias conditions, respectively (Fig. 7b). In both cases, the activation energy decreased with increasing bias voltage from 0 to 0.4 V. The fact that the activation energy remains the same at 0 V and 0.2 V but shifts at 0.4 V suggests that the defect is influenced by the applied bias. The increased bias may be shifting the Fermi level or modifying the depletion region in a way that affects the defect state. This is a common feature of interface defects, where their apparent activation energy depends on how the band alignment changes with bias [36,39]. The defect could be a trap state at the heterojunction, which starts to interact with the conduction or valence band more significantly at higher biases. Alternatively, it could be a defect in the buffer layer or near the interface, where the electric field modulates its energy.

It is important to emphasize that although admittance spectroscopy and DLTS provide powerful insights into electrically active defects, these techniques cannot directly identify the chemical origin of the defects. For this purpose, a correlation with theoretical studies, particularly defect formation energy calculations from density functional theory (DFT), is essential to guide defect attribution.

According to recent DFT studies [40], a wide range of native point defects are predicted in Sb_2Se_3, including vacancies, antisites, and interstitials. Among these, vacancy-type defects are generally considered dominant; however, the prevalence of specific defect types strongly depends on the composition of the vapor phase and the structural characteristics of the condensed phase during synthesis. Sb vacancy (V_{Sb}) is commonly associated with an activation energy of ~0.3–0.4 eV

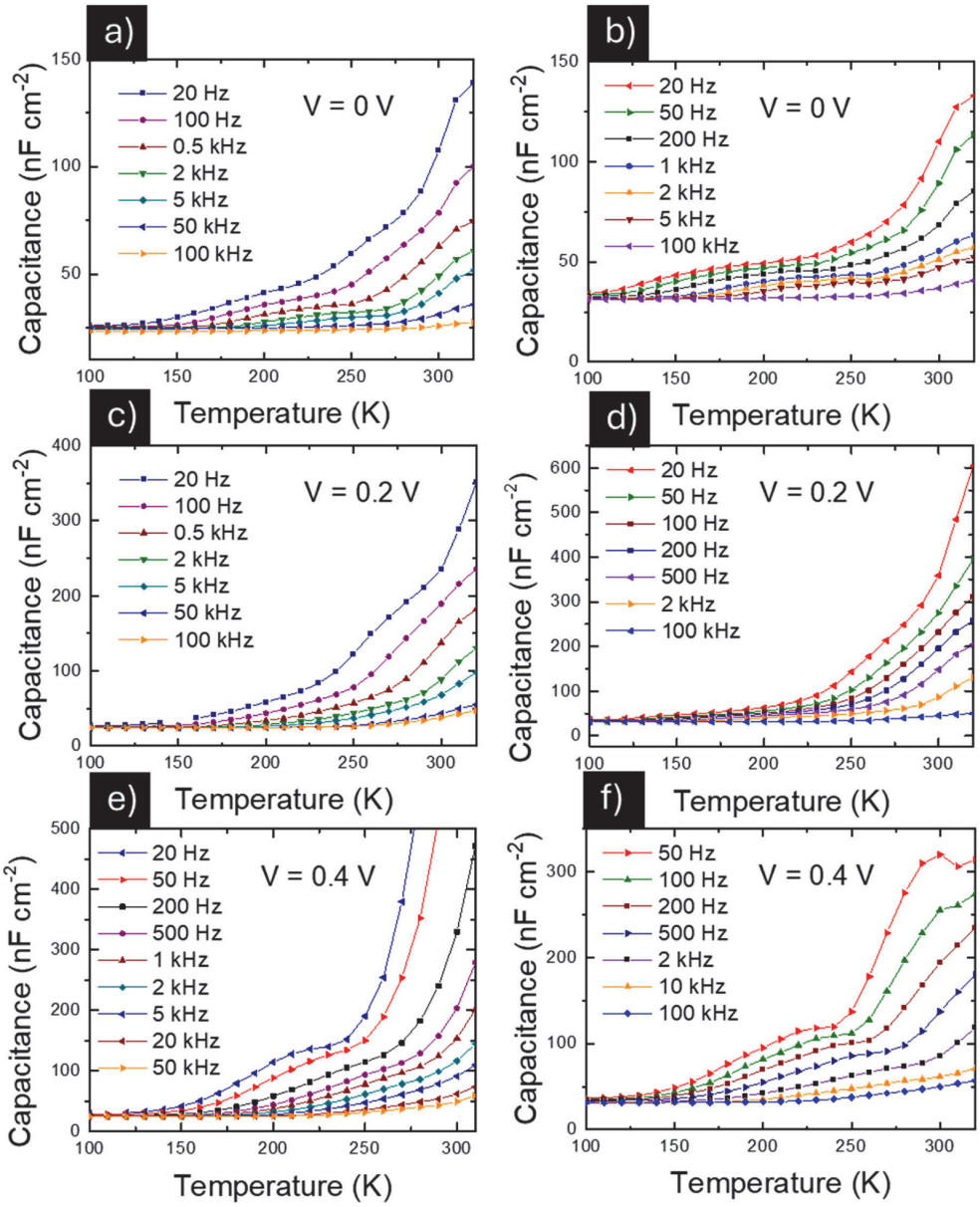

Fig. 6. C-f-T curves of Cl-CdS SCs measured under 0 V (a), 0.2 V (c), and 0.4 V (e) and Non-Cl-CdS SCs measured at 0 V (b), 0.2 V (d), and 0.4 V (f).

above the valence band maximum (VBM), while the Se vacancy (V_{Se}) lies ~0.5–0.7 eV below the conduction band minimum (CBM), depending on its charge state and local coordination [8,44,40]. Antisite defects such as Sb_{Se} and Se_{Sb} are both amphoteric in nature, with defect levels located at VBM +0.494 eV and VBM +0.697 eV, respectively. Due to their mid-gap positioning and comparable capture cross-sections for both electrons and holes, these antisite defects are potentially highly detrimental to photovoltaic performance, acting as efficient non-radiative recombination centers ([8,14,40,41]).

In our case, the extracted activation energies of 0.44 eV (non-Cl) and 0.47 eV (Cl-CdS SCs) devices fall in a range that aligns more closely with either V_{Sb} or Sb_{Se} defects. The similarity in E_A values, along with the above comparable trap densities observed, may indicate the presence of a similar dominant defect mechanism in both device types.

Regardless of the specific nature of the dominant defects, the enhanced device performance (~5 % PCE) observed in Cl-CdS/Sb_2Se_3 solar cells highlights the combined benefits of optimized VTD absorber growth conditions and Cl-processing of CdS ETL. SIMS analysis in our previous article [27] confirmed Cd diffusion into the Sb_2Se_3 absorber grown on Cl-processed CdS, and several studies have linked this diffusion to the effective passivation of deep antisite and vacancy defects, particularly near the interface [41]. These are likely deeper states with

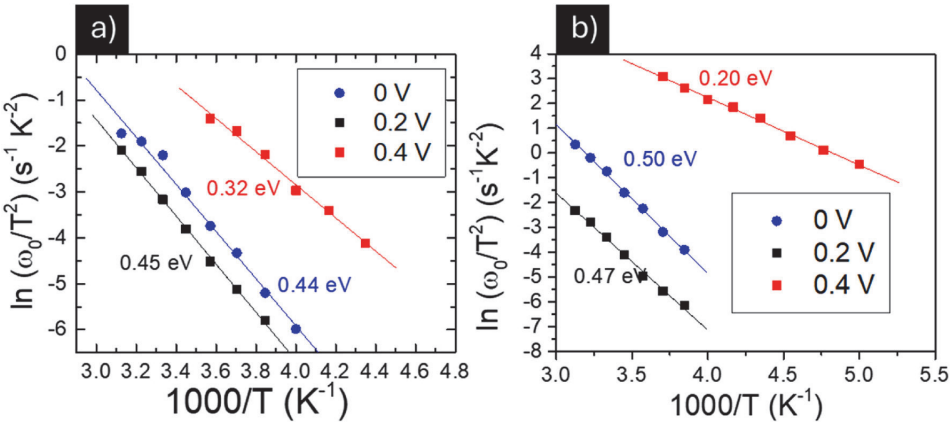

Fig. 7. Arrhenius plot of the inflection frequencies of Cl-CdS SCs (a) and Non-Cl-CdS (b) SCs measured under 0 V, 0.2 V, and 0.4 V bias.

higher activation energies that, unfortunately, were not detectable through the admittance spectroscopy measurements in this study. Additionally, deposition onto Cl-treated CdS promotes balanced Cd and Cl interdiffusion, which not only improves interface quality but may also facilitate the diffusion of nucleation centers, resulting in larger, better-oriented grains. These synergistic effects improve both the optoelectronic properties of the absorber and the quality of the heterojunction interface.

The achieved 10 % boost in PCE by optimizing the VTD growth rate in Cl-processed CdS-based devices is relevant; however, in terms of benchmarking, the highest PCE is reported for superstrate-configured Sb_2Se_3 solar cells fabricated via VTD are 7.6 % with a CdS ETL using a $CdCl_2$ post-deposition treatment (Wen et al., 2018). While our current efficiency remains below the state-of-the-art 7.6 % device, it is still comparable with other reported R&D efforts (with PCEs between 4.5 and 5.3 % [3,28] and was achieved without using 'classically employed' $CdCl_2$ PDT processing of CdS. It is also worth noting that although the 7.6 % result is frequently cited as a benchmark, its reproducibility has been limited. To our knowledge, no other group has independently replicated this performance using $CdCl_2$-treated CdS ETLs in VTD-based Sb_2Se_3 devices, i.e., in a simplified superstrate architecture (glass/FTO/CdS/VTD-Sb_2Se_3/Au) without additional absorber doping or charge-selective layers at the back contact. This suggests that the reported approach may involve nuanced processing conditions that are not yet fully disclosed/understood. Therefore, our study contributes to a more systematic understanding of how VTD parameters affect the Sb_2Se_3 growth rate and their implications on bulk and interface defect chemistry and device performance, an important step toward long-term goal of achieving more reproducible and scalable high-efficiency Sb_2Se_3 solar cells.

Importantly, these findings suggest that further performance gains are achievable if such defect states can be more effectively controlled or eliminated through further targeted material and interface engineering strategies. Recent strategies to mitigate defects at the CdS/Sb_2Se_3 interface include post-deposition selenium treatments and alkali metal doping, such as lithium incorporation into the CdS layer, followed by a $CdCl_2$ monolayer insertion to improve interface quality [42]. Tellurium alloying in Sb_2Se_3 has also been shown to adjust the Sb/Se ratio and suppress Sb_{Se} defect formation [43]. Additionally, photo-annealing has emerged as a promising technique to promote atomic rearrangement, enhancing lattice matching and reducing interfacial defect density, particularly Sb_{Se} antisites [41]. Together, these approaches underscore the importance of targeted defect passivation and interface engineering in improving Sb_2Se_3 solar cell performance.

4. Conclusions

This study established an optimized growth protocol for Sb_2Se_3 absorber films deposited via vapor VTD method by incorporating Ar gas to regulate the growth rate and optimizing the source-to-substrate distance ($D_{So\text{-}Sub}$) to achieve uniform and compact grain growth on CdS ETL. Sb_2Se_3 films were deposited on both chloride-processed and non-chloride-processed CdS (Cl-CdS, Non-Cl-CdS), allowing for a comparative analysis of their structural properties and solar cell performance. XRD analysis confirmed a predominant hk1 orientation in Sb_2Se_3 films, largely independent of $D_{So\text{-}Sub}$ variations. However, surface morphology studies revealed that films deposited at $D_{So\text{-}Sub} < 3$ cm exhibited significant roughness, whereas films at $D_{So\text{-}Sub} > 8$ cm displayed inhomogeneous grains and a dispersed structure. An optimal $D_{So\text{-}Sub}$ of ~6 cm resulted in uniform, compact, and well-structured Sb_2Se_3 grains. Superstrate-configuration solar cells (glass/FTO/CdS/Sb_2Se_3/Au) fabricated with Cl-CdS and with absorber deposited at $D_{So\text{-}Sub}$ of ~6 cm achieved a PCE of 5 %, representing an ~10 % improvement over CdS/Sb_2Se_3 devices with Non-Cl-CdS. A comprehensive analysis with considerations of the underlying physicochemical factors (including thermodynamic aspects) responsible for the enhanced properties of the VTD-grown Sb_2Se_3 absorber, related interface, as well as their implications to overall device functionality was provided. Temperature-dependent open-circuit voltage (V_{OC}) studies indicated decreased interface recombination in the CdS/Sb_2Se_3 device with Cl-CdS ETL compared to the device Non-Cl-CdS. Dark J-V analysis estimated a trap density of 10^{14} cm^{-3}, lower than previously reported values, confirming the high quality of Sb_2Se_3 films deposited through optimized VTD processing. Voltage-dependent admittance spectroscopy suggested a reduction in activation energy with increasing bias, suggesting that interface defects still contribute to the performance limitation. These findings highlight the critical role of deposition parameters, particularly $D_{So\text{-}Sub}$ and growth rate, in enhancing Sb_2Se_3 film growth and solar cell performance. However, persistent interface defects at the CdS/Sb_2Se_3 junction remain a challenging factor, necessitating further interface engineering strategies to minimize recombination losses and improve device efficiency.

CRediT authorship contribution statement

Sajeesh Vadakkedath Gopi: Writing – review & editing, Writing – original draft, Visualization, Validation, Investigation, Formal analysis, Data curation, Conceptualization. **Robert Krautmann:** Writing – review & editing, Writing – original draft, Visualization, Validation, Data

curation. **Atanas Katerski:** Methodology, Formal analysis, Data curation. **Raavo Josepson:** Visualization, Validation, Formal analysis, Data curation. **Dumitru Untila:** Validation, Formal analysis. **Jaan Hiie:** Methodology. **Malle Krunks:** Writing – review & editing, Validation. **Ilona Oja Acik:** Validation, Supervision, Project administration, Funding acquisition. **Nicolae Spalatu:** Writing – review & editing, Writing – original draft, Validation, Supervision, Project administration, Methodology, Investigation, Funding acquisition, Conceptualization.

Conflict of interest

We wish to draw the attention of the Editor to the following facts, which may be considered as potential conflicts of interest, and to significant financial contributions to this work:

The nature of potential conflict of interest is described below:

No conflict of interest exists.

We wish to confirm that there are no known conflicts of interest associated with this publication and there has been no significant financial support for this work that could have influenced its outcome.

Intellectual property

We confirm that we have given due consideration to the protection of intellectual property associated with this work and that there are no impediments to publication, including the timing of publication, with respect to intellectual property. In so doing we confirm that we have followed the regulations of our institutions concerning intellectual property.

Authorship

The International Committee of Medical Journal Editors (ICMJE) recommends that authorship be based on the following four criteria.

1. Substantial contributions to the conception or design of the work; or the acquisition, analysis, or interpretation of data for the work; AND
2. Drafting the work or revising it critically for important intellectual content; AND
3. Final approval of the version to be published; AND
4. Agreement to be accountable for all aspects of the work in ensuring that questions related to the accuracy or integrity of any part of the work are appropriately investigated and resolved.

All those designated as authors should meet all four criteria for authorship, and all who meet the four criteria should be identified as authors. For more information on authorship, please see http://www.icmje.org/recommendations/browse/roles-and-responsibilities/defining-the-role-of-authors-and-contributors.html#two.

We believe these individuals should be listed as authors because.

We confirm that the manuscript has been read and approved by all named authors.

We confirm that the order of authors listed in the manuscript has been approved by all named authors.

Contact with the editorial office

The Corresponding Authors declared on the title page of the manuscript are:

Sajeesh Vadakkedath Gopi and Nicolae Spalatu.

This author submitted this manuscript using his/her account in EVISE.

We understand that this Corresponding Author is the sole contact for the Editorial process (including EVISE and direct communications with the office). He/she is responsible for communicating with the other authors about progress, submissions of revisions and final approval of proofs.

We confirm that the shown below is accessible by the Corresponding Author, is the address to which Corresponding Author's EVISE account is linked, and has been configured to accept from the editorial office of American Journal of Ophthalmology Case Reports [nicolae.spalatu@taltech.ee]

Funding

Funding was received for this work.

All of the sources of funding for the work described in this publication are acknowledged below.

- *Estonian Research Council project PRG2676, "All inorganic semi-transparent thin film solar cells for solar windows and indoor photovoltaics"*
- *Estonian Ministry of Education and Research project (TK210; TK210U8) „Center of Excellence in Sustainable Green Hydrogen and Energy Technologies",*
- *the Clean Energy Transition Partnership under the 2022 CETPartnership joint call for research proposals, co-funded by the European Commission (GA N°101069750)*
- *Estonian Research Council, agreement No MOB3PRT2*
- *The European Union's H2020 programme under the ERA Chair project 5GSOLAR grant agreement No 952509.*
- *COST Action Research and International Networking on Emerging Inorganic Chalcogenides for Photovoltaics (RENEW-PV), CA21148, supported by COST (European Cooperation in Science and Technology)*

Declaration of competing interest

The authors declare that they have no known competing financial interests or personal relationships that could have appeared to influence the work reported in this paper.

Acknowledgements

This study was funded by the Estonian Research Council project PRG2676, "All inorganic semi-transparent thin film solar cells for solar windows and indoor photovoltaics", PSG689 "Bismuth Chalcogenide Thin-Film Disruptive Green Solar Technology for Next Generation Photovoltaics", the Estonian Ministry of Education and Research project TK210; TK210U8 "Center of Excellence in Sustainable Green Hydrogen and Energy Technologies", and the work supported by EU Horizon 2020 project 952509-5GSOLAR. This research was funded by CETPartnership, the Clean Energy Transition Partnership under the 2022 CETPartnership joint call for research proposals, co-funded by the European Commission (GA N°101069750), and with the funding organisation Estonian Research Council, agreement No MOB3PRT2. The article is based upon work from COST Action Research and International Networking on Emerging Inorganic Chalcogenides for Photovoltaics (RENEW-PV), CA21148, supported by COST (European Cooperation in Science and Technology).

Appendix A. Supplementary data

Supplementary data to this article can be found online at https://doi.org/10.1016/j.solmat.2025.113856.

Data availability

Data will be made available on request.

References

[1] Z. Li, X. Liang, G. Li, H. Liu, H. Zhang, J. Guo, J. Chen, K. Shen, X. San, W. Yu, R.E. I. Schropp, Y. Mai, 9.2%-efficient core-shell structured antimony selenide nanorod array solar cells, Nat. Commun. 10 (2019), https://doi.org/10.1038/s41467-018-07903-6.

[2] Wen, X., Chen, C., Lu, S., Li, K., Kondrotas, R., Zhao, Y., Chen, W., Gao, L., Wang, C., Zhang, J., Niu, G., Tang, J., n.d. Vapor Transport Deposition of Antimony Selenide Thin Film Solar Cells with 7.6% Efficiency. https://doi.org/10.1038/s41467-018-04634-6.

[3] R. Juskėnas, A. Naujokaitis, A. Drabavičius, V. Pakštas, D. Vainauskas, R. Kondrotas, Seed layer optimisation for ultra-thin Sb2Se3 solar cells on TiO2 by vapour transport deposition, Materials 15 (2022), https://doi.org/10.3390/ma15238356.

[4] R. Krautmann, N. Spalatu, R. Gunder, D. Abou-Ras, T. Unold, S. Schorr, M. Krunks, I.O. Acik, Analysis of grain orientation and defects in Sb 2 Se 3 solar cells fabricated by close-spaced sublimation, Sol. Energy 225 (2021) 494–500, https://doi.org/10.1016/j.solener.2021.07.022.

[5] Y. Zhao, S. Wang, C. Li, B. Che, X. Chen, H. Chen, R. Tang, X. Wang, G. Chen, T. Wang, J. Gong, T. Chen, X. Xiao, J. Li, Regulating deposition kinetics via a novel additive-assisted chemical bath deposition technology enables fabrication of 10.57%-efficiency Sb2Se3 solar cells, Energy Environ. Sci. 15 (2022) 5118–5128, https://doi.org/10.1039/d2ee02261c.

[6] C.H. Don, T.P. Shalvey, D.A. Sindi, B. Lewis, J.E.N. Swallow, L. Bowen, D. F. Fernandes, T. Kubart, D. Biswas, P.K. Thakur, T.L. Lee, J.D. Major, Reactive DC sputtered TiO2 electron transport layers for cadmium-free Sb2Se3 solar cells, Adv. Energy Mater. (2024), https://doi.org/10.1002/aenm.202401077.

[7] Y. Zhou, L. Wang, S. Chen, S. Qin, X. Liu, J. Chen, D.J. Xue, M. Luo, Y. Cao, Y. Cheng, E.H. Sargent, J. Tang, Thin-film Sb2Se3 photovoltaics with oriented one-dimensional ribbons and benign grain boundaries, Nat. Photonics 9 (2015) 409–415, https://doi.org/10.1038/nphoton.2015.78.

[8] N. Spalatu, R. Krautmann, A. Katerski, E. Karber, R. Josepson, J. Hiie, I.O. Acik, M. Krunks, Screening and optimization of processing temperature for Sb2Se3 thin film growth protocol: interrelation between grain structure, interface intermixing and solar cell performance, Sol. Energy Mater. Sol. Cell. 225 (2021), https://doi.org/10.1016/j.solmat.2021.111045.

[9] A. Graf, N. Maticiuc, N. Spalatu, V. Mikli, A. Mere, A. Gavrilov, J. Hiie, Electrical characterization of annealed chemical-bath-deposited CdS films and their application in superstrate configuration CdTe/CdS solar cells, in: Thin Solid Films, Elsevier B.V., 2015, pp. 351–355, https://doi.org/10.1016/j.tsf.2014.11.003.

[10] N. Maticiuc, N. Spalatu, V. Mikli, J. Hiie, Impact of CdS annealing atmosphere on the performance of CdS-CdTe solar cell, in: Applied Surface Science, Elsevier B.V., 2015, pp. 14–18, https://doi.org/10.1016/j.apsusc.2015.01.172.

[11] P. Prabeesh, V.G. Sajeesh, I. Packia Selvam, M.S. Divya Bharati, G. Mohan Rao, S. N. Potty, CZTS solar cell with non-toxic buffer layer: a study on the sulphurization temperature and absorber layer thickness, Sol. Energy 207 (2020) 419–427, https://doi.org/10.1016/j.solener.2020.06.103.

[12] L.J. Phillips, C.N. Savory, O.S. Hutter, P.J. Yates, H. Shiel, S. Mariotti, L. Bowen, M. Birkett, K. Durose, D.O. Scanlon, J.D. Major, Current Enhancement via a TiO 2 Window Layer for CSS Sb 2 Se 3 Solar Cells: performance limits and high V oc, IEEE J Photovolt 9 (2019) 544–551, https://doi.org/10.1109/JPHOTOV.2018.2885836.

[13] L. Wang, D.B. Li, K. Li, C. Chen, H.X. Deng, L. Gao, Y. Zhao, F. Jiang, L. Li, F. Huang, Y. He, H. Song, G. Niu, J. Tang, Stable 6%-efficient Sb2Se3 solar cells with a ZnO buffer layer, Nat. Energy 2 (2017), https://doi.org/10.1038/nenergy.2017.46.

[14] G. Chen, Y. Luo, M. Abbas, M. Ishaq, Z. Zheng, S. Chen, Z. Su, X. Zhang, P. Fan, G. Liang, Suppressing buried interface nonradiative recombination losses toward high-efficiency antimony Triselenide solar cells, Adv. Mater. 36 (2024), https://doi.org/10.1002/adma.202308522.

[15] J. Zhou, X. Zhang, H. Chen, Z. Tang, D. Meng, K. Chi, Y. Cai, G. Song, Y. Cao, Z. Hu, Dual-function of CdCl2 treated SnO2 in Sb2Se3 solar cells, Appl. Surf. Sci. 534 (2020), https://doi.org/10.1016/j.apsusc.2020.147632.

[16] Y. Wang, R. Tang, L. Huang, C. Qian, W. Lian, C. Zhu, T. Chen, Post-treatment of TiO2 film enables high-quality Sb2Se3 film deposition for solar cell applications, ACS Appl. Mater. Interfaces 14 (2022) 33181–33190, https://doi.org/10.1021/acsami.2c07157.

[17] M. Koltsov, R. Krautmann, A. Katerski, N. Maticiuc, M. Krunks, I. Oja Acik, N. Spalatu, A post-deposition annealing approach for organic residue control in TiO2 and its impact on Sb2Se3/TiO2 device performance, Faraday Discuss (2022), https://doi.org/10.1039/d2fd00064d.

[18] J. Tao, X. Hu, J. Xue, Y. Wang, G. Weng, S. Chen, Z. Zhu, J. Chu, Investigation of electronic transport mechanisms in Sb 2 Se 3 thin-film solar cells, Sol. Energy Mater. Sol. Cell. 197 (2019) 1–6, https://doi.org/10.1016/j.solmat.2019.04.003.

[19] H. Cai, R. Cao, J. Gao, C. Qian, B. Che, R. Tang, C. Zhu, T. Chen, Interfacial engineering towards enhanced photovoltaic performance of Sb2Se3 solar cell, Adv. Funct. Mater. (2022), https://doi.org/10.1002/adfm.202208243.

[20] D. Liu, R. Tang, Y. Ma, C. Jiang, W. Lian, G. Li, W. Han, C. Zhu, T. Chen, Direct hydrothermal deposition of antimony triselenide films for efficient planar heterojunction solar cells, ACS Appl. Mater. Interfaces 13 (2021) 18856–18864, https://doi.org/10.1021/acsami.1c02393.

[21] Y. Luo, G. Chen, S. Chen, N. Ahmad, M. Azam, Z. Zheng, Z. Su, M. Cathelinaud, H. Ma, Z. Chen, P. Fan, X. Zhang, G. Liang, Carrier transport enhancement mechanism in highly efficient antimony selenide thin-film solar cell, Adv. Funct. Mater. (2023), https://doi.org/10.1002/adfm.202213941.

[22] C. Chen, D.C. Bobela, Y. Yang, S. Lu, K. Zeng, C. Ge, B. Yang, L. Gao, Y. Zhao, M. C. Beard, J. Tang, Characterization of basic physical properties of Sb2Se3 and its relevance for photovoltaics, Front. Optoelectron. 10 (2017) 18–30, https://doi.org/10.1007/s12200-017-0702-z.

[23] X. Liu, C. Chen, L. Wang, J. Zhong, M. Luo, J. Chen, D.J. Xue, D. Li, Y. Zhou, J. Tang, Improving the performance of Sb2Se3 thin film solar cells over 4% by controlled addition of oxygen during film deposition, Prog. Photovoltaics Res. Appl. 23 (2015) 1828–1836, https://doi.org/10.1002/pip.2627.

[24] X. Hu, J. Tao, G. Weng, J. Jiang, S. Chen, Z. Zhu, J. Chu, Investigation of electrically-active defects in Sb2Se3 thin-film solar cells with up to 5.91% efficiency via admittance spectroscopy, Sol. Energy Mater. Sol. Cell. 186 (2018) 324–329, https://doi.org/10.1016/j.solmat.2018.07.004.

[25] L. Wang, M. Luo, S. Qin, X. Liu, J. Chen, B. Yang, M. Leng, D.J. Xue, Y. Zhou, L. Gao, H. Song, J. Tang, Ambient CdCl2 treatment on CdS buffer layer for improved performance of Sb2Se3 thin film photovoltaics, Appl. Phys. Lett. 107 (2015), https://doi.org/10.1063/1.4932544.

[26] S. Vadakkedath Gopi, N. Spalatu, M. Basnayaka, R. Krautmann, A. Katerski, R. Josepson, R. Grzibovskis, A. Vembris, M. Krunks, I. Oja Acik, Post deposition annealing effect on properties of CdS films and its impact on CdS/Sb2Se3 solar cells performance, Front. Energy Res. 11 (2023), https://doi.org/10.3389/fenrg.2023.1162576.

[27] S.V. Gopi, N. Spalatu, A. Katerski, J. Kuliček, B. Razek, E. Ukraintsev, M.Ś. Bařinková, G. Zoppi, R. Grzibovskis, A. Vembris, L. Ignatane, M. Krunks, I. O. Acik, An alternative chlorine-assisted optimization of CdS/Sb2Se3 solar cells: towards understanding of chlorine incorporation mechanism, J. Alloys Compd. 1005 (2024), https://doi.org/10.1016/j.jallcom.2024.176175.

[28] W. Wang, Z. Cao, H. Wang, J. Luo, Y. Zhang, Remarkable Cd-free Sb2Se3solar cell yield achieved by interface band-alignment and growth orientation screening, J Mater Chem A Mater 9 (2021) 26963–26975, https://doi.org/10.1039/d1ta08404f.

[29] G. Ghosh, The sb-se (antimony-selenium) system, JPE 14 (1993) 753–763, https://doi.org/10.1007/BF02667889.

[30] V. Volodin, A. Nitsenko, S. Trebukhov, X. Linnik, Y. Gapurov, Thermodynamics of formation and liquid–vapor phase transitions of antimony alloys with selenium and sulfur, Materials 17 (2024), https://doi.org/10.3390/ma17010125.

[31] S. Chen, M. Ishaq, W. Xiong, U. Ali Shah, U. Farooq, J. Luo, Z. Zheng, Z. Su, P. Fan, X. Zhang, G. Liang, Improved open-circuit voltage of Sb2Se3 thin-film solar cells via interfacial sulfur diffusion-induced gradient bandgap engineering, Sol. RRL 5 (2021), https://doi.org/10.1002/solr.202100419.

[32] Z. Feng, X. Liu, T. Tian, Z. Zhu, R. Jiang, J. Li, Y. Yuan, J. Gong, G. Gao, J. Tong, Y. Peng, S. Bai, F. Huang, X. Xiao, P. Müller-Buschbaum, Y.B. Cheng, T. Bu, Buried interface modulation using self-assembled monolayer and ionic liquid hybrids for high-performance perovskite and Perovskite/CuInGaSe2 tandem photovoltaics, Adv. Mater. (2025), https://doi.org/10.1002/adma.202412692.

[33] S. Chen, P. Luo, D. Lou Ren, C.Y. Duan, X.F. Ma, Z.H. Su, Z.H. Zheng, P. Fan, G. X. Liang, R. Tang, An effective engineering with simultaneous carrier density enhancement and interface optimization enables efficient Sb2Se3 solar cells, Appl. Surf. Sci. 619 (2023), https://doi.org/10.1016/j.apsusc.2023.156783.

[34] C. Duan, G. Chen, J. Zhao, C. Hu, W. Hu, U. Farooq, Z. Su, R. Tang, S. Chen, G. Liang, Plasma etching-induced surface modification and interfacial defect passivation for antimony triselenide thin film solar cells, Ceram. Int. 50 (2024) 12253–12262, https://doi.org/10.1016/j.ceramint.2024.01.129.

[35] J. Lin, A. Mahmood, G. Chen, N. Ahmad, M. Chen, P. Fan, S. Chen, R. Tang, G. Liang, Crystallographic orientation control and defect passivation for high-efficient antimony selenide thin-film solar cells, Materials Today Physics 27 (2022), https://doi.org/10.1016/j.mtphys.2022.100772.

[36] T.P. Weiss, S. Nishiwaki, B. Bissig, S. Buecheler, A.N. Tiwari, Voltage dependent admittance spectroscopy for the detection of near interface defect states for thin film solar cells, Phys. Chem. Chem. Phys. 19 (2017) 30410–30417, https://doi.org/10.1039/c7cp05236g.

[37] S. Levcenko, J. Just, A. Redinger, G. Larramona, S. Bourdais, G. Dennler, A. Jacob, T. Unold, Deep defects in Cu2ZnSn (S,Se)4 solar cells with varying Se content, Phys. Rev. Appl. 5 (2016), https://doi.org/10.1103/PhysRevApplied.5.024004.

[38] T. Walter, R. Herberholz, C. Müller, H.W. Schock, Determination of defect distributions from admittance measurements and application to Cu(In,Ga)Se2 based heterojunctions, J. Appl. Phys. 80 (1996) 4411–4420, https://doi.org/10.1063/1.363401.

[39] T.P. Weiss, I. Minguez-Bacho, E. Zuccalà, M. Melchiorre, N. Valle, B. El Adib, T. Yokosawa, E. Spiecker, J. Bachmann, P.J. Dale, S. Siebentritt, Post-deposition annealing and interfacial atomic layer deposition buffer layers of Sb2Se3/CdS stacks for reduced interface recombination and increased open-circuit voltages, Prog. Photovoltaics Res. Appl. (2022), https://doi.org/10.1002/pip.3625.

[40] C.N. Savory, D.O. Scanlon, The complex defect chemistry of antimony selenide, J Mater Chem A Mater 7 (2019) 10739–10744, https://doi.org/10.1039/c9ta02022e.

[41] X. Liang, X. Wang, Q. Chang, B. Yang, W. Dang, Z. Zhang, Y. Guo, L. Yang, Z. Li, Reduction of bulk and interface defects via photo-annealing treatment for high-efficiency antimony selenide solar cells, Energy Environ. Sci. (2024), https://doi.org/10.1039/d4ee02877e.

[42] C. Liu, A. Gong, C. Zuo, T. Liu, X. Liang, D. Ren, K. Shen, J. Zheng, Q. Xue, Z. Li, R. E.I. Schropp, B. Zou, Y. Mai, Heterojunction lithiation engineering and diffusion-induced defect passivation for highly efficient Sb2(S,Se)3 solar cells, Energy Environ. Sci. (2024), https://doi.org/10.1039/d4ee03135k.

[43] Y. Ma, B. Tang, W. Lian, C. Wu, X. Wang, H. Ju, C. Zhu, F. Fan, T. Chen, Efficient defect passivation of Sb2Se3 film by tellurium doping for high performance solar

cells, J Mater Chem A Mater 8 (2020) 6510–6516, https://doi.org/10.1039/d0ta00443j.

[44] M. Chen, M. Ishaq, D. Ren, H. Ma, Z. Su, P. Fan, D. Le Coq, X. Zhang, G. Liang, S. Chen, Interface optimization and defects suppression via NaF introduction enable efficient flexible Sb2Se3 thin-film solar cells, J. Energy Chem. 90 (2024) 165–175, https://doi.org/10.1016/j.jechem.2023.10.059.

[45] S. Chen, Y.A. Ye, M. Ishaq, D. Lou Ren, P. Luo, K.W. Wu, Y.J. Zeng, Z.H. Zheng, Z. H. Su, G.X. Liang, Simultaneous band alignment modulation and carrier dynamics optimization enable highest efficiency in Cd-Free Sb2Se3 solar cells, Adv. Funct. Mater. (2024), https://doi.org/10.1002/adfm.202403934.

Curriculum vitae

Personal data

Name:	Sajeesh Vadakkedath Gopi
Date of birth:	21.04.1994
Place of birth:	Thrissur, India
Citizenship:	Indian

Contact data

E-mail:	sajeesh.vadakkedath@taltech.ee, sajeesh94007@gmail.com

Education

2021–2025	Tallinn University of Technology, Estonia, Materials and Environmental Technology – PhD
2014–2016	S. N. College, Nattika, University of Calicut – M.Sc. Physics
2011–2014	Christ College Irinjalakuda, University of Calicut – B.Sc. Physics
2009–2011	N.H.S.S. Irinjalakuda, Board of Secondary Education, Kerala

Language competence

Malayalam	native
English	fluent
Hindi	fluent
Tamil	intermediate

Professional employment

2021–2025	Laboratory of thin film energy materials, Tallinn University of Technology, Estonia, Early-stage researcher.
2018–2020	Centre for Materials for Electronic Technology (C-MET), Thrissur, Project staff.

Supervised dissertations

Mohammad Kadkhodaei, Master's Degree, 2023, **Sajeesh Vadakkedath Gopi** (supervisor), Nimish Juneja (co-supervisor), Sb_2S_3 thin film solar cell for semi-transparent applications, Tallinn University of Technology, School of Engineering, Department of Materials and Environmental Technology.

Anam Quddas Qureshi, Master's degree, 2023, Development of Sb_2Se_3 thin film solar cells by vapor transport deposition, Robert Krautmann (supervisor), **Sajeesh Vadakkedath Gopi** (co supervisor), Tallinn University of Technology, School of Engineering, Department of Materials and Environmental Technology.

Eerik Martma, Bachelor's short project, 2022, Impact of $CdCl_2$ annealing temperature on CdS/Sb_2Se_3 solar cells. **Sajeesh Vadakkedath Gopi** (supervisor), Tallinn University of Technology, School of Engineering, Department of Materials and Environmental Technology.

Research projects

1. PRG627, Antimony chalcogenide thin films for next generation semi-transparent solar cells applicable in electricity producing windows
2. TAR16016EK, Advanced materials and high technology devices for energy recuperation systems.

3. PSG689, Bismuth chalcogenide thin film disruptive green solar technology for next generation photovoltaics.
4. VFP20035, ERA chair of emerging next generation photovoltaics.
5. CA21148, Emerging inorganic chalcogenides for photovoltaics.

List of publications

1. **Gopi, S. V.**, Krautmann, R., Katerski, A., Josepson, R., Untila, D., Hiie, J., Krunks, M., Acik, I. O., & Spalatu, N. (2025). Optimization of VTD Sb_2Se_3 absorber growth rate in CdS/Sb_2Se_3 thin film solar cells: A defect perspective on chloride vs non-chloride based devices. Solar Energy Materials and Solar Cells, 293, 113856. DOI: 10.1016/j.solmat.2025.113856
2. **Vadakkedath Gopi, S.**, Karuvanveettil, S., Packia Selvam, I., & Potty, S. N. (2025). Near-Infrared Plasmonic Planar Films: Advancements in Aluminum-Doped Zinc Oxide for Sensing and Telecommunications Applications. ACS Applied Electronic Materials, 7(6), 2557-2563. DOI: 10.1021/acsaelm.5c00014
3. **Gopi S. V.**, Spalatu N, Katerski A, Kuliček J, Razek B, Ukraintsev E, Bařinková MŠ, Zoppi G, Grzibovskis R, Vembris A, Ignatane L. (2024). An alternative chlorine-assisted optimization of CdS/Sb_2Se_3 solar cells: Towards understanding of chlorine incorporation mechanism. Journal of Alloys and Compounds. 1005, 176175. DOI: 10.1016/j.jallcom.2024.176175
4. Svirskaite LM, Kasparavičius E, Steponaitis M, Grzibovskis R, Franckevičius M, Katerski A, Naujokaitis A, Karazhanov S, **Gopi SV**, Aizstrauts A, Vembris A. (2024). Fluorene-and fluorenone-based molecules as electron-transporting SAMs for photovoltaic devices. RSC advances, 14, 14973-14981. DOI: 10.1039/D4RA00964A
5. Koltsov M, **Gopi SV**, Raadik T, Krustok J, Josepson R, Gržibovskis R, Vembris A, Spalatu N. (2023). Development of Bi_2S_3 thin film solar cells by close-spaced sublimation and analysis of absorber bulk defects via in-depth photoluminescence analysis. Solar Energy Materials and Solar Cells, 254, 112292. DOI: 10.1016/j.solmat.2023.112292
6. **Vadakkedath Gopi S**, Spalatu N, Basnayaka M, Krautmann R, Katerski A, Josepson R, Grzibovskis R, Vembris A, Krunks M, Oja Acik I. (2023). Post deposition annealing effect on properties of CdS films and its impact on CdS/Sb2Se3 solar cells performance. Frontiers in Energy Research, 11, 1162576. DOI: 10.3389/fenrg.2023.1162576
7. Prabeesh P, **Sajeesh VG**, Selvam IP, Potty SN. (2021). Influence of thiourea in the precursor solution on the structural, optical and electrical properties of CZTS thin films deposited via spray coating technique. Journal of Materials Science: Materials in Electronics, 32, 4146-4156.DOI: 10.1007/s10854-020-05156-y
8. Prabeesh P, **Sajeesh VG**, Selvam IP, Bharati MD, Rao GM, Potty SN. (2020). CZTS solar cell with non-toxic buffer layer: A study on the sulphurization temperature and absorber layer thickness. Solar Energy, 207, 419-427. DOI: 10.1016/j.solener.2020.06.103

Patents

1. A Coated Substrate For A Plasmonic Sensing Device And A Process Thereof, Ref. No. 568172, Indian patent, 2025.
2. A Transparent Heater And A Method Of Preparation Thereof, Ref. No. 473757, Indian patent, 2023.

Awards

1. Tallinn City Scholarship, https://haridus.postimees.ee/8143637/tallinn-tunnustas-raestipendiumiga-16-magistranti-ja-doktoranti, 2024.
2. Author of the best popular science article for research in Estonia portal in science in 3-minute competition. 2024.

Popular science publication

1. Finalist of Science in 3-minute competition, 2024, URL: https://youtu.be/da91QU8PoXI?si=sR2jXXBoF-1j-uug
2. Article in Research in Estonia portal, 2024, URL: https://researchinestonia.eu/2024/11/18/solar-cells-forest-fire-threats/

Elulookirjeldus

Isikuandmed

Nimi:	Sajeesh Vadakkedath Gopi
Sünnikuupäev:	21.04.1994
Sünnikoht:	Thrissur, India
Kodakondsus:	India

Kontaktandmed

E-post:	sajeesh.vadakkedath@taltech.ee, sajeesh94007@gmail.com

Haridus

2021–2025	Tallinna Tehnikaülikool, Eesti, Materjaliteadus ja keskkonnatehnoloogia – doktorantuur
2014–2016	S. N. College, Nattika, University of Calicut, MSc füüsika
2011–2014	Christ College, Irinjalakuda, University of Calicut, BSc füüsika
2009–2011	N.H.S.S. Irinjalakuda, Kerala osariigi keskharidusnõukogu

Keeleoskus

Malajalami keel	emakeel
Inglise keel	kõrgtase
Hindi keel	kõrgtase
Tamili keel	kesktase

Töökogemus

2021–2025	Õhukestekilelistekilede energiamaterjalide teaduslabor, Tallinna Tehnikaülikool, nooremteadur
2018–2020	Elektrooniliste materjalide tehnoloogiakeskus (C-MET), Thrissur, projektitöötaja

Juhendatud lõputööd

Mohammad Kadkhodaei, magistritöö, 2023, *Sb_2S_3 õhukeste kilede päikesepatareid poolläbipaistvates rakendustes*. Tallinna Tehnikaülikool, Inseneriteaduskond, Materjaliteaduse ja keskkonnatehnoloogia instituut. (Juhendaja: Sajeesh Vadakkedath Gopi, kaasjuhendaja: Nimish Juneja)

Anam Quddas Qureshi, magistritöö, 2023, *Sb_2Se_3 õhukeste kilede päikesepatareide arendamine aurutranspordi deposiidi meetodil*. (Juhendaja: Robert Krautmann, kaasjuhendaja: Sajeesh Vadakkedath Gopi). Tallinna Tehnikaülikool, Inseneriteaduskond, Materjaliteaduse ja keskkonnatehnoloogia instituut.

Eerik Martma, bakalaureusetöö, 2022, *$CdCl_2$ kuumtöötlustemperatuuri mõju CdS/Sb_2Se_3 päikesepatareidele*. (Juhendaja: Sajeesh Vadakkedath Gopi). Tallinna Tehnikaülikool, Inseneriteaduskond, Materjaliteaduse ja keskkonnatehnoloogia instituut.

Teadusprojektid

1. **PRG627** – Antimoni kalkogeniidide õhukesed kiled uue põlvkonna poolläbipaistvate päikesepatareide jaoks, mida saab kasutada elektrit tootvates akendes.
2. **TAR16016EK** – Täiustatud materjalid ja kõrgtehnoloogilised seadmed energia taaskasutussüsteemide jaoks.

3. **PSG689** – Vismuti kalkogeniidide õhukeste kilede roheline murranguline päikeseenergia tehnoloogia uue põlvkonna fotogalvaanikale.
4. **VFP20035** – Uue põlvkonna fotogalvaanika areneva tehnoloogia ERA-tool.
5. **CA21148** – Arenevad anorgaanilised kalkogeniidid fotogalvaanikaks.

Publikatsioonide loetelu

1. **Gopi, S. V.**, Krautmann, R., Katerski, A., Josepson, R., Untila, D., Hiie, J., Krunks, M., Acik, I. O., & Spalatu, N. (2025). Optimization of VTD Sb_2Se_3 absorber growth rate in CdS/Sb_2Se_3 thin film solar cells: A defect perspective on chloride vs non-chloride based devices. Solar Energy Materials and Solar Cells, 293, 113856. DOI: 10.1016/j.solmat.2025.113856
2. **Vadakkedath Gopi, S.**, Karuvanveettil, S., Packia Selvam, I., & Potty, S. N. (2025). Near-Infrared Plasmonic Planar Films: Advancements in Aluminum-Doped Zinc Oxide for Sensing and Telecommunications Applications. ACS Applied Electronic Materials, 7(6), 2557-2563. DOI: 10.1021/acsaelm.5c00014
3. **Gopi S. V.**, Spalatu N, Katerski A, Kuliček J, Razek B, Ukraintsev E, Bařinková MŠ, Zoppi G, Grzibovskis R, Vembris A, Ignatane L. (2024). An alternative chlorine-assisted optimization of CdS/Sb_2Se_3 solar cells: Towards understanding of chlorine incorporation mechanism. Journal of Alloys and Compounds. 1005, 176175. DOI: 10.1016/j.jallcom.2024.176175
4. Svirskaite LM, Kasparavičius E, Steponaitis M, Grzibovskis R, Franckevičius M, Katerski A, Naujokaitis A, Karazhanov S, **Gopi SV**, Aizstrauts A, Vembris A. (2024). Fluorene-and fluorenone-based molecules as electron-transporting SAMs for photovoltaic devices. RSC advances, 14, 14973-14981. DOI: 10.1039/D4RA00964A
5. Koltsov M, **Gopi SV**, Raadik T, Krustok J, Josepson R, Gržibovskis R, Vembris A, Spalatu N. (2023). Development of Bi_2S_3 thin film solar cells by close-spaced sublimation and analysis of absorber bulk defects via in-depth photoluminescence analysis. Solar Energy Materials and Solar Cells, 254, 112292. DOI: 10.1016/j.solmat.2023.112292
6. **Vadakkedath Gopi S**, Spalatu N, Basnayaka M, Krautmann R, Katerski A, Josepson R, Grzibovskis R, Vembris A, Krunks M, Oja Acik I. (2023). Post deposition annealing effect on properties of CdS films and its impact on CdS/Sb2Se3 solar cells performance. Frontiers in Energy Research, 11, 1162576. DOI: 10.3389/fenrg.2023.1162576
7. Prabeesh P, **Sajeesh VG**, Selvam IP, Potty SN. (2021). Influence of thiourea in the precursor solution on the structural, optical and electrical properties of CZTS thin films deposited via spray coating technique. Journal of Materials Science: Materials in Electronics, 32, 4146-4156.DOI: 10.1007/s10854-020-05156-y
8. Prabeesh P, **Sajeesh VG**, Selvam IP, Bharati MD, Rao GM, Potty SN. (2020). CZTS solar cell with non-toxic buffer layer: A study on the sulphurization temperature and absorber layer thickness. Solar Energy, 207, 419-427. DOI: 10.1016/j.solener.2020.06.103

Patendid

1. Kattekihiga Substraat Plasmonilisele Anduriseadmele ja Selle Valmistamise Protsess, viitenumber 568172, India patent, 2025.
2. Läbipaistev küttekeha ja selle valmistamise meetod, 2023, Ref. nr 473757, India patent.

Auhinnad

1. Tallinna linna stipendium, 2024 (viide).
2. Parima populaarteadusliku artikli auhind, „Teadus 3 minutiga" konkursil, 2024.

Populaarteaduslikud väljaanded

1. Finalist konkursil *Science in 3 Minutes*, 2024 (YouTube link)
2. Artikkel *Research in Estonia* portaalis, 2024 (viide)

ISSN 2585-6901 (PDF)
ISBN 978-9916-80-406-3 (PDF)